Distribution Agreement

In presenting this thesis or dissertation as a partial fulfillment of the requirements for an advanced degree from Emory University, I hereby grant to Emory University and its agents the non-exclusive license to archive, make accessible, and display my thesis or dissertation in whole or in part in all forms of media, now or hereafter known, including display on the world wide web. I understand that I may select some access restrictions as part of the online submission of this thesis or dissertation. I retain all ownership rights to the copyright of the thesis or dissertation. I also retain the right to use in all future works (such as articles or books) all or part of this thesis or dissertation.

Signature:

_____ _____

Eduardo D. Gigante Date

Relationship of the ciliary GTPase, ARL13B, and the GPCR, SMOOTHENED

By

Eduardo D. Gigante

Doctor of Philosophy

Graduate Division of Biological and Biomedical Sciences
Neuroscience

Tamara Caspary, Ph.D.
Advisor

Victor Faundez, MD, Ph.D.
Committee Member

Randy Hall, Ph.D.
Committee Member

Richard A. Kahn, Ph.D.
Committee Member

Peter Wenner, Ph.D.
Committee Member

Accepted:

Lisa A. Tedesco, Ph.D.
Dean of the James T. Laney School of Graduate Studies

Date

Relationship of the ciliary GTPase, ARL13B, and the GPCR, SMOOTHENED

By

Eduardo D. Gigante

B.S., Binghamton University, 2010

M.S., Binghamton University, 2012

Advisor: Tamara Caspary, Ph.D.

An abstract of

A dissertation submitted to the Faculty of the

James T. Laney School of Graduate Studies of Emory University

in partial fulfillment of the requirements for the degree of

Doctor of Philosophy

in the Graduate Division of Biological and Biomedical Sciences

Neuroscience

2021

Abstract

Relationship of the ciliary GTPase, ARL13B, and the GPCR, SMOOTHENED

By Eduardo D. Gigante

In vertebrates, the neurons of the brain and spinal cord are organized and specified during embryonic development. Cell fate decisions are influenced by extracellular ligands interacting with receptive progenitor cells. The progenitors of the neural tube are highly responsive to Sonic Hedgehog (Shh) ligand. In each progenitor, the core components of the Shh pathway dynamically localize to the membrane of the primary cilium. Shh ligand binds to its receptor Patched1 (PTCH1), causing PTCH1 export from cilia and removing PTCH1 mediated suppression over the G-protein coupled receptor SMOOTHENED (SMO). Activated SMO promotes the formation of activating GLI transcription factors which induce Shh-dependent genes. The mechanism by which PTCH1 suppresses SMO and the endogenous substrate that activates SMO are unknown, but they are linked to cilia. The ciliary GTPase ARL13B regulates Shh signaling at multiple levels, influencing the production of activating GLI transcription factor and SMO trafficking to cilia. ARL13B function on SMO is elusive because it is masked by ARL13B's downstream function. My central hypothesis is that ARL13B regulates the ciliary processes that activate SMO as its loss disrupts both SMO trafficking and Shh pathway activation.

This dissertation describes my work on the role of ARL13B in regulating the ciliary processes that traffic and activate SMO. I show that SMO activation of high level Shh signaling is dependent on its enrichment in cilia. I show that ARL13B regulates Shh signaling and the ciliary organization of the pathway's components from outside cilia, effectively uncoupling ARL13B's function from its location. I demonstrate new models of cystic kidney disease, and obesity and diabetes caused by excluding ARL13B from the ciliary environment. I present genetic evidence consistent with ARL13B function upstream of SMO, regulating a still unknown ciliary process. The core of this dissertation demonstrates that ARL13B plays an essential role in the regulation of SMO and the Shh pathway, and that it can fulfill this role from outside the cilium. Together, my results fill fundamental gaps in our knowledge of SMO activation and cilia and show that ARL13B has tissue specific ciliary and non-ciliary roles that still need to be deciphered.

Relationship of the ciliary GTPase, ARL13B, and the GPCR, SMOOTHENED

By

Eduardo D. Gigante
B.S., Binghamton University, 2010
M.S., Binghamton University, 2012

Advisor: Tamara Caspary, Ph.D.

A dissertation submitted to the Faculty of the
James T. Laney School of Graduate Studies of Emory University
in partial fulfillment of the requirements for the degree of
Doctor of Philosophy
in the Graduate Division of Biological and Biomedical Sciences
Neuroscience
2021

Acknowledgements

I think it's most appropriate to start by acknowledging the mice. Animal research is costly, and not just in dollars and cents.

This degree, and my living stipend, were funded by US taxpayer dollars awarded by the NIH. I know what a privilege this is. I will not take it for granted.

I owe any success I have had to the people who pushed or nudged me along.

My mother who pushed me to attend community college.

My community college Biology professor Dr. Peter Kraai who pushed me (literally) into my first Summer research experience.

Thank you to the scientists who let me work (make mistakes) in their labs. Dr. Stephen Boehm, Dr. Linda P. Spear, Dr. David Werner, Dr. Marisela Morales, Dr. Roy Wise, Dr. Randy Hall, and Dr. Tamara Caspary.

Thank you, Dr. David Werner, you took me on as your first graduate student without knowing what you were hiring. I appreciate the support you gave when I decided I didn't want to continue at Binghamton.

Thank you, Dr. Roy Wise. I joined your lab after leaving Binghamton, unsure what to do next and looking for guidance. Working for you pushed me to seek out better mentors.

Thank you, Dr. Marisela Morales, for letting me unofficially join your lab.

Thank you to Dr. David Root and Dr. David Barker. I felt very isolated and directionless during my three years at NIDA. You let me join you on your projects and be part of your research. Working with you reminded me how fun science can be. You inspired me to get my PhD and follow my interests.

Thank you, Dr. Alyssa Long. For helping me redesign primers when I couldn't run the same failed PCR again. Your organization and vast knowledge helped me accomplish whatever I managed to accomplish in the last 5 years. Thank you for making the V358A mouse, it might be the best work I have ever done.

Thank you, lab mates, Tim Rutkowski, Sarah Suciu, Sarah Bay, Laura Mariani, Robby Van Sciver, Rachel Bruce, Sandii Constable, and Tiffany Terry.

Thank you, committee members for your time and efforts. Your guidance and support has helped bring me to this achievement.

Thank you, Tamara. You took a chance on me; I had limited formal genetics education and a heavy background in behavioral neuroscience. I have grown more in the last 5 years than I did in the prior 27. I think what your mentorship did best was motivate me to push myself. If Dr. Kraai helped me find my direction, you helped me find my drive.

Thank you to my family for putting up with my aimlessness. You were skeptical about me going back to school to get this degree but supported me none the less.

Thank you to my mother and father for showing me that getting a PhD in your thirties and starting a family is, in fact, humanly possible.

Thank you to my grandparents and my father for coming to this country so that I could live this dream.

My grandfather Louis Palomeque was able to watch my defense from Syracuse, NY. He passed away just a few days after watching me achieve this goal. The love and support he gave me for the last 32 years helped bring me to this moment.

Finally, to my wife, Crystal. You're the reason this was possible. Since I met you, you believed in me, supported me, and kept me balanced. You are my guiding light. This document exists because of you.

For Elena.

Abbreviations

- Shh – Sonic Hedgehog
- vHh – vertebrate Hedgehog
- ivHh – invertebrate Hedgehog
- SMO - SMOOTHENED
- PTCH1 – PATCHED1
- E – embryonic day
- FBS – fetal bovine serum
- IFT – intraflagellar transport
- GAP – GTPase activating protein
- GEF – guanine nucleotide exchange factor
- GLIA – Gli activator
- GLIR – Gli repressor
- GPCR – G-protein coupled receptor
- GTP – guanosine nucleotide triphosphate
- JS – Joubert Syndrome
- MEF – mouse embryonic fibroblast
- P – postnatal day
- PBS – phosphate buffered saline
- PKD – polycystic kidney disease
- PFA – paraformaldehyde

Table of Contents

List of Figures and Tables

CHAPTER 1

CILIA-DEPENDENT HEDGEHOG SIGNALING AND ITS REGULATION BY CILIA PROTEINS

Parts of this chapter previously published as:

Gigante, E.D., and Caspary, T. (2020) Signaling in the primary cilium through the lens of the Hedgehog pathway. *WIREs Developmental Biology. doi.org/10.1002/wdev.377*

Licensed reproduction by John Wiley and Sons, number: 4960350495212

1.1 Introduction of cilia structure and function

Cilia are microtubule-based, cell-surface projections encased in a plasma membrane that is continuous with, yet biochemically distinct from, the membrane of the cell. Cilia are templated from a modified centriole called the basal body (Marshall 2008). The basic architecture and components of the cilium are highly conserved through evolution (Pazour et al. 2000; Pazour et al. 2002a). Primary cilia, also called sensory or immotile cilia, are found on most cell types (Bangs et al. 2015). When viewed in cross section, nine microtubule doublets are arranged in a circular fashion to form the axoneme. Motile cilia (and synonymous flagella), have an additional central pair of microtubules that are critical for the ciliary machinery that generates force, and thus motility (Fawcett et al. 1954; Manton et al. 1952). Over the last two decades our understanding of primary cilia has shifted dramatically. While they were once thought to be vestigial organelles, cilia are now appreciated as fundamental cell organelles with essential roles in cell signaling throughout an organism (Barr et al. 1999; Pazour et al. 2000; Huangfu et al. 2003). Disruption of cilia proteins and processes leads to human diseases, collectively termed ciliopathies (Baker et al. 2009).

The axoneme is the microtubule backbone of the cilium, composed of α– and β–tubulin polymers called protofilaments that are organized in doublets (Fawcett et al. 1954; Manton et al. 1952). From within the cell, the basal body determines the position and orientation of the cilium on the cell surface, and it assists with the physical anchoring of cilium to the intracellular surface (Marshall 2008; Lechtreck et al. 1999). Immediately distal to the basal body is the transition zone that prevents proteins from freely entering or exiting the cilium. The transition zone is comprised of several proteins: Y-shaped proteins that link the axoneme to the ciliary membrane, the ciliary necklace that prevents protein diffusion along the membrane, and distal appendages that link the basal body to the cell membrane. Together, the proteins of the transition zone act as a diffusion

barrier, excluding large or improperly targeted proteins from entering the cilium (Yang et al. 2018; Kee et al. 2012; Chih et al. 2011; Breslow et al. 2013; Lechtreck et al. 1999; Ishikawa et al. 2005; Reiter et al. 2012). Thus, the transition zone separates the cell from the cilium, creating an exclusive ciliary environment (**Figure 1.1**).

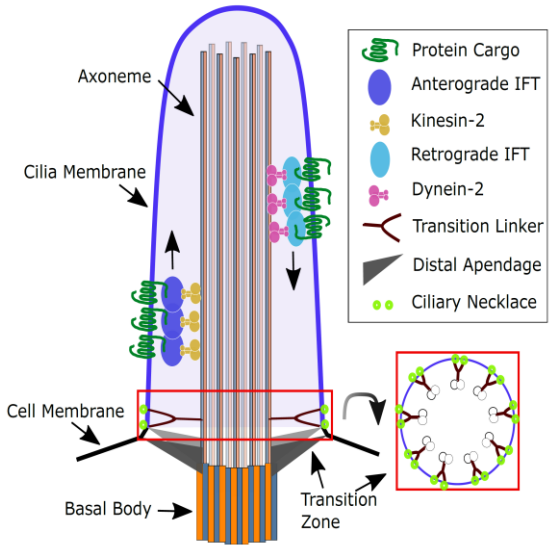

Figure 1.1 Model of ciliary structure.

The cilium is a microtubule projection comprised of 9 microtubule doublets that make up the axoneme. The axoneme is anchored to the basal body, which resides in the cell. Trafficking into and out of cilia is regulated by the transition zone at the proximal end of the cilium. The transition zone is comprised of Y-shaped linker proteins, ciliary necklace membrane proteins, and distal and sub-distal appendages. Together, the transition zone acts as a diffusion barrier, preventing the free movement of proteins into the cilium. Moreover, the transition zone regulates the active transport of proteins into and out of cilia. Finally, the transition zone provides structural support to the basal body and axoneme, anchoring the ciliary skeleton to the plasma membrane. Proteins are transported to the ciliary tip and back via anterograde and retrograde IFT, respectively. The ciliary membrane is contiguous to the cell's plasma membrane but the ciliary membrane displays a distinct lipid composition being enriched for PI(4)P.

Cilia provide a small and exclusive compartment where receptors and mediators of some signaling cascades rapidly interact to propagate intracellular responses. This is epitomized by G-protein coupled receptor (GPCR) signaling as multiple GPCRs display ciliary enrichment (Corbit et al. 2005; Domire et al. 2011; Mukhopadhyay et al. 2013; Brailov et al. 2000; Handel et al. 1999). Vertebrate Hedgehog (vHh) signaling requires the primary cilium for signal transduction (Huangfu et al. 2005; Huangfu et al. 2003). It serves as an exemplar of cilia-dependent signaling as it requires activation of the GPCR, SMOOTHENED (SMO), within the cilium and is intensely studied (Corbit et al. 2005; Rohatgi et al. 2009). Despite the strong focus, there are unknowns surrounding

the cilia-dependent and independent mechanisms that regulate SMO trafficking to, activation, and enrichment in cilia.

One ciliary protein that regulates SMO is the small atypical membrane associated GTPase ARL13B. This protein is detectable in cilia across model systems and in most ciliated cells. In mouse, loss of *Arl13b* disrupts Shh-dependent neural tube patterning in development (Caspary et al. 2007). Furthermore, SMO is aberrantly enriched in cilia, suggesting a role in SMO trafficking or ciliary exit (Larkins et al. 2011). Thus, my work aims to define the relationship among ARL13B, SMO and the primary cilium.

In this introduction, I will provide the background in four distinct areas, the intersection of which provide the basis of my investigations. First, I will introduce the cilium and the intraciliary machinery that help cilia function. Second, I will discuss Hh signaling focusing on the link between cilia and vHh signaling. This information is critical to understanding the dependence of the Sonic Hedgehog (Shh) pathway on the cilium. Third, I will introduce ARL13B and its multiple known roles before emphasizing ARL13B's role in regulating Shh signaling. This will enable me to highlight the obligate transducer of the Hedgehog pathway, the GPCR SMO, in relation to cilia and ARL13B. Finally, I will discuss the evolutionary origin of the Hedgehog pathway's dependence on cilia, and how examining the relationship between ARL13B and SMO will give us insight into this developmental change.

1.2 The Role of Intraflagellar Transport (IFT)

Cilia do not contain the molecular machinery for protein translation and synthesis so depend on a transport mechanism called intraflagellar transport (IFT) for moving proteins to, within, and from cilia (Rosenbaum et al. 1967). IFT refers to the transport process as well as the

class of proteins that mediate cargo transport. Initially described in the algae, Chlamydomonas reinhardtii, IFT is conserved in all ciliated species, including mammals (Kozminski et al. 1993; Rosenbaum et al. 2002; Pazour et al. 2002a; Pazour et al. 2000). A subcomplex of IFT proteins travels anterograde, to move ciliary cargos towards the distal tip of the cilium via a kinesin-2 motor, whereas a distinct subcomplex of IFT proteins treks retrograde, to return proteins from the tip using a dynein-2 motor (Pazour et al. 1998; Kozminski et al. 1995). Therefore, IFT mediates the construction and maintenance of cilia (Kozminski et al. 1995; Kozminski et al. 1993). During ciliogenesis, α– and β–tubulin are added at the distal tip of the ciliary axoneme through IFT (Johnson et al. 1992). Disruptions in these processes lead to cilia anomalies. Cells lacking anterograde IFT lack cilia, whereas those lacking retrograde IFT display bulbous cilia due to a traffic jam of proteins trapped inside (Huang et al. 1977; Adams et al. 1982). When IFT stops, cilia shorten indicating IFT is also required for cilia maintenance (Marshall et al. 2001).

1.3 Vertebrate Hedgehog signaling requires the cilium

The initial link between vertebrate Hh signaling and cilia surprised the field primarily because invertebrate Hh signaling was well studied in *Drosophila*, where the pathway was identified (Nusslein-Volhard et al. 1980). While flies do have cilia, subsequent studies in fly IFT mutants did not reveal any defects in invertebrate Hh signaling. Planaria (*Schmidtea mediterranea*) possess both motile cilia and Hh signaling, but they are not functionally linked (Rink et al. 2009). In evolutionary terms, the earliest link between cilia and Hh is in sea urchin which use motile cilia to transduce Hh signaling in developing muscle tissue (Walton et al. 2009; Warner et al. 2014). Subsequently, within deuterostomes, all members within the vertebrate lineage require primary cilia for Hh signaling (Park et al. 2006; Huang et al. 2009; Tay et al. 2010; Glazer et al. 2010a). It remains unclear whether vertebrates use motile cilia, in addition to primary cilia, for Hh signaling.

In addition to testing individual organisms for functional links of Hh and cilia, several clues come from examining when proteins that link the processes evolved. IFT25 and IFT27 regulate vHh but are unique among IFT components as they are lost in *C. elegans* and *Drosophila*, suggesting they may not play essential roles in cilia. Mice without *Ift25*, ciliate normally, but die shortly after birth with phenotypes consistent with low Hh signaling (Keady et al. 2012). *Ift27* mouse mutants display similar phenotypes. IFT25 and IFT27 are required for the export of SMO and PTCH1 out of cilia so may have evolved specifically to traffic Hh components (Eguether et al. 2014; Liew et al. 2014).

As the Hh pathway evolved to depend on the cilium, components of the Hh signaling pathway also evolved. Vertebrates have two Hh ligands in addition to Shh: Desert (Dhh) and Indian (Ihh), which play tissue-specific roles. Originally, its known function was limited to germ cell differentiation and new functions are still being discovered (Bitgood et al. 1996). More recently, Dhh blocks adipogenic pathways, preventing the formation of fat deposits in injured muscle (Kopinke et al. 2017). Ihh is best known for roles in skeletal development (St-Jacques et al. 1999). Similarly, the transcriptional mediator, Ci expanded to GLI1, GLI2 and GLI3 in vertebrates (Matise et al. 1998; Litingtung et al. 2000; Park et al. 2000; Alexandre et al. 1996; Hui et al. 1994). Components such as FUSED and SUFU exist in invertebrates and vertebrates but their functional importance is swapped as they evolved (Ruel et al. 2003; Svard et al. 2006; Cooper et al. 2005). KIF7 seems to carry out similar function in vertebrates to Costal-2 in invertebrates despite their poor sequence homology (Liem et al. 2009; Farzan et al. 2008). The exception is SMO, relatively unchanged; it is the sole, obligate transducer of the Hh pathway in both

invertebrate and vertebrate Hh signaling (Alcedo et al. 1996). (See (Briscoe et al. 2013) for a comparison of vHh and ivHh components).

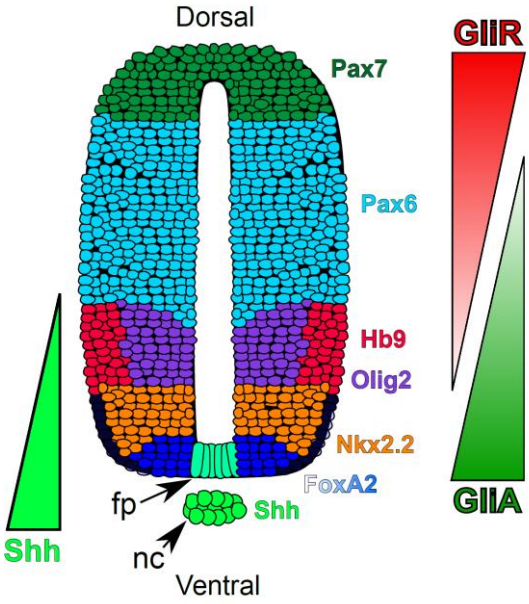

Figure 1.2 Neural tube cell fate specification.

Shh ligand is produced in the notochord (nc) and floor plate (fp) of the ventral neural tube and creates a ventral-to-dorsal concentration gradient. The floor plate and fates closest to the notochord required higher levels of Shh that correlate with higher levels of Gli activator (GliA) transcription factor. From the roof plate Gli repressor (GliR) transcription factors promote dorsal cell fates like Pax7 and Pax6. Therefore, the patterning of the neural tube can be envisioned as opposing GliA and GliR gradients.

Cilia are essential to transduce Hh signaling in vertebrates. Disruption of anterograde IFT in *Ift172* null mice ablates cilia resulting in a loss of all ventral cell fates in the developing neural tube, a Sonic Hedgehog (Shh)-dependent process (Huangfu et al. 2003) (**Figure 1.2**). The loss of ventral neural cell fates in *Ift172* mutants phenocopies mutants lacking *Shh*, indicating IFT172 is required for Shh signaling (Chiang et al. 1996; Huangfu et al. 2003). *Dnchc2*^{lln} mice, lacking a functional retrograde dynein motor, display bulbous cilia due to their protein trafficking defects and also do not specify ventral neural cell fates (Huangfu et al. 2005) (**Figure 1.3**). The simplest interpretation of defects in either anterograde or retrograde traffic leading to a loss of Shh response in the ventral neural tube is that the cilium itself is needed to transduce the pathway (Huangfu et al. 2003; Huangfu et al. 2005).

The complexity of the mechanisms linking cilia and Shh signal transduction are highlighted by mutations in different cilia proteins impacting signal transduction in distinct ways. Despite

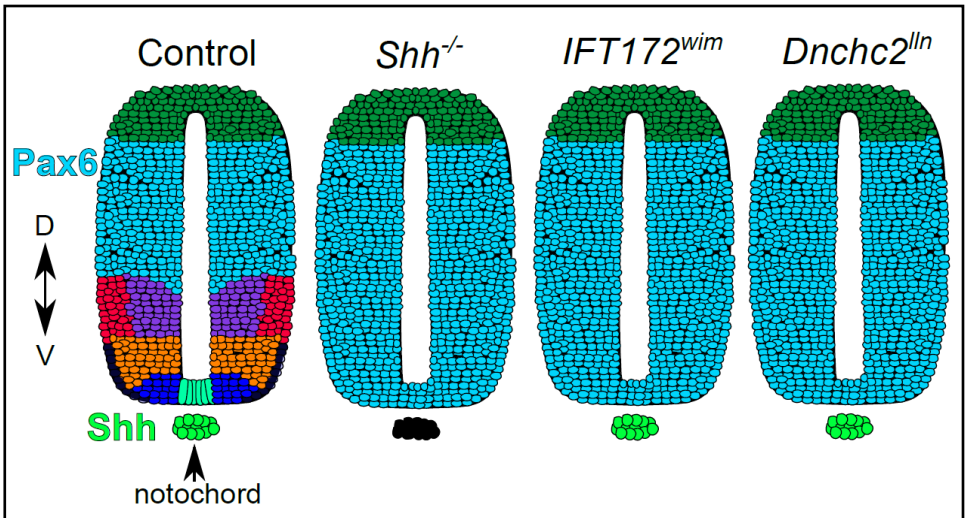

Figure 1.3 IFT mutants, like *Shh* mutants, fail to specify ventral cell fates.

Ventral neural tube patterning (colored cell fates) is an *in vivo* readout of Sonic Hedgehog (Shh) pathway activation. Loss of *Shh* results in a complete loss of Shh-dependent ventral cell fates. Disruption of anterograde or retrograde IFT in *Ift172*^{wim} and *Dnchc2*^{lln} mutants results in a loss of Shh-dependent cell fates and ventral expansion of PAX6 (blue), which marks Shh-independent cell fates. As these mutants phenocopy *Shh*$^{-/-}$ mutants, the cilium itself is required for transduction of the Shh signaling pathway.

most retrograde mutants displaying no ventral neural cell fates, *Ift122* and *Ift139* mutants show bulbous cilia and increased Shh signaling within the neural tube (Cortellino et al. 2009; Tran et al. 2008). Different cilia proteins impact the pathway to varying degrees or in multiple ways. Loss of the cilia-associated GTPase RAB23 leads to a dramatic expansion of ventral fates whereas loss of KIF7 results in a modest expansion of ventral fates (Eggenschwiler et al. 2001; Eggenschwiler et al. 2006); (Liem et al. 2009). Another ciliary GTPase, ARL13B, appears to both positively and negatively regulate Shh signaling as its loss causes both loss of the most ventral cell fates and expansion of the OLIG2-expressing domain (Caspary et al. 2007). Importantly, all these roles are conserved among vertebrates and cilia ablation in fish, frogs and other vertebrates leads to the vHh defects indicating that all vertebrates rely on cilia for Hh signal transduction (Huang et al. 2009; Chung et al. 2014; Chung et al. 2012).

1.4 Vertebrate Hedgehog components dynamically localize to cilia

In vertebrates, the link between cilia and Hh is reflected by the dynamic trafficking of the pathway's core components in and out of cilia (Corbit et al. 2005; Haycraft et al. 2005; Rohatgi et al. 2007) (**Figure 1.4**). In the absence of Hh, PTCH1 is visible along the ciliary membrane (Rohatgi et al. 2007). Upon stimulation with Hh, ciliary PTCH1 becomes undetectable whereas SMO is visibly enriched in cilia (Corbit et al. 2005). This enrichment is necessary for subsequent activation of SMO (Rohatgi et al. 2009). As SMO enriches in cilia, GPR161, a GPCR and negative regulator of Hh signaling exits cilia (Mukhopadhyay et al. 2013). Additional Hh components regulate GLI transport and processing, mediating pathway activation. Kinesin family member 7 (KIF7) is responsible for moving GLI2 and GLI3 to the ciliary tip by IFT (Liem et al. 2009; Endoh-Yamagami et al. 2009; Tay et al. 2005; Haycraft et al. 2005). The enrichment of the GLIs at the ciliary tip appears to be

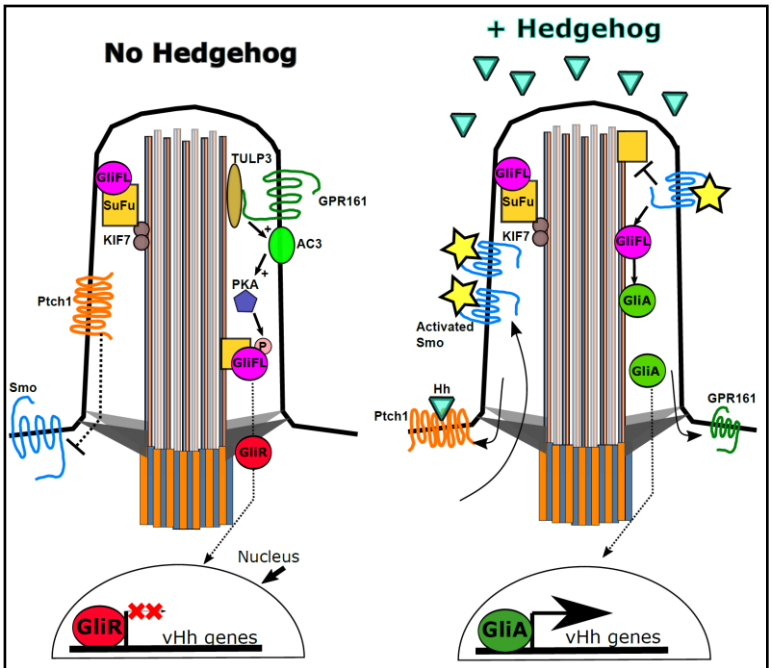

Figure 1.4. The major components of the Hedgehog pathway dynamically localize to cilia. (Left) In the absence of vHh, the PTCH1 receptor is enriched in cilia, suppressing the ciliary enrichment and activation of Smo. KIF7 aids in shuttling the SUFU-GLI complex to the ciliary tip. Negative regulator GPR161 activates adenylyl cyclase 3 (AC3), facilitating PKA activation. PKA phosphorylates the full length GLI (GLIFL) which promotes the formation of GLI repressor (GLIR). GLIR translocates to the nucleus and suppresses vHh-dependent gene targets. (Right) vHh ligand binds PTCH1, which is subsequently removed from the cilium permitting ciliary Smo enrichment and activation (star). Activated Smo promotes the dissociation of the GLI-SUFU enabling activated GLI (GLIA) formation. GLIA translocates to the nucleus to promote Hh-dependent gene transcription.

an essential step in SMO signaling to the GLIs, and thus for pathway activation (Liu et al. 2005; Haycraft et al. 2005).

Processing of the 3 GLI proteins is complex. Distinct phosphorylation of the full length GLI proteins determines processing to an activator form or cleavage to a repressor form. That said, GLI1 lacks the cleavage site so functions solely as an activator. In the neural tube, GLI2 acts as the predominant activator and GLI3 the prevalent repressor (Matise et al. 1998; Litingtung et al. 2000). To process repressor in the absence of Hh ligand, suppressor of fused (SUFU) forms an inhibitory complex with full-length GLI3 (Svard et al. 2006). The complex traffics out of the cilium where the kinases protein kinase A (PKA), GSK3β, and CKI phosphorylate full-length GLI3, to promote its cleavage to GLI3 repressor (GLIR) (Hammerschmidt et al. 1996; Tuson et al. 2011; Fumoto et al. 2006; Barzi et al. 2010). To generate GLI2 activator when ligand is present, activated SMO promotes dissociation of the GLI2-SUFU complex and phosphorylation of full-length GLI2 to its activator form (GLIA) at which point it is shuttled out of the cilium (Wen et al. 2010; Tukachinsky et al. 2010; Kim et al. 2009; Humke et al. 2010). GLIA and GLIR translocate to the nucleus to influence Hh-dependent gene targets.

In mutants lacking cilia or Shh, no ventral neural cell fates are specified because the relevant target genes are not induced. However, mutants lacking cilia die around E11.5 whereas those with no vHh signaling (*Smo*$^{-/-}$) die at E9.0 (Kasarskis et al. 1998; Zhang et al. 2001; Caspary et al. 2002). This highlights the distinct mechanisms underlying the absence of Shh-signaling dependent gene transcription when cilia are lost (Huangfu et al. 2003; Chiang et al. 1996). Loss of cilia ablates the formation of both GLI activator (GLIA) and GLI repressor (GLIR), so that target genes are neither activated nor repressed (Huangfu et al. 2005; Liu et al. 2005). In contrast, *Smo* single or

Shh/Ihh double mutants only produce GLIR so that target genes are repressed (Kasarskis et al. 1998; Zhang et al. 2001). Thus, SMO mutants display a more severe phenotype as they repress targets in non-neural tube tissue that are not repressed in the absence of cilia alone.

1.4.1 Other ciliary regulators of the Hedgehog pathway

Other Hh pathway regulators are enriched within the cilium. TULP3 acts a negative regulator of the Hh pathway and localizes to the ciliary tip (Norman et al. 2009; Mukhopadhyay et al. 2010). Loss of TULP3 causes a failure of cilia proteins ARL13B and INPP5E to localize to cilia (Han et al. 2019). Both ARL13B and INPP5E are known for their influence over vHh pathway components (Caspary et al. 2007; Constable et al. 2020; Larkins et al. 2011; Chavez et al. 2015; Garcia-Gonzalo et al. 2015). Adenylyl cyclases (AC) are responsible for generating cyclic AMP (cAMP), the allosteric activator of protein kinase A (PKA), a negative Hh regulator (Hammerschmidt et al. 1996). TULP3 is also responsible for recruiting the GPCR GPR161 to the cilium. GPR161 is coupled to stimulatory G-proteins that activate adenylyl cyclase (AC3) to increase cAMP levels (Bishop et al. 2007). Therefore, GPR161 acts as a negative regulator on vHh signaling through PKA. (Mukhopadhyay et al. 2013). GPR161 resides in cilia when the pathway is inactive. Ciliary SMO enrichment upon vHh activation promotes the removal of GPR161, and its inhibitory influence on the pathway, from cilia (Pal et al. 2016; Mukhopadhyay et al. 2013; Corbit et al. 2005). There are exceptions, not all vHh regulators have been identified in cilia. Curiously, BOC, GAS1, and CDO are well-established coreceptors with PTCH1 for the Hh ligand, but have yet to be observed in cilia (Allen et al. 2011; Izzi et al. 2011).

1.5 The ciliary membrane

The ciliary membrane is contiguous with the cell's plasma membrane, yet the distinct lipid composition of the ciliary membrane provides a specialized environment for signaling pathways. Phospholipids comprise the most abundant lipid on the plasma and ciliary membranes (Saarikangas et al. 2010). The composition of the ciliary membrane is particularly enriched for phosphoinositol-4- phosphate (PI(4)P) compared to the plasma membrane. This distinction is mediated, in part, by the inositol polyphosphate -5-phosphatase, INPP5E. INPP5E is trafficked to cilia in a complex containing the regulatory GTPase ARL13B and the phosphodiesterase PDE6D (Humbert et al. 2012; Nozaki et al. 2017). Defects in proteins critical to the transition zone result in INPP5E not localizing to cilia, causing changes to the ciliary membrane phospholipid composition (Garcia-Gonzalo et al. 2015; Slaats et al. 2016).

INPP5E is enriched in cilia and removes the 5-phosphate from PI(3,4,5)P3 (preferred substrate) and PI(4,5)P2 (hereafter called PIP_3 and PIP_2 respectively) membrane lipids that influence signaling pathways (Kisseleva et al. 2000). Loss of *Inpp5e* results in a loss of ciliary PI(4)P and an increase in ciliary PIP_2 (Chavez et al. 2015; Garcia-Gonzalo et al. 2015; Jacoby et al. 2009; Bielas et al. 2009). This causes PIP_2 and PIP_3 substrates to accumulate at the transition zone, disrupting the organization of transition zone scaffolding proteins. These data suggest that PIP composition may be critical to regulating protein entry and/or exit at the transition zone (Dyson et al. 2017). Moreover, TULP3 is a PIP_2 binding protein so increased ciliary PIP_2 promotes TULP3 and its associated GPR161 to localize within cilia (Badgandi et al. 2017; Garcia-Gonzalo et al. 2015). *In vitro*, this results in a dampened vHh response (Chavez et al. 2015; Garcia-Gonzalo et al. 2015). *In vivo*, *Inpp5e* mutants display increased Shh response in the caudal neural tube which corrects over time (Constable et al. 2020). It is unclear whether these differences are due to tissue-

specific context, the duration of signaling or another factor. Nonetheless, the biochemical composition of the ciliary membrane is critical for vHh signal transduction.

Sidebar on cilia history and ciliopathies.

Cilia are not recent evolutionary structures, they are ancient. The earliest description of cilia dates to 1675 by Anthony Van Leeuwenhoek, describing "incredibly thin feet or little legs, which were moved very nimbly" while observing protozoa in water droplets (Dobell 1932). These cilia, or flagella, were defined by their active motility that provided propulsion. After Van Leeuwenhoek's discovery, 200 years passed before the primary cilium was identified in the late 19th century. Zimmerman identified the "central flagella" and hypothesized that it had a sensory role (Zimmermann 1898). Again, a significant amount of time passed before their rediscovery in 1968 when the primary cilium was identified in lung epithelium (Sorokin 1968). In the decades since, researchers characterized the molecular machinery that regulate cilia and flagella, the intraflagellar transport (IFT) system, through work in the biflagellate algae, *Chlamydamonas* (Kozminski et al. 1993). Because cilia are ancient structures the basal machinery that establish and maintain cilia are well conserved throughout evolutionary history.

The last twenty years have seen a rapid expansion in our knowledge and appreciation of mammalian cilia. It began with the discovery of nodal cilia in the early embryo that are responsible for the establishment of left-right patterning (Nonaka et al. 2002; Nonaka et al. 1998). This was followed by the discovery that polycystins in the nematode *C. elegans*, previously known for their role in polycystic kidney disease, are conserved cilia proteins (Barr et al. 1999). The discovery that polycystic kidney disease gene *TG737* is in fact *IFT88*, previously discovered in *Chlamydomonas*, further linked kidney disease and cilia function (Pazour et al. 2000). Then, in 2003, Kathryn Anderson's lab discovered in mouse that Hedgehog signaling requires the primary cilium to function (Huangfu et al. 2003). This result shocked the field. Developmental biologists had been studying Hedgehog in vertebrates for nearly a decade without knowing that the system is linked to cilia.

Cilia biology benefits enormously from human genetics and visa-versa. Indeed, several of the major protein complexes in cilia are named due to the disease through which the relevant proteins got identified. These include the BBSome, named for Bardet-Biedl syndrome; the NPHP complex derived from nephronophthisis, and the MKS complex which originated from Meckel-Gruber syndrome. As complete ablation of cilia is embryonic lethal in mammals, ciliopathies are often caused by missense mutations that create hypomorphic alleles (Reiter et al. 2017; Waters et al. 2011). In addition to such disease-causing mutations being hugely informative to understand the diverse and specific functions of cilia proteins, ciliopathies present an interesting lack of genotype-phenotype correlation. In families in which distinct ciliopathy patients carry the same mutation, they can display quite different phenotypes. Oligogenicity is proposed to play a role but whole genome sequencing revealed that ciliopathies are Mendelian disorders with autosomal recessive mutations driving the disease (Shaheen et al. 2016). The variation in penetrance is likely due to modifiers. Thus, cilia biology and cilia-associated disease inform one another

1.6 Cilia protein and GTPase ARL13B

ARL13B is an Arf-like (Arl) GTPase, with a N-terminal GTPase domain containing the typical switches, and a long atypical C-terminal domain. As a regulatory GTPase, ARL13B acts as a molecular switch, cycling between inactive GDP-bound and active GTP-bound states. The exchange process is mediated by guanine nucleotide exchange factors (GEFs) that exchange bound GDP for GTP, and GTPase activating proteins (GAPs) that promote the hydrolysis of GTP to GDP. In the GTP bound state, Arfs and Arls associate with membranes where they facilitate cellular functions. Most commonly, Arfs and Arls are implicated in the regulation of membrane trafficking, in addition to other cellular roles. GTPases can have multiple downstream effectors and each GTPase can be targeted to several locations within a cell. It is thought that the control of GTPase localization is central to the determination of its cellular function (Kahn et al. 2014). Because GTPases can have multiple effectors, it is likely that a GTPase will have multiple targets at any specific location in the cell. For that reason, I will initially focus on discussing ARL13B's ciliary localization before moving into a discussion of ARL13B functions.

ARL13B localizes primarily at the ciliary membrane but it can be found elsewhere in the cell, a common trait of GTPases (Casalou et al. 2014; Barral et al. 2012; Caspary et al. 2007). ARL13B associates with the plasma membrane through post-translational modifications at the N-terminus. Cysteine residues C8 and C9 can be palmitoylated, promoting ARL13B anchoring to the cell membrane (Casalou et al. 2014; Seixas et al. 2016; Cevik et al. 2013; Mariani et al. 2016). Therefore, mutations of these residues can prevent ARL13B's ability to localize to cilia (Cevik et al. 2010; Roy et al. 2017). In addition, a VxPx motif in ARL13B's novel C-terminal domain is necessary for its ciliary localization (Mariani et al. 2016). Mutation of this sequence can preent accumulation of ARL13B in cilia, but this does not appear to affect the majority of ARL13B's

functions (Mariani et al. 2016). In fact, this cilia-excluded point mutant rescued *Arl13b* null phenotypes in cells (Mariani et al. 2016). ARL13B is concentrated at the cilium and therefore easy to visualize, but cellular ARL13B ($ARL13B^{V358A}$) does not coalesce around the base of the cilium or a secondary cellular organelle, making it very difficult to locate outside the cilium (Mariani et al. 2016). Like other GTPases, ARL13B has multiple localizations and serves distinct functions at each locale. In the following section I will introduce ciliary and non-ciliary functions of ARL13B.

1.6.1 The ciliary and non-ciliary functions of ARL13B

ARL13B is evolutionarily conserved as a cilia protein. The *Arl13b* gene was first cloned in zebrafish ($Arl13b^{sco}$) and its function linked kidney duct formation (Sun et al. 2004). In mouse, a null allele of *Arl13b* ($Arl13b^{hnn}$) was pulled out of a forward genetic screen and its function characterized in the developing neural tube (Caspary et al. 2007; Garcia-Garcia et al. 2005). ARL13B is present in nearly every type of cilia. Experiments *in vitro* and *in vivo* show that loss of *Arl13b* results in fewer ciliated cells and shorter cilia (Caspary et al. 2007; Larkins et al. 2011). However, in the kidney loss of *Arl13b* ablates cilia entirely. Cilia loss causes kidney cyst formation, suggesting ARL13B has an important role in ciliogenesis that is more critical in some contexts than others (Seixas et al. 2016). An examination of cilia in *Arl13b* mutants by transmission electron microscopy revealed a defect in microtubule outer doublet of the axoneme (Caspary et al. 2007). This prevented the B-tubule from attaching to the A-tubule, suggesting ARL13B has a specific role in the assembly of the microtubule outer doublets. Because of this structural defect, the assumption was that it caused the Shh signaling defects observed in $Arl13b^{hnn}$ mutants (Caspary et al. 2007). ARL13B is also responsible for coordinating the ciliary trafficking of other cilia proteins. ARL13B promotes the localization of INPP5E to cilia in a complex with phosophodiesterase 6D (PDE6D) and CEP164 (Humbert et al. 2012). ARL13B acts as the GEF

for ARL3, another ciliary GTPase and Joubert Syndrome causing gene (Gotthardt et al. 2015; Ivanova et al. 2017; Alkanderi et al. 2018). Disruptions in Arl3 are known to cause degenerative phenotypes in retina, linking Arl3 to both trafficking of lipidated cargos and IFT as loss of Arl3 prevents cilia formation (Hanke-Gogokhia et al. 2018; Hanke-Gogokhia et al. 2016).

Understanding ARL13B's functions is complicated, not only because its diverse presence in ciliated tissues suggests it serves multiple functions, but also because it is not exclusively a cilia protein. ARL13B may be involved in actin restructuring at the intracellular surface plasma membrane, through which it could influence many different cell functions (Casalou et al. 2014). GTP-bound ARL13B binds to subunits of the exocyst, a protein complex important in vesicle trafficking and targeting of vesicles from the Golgi to the plasma membrane (Seixas et al. 2016). This interaction is essential in kidney, where depletion of *Arl13b* and *Sec10*, an exocyst subunit, results in a loss of cilia and thus worsening of cystic kidney phenotypes. In parallel, there is evidence of ARL13B regulating endocytic trafficking, as ARL13B colocalizes with markers of endocytic recycling (Barral et al. 2012). In the developing cortex, ARL13B plays a critical role in the initial formation of the polarized radial glia scaffold (Higginbotham et al. 2013). In these cells, the loss of *Arl13b* causes a disorganization of neuronal placement in the developing cortex through disruption of neuronal migration (Higginbotham et al. 2012). ARL13B has a role in axon guidance as loss of *Arl13b* in commissural projection neurons causes disorganization of axons projecting from the dorsal to ventral neural tube. This is likely due to loss of *Arl13b* at the axon terminal, rather than at the cilium as axon guidance is normal in cilia-excluded *Arl13b*^{V358A} mutants (Ferent et al. 2019). Although, an *ex vivo* study of axon guidance in dissociated neurons found that cilia-excluded ARL13B^{V358A} was insufficient to rescue axon guidance defects (Zhang et al. 2004). Together, these data show that ARL13B serves many functions both in- and out of cilia.

1.6.2 The evolution of ARL13B

ARL13B is an evolutionarily conserved regulatory GTPase, present in the last eukaryotic common ancestor. Arl13 is an ancient protein that is lost in species lacking cilia (Li et al. 2004; Logsdon et al. 2004; Kahn et al. 2008; East et al. 2012; Schlacht et al. 2013). In species with cilia that lack Hh signaling such as *C. elegans* and *C. reinhardtii*, *Arl13* mutants display cilia defects (Cevik et al. 2010; Warburton-Pitt et al. 2014; Miertzschke et al. 2014; Cantagrel et al. 2008). In *C. elegans, Arl13* mutants can have several defects including; bulbous cilia, cilia that are truncated, disorder of the axoneme, or a complete loss of cilia (Cevik et al. 2010). In mouse, *Arl13b* mutants also show axonemal defects in the closing of the B-tubule doublet and cilia are frequently shorter than normal (Caspary et al. 2007; Larkins et al. 2011). Together this indicates Arl13/ARL13B has a highly conserved role in ciliary function (Cevik et al. 2013; Cevik et al. 2010; Warburton-Pitt et al. 2014; Gotthardt et al. 2015; Miertzschke et al. 2014).

1.6.3 *ARL13B* is one of 35 cilia genes that cause Joubert Syndrome

In humans, mutations in *ARL13B* cause an autosomal recessive ciliopathy Joubert Syndrome (JS) (Cantagrel et al. 2008; Doherty 2009; Parisi 2019; Thomas et al. 2015; Rafiullah et al. 2017; Kniffin 10/30/2018). *ARL13B* is one of 35 genes whose mutations may be causative for JS, all of which (except one,) are cilia associated, thus making cilia the central factor and implicating ciliary ARL13B in preventing JS (Chaki et al. 2012; Parisi 2019; Parisi et al. 2017). Several JS causing mutations have been discovered in *ARL13B*. The majority of JS causing mutations are found in the GTP sensing N-terminus, and one in the coiled-coil domain. Researchers have used JS causing, and engineered mutations, to characterize the functions of ARL13B (**Figure 1.5**). In particular, disease causing mutations Y86C, R79Q, and R200C are all devoid of GEF activity for ARL3, supporting ARL13B action as an effector for ARL3 (Ivanova et

al. 2017). Furthermore, *ARL3* has also been identified as a JS causing gene, suggesting that *ARL13B* induced JS is linked to ARL3 dysfunction (Alkanderi et al. 2018). There are also JS causing mutations in *INPP5E* that cluster in the phosphatase domain, impairing 5-phosphatase activity and altering the membrane composition of phosphoinositides (Bielas et al. 2009). As previously mentioned, ARL13B promotes the localization of INPP5E to cilia in a complex with phosphodiesterase 6D (PDE6D) and CEP164 (Humbert et al. 2012). Several JS causing cilia genes have been identified, but they do not all share the same phenotypes. The exception is the diagnostic criteria for JS, a distinctive malformation of the cerebellum and brain stem, commonly referred to as the molar tooth sign (Maria et al. 1997). Patients with JS also present with a range of phenotypes

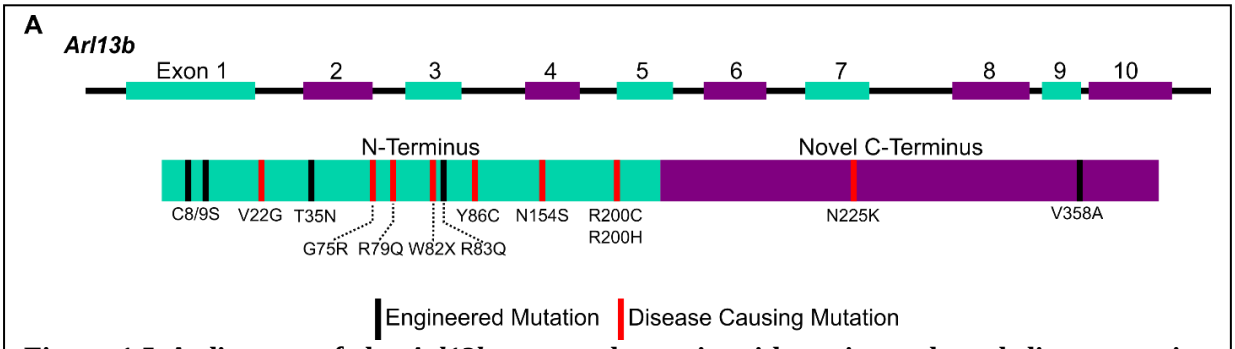

Figure 1.5 A diagram of the *Arl13b* gene and protein with engineered- and disease-causing mutations.

The *Arl13b* gene with labeled exons and below it a linear representation of the ARL13B protein. ARL13B is split into two halves, a conserved GTP-binding N-terminus and a novel C-terminus. The protein is labeled with engineered mutations (black) and disease-causing mutations (red). Beginning in ascending order. Mutations C8S/C9S removes palmitoylation sites that causes mislocalization of ARL13B to the cell body, diffuse in the cytosol (Cevik et al. 2010). Mutations V22G and N145S were identified in a compound heterozygous JS patient (Bachmann-Gagescu et al. 2015). The T35N mutation does not change ARL13B localization, but it is unable to rescue null phenotypes in zebrafish mutants (Duldulao et al. 2009). Mutations G75R and R79Q were identified in patients with homozygous mutations (Rafiullah et al. 2017). The R79Q mutation decreases GTP binding and poorly rescues *arl13b* null phenotypes in zebrafish (Cantagrel et al. 2008). The R83Q mutation in worms permits normal ciliary localization, but only partially rescues dye filling null phenotypes (Li et al. 2010). Compound heterozygous patients for W82X and R200C, R200C poorly rescues *arl13b* null phenotypes in zebrafish (Cantagrel et al. 2008). R200H and Y86C are homozygous patient mutations, patients with Y86C are the only *ARL13B* JS patients with obesity (Thomas et al. 2015; Shaheen et al. 2016). In the C-terminus, only two mutations have been reported, the N225K disease causing mutation and the CRISPR engineered V358A mutation (Shaheen et al. 2016). ARL13B^{V358A} is able to rescue *Arl13b* null phenotypes in cells, but it is undetectable in cilia (Mariani et al. 2016).

including: respiratory abnormalities, retinal disease, renal disease and hepatic disease (Parisi 2019; Thomas et al. 2015; Romani et al. 2013; Doherty 2009; Cantagrel et al. 2008).

1.6.4 ARL13B regulates Sonic Hedgehog signaling and ciliary trafficking of Hedgehog components

In mouse, the *Arl13b* null allele *hennin* (*hnn*) mutants have developmental defects linked to impaired Shh signaling (Caspary et al. 2007). ARL13B, which is normally highly enriched in cilia is absent from cilia in *hnn* mutants, suggesting $Arl13b^{hnn}$ is a null allele. The T-to-G causative *hnn* mutation maps to the splice acceptor site of exon 2 of *Arl13b*. Western blot analysis in embryos revealed a lack of ARL13B protein, confirming *hnn* is indeed a null allele. $Arl13b^{hnn}$embryos have a bifurcated and open head or exencephaly, a rough neural tube, and spina bifida. Loss of *Arl13b* also disrupted Shh-dependent neural tube patterning. While Shh is normally expressed in the notochord and floor plate of the neural tube, in $Arl13b^{hnn}$ embryos it is only present in the notochord. At the same time, characterization of Shh-dependent transcription with a *Ptch1-LacZ* allele revealed ligand-independent Shh gene transcription expanded across the dorsal-ventral axis of the neural tube. Normally, the PTCH1-LacZ gradient is steep, but in $Arl13b^{hnn}$ mutants it is relatively shallow, suggesting there is low-level constitutive activation of the pathway. The result is a ventral and dorsal expansion of low-level Shh-dependent cell fates Olig2 and Hb9. These data clearly support a role of ARL13B in the regulation of the Shh pathway.

Deciphering the relationship between ARL13B and SMO is a complicated task and may be due to ARL13B function at multiple steps in the Shh pathway. There is genetic evidence consistent with *Arl13b* function downstream of SMO from a cancer model of Shh-signaling, the malignant pediatric brain tumor medulloblastoma. The medulloblastoma is generated by a

constitutively active form of SMO that over activates the Shh transcriptional pathway (Xie et al. 1998). In this model, the deletion of *Arl13b* blocks SMO-induced Shh pathway activation (Bay et al. 2018). These data support ARL13B function downstream of SMO. However, data in mouse reveal that the relationship is not so simple. In the mouse neural tube, loss of *Smo* prevents the establishment of any Shh-dependent ventral cell fates (Kasarskis et al. 1998). Conversely, loss of *Ptch1* derepresses SMO, resulting in over establishment of Shh-dependent ventral cell fates (Caspary et al. 2002). If ARL13B simply functions downstream of SMO, then in both models the loss of both *Arl13b* should result in a phenotype similar to loss of *Arl13b* alone (Caspary et al. 2007). In both examples I have described, if ARL13B simply functions downstream of SMO, then the expected outcome of both experiments should be a double mutant that phenocopies the *Arl13b* mutant. This was not the outcome. Instead, both double mutants had intermediate phenotypes

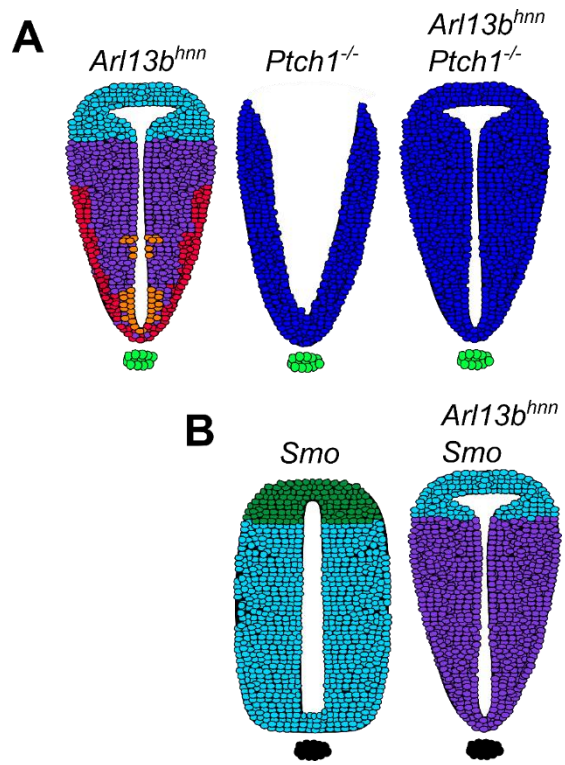

Figure 1.6 Loss of *Arl13b* modulates *Ptch1*, and *Smo* null phenotypes.

(A) In *Arl13b*^{hnn} mutants the neural tube is sparsely populated by Nkx2.2 positive cells (Orange) and predominantly Olig2 (Purple) and Hb9 (Red) positive cells. Shh (green) is still produced in the notochord. Loss of *Ptch1* causes unabated activation of SMO, so the neural tube is dominated by FoxA2 (Blue) positive cells, and the neural tube fails to close. In *Arl13b*^{hnn} *Ptch1* double mutants the neural tube is closed, and the embryo survives a few days more, suggesting a suppression of the hyperactive Shh pathway and *Arl13b* function downstream of *Ptch1*. (B) The neural tube of *Smo* mutants has no ventral cell fates. In *Arl13b*^{hnn} *Smo* double mutants, low-level Olig2 positive cells are present, suggesting that *Arl13b* functions downstream of *Smo*.

(**Figure 1.6**). Together, they suggest that the relationship between ARL13B and SMO is more complicated and support a model where ARL13B functions both upstream and downstream of SMO. But what is the role of ARL13B upstream of SMO?

Analysis of SMO localization in *Arl13b*^{hnn} cells revealed trafficking and localization defects. The dynamic localization of Hh components to cilia is a hallmark of the pathway's dependence on cilia. Critically, SMO is only enriched in cilia upon Hh pathway activation and the ciliary exit of its repressor PTCH1. However, in cells lacking *Arl13b*, SMO is abnormally enriched in cilia alongside PTCH1 (Larkins et al. 2011). Furthermore, SMO enrichment in cilia is usually uniform, but in *Arl13b*^{hnn} mutants it is punctate and compartmentalized in a proximal portion of the cilium (**Figure 1.7**). These data are consistent with ARL13B functioning at the level or upstream of SMO.

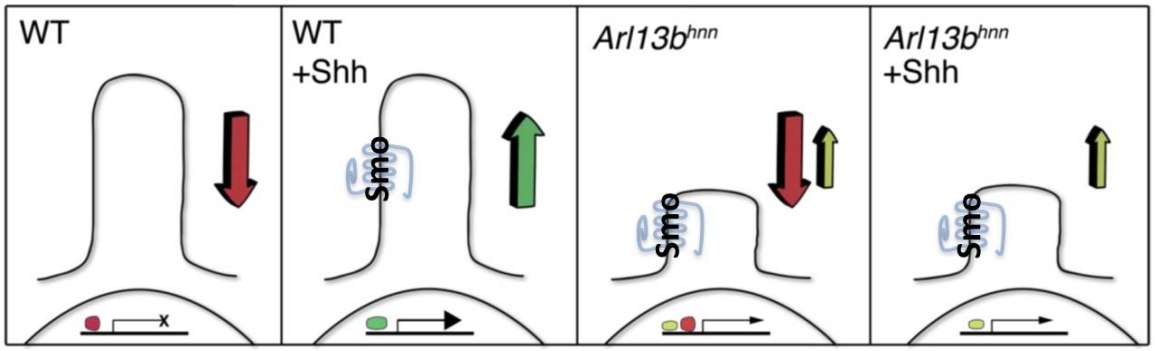

Figure 1.7 Loss of *Arl13b* impacts SMO trafficking and Gli activator.

Moving from left to right. (1) When Shh ligand is absent, SMO is absent from cilia and only Gli repressor (GliR) is made, blocking Shh-dependent gene transcription. (2) In the presence of Shh, SMO is activated and enriched in cilia, promoting the production of Gli activator (GliA). (3) When ARL13B is lost cilia are visibly shorter. SMO is aberrantly enriched in cilia but not activated, and normal levels of GliR with low-level Shh-independent GliA. (4) When ARL13B is lost and Shh is present, SMO is still in cilia and is promoting GliA production, blocking GliR, but because ARL13B is absent only low levels of GliA are achieved. In both 3 and 4, the assumption is that enriched SMO is not activated, at least not to its full level.

The ciliary processes that regulate SMO trafficking and activation are still being worked out Therefore, the mechanisms that ARL13B regulates to influence SMO trafficking are not known.

Given that ARL13B is responsible, directly or indirectly, for regulating the ciliary membrane composition perhaps it also organizes the ciliary processes that facilitate SMO activation (Humbert et al. 2012). Most compelling is the evolutionary link between ARL13B and the Shh pathway. *Arl13* duplicated to *Arl13a* and *Arl13b* in the urochordates, about the time in the deuterostome lineage in which Hh became functionally linked to primary cilia (Schlacht et al. 2013; Li et al. 2004; Kahn et al. 2008; East et al. 2012; Logsdon et al. 2004). Thus, ARL13B may be critical to the mechanism that solidified Hh signaling using the cilia within the deuterostomes, linking ARL13B function to SMO activation.

1.7 G-Protein coupled receptor SMOOTHENED

SMO is a member of the Frizzled (F-class) GPCR family. F-class GPCRs are classic seven transmembrane GPCRs, uniquely defined by their large extracellular, N-terminal cysteine rich domain (CRD) (Alcedo et al. 1996). In FRIZZLED (FZD) receptors, this domain readily associates with the WNT ligand (Janda et al. 2012; Dann et al. 2001). Despite sharing a receptor class with FZD receptors, and unlike them, SMO does not directly bind to the Hh ligand. Instead, Hh binds PTCH1 which removes suppression of SMO and permits SMO activation (Taipale et al. 2002). Currently, the endogenous ligand responsible for SMO activation is unknown, leading to SMO classification as an orphan receptor. In this section I will introduce SMO so that I might compare and contrast it with other GPCRs. This information serves as a foundation for the following section where I discuss known GPCR function in the cell and the cilium, highlighting the similarities and differences.

1.7.1 SMOOTHENED has the structural hallmarks of a GPCR

There are over 800 different GPCR genes, of which more than half encode olfactory GPCRs, and others are critical for vision and taste (Takeda et al. 2002). GPCRs are typically integrated in the plasma membrane and stimulated by binding of an extracellular ligand. SMO contains all the hallmarks of a GPCR. It has an N-terminal extracellular domain, 7 transmembrane α-helices, and a C-terminal intracellular domain (**Figure 1.8**). Unique to SMO and other F-class receptors is the large N-terminal cysteine rich domain (CRD) that is connected to the transmembrane domains by a smaller linker domain. Like all GPCRs, SMO is thought to undergo a conformational change when activated. This conformational change alters the orientation of the CRD relative to the transmembrane domains through a bend in the linker domain (Zhao et al. 2007; Huang et al. 2018; Byrne et al. 2016). The CRD plays an essential role in the activation of SMO and may be involved in the translocation and enrichment of SMO in cilia (Aanstad et al. 2009; Myers et al. 2017).

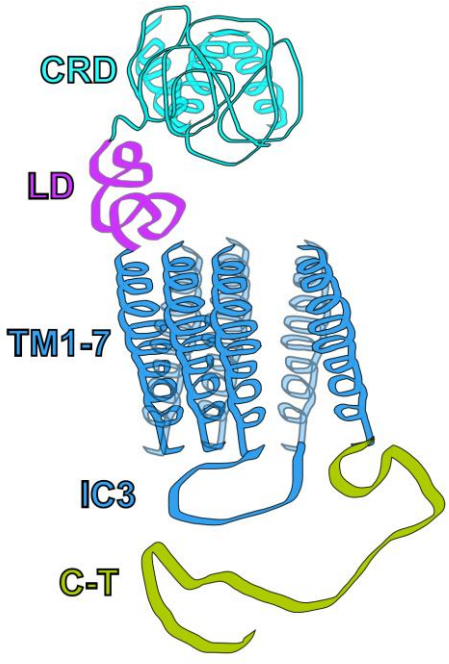

Figure 1.8. G-protein coupled receptor SMO.

Smoothened is an F-class G-protein coupled receptor (GPCR) defined by the N-terminal cysteine rich domain (CRD) containing small α-helices and ligand binding domains. A linker domain (LD) connects the CRD with the 7 transmembrane (TM1-7) domain of the receptor. The intracellular loop 3 (IC3) associates with intracellular $G\alpha_i$ G-proteins that are activated following the conformational change. The intracellular C-terminal (C-T) tail is critical for SMO transport and enrichment in cilia. Mutations to the C-T affect ciliary SMO traffic (Chen et al. 2011; Corbit et al. 2005).

Conformational changes can promote the dissociation of intracellular G-proteins for signal transduction. Inactive GPCRs associate with intracellular G-proteins, and it is through these heterotrimeric complexes that the receptors influence intracellular pathways. The heterotrimeric G-protein complex can be separated into three subunit families; Gα, Gβ, and Gγ. Together the heterotrimeric complex, Gαβγ, binds the intracellular loops of GPCRs. In an inhibitory state, the Gβγ complex serves to directly inhibit the Gα subunit (Lambright et al. 1996). When a GPCR is bound by an agonist and activated, the receptor undergoes a conformational shift that promotes the dissociation of the G-protein complex from the receptor. After which, the Gα subunit separates from the βγ subunits through the exchange of GDP for GTP. The dissociation of the Gα subunit from the Gβγ subunit frees both to influence downstream signaling in second messenger pathways. The Gα proteins can be sub-divided into four families, each with different signaling properties. To overcome the homology among the Gα subunits, individual GPCRs are selective of which G-proteins they bind to for their appropriate signal transduction (Flock et al. 2017; Van Eps et al. 2018). This allows them to stimulate a variety of pathways, affecting adenylyl cyclases, phospholipases, and phosphokinases, in turn activating second messenger pathways such as cyclic AMP (cAMP), PIP3, arachidonic acid, and calcium.

It is not yet clear which Gα subunit(s) associate with SMO. There are data that SMO binds $G\alpha_i$-inhibitory G-proteins, and does not bind to $G\alpha_s$ or $G\alpha_{13}$ (Polizio et al. 2011; Riobo et al. 2006; Qi et al. 2019; Decamp et al. 2000; Ogden et al. 2008). Yet, GLI activity is influenced by $G\alpha_s$, $G\alpha_{13}$, and $G\alpha_i$ suggesting additional GPCRs that function through $G\alpha_s$ and $G\alpha_{13}$ must be capable of modulating vertebrate Hh responses in cilia (Douglas et al. 2011; Barzi et al. 2011; Rao et al. 2016). One candidate is GPR161, a cilia-associated $G\alpha_s$-coupled GPCR, which negatively

regulates Hh signaling (Mukhopadhyay et al. 2013). While the details of SMO's G-protein coupling remains uncertain, SMO-Gα fusion proteins are now a useful tool to for assaying SMO's conformational state and thus activation indicating that SMO functions like other GPCRs (Myers et al. 2017).

1.7.2 Exogenous ligands inform our understanding of SMOOTHENED mechanisms

SMO is well studied as a drug target for cancer therapy purposes, therefore pharmacological compounds that alter its activity are informative in revealing mechanisms important for SMO activation (Rohatgi et al. 2009; Chen et al. 2002a; Chen et al. 2002b) (**Figure 1.9**). The caveat of these drugs is that they do not activate SMO through the endogenous mechanism, which involves the removal of PTCH1 mediated suppression by a Hh ligand. SMO, like other GPCRs, contains a heptahelical transmembrane domain to which several exogenous compounds are known to bind and either activate or inhibit SMO function. Two antagonists, SANT-1 and cyclopamine, block Shh-induced activation of SMO by binding in the ligand binding pocket of the heptahelical transmembrane domain and

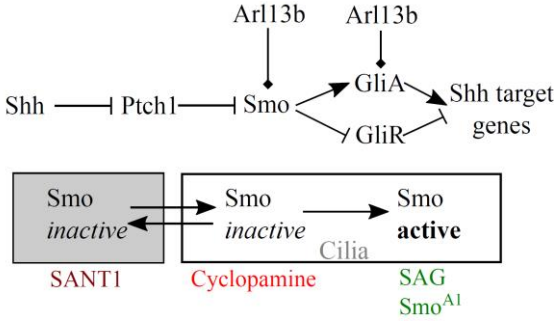

Figure 1.9 SMOOTHENED activation is considered a two-step process.

As the obligate transducer of the Shh signal, there is a great deal of regulation and focus on SMO. As discussed, SMO activation is a multi-step process that can be best explained through the use of exogenous ligands or point mutation. Consider the three states of SMO presented in this figure. SMO can be out of cilia and inactive, in cilia and inactive, or in cilia and active, possible through treatment with SMO antagonist (SANT1), antagonist Cyclopamine, or agonist SAG. Our current understanding of SMO is that it cycles in and out of cilia in an inactive state, depicted here as two opposing horizontal arrows. SMO entry into cilia can be restricted by SANT1, and SANT1 can block Shh or SAG induced activation of SMO. Cyclopamine provides the most interesting effect, it moves SMO into cilia, but prevents SMO activation, highlighting two states of activation. Finally, SAG accomplishes both, it moves SMO into cilia and activates the receptor. The central question of my thesis is how ARL13B contributes to these activation states of SMO. This figure is adapted from (Rohatgi et al. 2009).

preventing activating conformational changes in SMO (Rohatgi et al. 2009; Chen et al. 2002a; Chen et al. 2002b). While both ligands antagonize endogenous SMO activation, SMO localization is distinctly modified under the two conditions. SANT1 prevents SMO ciliary enrichment whereas cyclopamine induces SMO ciliary enrichment (Frank-Kamenetsky et al. 2002; Chen et al. 2002a). These data indicate that ciliary SMO enrichment is not synonymous with SMO activation and demonstrate that the trafficking of SMO to cilia is distinct from its activation (Rohatgi et al. 2009).

There is further support for a model wherein SMO activation and SMO enrichment are separate, but linked processes. SM agonist (SAG) binds the same ligand-binding pocket as the antagonists and promotes the conformational change necessary for SMO activation, and SAG treatment results in ciliary SMO enrichment (Chen et al. 2002b). All three ligands bind to the same pocket and each modulate SMO behavior, separating the two functions of enrichment and activation. Moreover, an activated variant of SMO identified in basal cell carcinoma, SMO^{W539L}, is highly enriched in cilia and results in high levels of Hh response (Xie et al. 1998; Taipale et al. 2000; Corbit et al. 2005). Despite its constitutively active status, SMO^{W539L} still requires normal cilia to activate the Hh pathway (Ocbina et al. 2008). SMO^{W539L} constitutive activation of the Hh pathway be block through disruption of PKA mediated SMO-Inversin associations at the base of the cilium (Zhang et al. 2019). Together, these data support a model wherein SMO is fully activated within cilia and that ciliary enrichment is necessary, but not sufficient, for SMO activation indicating that the process of SMO transport to cilia and its activation are mechanistically distinct (Wilson et al. 2009; Rohatgi et al. 2009).

1.7.3 Additional Ciliary GPCRs

SMO is one of many GPCRs demonstrated to enrich in primary cilia. Rhodopsin in the photoreceptor cells of the retina is the best-known example. This light-sensitive GPCR is found in disc-like membranes within the modified cilium of the rod cell (Röhlich 1975; Jan et al. 1974). Olfactory receptors are uniquely regulated so that only one variety of receptor is expressed in any one olfactory neuron. Olfactory neurons have multiple, long cilia where the olfactory receptors are concentrated. Through specific odorants, the olfactory receptors provide our sense of smell (Buck et al. 1991; Chess et al. 1994). A host of additional GPCRs are also localized to primary cilia including: somatostatin receptor 3 (SSTR3), melanin-concentrating hormone receptor 1 (MCHR1), serotonin receptor 6 (5HT6), dopamine 1 receptor 1 (D1R), neuropeptide Y receptor 2 (NPY2R), kisspeptin receptor 1 (KISS1R) and GPR161 (Handel et al. 1999; Berbari et al. 2008b; Shimada et al. 1998; Hamon et al. 1999; Brailov et al. 2000; Schulz et al. 2000; Marley et al. 2010; Domire et al. 2011; Loktev et al. 2013; Mukhopadhyay et al. 2013). Adenylyl cyclases, the GPCR signal transducers, are also found in cilia and are expressed in a tissue-specific manner. For example, neuronal cilia express adenylyl cyclase (AC3), whereas AC6 and AC5 are more common in bone and kidney, respectively (Bishop et al. 2007; Kwon et al. 2010; Wang et al. 2018). While the distinct ligands contribute to the functional differences among ciliary GPCRs they also work via distinct second messenger cascades. For instance, MCHR1 and KISS1R are peptide receptors that influence neurotransmission and endocrine signaling (Yasuda et al. 1992; Kotani et al. 2001; Berbari et al. 2008b). These receptors can signal through $G\alpha_q$ coupling, influencing both Ca^{2+} mobilization and phosphatidylinositol turnover (Fry et al. 2006; Kotani et al. 2001). In contrast, GPR161, 5HT6, and SSTR3 influence intracellular levels of cAMP, modulating PKA and its downstream targets (Ruat et al. 1993; Mukhopadhyay et al. 2013; Law et al. 1993). Importantly,

several of these ciliary GPCRs change localization upon stimulation (Pal et al. 2016; Green et al. 2016; Ye et al. 2018).

1.8 GPCR localization to cilia is a dynamic and highly regulated process

Clearly, the cilium has taken its rightful place as a fundamental cell organelle with critical roles in cell signaling. The intense focus of the past 15 years on vHh signaling has taught us several principles regarding cilia-dependent signaling. The cilium provides a privileged environment in which signaling components can interact. Importantly the machinery needed to build and maintain the ciliary axoneme and membrane is critical to the dynamic localization of signaling components. As a small exclusive organelle, the cilium is spatially ideal for facilitating a rapid response and the enrichment of many GPCRs, along with the distinct dynamics of cAMP and Ca^{2+} within the cilium and so suggest that it is being used this way.

Estimates put the cilium as about 1/4000 to 1/10,000th the volume of the cell and the field is rapidly adapting tools to study cilia biology (Nachury 2014; Phua et al. 2015). For example, advances in microscopy are allowing researchers to observe cilia at a more detailed resolution than ever before (Yang et al. 2018; Milenkovic et al. 2015; Yoon et al. 2019). Recent advances in proximity labelling within cilia is enabling the identification of new ciliary proteins that may be playing critical roles in signaling (Mick et al. 2015; Yang et al. 2019). Similarly, by adapting biosensors to the ciliary environment, the lipid composition of the membrane, Ca^{2+} flux and cAMP dynamics can be followed *in vivo* (Jiang et al. 2019; Su et al. 2013; Delling et al. 2016; Mukherjee et al. 2016; Li et al. 2016b; Yuan et al. 2015). Optogenetic versions of such constructs can manipulate these same aspects of ciliary biology (Eickelbeck et al. 2019; Jansen et al. 2015). Finally, as the processes that regulate ciliary localization and signaling are better understood, *in*

vivo gene editing techniques will enable researchers to target precise mutations that disrupt specific aspects of these processes, in contrast to removing cilia all together (Gigante et al. 2020b). Such advances are key to understanding the details of how intertwined the cilium is with the signaling pathways that inhabit it.

The compartmentalization and organization of GPCRs is an integral mechanism through which a cell can ensure the proper regulation of cell-specific functions. Cells control their responsiveness to endogenous ligands through the spatiotemporal regulation of GPCR expression and localization. A good example is the neural synapse, where GPCRs are concentrated to ensure response to an extracellular ligand. Activation of a neuron can trigger membrane remodeling by increasing or decreasing the presence of receptors in the membrane. For example, G-protein kinases phosphorylate open conformation GPCRs, allowing β-arrestin-mediated endocytosis through clathrin-coated pits (Lohse et al. 1992; Lohse et al. 1990). These endocytosed GPCRs are either returned to the intracellular pool of receptors or downregulated through lysosomal degradation. This is an effective means through which cells can regulate hyperactive signaling cascades (Eichel et al. 2018). Therefore, for GPCR biology in particular, understanding the mechanics of how the cilium facilitates signaling will be fascinating. While it is possible that the cilium is simply a space where GPCR signaling can take place efficiently, it is also plausible that the cilium provides a space where the cell can run parallel signaling events. In this section I will discuss the movement of GPCRs throughout the cilium and how this relates to the regulation of SMO.

1.8.1 Cilia are a specialized environment for GPCR signaling cascades

As a small compartment, the cilium is in many ways an ideal environment for GPCR signaling. Ciliary enrichment of GPCRs can be sensitive to pathway stimulation, which can ensure receptor availability-, or absence-, when needed. Given the high concentration of signaling molecules and small volume of the cilium, it likely requires much less G-protein activation to influence second messenger pathways (Nachury 2014). Due to the compartmentalization of the cilium, GPCR-dependent signaling can locally influence cAMP and Ca^{2+} levels within the cilia microenvironment, affecting other signaling pathways.

GPCRs are well known to modulate intracellular cAMP levels through adenylyl cyclases (AC). Within the cilium, GPCRs regulate AC3 through either activating or inhibiting mechanisms. By molecularly targeting cAMP reporters to cilia, several groups detect cAMP changes exclusively within cilia suggesting that ciliary cAMP changes are unable to influence cellular levels of cAMP (Marley et al 2013). This raises the potential that one function of cilia is to enhance the concentration and spatial localization of signaling cascades to either increase GPCR signaling efficiency or output (Nachury 2014). It remains unclear whether cAMP in cilia is evenly distributed or is restricted into sub-compartments within the cilium. There is crosstalk between some GPCRs that may suggest that cAMP levels are uniform within the cilium. For example, activation of SMO by SAG can attenuate the cAMP response via MCH receptors bound to MCH ligand (Bansal et al. 2019). This may be due to competition of G-proteins, one inhibitory and one excitatory, converging on cAMP production. More sensitive, cilia-specific biosensors to measure cAMP levels in cilia will aid in understanding the specificity and kinetics of GPCR-influenced fluctuations in ciliary cAMP levels (Mukherjee et al. 2016).

GPCR-dependent signaling also influences Ca^{2+} levels within cilia. Ciliary fluctuations in Ca^{2+} were first linked to defects in *C. elegans* carrying mutations in polycystin-1 and polycystin-2 (PC1 and PC2) (Barr et al. 1999). PC1 and PC2 are ciliary mechanosensory channels that facilitate Ca^{2+} entry into cilia in response to mechanic movement of the cilium (Nauli et al. 2003). In *Chlamydomonas*, Ca^{2+} levels in flagella fluctuate in response to mechanical stimuli, influencing the movement of IFT cargos (Collingridge et al. 2013). In mice, mutations to *Ift88* cause polycystic kidney disease and postnatal lethality (Pazour et al. 2000). Mutant *Ift88* mice have short kidney cilia and abnormal increases in ciliary PC2 levels, resulting in changes to ciliary Ca^{2+} flux (Pazour et al. 2000; Pazour et al. 2002b). In fact, almost any disruption to kidney cilia or IFT causes kidney disease (Ma et al. 2013; Jonassen et al. 2008). Because of the low volume of the cilium compared to the volume of the cell body, small fluctuations in Ca^{2+} are likely sufficient for influencing downstream processes.

As with cAMP, several methods can detect Ca^{2+} flux within the cilium even though the cellular Ca^{2+} level in unchanged. For example, using *in vivo* calcium sensors, a Ca^{2+} flux can be observed within the cilia of the embryonic left-right organizer (LRO) that is distinct from Ca^{2+} flux in the cells of the LRO. PC2 receptors localize to these sensory cilia, suggesting a role of Ca^{2+} flux in the establishment of laterality (Muller et al. 2012; Sakuma et al. 2002; Mcgrath et al. 2003; Yuan et al. 2015; Yoshiba et al. 2012). In kidney epithelial cells, cilia sense fluid flow and activate Ca^{2+} influx that can be measured in the cell (Nauli et al. 2003; Jin et al. 2014; Su et al. 2013). This change in calcium is dependent on PC2-mediated calcium flow (Jin et al. 2014). While the roles of Ca^{2+} and cAMP in signaling pathways vary across tissues, advances in signaling cascade detection will help shed light on these differences (Lee et al. 2015).

1.8.2 Ciliary trafficking of GPCRs

The variety of cilia localization sequences suggest there are multiple pathways into the cilium, each using distinct machinery. Cilia GPCRs SSTR3, 5HT6, and MCHR1 all share a cilia localization sequence on their intracellular loops that is distinct from that in SMO (Berbari et al. 2008a; Corbit et al. 2005). The SSTR3, 5HT6, and MCHR1 receptors contain an AXXXQ targeting sequence on the intracellular loops that confers cilia localization. In contrast, the SMO localization sequence WR is found on the C-terminus. Moreover, these GPCR specific sequences differ from those of other cilia proteins. For example, VxPx motifs are necessary for ciliary enrichment of some proteins but dispensable for other cilia proteins containing the same motif (Geng et al. 2006; Mariani et al. 2016). However, a distinct cilia localization sequence in fibrocystin is sufficient to drive ciliary enrichment of GFP (Follit et al. 2010). Consistent with GPCRs using distinct trafficking mechanisms, TULP3 works with IFT to promote the trafficking of SSTR3, NPY2R and MCHR1 to cilia but does not affect SMO transport. (Mukhopadhyay et al. 2010). Studying the mechanisms that regulate ciliary GPCRs other than SMO will shed new light on trafficking dynamics in cilia entry, exit, and retention of GPCRs. Moreover, because GPCRs serve to activate specific signaling cascades, careful focus should be paid to study cilia-GPCR dynamics in relevant contexts.

The BBSome is an octameric protein complex critical for ciliary trafficking of membrane proteins, including GPCRs. The BBSome interacts with IFT, expanding the ability of IFT to transport distinct cargo (Lechtreck et al. 2009). The BBSome recognizes the activated GPCRs through specific intracellular sequences that are revealed when the receptor adopts an active conformation (Jin et al. 2010; Klink et al. 2017). Therefore, the BBSome is responsible for binding and trafficking activated GPCRs across the transition zone (Ye et al. 2018). In fact, activated

GPR161 and SSTR3 both require β-arrestin and BBSome-mediated transport across the transition zone for proper ciliary exit (Green et al. 2016; Ye et al. 2018; Pal et al. 2016). This is of critical importance to vHh signaling because GPR161 exits the cilium upon vHh stimulation as SMO enriches in cilia (Pal et al. 2016). Activated SMO exits cilia through ARL6-BBSome mediated transport, shuttling SMO to cross the barrier while still integrated in the plasma membrane (Ye et al. 2018; Jin et al. 2010; Nachury et al. 2007). Therefore, without proper trafficking components, GPCRs will linger in the cilium.

1.8.3 Ciliary trafficking and retention of SMOOTHENED

SMO is an intensely studied GPCR, therefore the knowledge of SMO function is forever changing. To maintain the organization and flow of this introductory Chapter I have omitted some of the most recent findings. Instead, I have included these data in Chapter 7 where I give my perspectives on the field and SMO function. Furthermore, in Chapter 7 I will specifically highlight recent data and discuss how they lead me to reinterpret some of the lab's previously published work, particularly Chapter 3.

SMO transport into and out of cilia is highly regulated as illustrated by its mislocalization in numerous mutants including those involved in IFT, BBSome-trafficking and the transition zone. In mutants with defective retrograde cilia traffic, SMO visibly accumulates within cilia indicting that it normally exits via retrograde IFT (Ocbina et al. 2008; May et al. 2005). When retrograde mutations are combined with hypomorphic mutations in anterograde IFT, slightly less ciliary SMO accumulates than in the single retrograde mutants consistent with SMO being trafficked within the cilium via IFT (Ocbina et al. 2008). The unconventional IFT25 subunit facilitates SMO and Ptch export from cilia and facilitates GLI2 enrichment at the ciliary tip (Keady et al. 2012). Mutations

in *RPGRIP1L*, which regulates transition zone structure, display a lack of SMO accumulation arguing that the integrity of the transition zone is needed for SMO ciliary entry or residency (Shi et al. 2017). In *Arl13b* and *Bbs* mutants, SMO accumulates in cilia in a ligand-independent manner, likely due to defective ciliary exit (Larkins et al. 2011; Zhang et al. 2011; Eguether et al. 2014). The fact that mutations in proteins that control diverse aspects of cilia biology all show abnormal SMO enrichment reflects the multiple levels at which its trafficking is likely regulated.

In principle, the trafficking of SMO to cilia reflects the fact that GPCRs reside near the membrane at which they function, usually in endocytic vesicular pools, awaiting changes in membrane organization before localizing there. Indeed, by tagging SMO in live cells and looking at a subsequent timepoint, one group surmised that most SMO travels to the cilium in vesicles from the Golgi via IFT (Wang et al. 2009). However, using a distinct tagging method, another group concluded that SMO is transported from the Golgi to the plasma membrane of the cell body, before moving though lateral transport into the ciliary membrane (Milenkovic et al. 2009). They found that SMO at the cell membrane turned over quickly and may have not been detected in the first study looking at a single timepoint. These data indicate at least one pool of SMO is available on the plasma membrane for cilia localization and subsequent activation.

Once inside the cilium, SMO localization and retention depends on chaperone proteins that bind the SMO C-terminus. This region interacts with G protein-coupled receptor associated sorting protein 2 (Gprasp2) to assist with ciliary targeting (Jung et al. 2016), and Ellis-Van Creveld protein (EVC/EVC2) to promote interaction with the vHh pathway component SUFU (Dorn et al. 2012; Yang et al. 2012). Moreover, SMO retention and Shh signaling is enhanced by the phospholipase A2, arachidonic acid pathway (Arensdorf et al. 2017). The necessity of chaperone proteins agrees

with the idea of a gating function at the base of the cilium, likely mediated by the transition zone. The SMO C-terminus contains a cilia localization sequence that aids with targeting to cilia and ciliary retention (Corbit et al. 2005). Enrichment of the SMO^{W539L} receptor corresponds with phosphorylation of the SMO C-terminus by kinases CK1α and GRK2 (Chen et al. 2011).

The ciliary enrichment of an activated GPCR requires the receptor bypass the mechanisms that remove it from the cilium. The BBSome is known to promote the movement of MCHR1 and SSTR3 receptors across the transition zone and out of cilia (Jin et al. 2010; Nachury et al. 2007; Berbari et al. 2008b; Ye et al. 2018). To achieve this, the BBSome recruits β-arrestin to facilitate the binding of activated GPCRs (Ye et al. 2018). This agrees with our understanding of β-arrestin function, that it preferentially binds activated GPCRs to facilitate their endocytosis, this includes activated SMO (Latorraca et al. 2018; Chen et al. 2004). Perhaps the cilium and BBSome have co-opted this endocytic pathway to shuttle activated receptors out of cilia (Green et al. 2016; Pal et al. 2016; Kovacs et al. 2008). An alternative exit strategy of activated GPCRs, including SMO, is exocytosis from the ciliary tip (Nager et al. 2017). Because GPCRs undergo conformational changes when activated, perhaps there are multiple pathways for moving a GPCR in and out of cilia, depending on the receptor conformation. In the next section I will discuss models of SMO activation.

1.9 Models of endogenous SMOOTHENED activation

SMO is an orphan receptor as its endogenous ligand has yet to be identified. However, important clues emerge from the fact that SMO can be activated by synthetic oxysterol molecules that associate with the N-terminal cysteine rich domain (CRD) (Dwyer et al. 2007; Nachtergaele et al. 2012; Corcoran et al. 2006; Yavari et al. 2010). In fact, membrane-associated cholesterol, an

abundant and endogenous sterol, binds to the SMO CRD and moderately activates the Shh pathway in cell lines (Luchetti et al. 2016a; Byrne et al. 2016; Huang et al. 2016; Huang et al. 2018; Myers et al. 2013). Therefore, lowered cholesterol abundance can suppress SMO activation (Blassberg et al. 2016). The SMO CRD contains a sterol-binding domain and the D99 residue is covalently modified by cholesterol. Mutating this aspartic acid residue to asparagine blocks cholesterol binding. $Smo^{D99N/D99N}$ embryos phenocopy $Smo^{-/-}$ embryos indicating that the residue is essential for SMO activation (Xiao et al. 2017; Zhang et al. 2001; Kasarskis et al. 1998; Caspary et al. 2002). Additionally, Smith-Lemli-Opitz patients carry mutations in the dehydrocholesterol reductase *DHCR7* resulting in decreased freely available cholesterol and present with morphological abnormalities consistent with deficient Shh signaling (Blassberg et al. 2016). Together, cholesterol plays an essential role in the activation of SMO, but it has not been designated the endogenous ligand for SMO.

Ligand binding alters GPCR conformation into either an activated or inhibited state (Zhao et al. 2007). When cholesterol binds to the SMO CRD, the receptor adopts an activated conformation in which the CRD shifts via an intermediate linker domain to form a new association with the SMO transmembrane domains (Zhao et al. 2007; Byrne et al. 2016; Nachtergaele et al. 2013). A mutation in the SMO linker domain is associated with decreased Shh signaling, suggesting dysfunction in SMO active conformation (Gigante et al. 2018). That said, the CRD is not the only SMO sterol-binding site. Another site on the intracellular portion of the seven-transmembrane binding pocket can bind cholesterol and activate SMO (Deshpande et al. 2019; Hedger et al. 2019). This activation is independent of the CRD sterol-binding site. More than likely, this second sterol-binding site plays a modulatory role in SMO activation. SMO is not the only GPCR activated by cholesterol, and considering that the plasma membrane is a lipid rich

environment, GPCRs likely all have their conformational states modulated by lipid dynamics (Hanson et al. 2012; Hanson et al. 2008). As discussed above, the ciliary membrane is a tightly regulated lipid rich environment, and contains sterols sufficient for activating SMO (Raleigh et al. 2019). As our knowledge of sterol driven SMO activation expands, models will soon need to examine the link between sterols, SMO, and the cilium.

The possibility that endogenous sterols activate SMO raises a question regarding whether PTCH1 regulates sterols to inhibit SMO. PTCH1 is long-known to bind cholesterolyated vHh (Kowatsch et al. 2019; Porter et al. 1996; Rudolf et al. 2019). Recent data show the endogenous sterol 24,25-epoxycholesterol binds both PTCH1 and SMO, and activates vHh signaling (Qi et al. 2019). These data also revealed SMO receptor coupling to the $G\alpha_i$ inhibitory subunit. An association between SMO and $G\alpha_i$ has been previously reported, but the role of G-proteins in SMO activation of the Hh cascade remained controversial (Polizio et al. 2011; Riobo et al. 2006). Perhaps oxysterols modulate SMO conformation, aiding the receptor to adopt new confirmations that promote transient G-protein coupling. This is in line with models that predict SMO activation is a multistep process. As the field shifts its focus towards the role of sterols in SMO activation, it will be paramount to define the role of the cilium in the steps of SMO activation- along with how PTCH1 regulates the sterols in the context of the cilium.

1.10 The evolution of Hedgehog signaling

The initial link between vHh signaling and cilia surprised the field primarily because invertebrate Hh signaling was well studied in *Drosophila*, where the pathway was identified (Nusslein-Volhard et al. 1980). While flies do have cilia, subsequent studies in fly IFT mutants did not reveal any defects in invertebrates Hh signaling. As fish, frogs and other vertebrates all

required cilia to transduce Hh signaling, the two were thought to be linked only in vertebrates (Park et al. 2006; Huang et al. 2009; Tay et al. 2010; Glazer et al. 2010b). However, sea urchin embryos rely on motile cilia for Hh signal transduction in developing muscle (Walton et al. 2009; Warner et al. 2014). This work suggested that protostome lineages such as flies diverged from deuterosomes with respect to using cilia for Hh transduction. Additionally, it raised the question of whether vertebrates use motile cilia, in addition to primary cilia, for Hh signaling.

The regulatory logic of the Hh pathway in flies and is conserved in vertebrates (Nusslein-Volhard et al. 1980; Goodrich et al. 1996; Hahn et al. 1996). In the off state, the Hh receptor Patched (PTCH1 in vertebrates) inhibits SMO, limiting its GPCR activity (Rohatgi et al. 2007). The Ci transcription factor (GLI proteins in vertebrates) is cleaved into a repressor form, which inhibits the transcription of target genes, a process mediated by COS2 (KIF7 in vertebrates) (Zhang et al. 2005; Kalderon 2004; Tay et al. 2005). When Hh ligand is present, it binds the PTCH1 receptor, alleviating PTCH1 mediated repression of SMO (Stone et al. 1996). SMO is subsequently activated and full-length Ci, instead of being cleaved, is activated through posttranslational modification, which then turns on target genes (Aza-Blanc et al. 1997).

Several clues to how Hh and vertebrate primary cilia are linked come from examining when proteins evolved relative to ciliation in various species. IFT25 and IFT27 are unique among IFT components as they are lost in several ciliated species suggesting they may not play roles in cilia. Mice without *Ift25*, ciliate normally, but die shortly after birth with phenotypes consistent with low Hh signaling (Keady et al. 2012). *Ift27* mouse mutants display similar phenotypes. IFT25 and IFT27 are required for the export of SMO and PTCH1 out of cilia so may have evolved to traffic Hh components to cilia (Eguether et al. 2014; Liew et al. 2014).

Finally, the mechanism through which PTCH1 inhibits SMO remains unknown, but is likely linked to cilia. The two proteins do not interact directly and PTCH1's inhibition on SMO is not stoichiometric (Taipale et al. 2002). It is possible that PTCH1 shields SMO from its ligand or that PTCH1 removes or sequesters SMO's ligand (Zhang et al. 2018; Deshpande et al. 2019; Qi et al. 2019; Kowatsch et al. 2019). It is also not clear what the endogenous ligand for SMO is- or exactly how the receptor is activated, but it is likely occurring in cilia. The evolutionary change that shifted Hedgehog signaling into the cilium will remain uncertain, but the evolutionary origin of the switch occurred around the same time *Arl13* duplicated into *Arl13a* and *Arl13b*. *Arl13* is ancient, present in the last eukaryotic common ancestor, with conserved function as a regulator of membrane transport and protein trafficking that is maintained across model systems.

1.11 Summary and Dissertation Roadmap

In this chapter, I laid out the history and relevant background for my thesis project emphasizing the data supporting my hypothesis, that ciliary protein ARL13B is an essential regulator of the ciliary processes that regulate and activate SMO.

In Chapter 2, I detail the methods I used. Chapters 3 and 4 are published. In Chapter 3, I characterize a novel mouse mutant and argue localization of SMO to the cilium is required for the highest levels of Shh signal transduction. In Chapter 4, I show that – despite all expectations – cilia protein ARL13B is not required in cilia to regulate Shh signaling. In Chapter 5, I present data that ARL13B is required in cilia to prevent the development of kidney cysts and obesity. In Chapter 6, I address the core question of this dissertation, whether (and perhaps how) ARL13B is involved in the ciliary processes that activate SMO. In Chapter 7, I will broadly discuss my findings with

the perspective of new discoveries in the field. Thus, I highlight how my work will expand our knowledge of the enigmatic links between cilia, SMO, and the role of ARL13B.

CHAPTER 2

MATERIALS AND METHODS

Parts of this chapter previously published as:

Gigante, E.D., Bushey Long, A., Ben-Ami, J., and Caspary, T. (2018) Hypomorphic Smo mutant with inefficient ciliary enrichment disrupts the highest level of vertebrate Hedgehog response. *Developmental Biology, Vol 437:2. 152-162.* doi.org/10.1016/j.ydbio.2018.03.019

Gigante, E.D., Taylor, M.R., Ivanova, A.A., Kahn, R.A., and Caspary T. (2020) ARL13B regulates Sonic hedgehog signaling from outside primary cilia. *eLife 2020;9:e50434* doi:10.7554/eLife.50434.

2.1 Mice

All mice were cared for in accordance with NIH guidelines and Emory's Institutional Animal Care and Use Committee (IACUC). Alleles used were: *Smo*^{cbb} [MGI: 5911831], *Patched1-lacZ* [MGI: 1857447], *Smo*^{bnb} [MGI: 2137553], *Arl13b*^{V358A} (*Arl13b*^{em1Tc}) [MGI: 6256969], *Arl13b*^{hnn} [MGI: 3578151], and FVB/NJ (Jackson Laboratory).

2.1.1 Mapping and identification of the cabbie mutation

The *cabbie* mutation was identified in a screen for recessive ENU mutations that caused morphological defects during midgestation. Induced on a C57BL/6J background and backcrossed onto FVB/NJ, *cbb* was mapped to chromosome 6 using a low-density Illumina chip. The *cbb* mutation was refined to a 5-MB interval (D6Mit159 to D6Mit268) using SSLP marker-based PCR. Through whole-exome sequencing (Mouse Mutant Resequencing Project, Broad Institute) and subsequent analysis using SeqAnt, a cytosine-to-adenine SNP in exon 3 of the *Smoothened* (*Smo*) gene was identified (Shetty et al. 2010). Genotyping was performed by PCR using D6MIT159 primers (Fwd: 5'- CATATTCAAGACGGAGACTAGTTCC-3', Rev: 5'- CACATGAAACACATGCACACA-3') to amplify a strain-specific variation 3 kb upstream of the *cbb* point mutation (see **Table 1** and **Table 2**). We confirmed the linkage of this marker via analysis of 225 E10.5 embryos from our breeding pedigree: 175/176 embryos phenotypically classified as normal genotyped as "control" (homozygous or heterozygous FVB at D6MIT159), and 49/49 embryos phenotypically classified as *cbb* genotyped as "mutant" (homozygous C57BL/6 at D6MIT159). We saw no differences between wild-type or heterozygous *Smo*^{cbb} embryos and show the heterozygous phenotype as "control" in Chapter 3.

2.1.2 ARL13B^{V358A} mouse allele generation and identification

To generate the V358A point mutation in the mouse, a CRISPR gRNA (CCAGTCAATACAGACGAGTCTA) targeting exon 8 of the *Arl13b* locus along with a donor oligo (5'-CCTATATTCTTCTAGAAAACAGTAAGAAGAAAACCAAGAAACTACGAATG AAAAGGAGTCATCGGGCAGAACCAGTGAATACAGACGAGTCTACTCCAAAGAGTCC CACGCCTCCCCAAC-3'; underlined bases are engineered) were designed to generate a T-to-C change creating the V358A point mutation and C-to-G change creating a TspRI restriction site that could be used for genotyping (Millipore Sigma). The gRNA (50 ng/μl), oligo donor (50 ng/μl) and CRISPR protein (100 ng/μL) were injected by the Emory Transgenic and Gene Targeting core into one-cell C57Bl/6J zygotes. Zygotes were cultured to 2-cell before being transferred to pseudopregnant females. Genomic tail DNA from resulting offspring was amplified using PCR primers (5'-GAAGCAGGCATGGTGGTAAT-3' & 5'-TGAACCGCTAATGGGAAATC-3') located upstream and downstream of the donor oligo breakpoints. The products were sequenced (5'-GAAGCAGGCATGGTGGTAAT-3') and 2 animals were identified heterozygous for the desired change and with no additional editing. One founder (#173) was bred to FVB/NJ for three generations prior to performing any phenotypic analysis. Males from at least two distinct meiotic recombination opportunities were used in each generation that to minimize potential confounds associated with off-target CRISPR/Cas9 editing. Both founders were bred by Sarah Suciu to C57BL/6 mice in an attempt to establish lines on that background but without success.

Genotyping was performed on DNA extracted from ear punch or yolk sac via PCR (see **Table 1**). To identify V358A a SNP was engineered in the forward primer that, in combination with the V358A mutation, created a Cac8I restriction site. Thus, the PCR product was digested

with Cac8I enzyme, run out on a 4% agarose gel and the relevant bands were detected: undigested wild type (~192bp) and digested mutant bands (~171bp). This is a nested PCR that required an initial reaction, see **Table 1** and **Table 2**. Reaction A product should be diluted 1:1000 (1:40 then 1:78) before running reaction B. Only 2 μL of reaction B should be digested for easy identification of heterozygous and mutant bands. The digested product should be run out on a 4% gel for at least 90 minutes.

2.2 Phenotypic analysis of embryos

2.2.1 Dissection and Processing

Timed matings of heterozygous mice were performed to generate embryos of the indicated stage, generally E9.5-18.5. As there can be up to a 12-hour difference in development within a litter, somite-matched embryos were examined at each stage when possible. Embryos were dissected in cold phosphate-buffered saline and yolk sac collected for genotyping. Intact embryos were collected for whole mount images. Embryos were fixed in 4% paraformaldehyde for a minimum of 1 hour at 4°C. After fixation, embryos were rinsed with PBS to remove excess PFA and replaced with a 30% sucrose solution in 0.1M phosphate buffer (see recipes). Embryos for skeletal processing were skinned and eviscerated before alizarin red and alcian blue staining (Caspary et al. 2007; Shen et al. 1997).

2.2.2 Embedding and cryosectioning

Embryos were embedded separately in OCT if the genotypes were unknown and together if genotypes were known. If embedded together, embryos were catalogued in a reproducible manner for later identification. To isolate the specific regions of neural tube at the forelimb and

hindlimb levels, embryos were separated into three pieces before embedding. Embryos were sectioned just caudal of the forelimbs, and the head removed under the brachial arches, as well as just rostral to the hindlimbs. These pieces were embedded with the neural tube side down in the block as depicted in **Figure 1.1**, enabling the desired tissue to be collected immediately. This method was developed to reduce the amount of time sectioning each block, the number of sections that needed to be collected, and the number of slides per embryo. Sections acquired were ~10 μM thick and placed on Superfrost plus glass slides. Slides were dried at least 30 minutes or overnight.

2.2.3 Antibody staining

Prior to antibody staining sections were outlined with a hydrophobic pen and allowed to dry for 10-15 minutes or while the slides continued to dry after sectioning. Slides were then moved to a humidified chamber and rehydrated with PBS for 10 minutes. The PBS was then replaced with 150-200 μL of antibody wash buffer (5% heat-inactivated goat serum, 0.1% Triton-X in PBS) and incubated for 1 hour at room temperature. After 1-hour, slides were incubated with 150-200 μL primary antibody in antibody wash buffer. Primary antibody was left on the slides overnight at 4°C in the humidified chamber. The following day slides were rinsed with PBS or antibody buffer, three washes for 10-30 minutes each. Slides were then incubated in dark with secondary antibody for 1-2 hours. Slides were cryo protected with ProLong and a glass cover slide and allowed to cure overnight before image processing. See **Table 3** for preferred secondary antibody combinations.

Cilia markers such as acetylated α-tubulin, ARL13B, SMO, and IFT88 all work with the standard antibody staining protocol outlined above. For Inpp5e staining: used hydrophobic pen and rehydrated slides with PBS as described above. Permeabilized with 0.1% Triton X-100 in PBS for 5 minutes, then rinsed three times with PBS for 3 minutes each. Blocked for 1 hour at room

temperature in a blocking solution of 1% BSA in PBS. Added primary antibody (1:150) in blocking buffer for 1 hour at room temperature. Washed slides with PBS three times for 3 minutes. Applied secondary antibody in blocking solution for 1 hour at room temperature. Washed three times with PBS for 3 minutes each. Mounted coverslip with ProLong. For Arl3 staining: slides were fixed with 4% PFA for 15 minutes at 37C. Slides were rinsed in PBS before incubation with 0.1% Triton X-100 for 5 minutes. Primary ARL3 and secondary staining proceeded following the standard protocol outlined above. For a list of cilia antibodies see **Table 4**.

2.3 Western blot of ARL13B protein in whole embryo lysates

Embryo lysates were prepared with RIPA buffer and SigmaFast protease inhibitors (see recipes) (Nachtergaele et al. 2013). Dissected, embryos were placed in individual 1.5 mL tubes containing 200 μL RIPA buffer, homogenized by sonication (WH 322) with short 2 second bursts, allowing for 5 to 10-minute rests between. Lysates were clarified by spinning at 30,000 RPM at 4°C for at least 15 minutes (tabletop centrifuge Eppendorf; Escagy lab). The supernatant was isolated and the pellet containing large organelles and membrane was discarded.

A protein estimation was performed on each sample with ~10 μLs of the lysate. The 10 μLs was diluted 1:20 in PBS. Protein estimation was performed with Pierce BCA protein assay kit (ThermoFisher 23227) the protocol outlined by the manufacturer. The remaining sample was mixed 1:4 with 4x Laemlli buffer (Bio-Rad) with β-mercaptoethanol. Samples were then boiled for ~7 minutes. The final protein estimations were corrected for the 1:20 dilution and the 1:4 dilution in Laemlli buffer to identify the appropriate amount of sample.

Samples were run on a 10-well gel from Bio-Rad, comprised of 7.5% acrylamide Stain-Free gel (Bio-Rad 4568023), submerged in running buffer. Gels were run at 155 Volts for 60 minutes or until the dye front exits the bottom of the gel. Using a ChemiDoc Touch Imaging System (Bio-Rad; WH322) cross-linking was activated for 45 seconds before a 5 second image of total protein was acquired. Blots were then transferred to a PVDF membrane using a high-speed transfer stack (Bio-Rad 1704156), run on the high MW mini gel setting. PVDF blots were trimmed and soaked in T-20 Blocking buffer (ThermoFisher 37539) for 1 hour at room temperature. Mouse anti-Arl13b (1:5000 NeuroMab N295B/66) was diluted in T-20 buffer and added to the blot. Blots were gently agitated on horizontal rocker located in the hallway 4°C walk-in cooler overnight. The following day blots were rinsed with Tris-buffered saline with 0.1% Tween-20 (TBS-T) for three washes, 5 minutes each at room temperature. Blots were pre-blocked in TBS-T with 5.0% dried milk (Bio-Rad 1706404) for 15 minutes before incubation with anti-mouse secondary antibody conjugated with horseradish peroxidase (HRP; 1:5000), also in TBS-T with 5.0% milk. During secondary antibody incubation the blots were agitated for 1 hour at room temperature. Blots were quickly rinsed with TBS-T and washed three additional times for five minutes each. Blots were then incubated with 1:1 chemiluminescence (ThermoFisher 34577) for ~ 7 minutes before imaging in the ChemiDoc unit. Blots were exposed for 5-20 seconds, or auto exposed to minimize pixel saturation. Final data was analyzed in the Image Lab software package designed by Bio-Rad and normalized to total protein measurements from the day before (Thacker et al. 2016; Rivero-Gutiérrez et al. 2014). There are two normalization options, one is to use the entire lane as a measure of total protein or use a single band across all samples as the control. Either will yield similar values. Normalized values were analyzed by one-way ANOVA and Tukey's multiple comparisons in GraphPad's Prism 9 software.

2.4 Derivation of mouse embryonic fibroblasts (MEFs)

All cell culture experiments were performed in a clean tissue culture hood (WH 322A). All cells were maintained in a humidified cell incubator with 5% CO_2 and maintained at 37°C, unless otherwise specified.

2.4.1 Isolating primary MEFs

Mouse embryonic fibroblasts (MEFs) were isolated and immortalized as previously described (Mariani et al. 2016). The day before dissections multi-well plates were incubated with 0.1% gelatin. The size of the wells is determined by the age of the litter. Suggested sizes are as follows; E9.5 in 24 well, E10.5 in 12 well, E11.5 in 6 well, and E12.5 in 40mm dish. Embryos were dissected in cold PBS and eviscerated with their heads and internal organs removed. Each individual embryo was then isolated in a 1mL syringe with ~200 μL PBS and capped with a 26-guage needle. Each embryo was given its own syringe and numerical identifier for tracking.

The gelatin solution from the previous day was removed from each well, and wells were rinsed with PBS twice. Each well was then filled to 50% maximum volume with DMEM with 10% fetal bovine serum (FBS) and 1% penicillin/streptomycin. Embryos were passed through the needle several times to separate the cells. Plates were then agitated briefly to ensure an even distribution in each well. Plates were incubated at 37°C in 5% CO_2. Cells were checked for confluency on a daily basis before passaging into two 10 cm dish at ~90% confluency: one for propagating and immortalization, and one for freezing and storage as a backup.

2.4.2 Immortalizing MEFs

In my hands, the FV358A-67.9, 67.7, and 67.3 (*Arl13b*$^{+/+}$, *Arl13b*$^{V358A/+}$, and *Arl13b*$^{V358A/V358A}$, respectively) immortalized cell lines were generated from E10.5 embryos dissected by me, and cultured and maintained by Megan Taylor (former undergrad). Alyssa generated the AW4-387.2 and 387.1 (*Smo*^{wt} and *Smo*$^{cbb/cbb}$, respectively) with help from Joey Ben-Ami (former undergrad). The immortalization process is as follows. MEFs were isolated as described in 2.4.1. At passage 2 or 3, cells were cultured until 50-75% confluent before proceeding. It is important to use passage 2 or 3 cells for immortalization because these passages are much less likely to contain unwanted cell types. Once confluent, cells were transfected with SV40 T antigen construct (Plasmid 161). See section 2.4.4 for details on setting up a transfection reaction. Following the transcription protocol, MEFs were cultured until 80-90% confluent and split into two 10-cm gelatinized plates, one 1:4 and the other 1:10. The higher seed plate was frozen down as a backup and the lower density plate was allowed to grow until confluent. Cells were continually passaged and split in this manner until passaged 6 times. Once achieved, the cells could be considered immortalized.

2.4.3 Working with MEFs

MEFs have a doubling time of ~24 hours, so experiments were planned over the number of 24-hour periods between initial seeding of cells, and final experimentation. For example, a 48-hour protocol on coverslips required MEFs be seeded at a density of 0.2-0.5 x 10^5 cells/mL. After 24 hours of recovery, the cells can be manipulated by ligand for another 24 hours before they will become confluent. In some experiments cells were treated for 24 hours with 0.5% FBS Shh conditioned media or 0.5% FBS media to induce ciliogenesis (Larkins et al. 2011). Low serum

media is required for the induction of ciliogenesis in MEFs, but confluency can also impact ciliation rates.

2.4.4 Transfecting MEFs

Cells were plated the day before transfection such that they reach ~60-80% confluency the following day. DNA and thawed Magnetofectamine (OZBiosciences MTX2 1000) reagent were mixed together at a ratio of 1:3. To this mixture, add 100 μLs of prewarmed OPTI-mem and incubated for 20 minutes at room temperature. To this mixture, 1 volume of magnetic beads was added (for example 0.6 uLs for 600ng of DNA) and incubated for 20 minutes at room temperature. The cultured cells from the day before were then placed on top of the magnetic plate in the tissue culture hood. The complete transfection reaction was then added dropwise to the appropriate wells. Keeping the magnetic plate under the plate of cells, the cells were then returned to the incubator and left for 20 minutes. Afterwards, the magnetic plate was removed, and cells left in the incubator for an additional 4 hours. Once this step was complete the media was replaced on call conditions with complete MEF media. This media change was essential to prevent cytotoxicity. The cells were then allowed to recover overnight.

2.4.5 MEF antibody staining of cilia

MEFs were seeded at $0.5x10^5$ cells/mL onto uncoated 5mm round glass coverslips in a 6-well plate in 2-3mLs of complete media on day 0. The following day, the media was replaced with low serum media (0.5% FBS in DMEM) for an additional 24 hours. On day 2 the coverslips were rinsed with PBS and incubated with 4% paraformaldehyde for 5 minutes. Coverslips were again rinsed with PBS and incubated with antibody wash buffer (10% heat inactivated goat serum, 0.1% Triton X in PBS) for 15 minutes. Coverslips were removed from antibody wash buffer and placed

on a modified 12-well plate to act as a humidified chamber. A 60 μL volume of primary antibody was gently added to the top of each coverslip. Plates were incubated overnight at 4°C. See **Table 4** for antibody combinations employed.

The following day the primary antibody solution was aspirated off the coverslip edge and rinsed with antibody wash buffer, three times for 10 minutes each. Coverslips were then incubated with 60 μL of secondary antibody in antibody wash buffer for 1 hour at room temperature and stored in a dark place. Coverslips were washed with PBS three times and kept in the dark between washes. Coverslips were dried with a Kimwipe before being inverted and mounted onto a SuperFrost microscope slide with ProLong. Removing the moisture allowed the ProLong to cure properly overnight, too much liquid prevented this from occurring and allowed the slides to move, ruining the sample.

2.4.6 Ciliobrevin-D treatment

Control and *Ar13b*$^{V358A/V358A}$ MEFs were seeded as outlined previously and incubated in 0.5% FBS media for 24 hours in cell incubator. Media was removed and 30 μM ciliobrevin-D (Millipore Sigma; 25041) or 0.1% DMSO (Sigma D2438) in 0.5% FBS in DMEM added for 60 minutes. MEFs were fixed and stained as described above (2.4.5). The 60 minute incubation with Ciliobrevin-D was chosen because Ciliobrevin-D causes microtubule disorganization and cilia disassembly after 60 minutes (Firestone et al. 2012).

2.4.7 Image Quantification of MEF cilia

Images were acquired on a Leica CTR6000 microscope using SimplePCI software with 20X or 40X air objective. For each experiment, exposure conditions were set based on control

fluorescent levels before acquiring images of experimental samples. Images were saved in .tif format and files retained the three individual RGB channel data. Fluorescent intensities of *Arl13b*^{V358A} and control cells were measured using ImageJ software. Cilia were first identified by positive acetylated α-tubulin and an outline was hand drawn around the length of the cilium. The channel was switched to the protein of interest and a measurement of the average fluorescent intensity was acquired. To acquire a background reading, the same outline was then moved adjacent to the cilium, but still within the cell body, to an area that most closely matched the background at the cilium. In all cases immunofluorescent averages of proteins of interest in cilia were normalized to cell-body intensities (**Figure 4.3-Figure Supplement 1**). For samples with antibodies targeting Gli2, Gli3, and Sufu the ciliary tip was isolated and measured. The cilia tip was identified by weak acetylated α-tubulin staining. If the tip was not easily identified, the cilia base was identified by acetylated α-tubulin positive fibrils in the cell body that cluster at the base of the cilium (Larkins et al. 2011).

For samples with antibodies targeting SMO, PTCH1, ARL3, and INPP5E the entire cilium was measured. The ratio of fluorescence intensities of the protein of interest relative to the cell body background was organized as violin plots. Within each plot the dashed lines represent the median and interquartile range. The number of cilia examined per genotype and per condition are listed below their respective plot. All data, except for SMO which varied both genotype and treatment, were analyzed by one-way ANOVA. In the event of a significant ANOVA, Tukey's multiple comparisons were employed to determine significance as all groups were compared. SMO fluorescent intensity data were analyzed by two-way ANOVA. As only specific groups were compared, the significance of those comparisons across and between groups were made using

Sidak's post-hoc to not inflate the significance of those comparisons Data were analyzed in GraphPad Prism 7 software.

For cells treated with Ciliobrevin-D, as described in section 2.4.6, cilia were identified by staining with antibodies directed against acetylated α-tubulin, IFT88, and ARL13B. Fluorescent intensities were measured in ImageJ software. Cilia were identified as described in the paragraph above. IFT88 fluorescent levels were measured at the ciliary tip. Each ciliary measurement was normalized to its own cellular background. To make comparisons among cell lines of distinct genotype with and without ciliobrevin-D treatment, data were analyzed by two-way ANOVA. To analyze the specific differences across groups, multiple comparisons were made using Sidak's post-hoc.

2.4.8 RT-qPCR analysis of Shh transcriptional targets in MEFs

Confluent experimental MEFs in 6-well plates were harvested by trypsinization, spun down, and flash frozen. RNA was isolated by QIAGEN RNeasy kit (74104) with QIAshredder homogenizer columns (QIAGEN 79656) following the manufacturer's instructions. RNA quantities were measured by Nanodrop (Thermo Scientific NanoDrop 1000) and cDNA was synthesized with iScript Reverse Transcription Supermix (Bio-Rad;1708840) using 200 ng of RNA per reaction following the manufacturer's instructions. Primers (**Table 5**) used were: *Ptch1* 5'-TGCTGTGCCTGTGGTCATCCTGATT-3', and 5'-CAGAGCGAGCATAGCCCTGTGGTTC-3'*; Gli1* 5'-CTTCACCCTGCCATGAAACT-3', and 5'-TCCAGCTGAGTGTTGTCCAG-3'*; Pold3* 5'-ACGCTTGACAGGAGGGGGCT-3', and 5'-AGGAGAAAAGCAGGGGCAAGCG-3' (Mariani et al. 2016).

RT-qPCR reactions were performed in technical triplicate on three biological replicates as previously described (Mariani et al. 2016). Each reaction contained 2μL of diluted cDNA, 10μL of Bio-Rad Sso Advanced Universal SYBR Supermix (1725270), 3μL each of 1:100 forward and reverse primer, and 2μL of water. All ingredients, except the cDNA sample were combined to form a Master mix and added to each well of the PCR plate. While adding master mix the plate was kept on ice. Once the master mixes were added to each well, the plate was gently spun down. Then, cDNA sample was reverse pipetted into the appropriate wells. The sample was placed halfway down each well and placed on the wall of the well, not into the solution. Once all samples were added the plate was then sealed, spun down, vortexed, and spun down again. This insured that all samples were exposed to PCR reactions at the same instant. Each plate was run on a Bio-Rad CFX96 Touch Real Time PCR Detection System, and data were collected using Bio-Rad CFX Manager 3.1. The PCR program conditions were as follows; 95°C for 5 min; 45 cycles of 95°C for 15 seconds, 57°C for 30 sections, plate read; followed by a melt curve beginning at 65°C and ending at 95°C.*Gli1* and *Ptch1* expression levels were normalized to each sample's corresponding *Pold3* level. Normalized RT-qPCR data were analyzed by ANOVA with Bonferroni correction for multiple comparisons.

2.5 Protein purification and ARL3 GEF assay of Arl13b

These experiments were performed by Anna Ivanova, formerly of the Kahn lab. Plasmids directing the expression of mouse GST-ARL13B or GST-ARL13B^{V358A} proteins were transiently transfected into HEK cells and the recombinant proteins were later purified by affinity chromatography using glutathione-Sepharose, as described previously (Cavenagh et al. 1994; Ivanova et al. 2017). Human ARL3 (98.4% identical to mouse ARL3) was expressed in BL21

bacteria and purified as previously described (Van Valkenburgh et al. 2001). The ARL3 GEF assay was performed as previously described (Ivanova et al. 2017). Briefly, ARL3 (10μM) was pre-incubated with [^{3}H]GDP (1 μM; PerkinElmer Life Sciences, specific activity ~3,000 cpm/pmol) for 1 h at 30°C in 25 mM HEPES, pH 7.4, 100 mM NaCl, 10 mM $MgCl_2$. In contrast, pre-loading of ARL13B (10μM) was achieved by incubation in 100 μM GTPγS for 1 min at room temperature, due to its much more rapid exchange kinetics. The GEF assay was initiated upon addition of ARL3 (final = 1μM), ARL13B (final = 0 or 1μM), 10 μM GTPγS, and 100 μM GDP (to prevent re-binding of any released [^{3}H]GDP), in a final volume of 100 μL. The intrinsic rate of GDP dissociation from ARL3 was determined in parallel as that released in the absence of any added ARL13B. The reactions were stopped at different times (0–15 min) by dilution of 10μL of the reaction mixture into 2 ml of ice-cold buffer (20 mM Tris, pH 7.5, 100 mM NaCl, 10 mM $MgCl_2$, 1 mM dithiothreitol). The amount of ARL3-bound [^{3}H]GDP was determined by rapid filtration through BA85 nitrocellulose filters (0.45 μm, 25 mm, Whatman), with 3 x 2 mL washes, and quantified using liquid scintillation counting. Time points are routinely collected in at least duplicate and each experiment reported was repeated at least twice, yielding very similar results. Data were analyzed in GraphPad Prism 7 software.

2.6 Structural prediction of SMO

A putative structure of the SMO^{N223K} mutant protein was modeled by a former graduate student, Jennifer Colucci, of the Ortland lab, using PyMol (Version 2.0; Python) and UCSF Chimera resource (version 1.12) (Pettersen et al. 2004). The mutation model was formed by 500 sequential iterations of energy minimization and geometry optimization on crystallized human SMO receptor bound to SAG ligand (PDB: 4QIN) (Wang et al. 2014).

2.7 Cell-based, cAMP-sensitive GloSensor assay for SMO activation

2.7.1 Working with HEK-293FT cells

HEK-293FT (HEK) cells were used for their high rate of transfection and high expression of protein. Wells were preincubated with 0.2 mg/mL poly-D-lysine in 96-well plates to help HEK cells adhere for assay readout. Plates were preincubated the day before experimental use and kept in cell incubator overnight 37°C. The following day plates were rinsed several times with PBS and allowed to dry before experimental use. Glass coverslips were coated with 0.1% gelatin to promote cell adherence, the cells will wash off during antibody staining steps previously outlined in this chapter. HEK cells were cultured in a modified DMEM solution with 10% FBS (See recipes section). All solutions were added slowly down the side of a plate to avoid pushing cells off the surface. Due to their poor adherence, HEK cells can be quickly passaged by resuspending with only media. However, this method was not used when seeding cells for experimental use. Forcibly removing HEK cells from a plate caused them to form aggregates that disrupt the cell counter's ability to differentiate between clusters and single cells. HEK cells were sensitive to 0.25% trypsin, and cell passage only required one to two minutes incubation at room temperature. Over incubation in trypsin would cause cytotoxicity and cell death. Cells incubated with trypsin were less likely to aggregate and provided more accurate cell density readings. To increase cell yield, plates were physically agitated briefly, before cells were aspirated and resuspended in complete media.

2.7.2 The cAMP-sensitive GloSensor assay for SMOOTHENED activation

HEK cells were plated on day 0 in a 6-well plate at 1.1 x 10^5 cells/mL, a total of 3 mL per well. On day 1, the media was replaced on all cells to be transfected ~2 hours before the start of transfection protocols. The transfection mixture was prepared as follows; 3:1 Lipofectamine 2K to

DNA volume in 200 μLs of Opti-MEM (ThermoFisher 31985062), incubated for ~5 minutes. The desired plasmids were mixed together in 200 μL of Opti-MEM (see table 6 and section 2.7.3). Then, lipofectamine containing media was added to the plasmid containing media and mixed gently. This reaction was incubated for 15 minutes at room temperature. The complete transfection reaction was then added dropwise into the appropriate wells and cells were incubated overnight at 37°C. Finally, in preparation for the following day, ~100 μL of 0.2 mg/mL poly-D-lysine was added to each well of a 96 well plate and incubated overnight at 37°C.

On day 2, only healthy conditions that responded well to the transfection were used in the remaining steps of the experiment. The media was replaced on unhealthy cells and allowed an additional 24-hour recovery. First, the 96-well plate from day one was rinsed twice with sterile PBS and allowed to dry for several hours. Cells were then briefly washed with PBS and incubated with 150 μL of 0.25% trypsin. Once the cells began to lift off the plate, they were resuspended in 1 mL complete media. Immediately, 10 μL of cells was mixed with 10 μL of Trypan Blue (ThermoFisher 15250061), and 10 μL of the 1:1 mix was added to a TC20 cell counter slide (Bio-Rad 1450015) used for cell counting on a Bio-Rad TC20 cell counter (WH322). A dilution of 1.0 x 10^5 cells/mL was prepared for each sample. Each well received 200 μL of diluted cells and the plate was incubated overnight at 37°C.

The assay was continued if the cells recovered well the following day. Media was aspirated and cells were washed twice with Ca^{2+} Ringers solution (see recipes section). Then, cells were incubated with 100 μLs of D-luciferin (see recipes section) in Ringers solution and incubated in the dark at room temperature for 1 hour. During this incubation step, both forskolin (see recipes section) and SMO drugs were prepared in Ringers solution (see recipe section). After incubation,

50 μL of the SMO drug or 50 μL of Ringers buffer control was added to each well and be incubated for 10 minutes. Data were acquired using a POLARstar Omega plate reader, located in 5175 RRC. In the plate reader, 1 second readings were acquired at 2-minute intervals, a total of 5 baseline and 20 or more post-forskolin readings. After the 5 baseline readings, 50 μL of 4 μM Forskolin was added to every well. This should induce a large response curve, maxing out above 10,000 Luciferase units.

2.7.3 Plasmid combinations for the cAMP-sensitive GloSensor assay.

As published by Myers et al., (Myers et al. 2017), the following amounts of plasmid should stay constant; 200 μg SMO, 400 μg PTCH1, and 800 μg GloSensor (see example plate in **Table 6)**. The readout from cells transfected with only GloSensor represented the maximal luciferase response possible. The readout from cells transfected with only empty vector plasmid provided a background reading for cells with luciferin but no luciferase for processing. The readout from this condition remained flat throughout the entire experiment. This experiment included a transfection efficiency control using an enhanced GFP plasmid on cells that were plated on cover slips (pretreated with 0.1% gelatin). Using 1400 μg of plasmid to acquire an accurate reading of what % of cells were transfected with experimental plasmids. Cells transfected with enhanced GFP were rinsed with PBS and fixed with 4% PFA for 15 minutes. Cells were then incubated with an antibody wash buffer (see section 2.4.5) for 10 minutes with 1:3000 Hoechst nuclear stain. Coverslips were inverted onto a microscope slide with ProLong. Slides were then immediately imaged for a readout of transfection efficiency or allowed to cure overnight in dark.

2.8 Analysis of obesity and diabetes phenotypes in *Arl13b*$^{V358A/V358A}$ mice.

2.8.1 Weight curves

Mice expressing *Arl13b*^{V358A} (*Arl13b*^{em1Tc}) [MGI: 62256969] and/or *Arl13b*^{hnn} [MGI: 3578151] were maintained on an FVB/NJ background (Jackson Laboratory). Male and female mice were group housed by sex at 3 weeks postnatal and provided *ad lib* 24-hour access to standard chow with 5% fat (LabDiet #5053) or breeder chow with 8% fat (LabDiet #5058) and water. Breeding pairs to generate mice for weight curve generation were also maintained on breeder chow. Mice were weighed weekly from postnatal day (P)21 to P70. All mice were handled in the same manner and picked up by their tails. Raw weight data are presented as average weight in grams for each genotype, separated by sex and age. Data analysis performed in Prism (GraphPad V8.3.1). Weight data were analyzed by a mixed-effects model of repeated measures. This method of analysis allows for randomly missing values. In the event of a significant effect and interaction, multiple comparisons were made between each genotype at all timepoints using Sidak's post hoc. A significant difference was identified by a p-value < 0.05, and p-values were adjusted for multiple comparisons.

2.8.2 Glucose and insulin tolerance tests

Male and female adult mice (3-4 months) were allowed 24-hour access to breeder chow and water. For tests of glucose tolerance, mice were individually housed on ALPHA-dri bedding (Shepherd) with no food and *ad lib* access to water for 15-18 hours overnight. The following day mice were weighed, anesthetized, and a baseline blood glucose level was acquired from the tail. Blood glucose was measured by an AlphaTRAK2 blood glucose monitoring system for dogs and cats (Zoetis). AlphaTRAK2 was set to "dog" setting for strip calibration. Mice were then given an

intraperitoneal (i.p.) 1.0 g/kg bolus of 0.25 g/mL D-glucose (Sigma G7021) solution in sterile water that was prepared the day before. Blood glucose was measured 10, 20, 30, 60, 90, and 120 minutes after injection.

Similarly, in a study to measure insulin tolerance, mice were separately housed on ALPHA-dri bedding with no food for 2-3 hours before the test. Again, mice were weighed, anesthetized, and a baseline blood glucose measurement was acquired. Mice were given an i.p. bolus of 0.75 U/kg of insulin (Humulin R: Eli Lilly and Company) in 0.9% sterile saline. Blood glucose was measured 15, 30, 45, and 60 minutes after administration. Animals subjected to both glucose and insulin tolerance testing had at least 10 days of recovery between the tests. Furthermore, the amount of total tissue removed from any one mouse's tail was limited to under 5 mm.

Blood glucose data are presented as average blood glucose levels in mg/dL over the course of the experiment and average area under the curve. Fasted blood glucose levels were analyzed by two-tailed unpaired t-test. Full data sets were analyzed by a repeat-measures two-way ANOVA. In the event of a significant effect or interaction, comparisons were made between genotypes, or within genotype with comparisons made between baseline and experimental time points by Sidak's post-hoc. Blood glucose levels were processed by total trapezoidal area under a curve (AUC) analysis for each animal and the summed areas were averaged by genotype. The average area for each group were analyzed by a student's unpaired two-tailed t-test. Significance was identified by a p-value < 0.05.

2.8.3 C-Fos staining of hypothalamic neurons in ARL13B^{V358A} mice

Adult mice received an i.p. bolus of 0.75 U/kg of insulin or saline 90 minutes prior to perfusion. Mice were then anesthetized and transcardially perfused with ~10 mLs of cold PBS

followed immediately by ~5 mLs of cold 4% paraformaldehyde in PBS. Brains were carefully dissected and post-fixed over night at 4°C in 4% paraformaldehyde. The following day brains were removed from PFA and placed in a 30% sucrose in 0.1M phosphate buffer (see recipes) for 72 hours at 4°C with solution changes every 24 hours. Following sucrose sink, brains were dried off and rapidly frozen on dry ice before being embedded in cryoprotectant OCT (Tissue-Tek 4583).

Brains were coronally sectioned on a cryostat at a width of ~40 μM and immediately placed in 1x PBS. Antibody staining was performed on free-floating brain sections in baskets. Sections were rinsed three times in PBS for 5 minutes each before incubated in blocking buffer (5% heat inactivated goat serum in PBS with 0.1% Triton-X) for 1 hour at room temperature. Sections were then incubated with c-Fos antibody (anti-rabbit, Millipore 1:5000) in blocking solution for 48 hours at 4°C on an orbital shaker or rocker. Following primary antibody stain, sections are rinsed three times in 1x PBS followed by a 2-hour incubation with goat anti-rabbit secondary antibody (Alexafluor 488; 1:500) and DNA stain Hoechst (1:3000) at room temperature with constant agitation. Sections are again rinsed three times with 1x PBS and mounted onto Superfrost Plus slides and allowed to dry for one hour before cover slipped with Prolong.

Slides were imaged on the Leica CTR6000 microscope using SimplePCI software, images taken at 5x for depictions of whole regions and 20x for cell counting. Cells were hand counted in FIJI or with the automated program, Cell Profiler. Cell Profiler was set up with careful calibration of the background and signal levels and was programed to identify regions of interest. Statistical comparisons of c-Fos positive cells were made in both saline and pharmacologically-treated samples in all genotypes, and analyzed via a two-way ANOVA with posthoc analysis.

2.9 Recipes

0.1M Phosphate buffer, pH 7.3. 69mL of 0.2M monobasic stock + 231mL of 0.2M dibasic stock. Bring to final volume with 600mL of dH_20.

0.2M monobasic stock. 13.9g sodium phosphate monobasic monohydrate (Fisher BP330 or Sigma S9638) in final volume of 500mL dH_20.

0.2M dibasic stock. 53.65g sodium phosphate dibasic heptahydrate (Amrexco 0348) or 28.4g sodium phosphate dibasic anhydrous (Fisher S374) in final volume 1L dH_20.

Ca^{2+} Ringers Buffer

1 Liter. In 800 mLs of milliQ water dissolve the following chemicals before bringing the volume to 1 L and autoclaving the final solution. Adapted from Jordt et al; Nature 2004.

Chemical	Weight	Concentration
NaCl (Sigma S9888)	9.05 grams	155 mM
KCl (Sigma P9541)	335.475 mg	4.5 mM
$CaCl_2$-$2H_20$ (Sigma C4901)	294.02 mg	2 mM
$MgCl_2$-$6H_20$ (Sigma M8266)	203 mg	1 mM
D-Glucose (Sigma G8270)	1.8 grams	10 mM
HEPES-Na (Sigma 54457)	1.19 grams	5 mM

Poly-D-Lysine (Sigma P6407)

Mix 5 mg of Poly-D-Lysine in 25 mL of sterile water, creating a 0.2 mg/mL working solution. It should be filter sterilized and aliquots can be stored at -20°C and thawed before use.

D-Luciferin Stock (GoldBio LUCK-1G)

Prepare a 15 mg/mL stock that can be diluted 33.33x in Ringers buffer, creating a 450 μg/mL working solution. Simply take 300 μLs of the stock and mix in 9.7 mLs of Ringers buffer. Aliquots can be stored at -20°C.

Forskolin (Sigma F3917)

Solubilize 10 mg of forskolin in 2 mLs of 100% DMSO. Make several small 100 μL aliquots to store at -20°C. This stock is 12.18 mM. To create the working solution, take 6.56 μL of stock and add to 200 μLs of 100% DMSO, yielding a .4 mM working solution. Take 50 μLs of working solution and add to 4950 μL of Ringers Buffer, yielding a 4 μM solution to add to each well. The final desired concentration in each well is 1 μM.

Smoothened Agonist (SAG) – (Sigma 36450-63-6)

Generate 10 mM stock aliquots in 100% ethanol and store at -20°C. Take 1 μL and dilute in 19 μLs of media, take 1 μL into 5 mL of media for a 100 nM solution.

HEK293-FT Complete Media

500mL Corning DMEM High Glucose 10-013

To it add; 50 mL of FBS, 5 mL of 200 mM L-Glutamine (ThermoFisher 25030149) (100X), 5 mL of 10 mM MEM Non-Essential Amino Acids (ThermoFisher 11140050) (100x), 5 mL of Pen-Strep (ThermoFisher, 10478016), 5 mL G418 (ThermoFisher 10131027) if freezing cells down. Media was sterile filtered with a 0.45 μm filtration device. Store at 4°C for up to 1 year.

MEF media

500mL Corning DMEM High Glucose 10-013

To it add; 50 mL of FBS and 5 mL of Pen-Strep. Store at 4°C for up to 1 year.

RIPA Buffer

50mM sodium-Tris ph7.4 (Sigma 648315), 150mM sodium chloride, 2% NP-40, 0.5% sodium deoxycholate (ThermoFisher 89904), 0.1% sodium dodecyl sulfate (SDS; ThermoFisher 28312), 1mM dithiothreitol (DTT; ThermoFisher15508-013). 1 SIGMAfast protease inhibitor tablet (Sigma S8830).

Allele	Primers	Program	Product	Outcome
Arl13b^{hnn} A	Ex2 3F 5' GGACGGTTGAGAACCACTGT Ex2 2R 5' GTAGGGGGACACCAAGAAGC	Ed Hnn	~250bp	**Dilute 1:1000 and run reaction B.**
Arl13b^{hnn} B	Xmn1 F 5' GGACGGTTGAGAACCACTGT Xmn1 R 5' CACAAAGCAAGGATGAACGAC	Ed Hnn	218bp	**Digest with Xmn1 and run on 4% gel. Mutant band cuts to 200bp.**
Arl13b^{V358A} A	231 1F 5' GAAGCAGGCATGGTGGTAAT 231 2R 5' TGAACCGCTAATGGGAAACT	Ed Hnn	~200bp	**Dilute 1:1000 and run reaction B.**
Arl13b^{V358A} B	BstC81F 5' GAATGAAAAGGAGTCAGCGGG 231 2R 5' TGAACCGCTAATGGGAAACT	Ed Hnn	~200bp	**Digest with Cac81 and run on 4% gel. Mutant band cuts to 179bp.**
Arl13b^{fl}	CondF 5' AGGACGGTTGAGAACCACTG Con200R 5' CGACCATCACAAGTGTCACC	ConArl	~200bp Flox 150bp WT	**Run product on 2% gel with ladder.**
Arl13b^{del}	CondF 5' AGGACGGTTGAGAACCACTG Con949R 5' AACTGGGACACCCAAATGAG	ConArl	~800bp WT ~400bp Del	**Run product on 2% gel with ladder.**
Ift172^{wim} A	D5mit148F 5' GCTGCAAAGAAGAGAGAGGG D5mit148R 5' CCTCTGGCCAGCATGATATA	Eppitaq		**Run in parallel with reaction B. Run on 4% gel.**
Ift172^{wim} B	Shh201F 5' TTGTCCTCTGGCTTCCAACTGG Shh201R 5' CTTCAACCCTCTCCTTTCATTGC	Eppitaq		**Run in parallel with reaction A. Run on 4% gel.**
Smo^{cbb}	D6mit159altF 5' CATATTCAAGACGGAGACTAGTTCC D6mit159R 5' CACATGAAACACATGCACACA	Eppitaq		**Run on 4% gel.**
Smo^{bnb} A	D6mit159F 5' CATATTCAAGACGGAGACTAGTTCC D6mit159R 5' CACATGAAACACATGCACACA	Eppitaq		**Run in parallel with reaction B. Run on 4% gel.**
Smo^{bnb} B	D6mit268F 5' AGTCAGAATATGGCAAGTCAGTG D6mit268R 5' TTTCAGAGTCTTTCTTTCAGTATCTCC	Eppitaq		**Run in parallel with reaction A. Run on 4% gel.**
Ptch-LacZ	ScottLacZF 5' CATCCACGCGCGCGTACATC ScottLacZR 5' CCGAACCATCCGCTGTGGTAC	Eppitaq	~350bp	**Run on 4% gel. Carrier band is screaming positive.**
Table 1. Forward and Reverse primers for designated allele identification by PCR.				

Program	Step 1	Step 2			Step 3	Cycles
Eppitaq	94°C-5m	94°C-20s	55°C-30s	72°C-30s	72°C-7m	55
Ed Hnn	94°C-2m	94°C-30s	55.4°C-30s	72°C-30s	72°C-5m	30
ConArl	94°C-5m	94°C-30s	59°C-30s	72°C-45s	72°C-7m	50

Table 2. Temperatures and cycle times for PCR programs.

Antibody	Clone/Catalogue #	Dilution	Secondary
Sonic Hedgehog	DSHB 5E1	1:10	Goat anti-mouse IgG 488
FoxA2	DSHB 3A2	1:10	Goat anti-mouse IgG 488
Nkx2.2	DSHB 74.5A5	1:100	Goat anti-mouse IgG 488
Hb9	DSHB 81.5C10	1:10	Goat anti-mouse IgG1 488
Nkx6.1	DSHB F55A10	1:100	Goat anti-mouse IgG1 488
Pax6	DSHB	1:100	Goat anti-mouse IgG1 488
Olig2	Millipore AB9610	1:500	Goat anti-rabbit 555/568

Table 3. Antibody dilutions for neural tube patterning.

Antibody	Reference	Dilution	Secondary
acetylated α-tubulin	Millipore Sigma; T6793	1:2500	Anti-Mouse
ARL13B	NeuroMab N295B/66	1:1000	Anti-Mouse
ARL13B	Protein Tech 17711-1-AP	1:1000	Anti-Rabbit
ARL13B (503)	Caspary Lab	1:500	Anti-Rabbit
ARL13B (504)	(Caspary et al. 2007)	1:500	Anti-Rabbit
ARL13B (504)	(Caspary et al. 2007)	1:500	Anti-Rabbit
SMO	K. Anderson	1:1000	Anti-Rabbit
IFT88	B. Yoder	1:1000	Anti-Rabbit
ARL3	(Cavenagh et al. 1994)	1:1000	Anti-Rabbit
Inpp5e	Protein Tech 17797-1-AP	1:150	Anti-Rabbit
Gli2	J. Eggenschwiler	1:200	Anti-Guinea pig
Gli3	R&D AF3690	1:200	Anti-Goat
Ptch1	R. Rohatgi	1:150	Anti-Rabbit
Sufu	SC10933, Santa Cruz	1:100	Anti-Goat
Hoechst	Nuclear Stain	1:3000	
Alexa Fluor	ThermoFisher	1:300	Various

Table 4: Cilia specific and secondary antibodies.

Gene	Primers
Gli1	**5’ -CTTCACCCTGCCATGAAACT-3’** **5’ -TCCAGCTGAGTGTTGTCCAG-3’**
Ptch1	**5’ -TGCTGTGCCTGTGGTCATCCTGATT- 3’** **5’ -CAGAGCGAGCATAGCCCTGTGGTTC-3’**
Pold3	**5’ -ACGCTTGACAGGAGGGGGCT-3’** **5’ -AGGAGAAAAGCAGGGGCAAGCG- 3’**

Table 5. qPCR primers and mRNA targets.

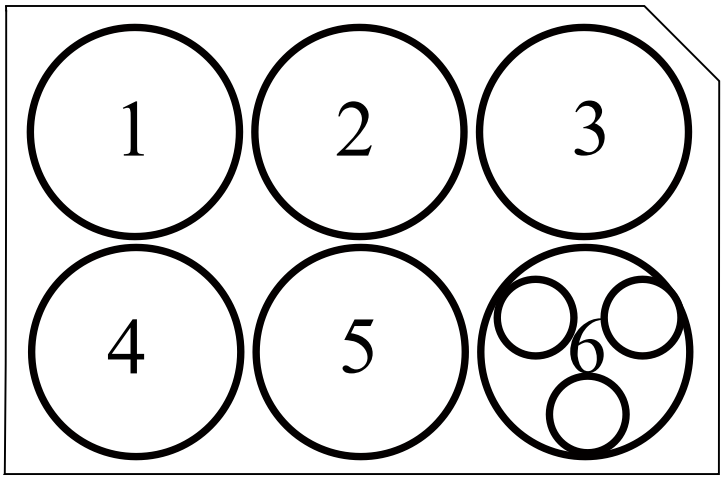

	Smo	Ptch1	GloSensor	Empty	eGFP
Well 1	200 μg	-	800 μg	400 μg	-
Well 2	200 μg	400 μg	800 μg	-	-
Well 3	-	-	800 μg	600 μg	-
Well 4	-	-	-	1400 μg	-
Well 5	-	-	-	-	-
Well 6	-	-	-	-	1400 μg

Table 6. Layout for Myers assay transfections in HEK-293FT cells.

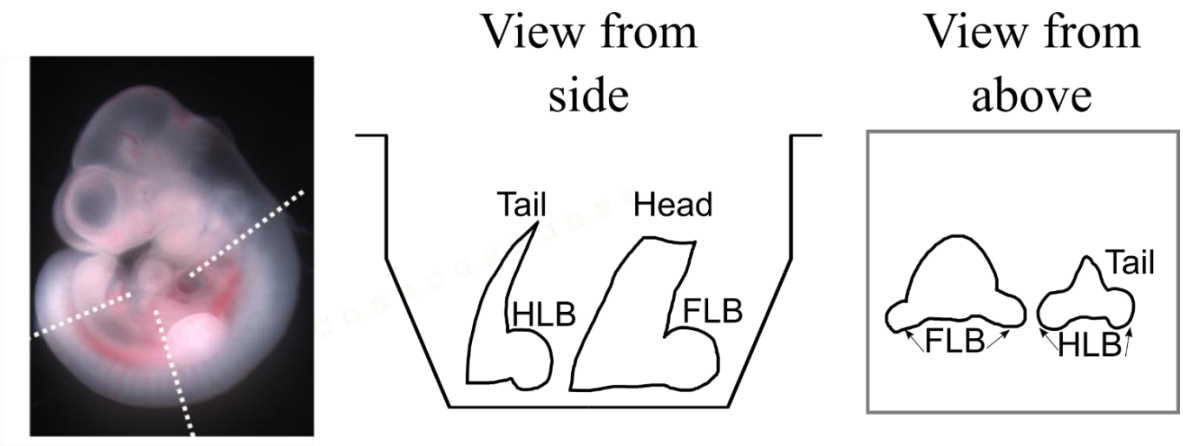

Figure 2.1

Examples of how to cut and embed embryos for excellent neural tube patterning results. HLB hindlimb bud, FLB forelimb bud.

CHAPTER 3

SMOOTHENED IS REQUIRED IN CILIA FOR THE HIGHEST LEVELS OF SONIC HEDGEHOG RESPONSE

This chapter previously published as:

Gigante, E.D.*, Bushey-Long, A.*, Ben-Ami, J., and Caspary, T. (2018) Hypomorphic Smo mutant with inefficient ciliary enrichment disrupts the highest level of vertebrate Hedgehog response. *Developmental Biology, Vol 437:2. 152-162.* doi.org/10.1016/j.ydbio.2018.03.019

* Equal contribution.

3.1 Summary

This *Smoothened* allele is one of several different mutants that came out of a forward genetic screen performed in the lab many years before my arrival. The criteria of the screen were to find dorsal neural tube defects using a Pax3-GFP reporter. What may not come as a surprise anymore is the number of cilia or cilia-associated genes (like *Smoothened*) that were mutated in this screen. This specific allele was identified for its craniofacial defect at embryonic day (E)10.5, which is a day later than the lethal stage seen in *Smoothened* null embryos. Mapped to *Smoothened*, the mutation causes a single base-pair change, resulting in an asparagine-to-lysine change at residue 223. In the paper I go into the potential structural consequences of this residue change. There are very few *Smoothened* mutants that have been generated in a physiologically relevant manner such as this. A great deal of our knowledge of SMO dynamics come from cell culture studies. What's true in cells is not always true *in vivo*, which I show is true of this mutant.

Homozygous mice will survive until birth but have a severe malformation of the mandible and nasal cavity. My untested hypothesis is these mice fail to thrive due to an inability to respirate. Newborn mice take gasping open-mouth breaths when born and it seems these mice are unable to do that. Mice do most of their breathing through their nose, so if it isn't due to the gasping the smaller nasal cavity could also be a contributing factor. Through characterization of the E10.5 embryo, I found that Shh signaling is moderately reduced, enough to cause developmental defects but not enough to cause prenatal lethality.

There is a great deal we don't yet know about SMO, and this allele could shed new light on SMO function. In this chapter I will lay out the relevant background of vertebrate Hedgehog signaling. I will lay out the evidence for the classification of this receptor as a hypomorph. With

help from a structural biology lab, I attempt to understand the consequences this mutation has on protein folding that can inform the observed hypomorphic function.

3.2 Introduction

Hedgehog (Hh) signaling is essential for embryogenesis and tissue homeostasis (Briscoe et al. 2013; Ingham et al. 2001). In vertebrates, there are three classes of Hh ligands: Sonic (Shh), Indian (Ihh), and Desert hedgehog (Dhh), all of which require the G protein-coupled receptor (GPCR) SMOOTHENED (SMO) for signal transduction (Echelard et al. 1993; Krauss et al. 1993; Riddle et al. 1993; Zhang et al. 2001). In the absence of Hh ligand, the Hh receptor Patched1 (Ptch1) inhibits SMO, which results in the downstream Gli transcription factors being cleaved to transcriptional repressors. Upon binding of Hh ligand to Ptch1, the inhibition is lost, leading to SMO activation and downstream signaling. The activation of SMO involves multiple steps that include conformational change, phosphorylation (Chen et al. 2011; Meloni et al. 2006; Chen et al. 2004), and ciliary enrichment (Chen et al. 2011; Eggenschwiler et al. 2001; Milenkovic et al. 2009; Boehlke et al. 2010). The processes that regulate SMO activation are part of the mechanism by which the level of Hh response is regulated for specific biological processes. Too much Hh leads to tumorigenesis, whereas too little leads to birth defects, including skeletal and craniofacial anomalies (Bale et al. 2001; Hatten et al. 2011; Muenke et al. 2000; Nanni et al. 1999; Roessler et al. 1996; Roessler et al. 1997; Vorechovsky et al. 1997; Wolter et al. 1997).

In vertebrates, primary cilia, the solitary microtubule-based projections found on virtually all cell types, are required for Hh signal transduction (Huangfu et al. 2003). Cilia are built and maintained via intraflagellar transport, which uses kinesin and dynein motors for anterograde and

retrograde traffic, respectively. The core Hh pathway components traffic dynamically in and out of cilia in a Hh ligand-dependent manner. In the absence of Shh, Ptch1 is visible in cilia (Rohatgi et al. 2007). Upon stimulation with Shh, Ptch1 becomes undetectable in cilia, whereas SMO is enriched (Corbit et al. 2005). This enrichment, while not sufficient for SMO activation, is considered a necessary step in activating SMO (Rohatgi et al. 2009).

SMO is a 7-transmembrane domain GPCR characterized by a large cysteine-rich domain (CRD) at its amino terminus, which plays an essential role in SMO dimerization and function (Zhao et al. 2007). The SMO CRD is known to associate with sterols, and recent evidence shows cholesterol can directly activate SMO, consistent with the findings that impaired cholesterol synthesis in Smith-Lemli-Opitz syndrome impairs SMO activation (Blassberg et al. 2016; Huang et al. 2016; Luchetti et al. 2016b; Xiao et al. 2017). However, the exact processes involved in activation of SMO remain uncharacterized. Methods to measure SMO activation have been limited to downstream processes such as SMO phosphorylation (Chen et al. 2004; Meloni et al. 2006; Chen et al. 2011), trafficking (Milenkovic et al. 2009; Kovacs et al. 2008; Eggenschwiler et al. 2001), and transcriptional pathway output. SMO activation may involve its phosphorylation at multiple sites in its C-terminal tail, which induce a conformational change of SMO to an active state (Chen et al. 2011). It's unclear where this conformational change occurs, as there is evidence that SMO continuously cycles through the cilium (Ocbina et al. 2008). Graded increases in Hh stimulation induce increasing amounts of phosphorylation carried out by several kinases, including PKA, CK1α, GRK2, and CK1γ (Chen et al. 2011; Li et al. 2016a).

SMO has a heptahelical ligand-binding domain known to interact with several exogenous compounds that have helped us better understand SMO activation and how it relates to the

primary cilium. For instance, SMOOTHENED agonist (SAG) directly activates SMO, bypassing Ptch1-mediated inhibition, and enriches SMO in the cilium (Chen et al. 2002b; Frank-Kamenetsky et al. 2002; Rohatgi et al. 2009). The exact mechanism of ciliary SMO enrichment involves several proteins, including β-arrestin and kinesin motors (Kovacs et al. 2008). In cells lacking cilia, SAG treatment induces partial phosphorylation of SMO, which can be blocked by inhibiting CK1α (Li et al. 2016a).

In mice, loss of *Smo* is lethal just prior to embryonic day 9.5 (E9.5) since there is no transduction of signaling from Shh, Ihh, or Dhh (Caspary et al. 2002; Zhang et al. 2001). The roles of Shh and Ihh in processes like craniofacial and skeletal development as well as neural patterning stem largely from work on *Shh* or *Ihh* mutant mice. Shh signaling exerts a strong influence on craniofacial development, and small changes to the pathway output can dramatically alter the facial midline (Zaghloul et al. 2011). Between E9.5 and E10.5, Shh expression slowly increases in the pharyngeal endoderm, along the midline of the facial ectoderm, and in the ventral forebrain neuroectoderm (Jeong et al. 2005). Here, Shh expression promotes neural crest cell survival and is essential for craniofacial organization, especially for structures in the midline. The olfactory placodes and nasal pits normally develop bilaterally in the ectoderm overlying the ventral forebrain. In embryos without *Smo* or *Shh*, a single nasal pit is located medially, indicating Hh signaling is required for proper craniofacial separation (Caspary et al. 2002; Chiang et al. 1996; Zhang et al. 2001). Loss of *Shh* disrupts the bilateral symmetry of facial development, resulting in defects such as cyclopia and holoprosencephaly; these defects are well documented in humans and mice (Belloni et al. 1996; Chiang et al. 1996; Roessler et al. 1996). Shh promotes the development of skeletal tissues of the limb buds and digits, spine, ribs, face, and skull (Chiang et al. 1996). At birth, the long bones of the forelimb (the humerus, radius,

and ulna) are ossified, along with centers at the base of each digit. Ihh inhibits chondrocyte differentiation and instead supports bone ossification by promoting chondrocyte proliferation in cartilaginous tissues, and facilitates bone lengthening in the limbs at the growth plate (St-Jacques et al. 1999).

Shh plays a critical role in specifying the cell fates of neural progenitor cells in the developing neural tube (Chiang et al. 1996). Shh ligand is expressed in the notochord and produces a ventral-to-dorsal activity gradient that determines specific cell fates based on the level of Shh activity (Ericson et al. 1997). For example, the cells at the ventral midline of the neural tube experience the highest level of Shh activity and are specified as floor plate expressing FoxA2 and Shh (Briscoe et al. 2000). The cells adjacent to the floor plate express Nkx2.2, while the next adjacent domain expresses Olig2 (Briscoe et al. 1999; Lu et al. 2000). The level of Shh activity integrates the concentration and duration a progenitor cell is exposed to ligand (Dessaud et al. 2010; Dessaud et al. 2007; Ribes et al. 2010). *Smo* null mutants specify no ventral cell fates (Caspary et al. 2002; Zhang et al. 2001).

In this study, we reveal that an N-ethyl-N-nitrosourea (ENU)-induced mouse mutant, *cabbie* (*cbb*), is a novel allele of *Smo*. We identified *cbb* in the course of a forward genetic mouse screen for recessive mutations affecting embryonic neural development and picked up *cbb* due to the craniofacial defects we saw at E10.5. *cbb* mutants die shortly after birth. We show *cbb* embryos display defects that affect cells requiring the highest level of Shh activity. Furthermore, we find that the SMO protein in *cbb* mutants does not enrich properly in cilia. Taken together, our data argue that proper ciliary SMO enrichment is necessary for full SMO activation.

3.3 Results

3.3.1 *cabbie* is a novel *Smoothened* allele

We identified the *cbb* mutation in a recessive ENU screen for embryos with abnormal morphology at E10.5. *cbb* embryos displayed a reduced frontonasal prominence (FNP), and the nasal pits collapsed towards the midline (**Figure 3.1A,B and Figure 3.2A,B**). We induced the *cbb* mutation on a C57BL/6 background and backcrossed to FVB so that we could use polymorphic markers and linkage analysis to map the *cbb* mutation. We found that *cbb* was located on chromosome 6. Through whole-exome sequencing, we identified a cytosine-to-adenine transversion in exon 3 of the *Smo* gene. The change is predicted to mutate a conserved asparagine (amino acid 223) to a lysine (**Figure 3.1C**) at a position between the N-terminal cysteine-rich domain (CRD) and transmembrane domain 1 (**Figure 3.1D**).

To determine whether the C→A mutation underlies the *cbb* phenotype, we performed a complementation test with a null allele of *Smo*: *bent body (bnb)* (Caspary et al. 2002; Kasarskis et al. 1998). Smo^{bnb} single mutant embryos display a distinct head shape, small body size, failed embryonic turning, and lethality just before E9.5 (**Figure 3.1G**), whereas Smo^{cbb} single mutants survived until just after birth. At E9.5, $Smo^{cbb/bnb}$ embryos display a reduced FNP and first branchial arch (**Figure 3.1H**). By E10.5, $Smo^{cbb/bnb}$ embryos are often small compared to control littermates (**Figure 3.1 I,J**). $Smo^{cbb/bnb}$ heteroallelic embryos died at E10.5-11.5, indicating that the alleles fail to complement and the C→A mutation is causative. Thus, the $Smo^{cbb/bnb}$ phenotype was less severe than the $Smo^{bnb/bnb}$ null phenotype, suggesting Smo^{cbb} is a hypomorphic allele of *Smo*.

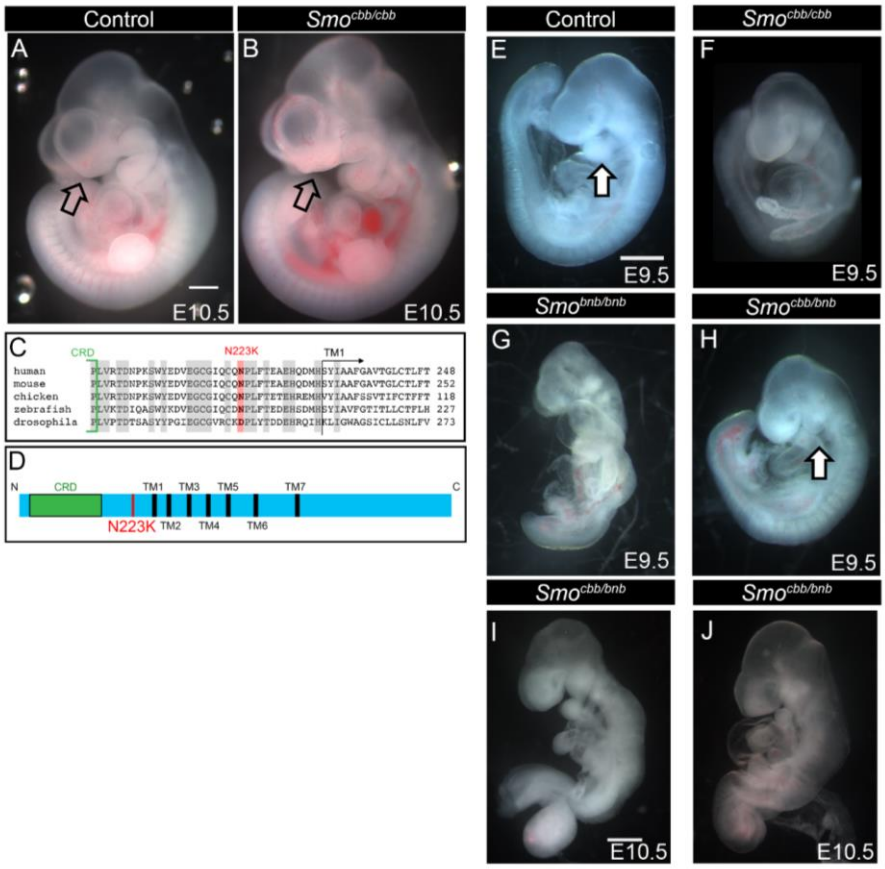

Figure 3.1 *Smo*^{cbb} is a novel allele of *Smo*.

(A and B) E10.5 control and *Smo*^{cbb} somite-matched embryos. Open arrows point to the FNP. (C) The *cbb* mutation changes a conserved asparagine residue to lysine; the species alignment shows the changed residue in red and conserved residues in gray. (D) Within the Smo protein, N223K (red) is located between the CRD (green) and transmembrane domain 1 (TM1, black). Somite-matched control (E) and *Smo*$^{cbb/cbb}$ (F) embryos at E9.5. The mutant embryo is nearly indistinguishable from control embryos at E9.5. Of 95 E9.5 embryos dissected: 9 were abnormal or dead, 61 were correctly identified as controls, 6 were correctly identified as *Smo*^{cbb} mutants, and 19 were called controls but genotyped as *Smo*^{cbb}. (G) *Smo*^{bnb} embryos (null allele) are small with a distinct head shape, small somites, and incomplete embryonic turning. (H) *Smo*$^{cbb/bnb}$ E9.5 embryo. *Smo*^{cbb} fails to complement *Smo*^{bnb}. Filled arrows in (E) and (H) point to branchial arch 1. (I and J) At E10.5, *Smo*$^{cbb/bnb}$ embryos are viable, but phenotypically delayed with some variability in head size, cardioedema, branchial arch development, and viability. Scale bars are 500 microns.

3.3.2 *Smo*^{cbb} causes craniofacial and skeletal defects

To determine the functional consequences of the *Smo*^{cbb} allele, we examined craniofacial and skeletal development since both processes depend on Hh signaling. *Smo* null embryos display a single medially located nasal pit by E9.0, their point of lethality (Caspary et al. 2002; Kasarskis et al. 1998; Zhang et al. 2001). In contrast, *Smo*^{cbb} mutants are commonly indistinguishable from controls at E9.5 (**Figure 3.1F**). By E10.5, *Smo*^{cbb} embryos display abnormal outgrowth of the nasal processes and a rotation of the nasal pits (**Figure 3.2 A,B**). The *Smo*^{cbb} phenotype progresses as development continues. At birth, *Smo*^{cbb} mutants display hypoplastic mandibles (**Figure 3.2 C-F**), nasal and maxillary bones (**Figure 3.2 G,H**). These data suggest *Smo*^{cbb} permits Hh signaling, yet the highest level of response is not achieved, consistent with *Smo*^{cbb} being a hypomorphic allele.

We examined the skeletons of *Smo*^{cbb} embryos, where Shh and Ihh each play critical roles. Despite the craniofacial defect, we found many of the bones of the skull developed in the appropriate size and position (**Figure 3.2 G,H**). We saw that the long bones of *Smo*^{cbb} postnatal day 0 (P0) pups are shorter than those of littermate controls (**Figure 3.2 I,J**). In the caudal vertebral column, the centers of each vertebra ossify in the control pups (**Figure 3.2 K,S**); however, in the *Smo*^{cbb} pups, the vertebral bodies are barely present (**Figure 3.2 L,T**). In the limbs, we consistently saw digit defects across *Smo*^{cbb} pups, but the number of digits and presence of ossification centers varied in front- and hindlimb paws (**Figure 3.2 O-R**). In addition, the mandibles in *Smo*^{cbb} embryos are consistently smaller than littermate controls, but in some cases, we observed premature fusion at the symphysis (**Figure 2 M,N**). Such subtle

phenotypic variability among *Smo*^{cbb} mutants is consistent with this being a hypomorphic allele affecting processes that require the highest levels of Hh signaling.

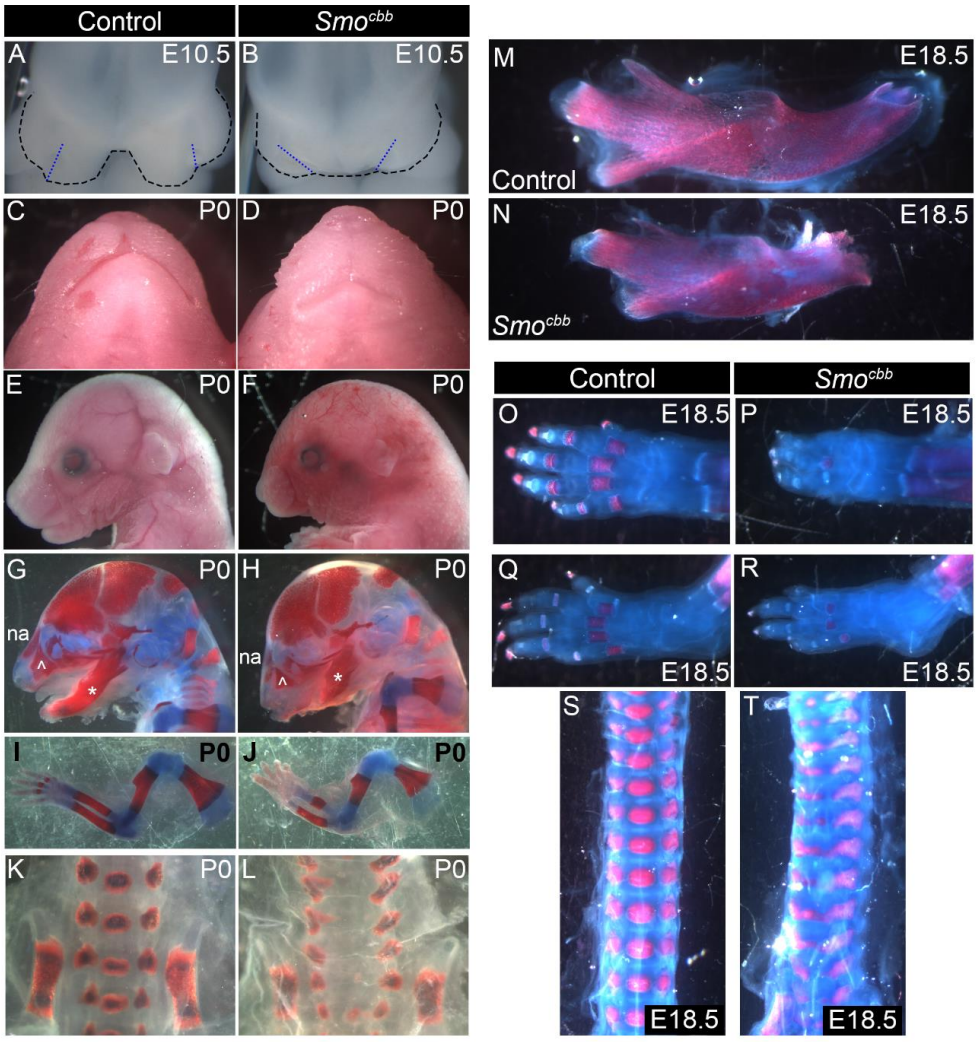

Figure 3.2 Defective craniofacial and skeletal development in *Smo*^{cbb} mutants.

(A and B) At E10.5, *Smo*^{cbb} mutants showed abnormal outgrowth of the nasal processes and a rotation of the nasal pits. *n* = 176 control and 54 *Smo*^{cbb} embryos. (C and D) By P0, *Smo*^{cbb} mutants displayed a more posterior location of the mouth compared to control littermates and (E and F) a concomitant reshaping of the face, especially the lower jaw. (G and H) Skeletal preparations of P0 pups show the hypoplastic mandibles (*), nasal (na) and maxillary (^) bones in the *Smo*^{cbb} mutants. (M and N) Isolated mandibles from E18.5 pups stained with alcian blue and alizarin red. (I and J) The forelimbs of *Smo*^{cbb} mutants show shorter long bones and a lack of ossification (red staining) in the digits. (O and P) Higher magnification view of E18.5 front paws. (Q and R) Higher magnification view of E18.5 hind paws. (K, L, S, and T) Spinal columns from *Smo*^{cbb} animals show small or absent vertebral bodies. Paired images were taken at the same magnification.

3.3.3 *Smo*^{cbb} mutant embryos display abnormal neural tube patterning

Neural cell fates in the embryonic neural tube depend on Shh activity (Chiang et al. 1996). To monitor Shh activity in the neural tube, we used a *Ptch1-lacZ* allele since *Ptch1* is a transcriptional target of Shh signaling (Goodrich et al. 1997). In the control neural tube at E10.5, we saw a steep ventral-to-dorsal gradient of lacZ staining, whereas in the neural tube of *Smo*^{cbb}, we saw a diminished lacZ gradient, indicating reduced Shh activity (**Figure 3.3 A,B**). To determine whether the reduced Shh activity led to changes in cell fate, we examined neural patterning in *Smo*^{cbb} embryos. We found Shh staining in the notochord of both control and *Smo*^{cbb} mutants at E10.5, suggesting the ligand is produced normally (**Figure 3.3 C,D**). At the ventral midline of the control neural tube, we observed Shh staining in the columnar cells of the floor plate (**Figure 3.3C**); however, we detected few Shh-positive columnar cells in the *Smo*^{cbb} embryos, indicating a reduced floor plate (**Figure 3.3D**). The floor plate is the secondary signaling center that produces Shh ligand (Ericson et al. 1997) and expresses FoxA2 (**Figure 3.3E**). In E10.5 *Smo*^{cbb} mutants, we observed fewer FoxA2-positive cells, some co-expressing Nkx2.2 (**Figure 3.3F**). The motor neuron precursors (Olig2-positive) are dorsally adjacent to the Nkx2.2 population (**Figure 3.3G**). In *Smo*^{cbb} mutants, the Olig2 cells expanded ventrally, but not dorsally, compared to control neural tubes (**Figure 3.3H**). Taken together, these data suggest that less Shh production in the floor plate leads to lowered Shh response at the ventral midline and the appropriate Shh response at the dorsal Olig2 boundary.

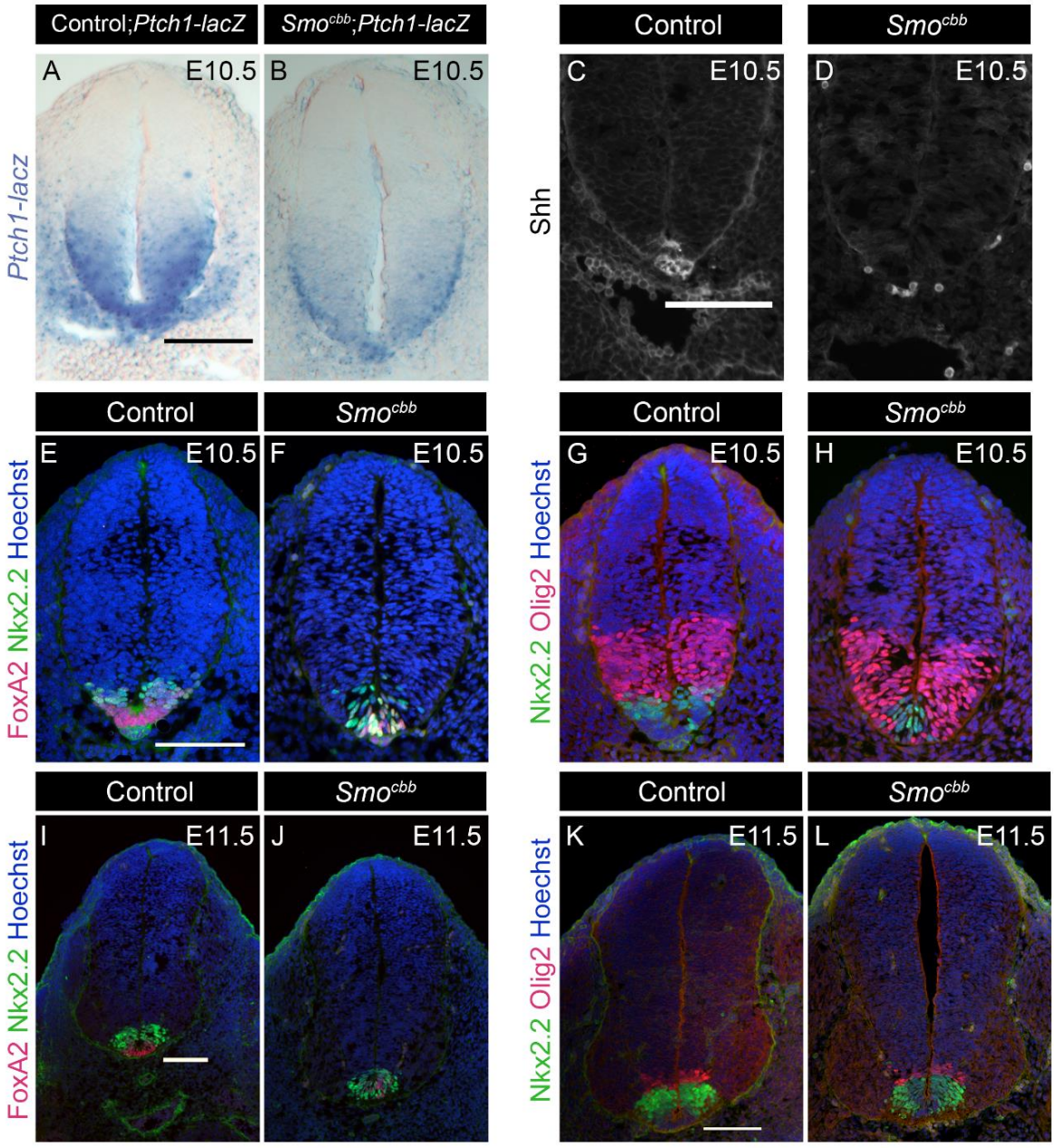

Figure 3.3 Ventral shift of neural tube patterning in *Smo^{cbb}* mutant.

(A and B) Ptch1-lacZ gradient in Control;*Ptch1-lacZ* and *Smo^{cbb}*;*Ptch1-lacZ* neural tube sections. (C and D) Expression of Shh is greatly diminished or absent in *Smo^{cbb}*. (E and F) E10.5 and (I and J) E11.5 sections stained for FoxA2 (red) and Nkx2.2 (green). (G and H) E10.5 and (K and L) E11.5 sections stained for Olig2 (red) and Nkx2.2 (green). Images are axial sections of somite-matched embryos through hindlimb-level neural tube. Scale bars are 100 microns.

Progenitors in the neural tube are sensitive to both concentration and duration of Shh exposure (Dessaud et al. 2007; Dessaud et al. 2010; Ribes et al. 2010). To examine the possibility that *Smo*^{cbb} mutants might delay the kinetics of SMO activation leading to late cell fate specification in the neural tube, we examined neural tube patterning in E11.5 embryos. In control embryos at E11.5, we saw FoxA2-positive columnar cells in the floor plate and adjacent Nkx2.2- and Olig2-positive cells (**Figure 3.3I,K**). In *Smo*^{cbb} mutants at E11.5, we observed few columnar cells expressing FoxA2 at the midline, which instead was populated by Nkx2.2-positive cells, indicating the floor plate remained unspecified. In contrast to E10.5 *Smo*^{cbb} mutants, we saw no coexpression of FoxA2 and Nkx2.2 (**Figure 3.3J**). The Olig2 domain appeared adjacent to the Nkx2.2 domain in both control and *Smo*^{cbb} mutants (**Figure 3.3K,L**). Together, these data argue that *Smo*^{cbb} has disrupted the highest levels of Shh activity, and this disruption is not restored over time.

3.3.4 *In vitro* analysis of Shh-dependent transcriptional targets in cultured mutant fibroblasts

To directly examine the level of Shh response, we derived and immortalized mouse embryonic fibroblasts (MEFs) from *Smo*^{cbb} and control littermates. We measured transcription of the Shh target genes *Ptch1* and *Gli1* in the absence and presence of Shh. In control MEFs, we found increased *Gli1* and *Ptch1* expression 24 hours after treatment with Shh (**Figure 3.4A**, black comparisons); however, we detected a significantly lower response in stimulated *Smo*^{cbb} MEFs, indicating that the SMO^{N223K} mutation impaired Shh signal transduction (**Figure 3.4A**, red comparisons).

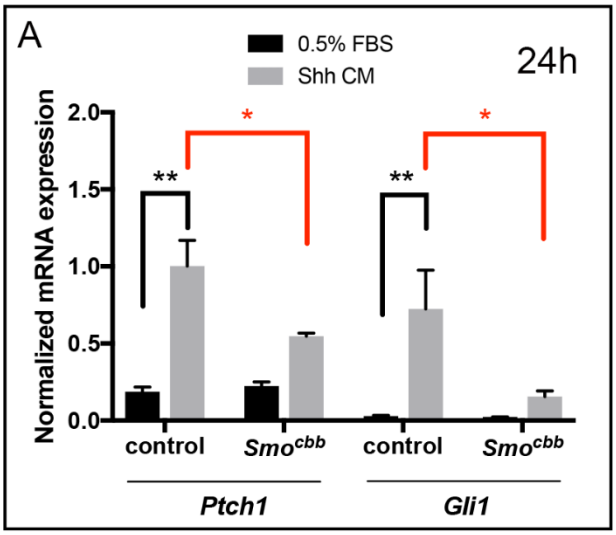

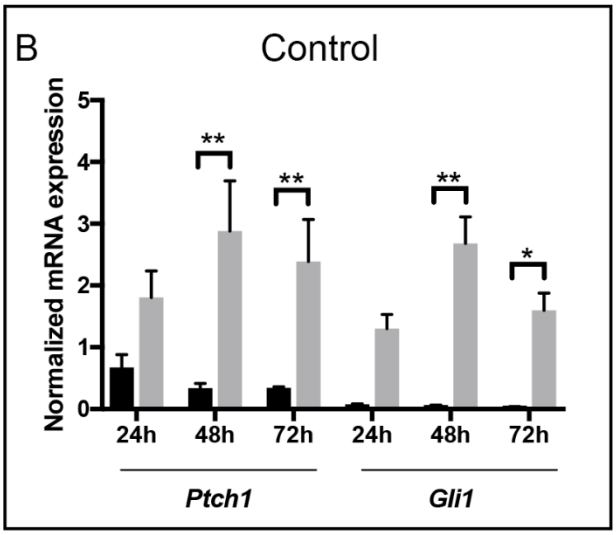

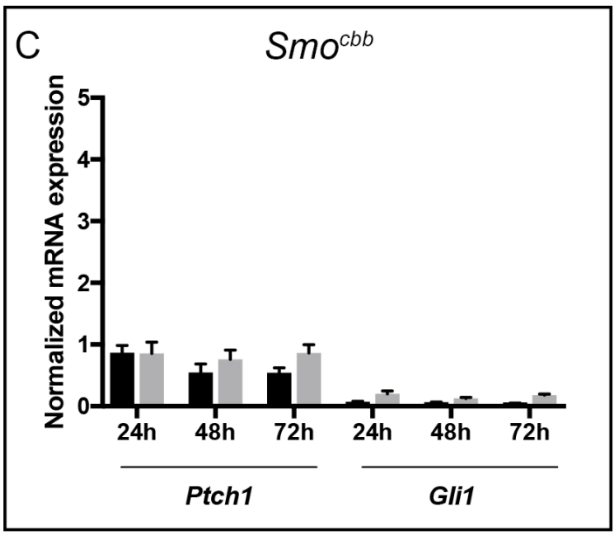

Figure 3.4 Analysis of Shh target transcription in *Smo*^{cbb} MEFs.

(A) Control MEFs showed robust induction of Shh transcriptional targets, *Ptch1* and *Gli1,* 24 hours after treatment with Shh-conditioned media (Shh CM), whereas *Smo*^{cbb} MEFs showed a small induction that did not reach statistical significance (black comparisons). The small expression levels of both *Ptch1* and *Gli1* in treated *Smo*^{cbb} MEFs were significantly reduced compared to Shh-treated control MEFs (red comparisons). (B) Control MEFs showed robust induction of Shh transcriptional targets, *Ptch1* and *Gli1,* 24, 48, and 72 hours after treatment with Shh-conditioned medium (reapplied every 24 hours), whereas *Smo*^{cbb} MEFs (C) showed a small induction that did not reach statistical significance. (**, $p < 0.001$; *, $p < 0.01$)

The reduced *Ptch1* and *Gli1* transcription we saw in the *Smo*^{cbb} MEFs upon Shh stimulation could reflect the moderate level of Shh activity seen in the embryo. Because the duration of Shh activity during development plays a key role in neural cell fate and digit specification, another possibility is that the SMO^{N223K} mutant has altered signal transduction kinetics (Scherz et al. 2007; Dessaud et al. 2010; Dessaud et al. 2007; Ribes et al. 2010). To examine this possibility, we compared the Shh transcriptional response in control and *Smo*^{cbb} MEFs at 24, 48, and 72 hours. For the 48- and 72-hour time points, we re-stimulated with fresh Shh-conditioned culture medium every 24 hours. As expected, we found Shh stimulation induced *Ptch1* and *Gli1* transcription in control MEFs at all three time points, with the highest activity at 48 hours (**Figure 3.4B**). In contrast, we found *Smo*^{cbb} MEFs did not display higher levels of transcriptional response after longer exposure to Shh. Expression of *Ptch1* and *Gli1* remained unchanged across all three time points (**Figure 3.4C**). These data suggest that the SMO^{N223K} mutation disrupts the full activation of SMO.

3.3.5 N223K disrupts the SMO ligand-binding pocket and SAG binding to SMO

The asparagine-to-lysine change at position 223 in the *Smo*^{cbb} allele is located within the linker domain of the protein, downstream of the cysteine-rich domain (CRD) and immediately prior to the beginning of transmembrane domain 1 (**Figure 3.5A,B**). The corresponding residue in the human SMO receptor contributes to a ligand-binding pocket, where SMO agonists and antagonists bind. In fact, one solved crystal structure shows SMO agonist (SAG) associates with the ligand-binding pocket, and hydrogen bonds with the asparagine corresponding to N223 in the mouse protein (Wang et al. 2014; Wang et al. 2013). Based on the solved structure, we modeled the N223K mutation (N219K in human) and found that a change from asparagine to lysine is

predicted to occlude the SMO binding pocket and interfere with the binding of SAG, a potent agonist (**Figure 3.5C,D**), suggesting that SMO^{N223K} might be SAG-insensitive.

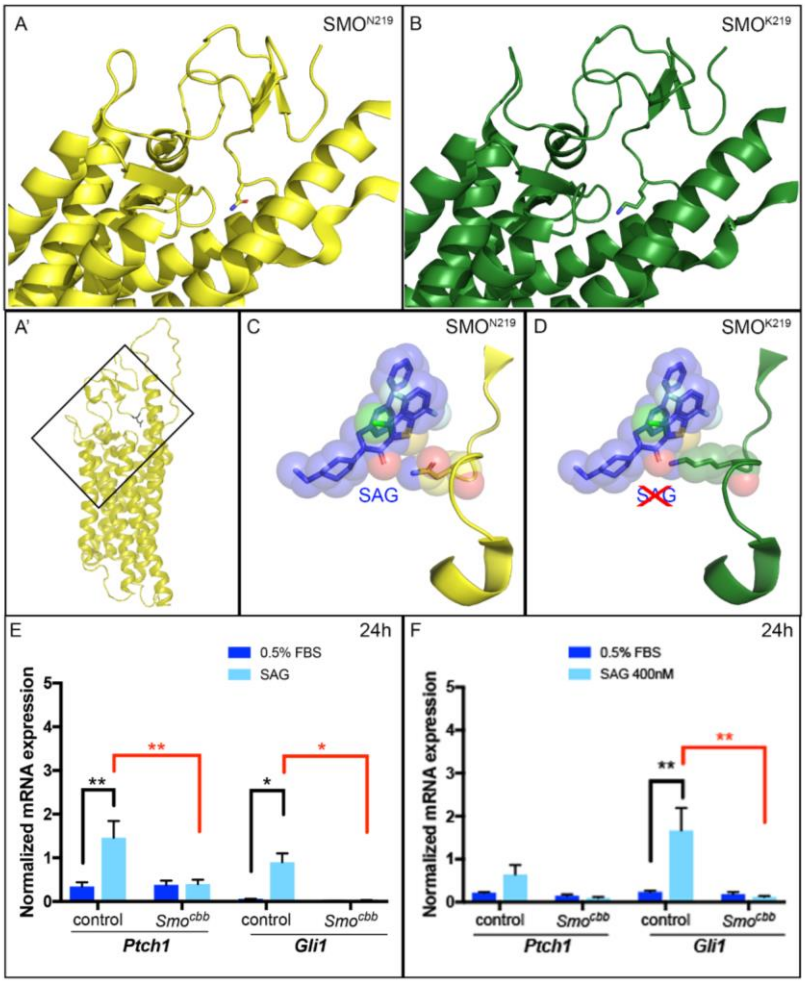

Figure 3.5 The N223K mutation disrupts the SMO ligand-binding pocket and is insensitive to SAG.

A three-dimensional ribbon model of the human SMO receptor with (A) asparagine or (B) predicted model with lysine at residue 219. (A') Full model of human SMO receptor (aa194-557) with box representing the region of the molecule enlarged for clarity in (A) and (B). The membrane-spanning alpha helices are arranged so that the extra-cellular N-terminus of the protein is toward the top of the model. (C) N219 makes a hydrogen bond with Smo agonist (SAG; blue) as part of the ligand-binding pocket. (D) K219 is predicted to sterically clash with SAG, indicated by the crossed-out SAG. The ribbon backbone of SMO shown in (C) and (D) represents aa215-225, with the N-terminal end toward the top. (E) Control MEFs showed increased expression of *Ptch1* and *Gli1* after 24 hours of treatment with SAG, whereas Smo^{cbb} MEFs did not (black comparisons). Expression levels of both *Ptch1* and *Gli1* in treated Smo^{cbb} MEFs were reduced compared to SAG-treated controls (red comparisons). (F) Treatment with 400nM SAG was unable to direct expression of *Ptch1* or *Gli1* in Smo^{cbb} MEFs. (**, $p < 0.001$; *, $p < 0.01$)

To test this directly, we treated control and *Smo*^{cbb} mutant MEFs with SAG and measured Shh transcriptional response. We detected increased *Ptch1* and *Gli1* expression in SAG-treated control MEFs compared to untreated cells (**Figure 3.5E**, black comparisons). In contrast, we found *Smo*^{cbb} mutant MEFs are unresponsive to SAG treatment; we saw no change in *Gli1* or *Ptch1* expression, and the level of expression in SAG-treated *Smo*^{cbb} MEFs was statistically lower than in control MEFs (**Figure 3.5E**, red comparisons). Next, we tested whether the *Smo*^{cbb} MEFs could respond to a higher dose of SAG (400 nM, four times higher than in the previous experiment). This dose was also ineffective at increasing Shh transcriptional response in mutant MEFs, suggesting the N223K mutation renders the SMO receptor refractory to SAG. (**Figure 3.5F**). We note that while neither Shh nor SAG statistically induced *Gli1* or *Ptch1* expression, the slight response we detected in Shh-treated *Smo*^{cbb} MEFs may be biologically distinct from the lack of expression we saw in SAG-treated *Smo*^{cbb} MEFs (**Figures 3.4A,5E**). Together, these data are consistent with the SMO^{N223K} mutation altering the ligand-binding pocket, such that SAG cannot effectively bind and activate the receptor.

3.3.6 SMOOTHENED localization defect in *Smo*^{cbb} *in vivo* and *in vitro* after Shh and SAG activation

In vertebrates, SMO is enriched in cilia upon pathway activation, a step that is necessary but not sufficient for SMO activation (Corbit et al. 2005; Rohatgi et al. 2009). We looked at SMO localization in relation to the primary cilium upon Shh stimulation in control and *Smo*^{cbb} MEFs. We examined ciliated cells and classified ciliary staining as fully SMO positive, partially SMO positive, or SMO negative (reviewers blinded to genotype, see Methods, **Figure 3.6A**). In Shh-treated MEFs, we found 70% of control cilia are fully SMO positive, compared to 32% in

Smo^{cbb} cilia (**Figure 3.6B**). Similarly, in SAG-treated MEFs, we saw that 76% of control cells' cilia are fully SMO positive, compared to 34% of *Smo*^{cbb} cells' cilia (**Figure 3.6B**). SMO antagonist cyclopamine leads to ciliary enrichment of SMO and binds deeper in the same binding pocket as SAG. In cyclopamine-treated cells, we saw 27% of *Smo*^{cbb} cilia are fully SMO positive compared to 32% in control MEFs (**Figure 3.6B**). Moreover, we measured a decrease in baseline SMO localization in 0.5% FBS-treated *Smo*^{cbb} MEF cilia compared to controls, indicating an inherent defect in SMO^{N223K} enrichment (**Figure 3.6B**). These data argue that ciliary enrichment of SMO is impaired in *Smo*^{cbb} MEFs, and the enrichment defect in *Smo*^{cbb} MEFs is the same whether we stimulated with a ligand that activates SMO through the endogenous pathway (Shh-conditioned media) or with pharmacological agents that drive ciliary enrichment of SMO (SAG and cyclopamine).

To investigate ciliary enrichment of SMO *in vivo,* we examined SMO localization in the E10.5 neural tube. We looked at ciliated cells of the floor plate (where Shh activity is normally at the highest levels) for co-localization of SMO and ciliary marker Arl13b. In the floor plate, where Shh signaling is highest in the neural tube, ~75% of cilia are SMO-positive in control sections compared to ~25% in *Smo*^{cbb} (**Figure 3.6C,D**). These same cells express FoxA2 and Nkx2.2 cell fates in wild-type, whereas in *Smo*^{cbb} mutants they only express Nkx2.2 (**Figure 3.3E,F**). Thus, SMO^{N223K} appears to remain present in cilia at the ventral neural tube, but at much lower levels compared to wild-type. In the context of our data showing that *Smo*^{cbb} mutants do not achieve the highest levels of Shh activity in the floor plate, these results indicate that efficient SMO ciliary enrichment is required for the highest levels of Shh response.

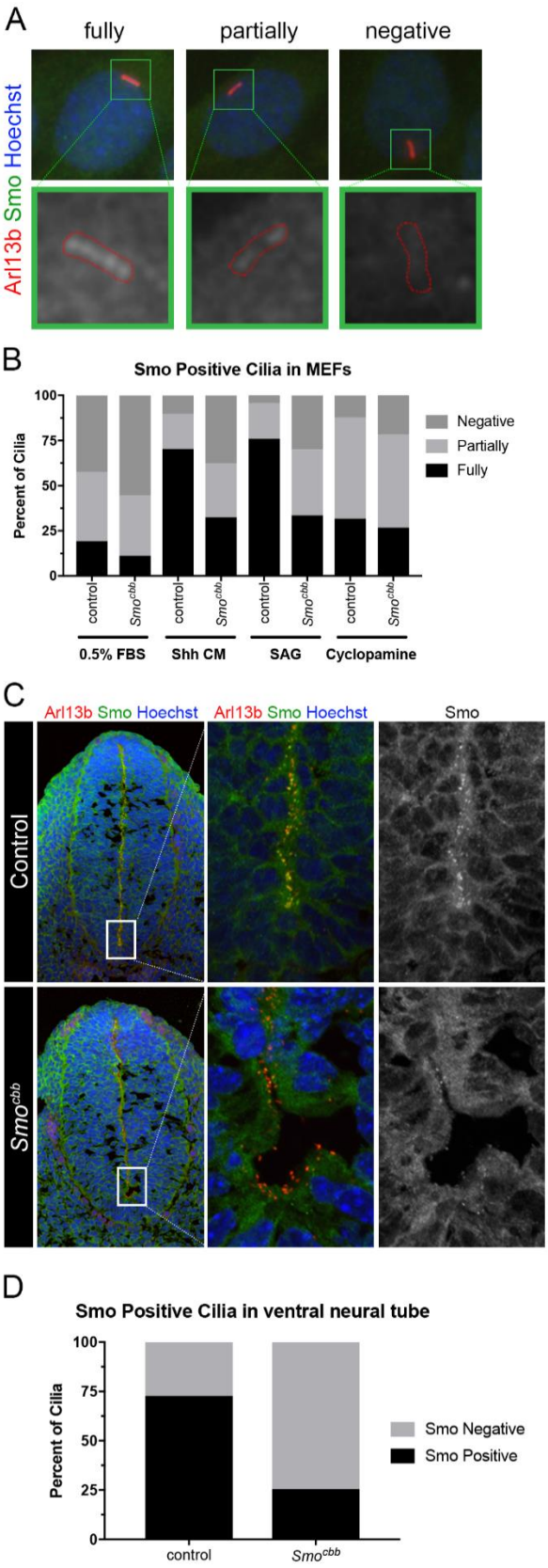

Figure 3.6 Smo^{N223K} causes a cilia localization defect in MEFs and E10.5 neural tube.

(A) Ciliary staining of Smo (green) in cilia (Arl13b; red) is classified as fully Smo positive, partially Smo positive, or Smo negative. The green channels of the top row insets are presented enlarged in the bottom row. Images are of monolayer MEFs on cover slip at 40X. (B) Quantification of Smo localization in control and *Smo*^{cbb} MEFs treated with 0.5% FBS (control n = 290, *Smo*^{cbb} n = 312), Shh-conditioned media (Shh CM) (control n = 256, *Smo*^{cbb} n = 259), SAG (control n = 167, *Smo*^{cbb} n = 162), or cyclopamine (control n = 164, *Smo*^{cbb} n = 157). (C) Ciliary localization of Smo in control and *Smo*^{cbb} E10.5 neural tube. Cilia are stained for Arl13b (red) and Smo (green). Insets show cilia in the neural tube lumen at the floor plate. Neural tube images are of axial sections of somite-matched embryos through hindlimb-level neural tube at 20X. Insets are confocal z-stack of 10 images at 60X. (D) Quantification of Smo localization in control and *Smo*^{cbb} neural tube sections.

3.4 Discussion

Here, we identified a mouse mutant displaying craniofacial, skeletal, and neural tube patterning defects and showed the defects are due to a N223K mutation in the SMO protein. We characterized several phenotypes in *Smo*^{cbb} homozygous embryos consistent with loss of maximal Hh signaling, among them a narrow FNP, a reduced floor plate in the neural tube, and shortened long bones. The *Smo*^{cbb} allele failed to complement a *Smo*^{bnb} null allele, indicating that the N223K mutation in SMO is causative. The *Smo*$^{cbb/bnb}$ compound mutant phenotype is less severe than *Smo*^{bnb} null, yet more severe than *Smo*^{cbb}, suggesting a partial-loss-of-function allele. *Smo*^{cbb} embryos survive until birth, indicating SMO^{N223K} receptor functions sufficiently for gestation to proceed. In contrast, we detected no significant induction of Shh target gene transcription in *Smo*^{cbb} MEFs, which could mean the N223K mutation disrupts the ability of SMO to be fully activated. Consistent with this, we showed that SMO^{N223K} protein is inefficiently enriched in cilia upon Shh stimulation.

Within vertebrates, the *Smo*^{cbb} mutation, N223K, occurs at a conserved residue corresponding to N219 in human SMO (hSMO), which lies within a linker domain between the CRD of the N-terminus and the first transmembrane domain. This linker domain is thought to facilitate CRD association with extracellular loop 1 when bound to oxysterols and cholesterol, which in turn is critical for SMO regulation (Byrne et al. 2016; Wang et al. 2014; Wang et al. 2013). One proposed mechanism for this is via a cysteine-cysteine disulfide bond between the N-terminus and extracellular loop 1 mediated by residue C217 in hSMO (Wang et al. 2013). Residue N219 in hSMO forms a critical hydrogen bond with SAG as part of the ligand-binding pocket. Without SAG, N219 forms two hydrogen bonds with L221 and D384 on extracellular

loop 2. When bound to SAG, N219 releases its D384 bond and instead binds the SAG molecule, forming a lid on the ligand-binding pocket (Wang et al. 2014). In a simulation of human SMO N219K (**Figure 3.5**), the L221 bond is lost, and only the D384 association remains, which may disrupt SAG binding. Alternatively, lysine is a larger residue than asparagine and is predicted to structurally interfere with the binding of SAG. A lack of SAG binding with SMO^{N223K} is consistent with the lack of SAG-induced gene transcription in Smo^{cbb} upon SAG treatment. Nevertheless, we do see some SAG-induced SMO enrichment in cilia; therefore, it is also possible that SAG binds SMO^{N223K}, and the downstream phenotypes we saw are due to a conformational change of SMO^{N223K}. When MEFs are treated with antagonist cyclopamine, we saw similar levels of SMO ciliary enrichment in both Smo^{cbb} and control MEFs. Cyclopamine is not known to associate with N223 when binding to SMO, and it is therefore unlikely that N223K alters cyclopamine binding directly (Chen et al. 2002b; Chen et al. 2002a). However, because N223 is located at the entrance of the ligand-binding pocket, N223K could interrupt the entry of cyclopamine. Because Smo^{cbb} MEFs do not transduce Shh-dependent genes in response to Shh or SAG, we cannot determine whether cyclopamine can antagonize the SMO^{N223K} receptor and block Shh gene transcription.

One of the most striking results in our studies is the fact that Smo^{cbb} embryos survived to birth, implying some Hh transduction; however, Smo^{cbb} MEFs did not display a statistically significant transcriptional response upon Shh stimulation, even after 72 hours of treatment (**Figure 3.4**). One interpretation of these data is that the induction we saw in Smo^{cbb} MEFs, while not statistically significant, is biologically significant. Consistent with this interpretation is the fact that we saw no induction of *Gli1* or *Ptch1* transcription when we stimulated the Smo^{cbb} MEFs with moderate or high doses of SAG (**Figure 3.5 C,D**). If this interpretation is correct,

then the time course in MEFs would mean that the N223K mutation disrupts the actual activation status of SMO, as opposed to the kinetics of its activation. Of course, the alternative explanation is that MEFs *in vitro* do not reflect what occurs in the living embryo *in vivo*.

Our work *in vivo* provided an unexpected finding about the level of Shh signaling in the notochord. The notochord is the source of the Shh morphogen, which is why this is where the highest concentration of ligand is seen (Echelard et al. 1993; Riddle et al. 1993). Previous work showed that the notochord degenerates in the absence of SMO, arguing that Shh signaling is required to maintain the notochord (Caspary et al. 2002). Our analysis of Smo^{cbb} mutants showed that the notochord is intact, but the floor plate is not properly specified, along with a clear deficit in SMO-positive cilia in the ventral floor plate. These data suggest that the floor plate, but not the notochord, requires the highest level of Shh signaling.

The reduced floor plate in Smo^{cbb} mutants appears to produce less Shh ligand than in controls. In the improperly specified Smo^{cbb} floor plate, we observed some Nkx2.2 and FoxA2 co-expressing cells, suggesting that cell identity is poorly defined at this stage. However, at E11.5, we noted a lack of co-labeled cells, suggesting that cell fates resolve over time. This indicates that Shh signal integration is delayed, but it does occur. That said, the simple model of neural patterning would predict that fewer floor plate cells expressing less Shh would lead to patterning defects in all the ventral cell fates. In fact, we observed the ventral expansion of Nkx2.2 and Olig2 fates but the dorsal position of the Olig2 domain is the same as in controls. This is reminiscent of *Gli2* mutants, which also do not specify a floor plate, but display a ventral expansion of intermediate cell fates and maintain the dorsal position of the Olig2 domain (Ding

et al. 1998; Matise et al. 1998). Thus, the highest levels of Shh response appear necessary exclusively at the ventral midline of the neural tube.

In *Smo*^{cbb} mutants, the reduced floor plate, the lack of vertebral bodies in the backbone, the shortening of the long bones of the limbs, and the rotated nasal pits, all reflect a loss of the highest levels of Shh activity. In fact, the skeletal phenotype closely resembles that of the *Gli2* null embryo that shares late gestational lethality (Mo et al. 1997), further supporting a loss of high-level Shh. While recent evidence suggests that SMO activation can occur in a cilia-independent manner, the highest levels of activation appear to depend upon ciliary enrichment (Fan et al. 2014). Our finding that SMO^{N223K} is inefficiently trafficked to cilia suggests a model whereby the N223K mutation disrupts efficient protein trafficking to the cilium. The survival of *Smo*^{cbb} pups to birth argues that signaling is partially intact. The fact that SAG treatment has no impact on the ciliary enrichment of mutant SMO^{N223K} protein fits in well with both our proposal that SAG cannot bind SMO^{N223K} and the notion that phosphorylation of SMO outside the cilium initiates the switch of SMO to an active state. SMO is trafficked to cilia after the initial activation event that likely causes a change in its conformation in order to expose the C-terminal tail that is required for its ciliary enrichment (Corbit et al. 2005). G protein-coupled receptor associated sorting protein 2 (Gprasp2) interacts with the SMO C-terminus in addition to a protein, Pitchfork, in a complex that contains the kinesin Kif3b motor subunit (Jung et al. 2016). Additional evidence showing that β-arrestin binds SMO and facilitates the recruitment of kinesin motor Kif3a leads to a model whereby the whole complex is needed for SMO transport to the cilium (Kovacs et al. 2008). Future work is required to determine whether appropriate conformational changes occur in SMO^{N223K}, whether disulfide bonds that mediate the association

between the sterol-bound CRD and the extracellular loop of SMO^{N223K} can be maintained, or whether the complexes that mediate ciliary trafficking form with SMO^{N223K}.

The overall conservation of the components and regulatory logic of Hh signaling, from flies through vertebrates, make the unique necessity of cilia for Hh signaling transduction in vertebrates particularly intriguing (Goetz et al. 2010; Huangfu et al. 2006). The *Smo*^{cbb} mutation may be a particularly relevant tool for understanding the relationship between Hh signaling and cilia in vertebrates because the poor SMO^{N223K} ciliary enrichment could represent a disruption specifically in the process co-opted by vertebrates for Hh regulation. At the most extreme end of interpretation, the *Smo*^{cbb} phenotype may reflect the evolutionarily conserved Hh mechanism, and it may be that to gain higher levels of Hh activity, another level of activation in the cilium evolved.

CHAPTER 4

ARL13B IS NOT REQUIRED IN CILIA FOR NORMAL SONIC HEDGEHOG SIGNALING

This chapter previously published as:

Gigante, E.D., Taylor, M.R., Ivanova, A.A., Kahn, R.A., and Caspary T. (2020) ARL13B regulates Sonic hedgehog signaling from outside primary cilia. *eLife 2020;9:e50434* doi:10.7554/eLife.50434.

4.1 Summary

The presumption is that a protein functions from where it resides. ARL13B is one of the best-known cilia proteins, widely used by the field as a cilia marker across species. It is not restricted to cilia, but it is easily detected there, so the presumption is that it likely functions in cilia. When the null allele was discovered by the Caspary lab, we emphasized two key points. 1) ARL13B is required for normal Sonic Hedgehog signaling and the organization of Hedgehog components in cilia. 2) Loss of ARL13B results in structural defects in the axoneme and short cilia. The conclusion was that the structure defects are causative of the signaling defects.

In this study, I directly tested if ARL13B is required in cilia for it to function by mutating its cilia-localization sequence (RVEP-to-RAEP), preventing it from enriching in cilia. To my surprise, homozygous *Arl13b*$^{V358A/V358A}$ mice have normal Sonic Hedgehog signaling, normal development, and are completely viable. What's more, analysis of cilia in cultured cells showed cilia are shorter than normal in these mutants. This suggests that the structural defects observed in *Arl13b* null cilia are not causing the signaling defects. Effectively, I uncoupled ARL13B function in signaling pathways from its residency in cilia. In this chapter I explore these outcomes based on the manuscript published in *eLife* in early 2020.

4.2 Introduction

The Hedgehog (Hh) signaling pathway is essential for embryogenesis in a wide variety of organisms. Initially discovered in *Drosophila* where there is a single Hh ligand, the core components of the Hh pathway are conserved in vertebrates (Nusslein-Volhard et al. 1980). These include the vertebrate Hh receptor Patched1 (PTCH1), the obligate transducer of the pathway SMOOTHENED (SMO), as well as the GLI transcription factors (Ci in *Drosophila*) that act as

both activators (GLIA) and repressors (GLIR) to control target gene transcription (Briscoe et al. 2013). There are three Hh ligands in vertebrates, Sonic (Shh), Indian (Ihh) and Desert (Dhh), that regulate a multitude of developmental processes including formation of the limbs and digits, the bones of the skull and face, and the patterning of the neural tube (Placzek et al. 2018). Diminished Hh signaling during embryogenesis results in birth defects whereas increased Hh signaling leads to tumors, highlighting the importance of the pathway and its regulation (Raleigh et al. 2019).

Given the deep homology between invertebrate and vertebrate Hh signaling, the discovery that primary cilia are required for vertebrate, but not invertebrate, Hh signaling was unexpected (Huangfu et al. 2003; Huangfu et al. 2006). Vertebrate Hh components dynamically traffic within primary cilia in response to Hh ligand (Corbit et al. 2005; Haycraft et al. 2005; Rohatgi et al. 2007). In the absence of ligand, PTCH1 is enriched on the ciliary membrane and SMO is barely detectable (Corbit et al. 2005; Rohatgi et al. 2007). Furthermore, full length GLI proteins traffic to the ciliary tip and back to the cytoplasm before being cleaved to their repressor form, which actively shuts down Hh target gene transcription in the nucleus (Kim et al. 2009; Liu et al. 2005; Wen et al. 2010; Humke et al. 2010). In contrast, upon ligand stimulation (Shh, Ihh or Dhh), the PTCH1 receptor binds the ligand and shuttles out of cilia (Rohatgi et al. 2007). Subsequently, SMO is enriched in the cilium and is subsequently activated (Kong et al. 2019; Corbit et al. 2005). Activated SMO promotes the processing of full-length GLI transcription factors into GLIA, which turns on target genes (Aza-Blanc et al. 2000; Ruiz I Altaba 1998). Ablation of cilia results in an absence of GLIA and GLIR production, rendering the pathway inert and leading to an absence of transcriptional response (Huangfu et al. 2005). The dynamic ciliary movement of Shh components appears to be critical to pathway function, as alterations to cilia disrupt pathway output (Caspary et al. 2007; Huangfu et al. 2006; Liem et al. 2012; Liem et al. 2009; Goetz et al. 2009; Murdoch et al. 2010;

Tuz et al. 2014; Cortellino et al. 2009; Houde et al. 2006; Liu et al. 2005; Tran et al. 2008; Taylor et al. 2015).

Given that the fundamental logic of the pathway is conserved from flies through vertebrates, and that flies transduce Hh signals without relying on primary cilia, both evolutionary and mechanistic questions are raised as to how vertebrate cells co-opted the primary cilium for Hh signal transduction. One distinction lies in the fact that vertebrates use Hh signaling over a longer distance than flies, leading to the proposal that the primary cilium is a critical part of a mechanism underlying long range signaling (Bangs et al. 2015). For example, in neural patterning Shh is initially expressed in the notochord and is secreted to specify fates more than 20 cells away (Chiang et al. 1996; Briscoe et al. 2001; Roelink et al. 1994). At the evolutionary level, comparisons among organisms with cilia and or Hh have provided some clues. The round worm *C. elegans* have cilia yet do not possess Hh signaling as they don't have most of the genes encoding the core components of Hh signal transduction (Consortium 1998; Roy 2012). Curiously, a few components of Hh signaling such as fused and costal 2 are in the *C. elegans* genome where they are functionally important for ciliogenesis (Ingham et al. 2011). Additionally, *C. elegans* retained a PTCH1 homolog important for development and pattern formation, but no Hh or SMO (Zugasti et al. 2005; Kuwabara et al. 2000). In contrast, planaria flatworms possess both cilia and Hh signaling but the cilia are not required to transduce Hh signaling (Rink et al. 2009). The first known evolutionary link between cilia and Hh is in sea urchins which transduce Hh signal in developing muscle tissue via motile cilia (Warner et al. 2014; Sigg et al. 2017). Subsequently, in vertebrates Hh signaling requires primary cilia. These data suggest that the mechanistic link of cilia and Hh is limited to deuterostomes and raises the question of whether the relationship of Hh and primary cilia originated near the last common ancestor of vertebrates, the urochordates.

ARL13B is a member of the ARF family of regulatory GTPases and is highly enriched on the ciliary membrane (Caspary et al. 2007). In mice, a null mutation of *Arl13b* leads to short cilia and to alterations in Shh signal transduction (Caspary et al. 2007; Larkins et al. 2011). ARL13 is ancient, predicted to be present in the last common eukaryotic ancestor. ARL13 appears to have been lost during evolution in organisms that lack cilia and duplicated to ARL13A and ARL13B in the urochordates, thus ARL13B is proposed to hold important clues in deciphering the links between primary cilia and vertebrate Hh signaling (Schlacht et al. 2013; Li et al. 2004; Kahn et al. 2008; East et al. 2012; Logsdon et al. 2004).

ARF regulatory GTPases, like ARL13B , are best known to play roles in membrane trafficking (D'souza-Schorey et al. 2006). As is true for a large number of regulatory GTPases, ARL13B is functionally diverse (Sztul et al. 2019). It regulates endocytic traffic (Barral et al. 2012), as well as the phospholipid composition of the ciliary membrane through recruitment of the lipid phosphatase INPP5E to the ciliary membrane (Humbert et al. 2012). ARL13B also has a conserved role as a guanine nucleotide exchange factor (GEF) for ARL3, another ciliary ARF-like (ARL) protein (Gotthardt et al. 2015; Zhang et al. 2016; Hanke-Gogokhia et al. 2016; Ivanova et al. 2017). ARL13B regulates intraflagellar transport (IFT), the process that builds and maintains cilia (Cevik et al. 2010; Li et al. 2010; Nozaki et al. 2017). It is known to interact with several proteins associated with cilia, including the exocyst, tubulin and UNC119 (Seixas et al. 2016; Zhang et al. 2016; Larkins et al. 2011; Revenkova et al. 2018). Critical to this work, loss of ARL13B disrupts Shh signal transduction in at least two distinct ways: SMO enrichment in cilia occurs even in the absence of ligand and GLI activator production is diminished, although GLI repressor is made normally (Caspary et al. 2007; Larkins et al. 2011).

Due to the high enrichment of ARL13B on the ciliary membrane, ARL13B is assumed to function in its diverse roles from within the cilium. However, ARL13B is present in early endosomes and circular dorsal ruffles on the cell surface (Barral et al. 2012; Casalou et al. 2014). We previously showed that a ^{V358A} variant of ARL13B does not localize to cilia as it disrupts a known VxPx cilia localization sequence (Higginbotham et al. 2012; Mariani et al. 2016). Exogenous overexpression of a ARL13B^{V358A} construct in *Arl13b* null cells does not rescue ARL13B -dependent phenotypes such as cilia length as well as interneuron migration and connectivity, consistent with ciliary ARL13B mediating these processes (Higginbotham et al. 2012; Mariani et al. 2016). In contrast, we found that overexpressed ARL13B^{V358A} does rescue the Shh-dependent ciliary enrichment of SMO in mouse embryonic fibroblasts, arguing that ARL13B may function outside the cilium to regulate SMO traffic (Mariani et al. 2016). Together, these results raise the question of where ARL13B functions.

To define where ARL13B functions in relation to cilia, we wanted an *in vivo* model so generated mice carrying the ARL13B^{V358A} point mutation using CRISPR/Cas9. Here we demonstrate that ARL13B^{V358A} protein is undetectable in *Arl13b*$^{V358A/V358A}$ cilia in both neural tube and mouse embryonic fibroblast cilia, even after blocking retrograde ciliary traffic. We report that *Arl13b*$^{V358A/V358A}$ mice are viable, fertile, and transduced Shh signal normally. We found ARL3 and INPP5E did not localize to the short cilia present in/on *Arl13b*$^{V358A/V358A}$ cells. These data indicate that ARL13B ’s roles within and outside cilia can be uncoupled; ARL13B ’s role in regulating cilia length is from within cilia, whereas its control of Shh signaling appears to be from outside the cilium. Thus, these data imply that the cilia defects seen in the complete absence of ARL13B do not underlie the alterations in Shh transduction, which is unexpected given the requirement of cilia for Shh signal transduction.

4.3 Results

4.3.1 ARL13B^{V358A} displays normal GEF activity

We previously showed that mouse ARL13B^{V358A} protein retained normal intrinsic and GAP-stimulated GTP hydrolysis activities by analyzing GST-ARL13B^{V358A} purified from human embryonic kidney (HEK) cells (Mariani et al. 2016). In order to test ARL13B^{V358A} GEF activity for ARL3, we used the same GST-ARL13B^{V358A} protein preparation and measured the rates of spontaneous or GEF-stimulated GDP dissociation from ARL3 in the presence and absence of ARL13B or ARL13B^{V358A}. ARL3 spontaneously releases pre-bound GDP quite slowly under the conditions in the assay, though release is linear with time, and by extrapolation requires just under 30 min for 50% of pre-bound [^{3}H]GDP to dissociate (**Figure 4.1**). In marked contrast, addition of ARL13B under the same conditions caused the release of 50% of the GDP within ~10 seconds and close to 100% in one minute. We detected no differences between the wild type and mutant ARL13B^{V358A} proteins in this assay, consistent with this point mutation having no effect on ARL13B GEF function (**Figure 4.1**). This result is consistent with GEF activity being conserved within the protein's GTPase domain while the ^{V358A} mutation is located in the C-terminal domain (Gotthardt et al. 2015).

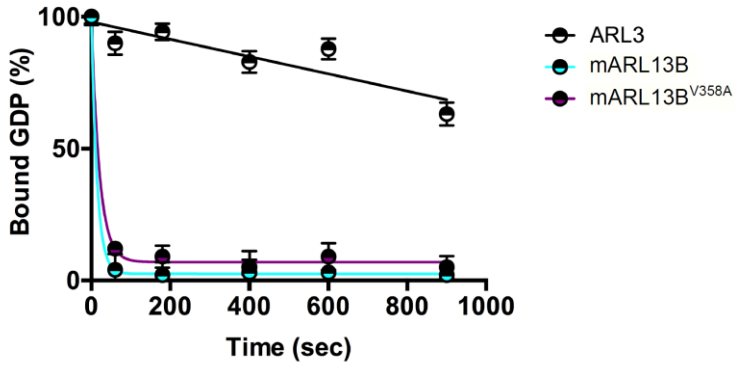

Figure 4.1 ARL3 GEF activity is retained in the Arl13b^{V358A} mutant.

Time course of the release of pre-bound [^{3}H]GDP from purified, recombinant ARL3 in the absence (ARL3) or presence of mouse wild type ARL13B or ARL13B ^{V358A} (mARL13B) are shown. See Methods for details. Error bars ± standard deviation.

These data indicate that ARL13B^{V358A} retains all known ARL13B biochemical activities, suggesting that the ^{V358A} mutation only disrupts ARL13B localization.

4.3.2 CRISPR engineered *Arl13b*$^{V358A/V358A}$ mice express cilia-excluded ARL13B protein.

To determine the consequences of ARL13B^{V358A} expression *in vivo*, we used CRISPR/Cas9 editing to change residue 358 from valine to alanine (**Figure 4.2A**). We performed sequencing of the region that flanked exon 8, using primers outside the region of the donor oligonucleotide. We confirmed the heterozygous T to C base pair change for a valine to alanine change at residue 358 (**Figure 4.2B**). We backcrossed heterozygous F1 progeny to FVB/NJ for three generations before analysis to minimize any off target confounds (see details in Methods).

Figure 4.2 Generation of the *Arl13b*$^{V358A/V358A}$ mouse.

(A) Schematic of *Arl13b* gene and donor oligo (orange bar) at exon 8 used to generate the V358A causing point mutation. Arrows indicate primers used for allele validation. (B) *Arl13b* DNA and relevant amino acid sequence with the RVEP sequence in the orange box and the T-to-C mutation highlighted in pink. (C) Confocal images of cilia marker IFT88 (green) and ARL13B (magenta; NeuroMab) staining in neural tube of E10.5 somite-matched embryos. ARL13B -positive cilia are visible in *Arl13b*$^{+/+}$ and *Arl13b*$^{V358A/+}$, but not in *Arl1b*$^{V358A/V358A}$ embryos. (See Figure 2 – Figure supplement 1 for images of neural tube cilia under saturating conditions.) At least 5 embryos per genotype across five litters were examined. Scale bars are 50 μm. (D) ARL13B Western blot of E10.5 whole embryo lysates, wild type (+/+), *Arl13b*$^{V358A/+}$ (*A*/+) and *Arl13b*$^{V358A/V358A}$ (*A/A*) and (E) quantification presented as average intensity normalized to total protein ± standard deviation. Representative blot of whole embryo lysates (n = 3 embryos per genotype with technical duplicate of each). * $p < 0.05$, one-way ANOVA and Tukey's multiple comparison.

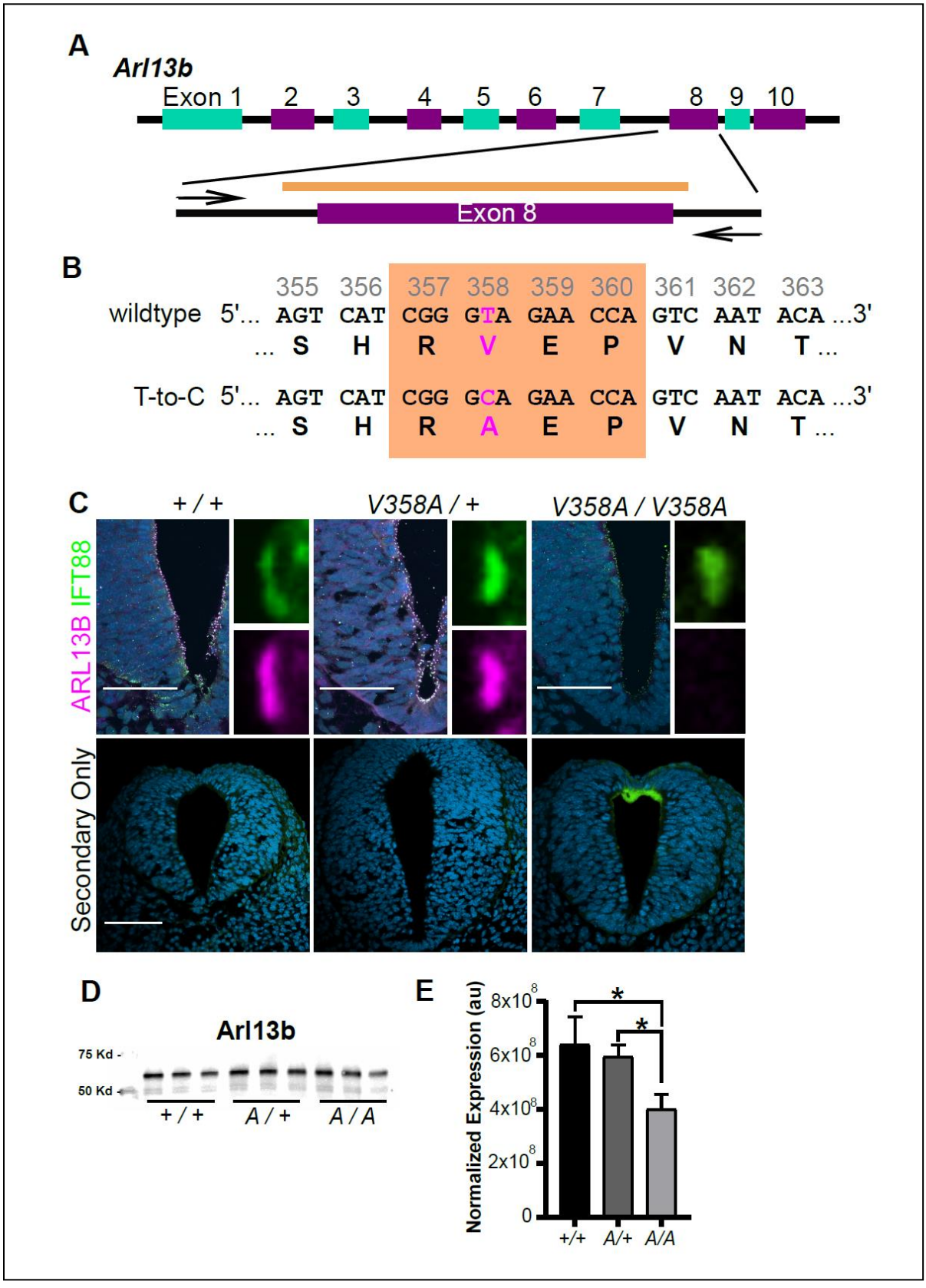
A
Arl13b
Exon 1 2 3 4 5 6 7 8 9 10
Exon 8
B
355 356 357 358 359 360 361 362 363
wildtype 5'... AGT CAT CGG GTA GAA CCA GTC AAT ACA ...3'
... S H R V E P V N T ...
T-to-C 5'... AGT CAT CGG GCA GAA CCA GTC AAT ACA ...3'
... S H R A E P V N T ...
C
+ / +
V358A / +
V358A / V358A
ARL13B IFT88
Secondary Only
D
Arl13b
75 Kd -
50 Kd -
+ / +
A / +
A / A
E
Normalized Expression (au)
8x10^8
6x10^8
4x10^8
2x10^8
0
+/+
A/+
A/A
*
*

To determine whether ARL13B^{V358A} is detectable in neural tube cilia, we performed immunofluorescence using antibodies directed against ARL13B and the cilia marker IFT88. At embryonic day (E)10.5, we saw IFT88 staining, indicating the presence of cilia. In neural tube cilia of *Arl13b*$^{+/+}$ and *Arl13b*$^{V358A/+}$ embryos, we observed equivalent ARL13B staining but could not see ARL13B signal in neural tube cilia of *Arl13b*$^{V358A/V358A}$ embryos (**Figure 4.2C**). We exposed the images longer, to saturation, and while we observed low-level staining throughout the cell, we saw no ciliary ARL13B indicating the ARL13B^{V358A} protein is undetectable in cilia *in vivo* (**Figure 4.2 – Figure supplement 1**).

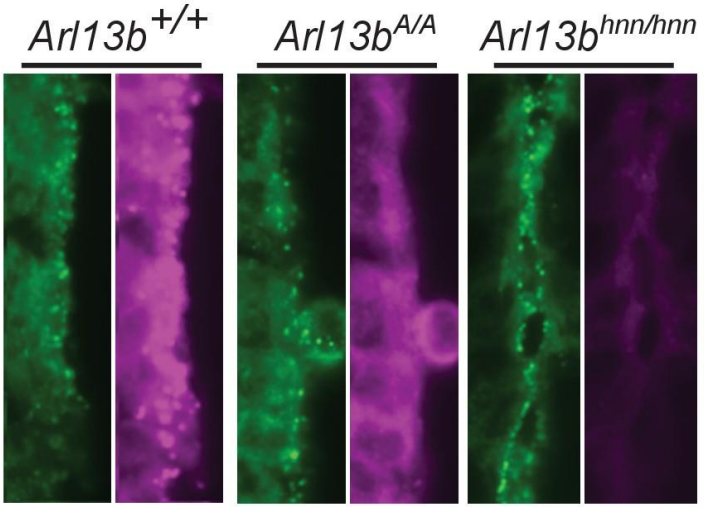

Figure 4.2 – Supplement 1 Overexposure of *Arl13b*$^{V358A/V358A}$ cilia in E10.5 neural tube reveals no clear Arl13b^{V358A} presence in cilia.

Overexposure of cilia in E10.5 *Arl13b*$^{+/+}$, *Arl13b*$^{V358A/V358A}$, and *Arl13b*$^{hnn/hnn}$ embryonic neural tube, stained for IFT88 and ARL13B (NeuroMab). The ARL13B channel was overexposed for four seconds instead of one second.

One possible explanation for the absence of ciliary ARL13B in the *Arl13b*$^{V358A/V358A}$ embryos is that the ARL13B^{V358A} protein is not expressed or is unstable. To determine whether ARL13B protein expression is affected by the ^{V358A} mutation, we performed Western blots on E10.5 whole embryo lysates (**Figure 4.2D**). We found a ~7% (±20%) reduction of ARL13B levels in *Arl13b*$^{V358A/+}$ embryos and a ~37% (±6%) decrease of ARL13B levels in *Arl13b*$^{V358A/V358A}$ embryos, compared to WT (**Figure 4.2E**). This decrease may reflect a change in ARL13B^{V358A} stability compared to ciliary ARL13B or could signify ARL13B^{V358A} protein having a distinct half-

life when localizing to different cellular compartments. Regardless, these data indicate that ARL13B^{V358A} is expressed in *Arl13b*$^{V358A/V358A}$ embryos.

4.3.3 ARL13B^{V358A} protein is undetectable in cilia in mouse embryonic fibroblasts.

To more closely investigate whether any ARL13B^{V358A} protein could localize to cilia, we generated immortalized mouse embryonic fibroblasts (MEFs). We performed double labeling to first identify cilia using acetylated α-tubulin or IFT88 antibodies and subsequently determined whether ARL13B is present in cilia. We used five distinct antibodies against ARL13B : 4 antibodies against amino acids 208-427 of the mouse ARL13B protein (1 mouse monoclonal (NeuroMab), 3 rabbit polyclonal antibodies (Caspary et al. 2007)), as well as 1 antibody against the full-length human ARL13B protein (rabbit polyclonal (Protein Tech)). By eye, we observed strong ciliary staining of ARL13B with each of the antibodies in *Arl13b*$^{+/+}$ and *Arl13b*$^{V358A/+}$ cells, but we are unable to identify any evidence of ARL13B staining above background within cilia in *Arl13b*$^{V358A/V358A}$ cells with any of these five antibodies (**Figure 4.3A**). Taken together, these data support our conclusion that ARL13B^{V358A} is not detectable in cilia using the currently available, validated ARL13B antibodies. While we observed no evidence of detectable ciliary ARL13B in *Arl13b*$^{V358A/V358A}$ MEFs, it is possible that a small amount of ARL13B^{V358A} is constantly trafficking in and out of cilia, at steady-state levels that remain below the limits of detection. To begin to address this possibility, we blocked retrograde ciliary transport, reasoning that any ARL13B undergoing trafficking in and out of cilia would accumulate. We treated cells with ciliobrevin-D, which blocks the retrograde motor protein dynein (Firestone et al. 2012). As a positive control, we examined IFT88 and GLI3, a ciliary protein and a Hh component, respectively; both are known to accumulate at ciliary tips upon blocking of retrograde transport. We found IFT88 and GLI3

enrichment at ciliary tips in *Arl13b*$^{+/+}$, *Arl13b*$^{V358A/+}$ and *Arl13b*$^{V358A/V358A}$ cells upon ciliobrevin-D treatment relative to the respective DMSO-treated controls with no difference in IFT88 or GLI3 staining among the 3 genotypes (**Figure 4.3B and C**). To determine whether ARL13B accumulated in cilia of ciliobrevin-D-treated MEFs, we examined cells co-stained for acetylated α-tubulin and ARL13B. In *Arl13b*$^{+/+}$ and *Arl13b*$^{V358A/+}$ cells, we saw that about 90% of acetylated α-tubulin-positive cilia also stained for ARL13B in DMSO-treated control or ciliobrevin-D treated MEFs (**Figure 4.3D and E**). In *Arl13b*$^{V358A/V358A}$ MEFs, we saw no ciliary ARL13B staining in DMSO-treated control or ciliobrevin-D-treated cells using 2 antibodies against distinct epitopes (**Figure 4.3D and E)**. Thus, even when retrograde traffic out of cilia is disrupted, we are unable to detect ARL13B protein in cilia in *Arl13b*$^{V358A/V358A}$ MEFs.

Figure 4.3 Arl13b^{V358A} is undetectable in cilia and cannot be enriched by inhibition of retrograde transport.

(A) Antibodies against ciliary markers acetylated α-tubulin or IFT88 (magenta) and ARL13B (cyan) in *Arl13b*$^{V358A/V358A}$ MEFs. Representative images show staining for five indicated ARL13B antibodies: (PT) polyclonal rabbit antibody against full-length human ARL13B from ProteinTech, (503, 504, 505) polyclonal rabbit sera from three distinct rabbits raised against C-terminus of mouse ARL13B (amino acids 208-427) (Caspary et al. 2007), and (NM) monoclonal mouse antibody against C terminus of mouse ARL13B from NeuroMab. *Arl13b*$^{+/+}$ and *Arl13b*$^{V358A/+}$ show ciliary ARL13B staining. Table lists ARL13B -positive cilia and the total number of cilia identified by acetylated α-tubulin or IFT88 antibody in parentheses. Cilia appear shorter in *Arl13b*$^{V358A/V358A}$ cells (see Fig. 6). (B) IFT88 and (C) GLI3 (green) is enriched in the tips of cilia in *Arl13b*$^{+/+}$ (+/+), *Arl13b*$^{V358A/+}$ (*A*/+) and *Arl13b*$^{V358A/V358A}$ (*A/A*) cells following ciliobrevin-D treatment. Violin plots depict relative fluorescence of IFT88 and GLI3 at cilia tip to cell body with number of cilia measured (n) listed beneath each plot. (D & E) Table lists ARL13B (cyan) positive cilia (rabbit anti-ARL13B ; ProteinTech or mouse anti-ARL13B ; NeuroMab) and the total number of cilia (acetylated α-tubulin: magenta) examined in control (DMSO) and ciliobrevin-D treated (30μM CB) cell lines. Representative images show staining for cilia and ARL13B. Staining of IFT88 and GLI3 analyzed by two-way ANOVA and Sidak's multiple comparisons. (*** $p < 0.001$, **** $p < 0.0001$).

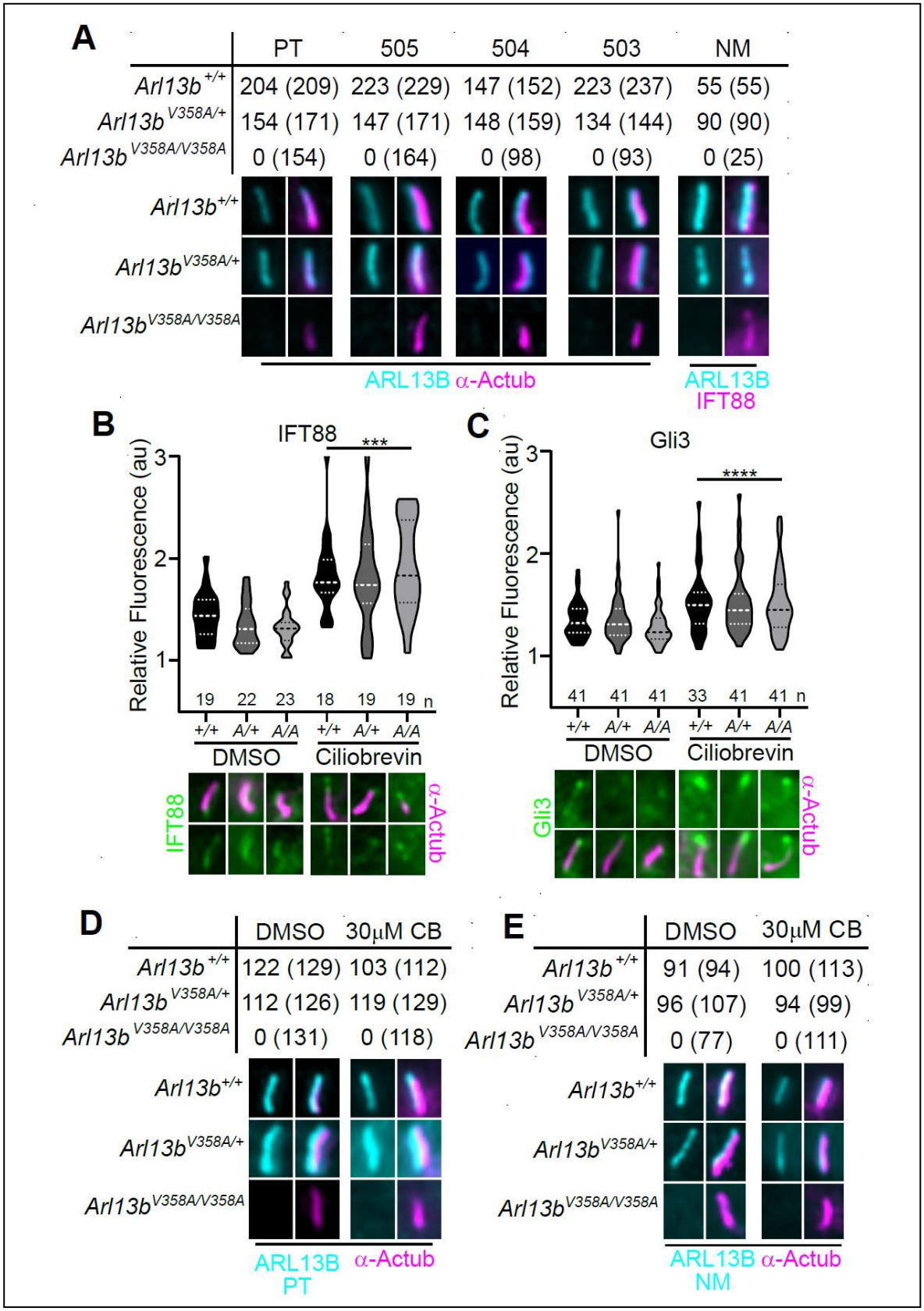
A
PT
505
504
503
NM
Arl13b+/+
204 (209)
223 (229)
147 (152)
223 (237)
55 (55)
Arl13bV358A/+
154 (171)
147 (171)
148 (159)
134 (144)
90 (90)
Arl13bV358A/V358A
0 (154)
0 (164)
0 (98)
0 (93)
0 (25)
Arl13b+/+
Arl13bV358A/+
Arl13bV358A/V358A
ARL13B α-Actub
ARL13B
IFT88
B
IFT88
***
Relative Fluorescence (au)
19 22 23 18 19 19 n
+/+ A/+ A/A +/+ A/+ A/A
DMSO
Ciliobrevin
IFT88
α-Actub
C
Gli3
****
Relative Fluorescence (au)
41 41 41 33 41 41 n
+/+ A/+ A/A +/+ A/+ A/A
DMSO
Ciliobrevin
Gli3
α-Actub
D
DMSO
30μM CB
Arl13b+/+
122 (129)
103 (112)
Arl13bV358A/+
112 (126)
119 (129)
Arl13bV358A/V358A
0 (131)
0 (118)
Arl13b+/+
Arl13bV358A/+
Arl13bV358A/V358A
ARL13B
α-Actub
PT
E
DMSO
30μM CB
Arl13b+/+
91 (94)
100 (113)
Arl13bV358A/+
96 (107)
94 (99)
Arl13bV358A/V358A
0 (77)
0 (111)
Arl13b+/+
Arl13bV358A/+
Arl13bV358A/V358A
ARL13B α-Actub
NM

We re-examined these data and repeated our analyses using over-exposed images. After defining the region of interest using the acetylated α-tubulin staining, we subsequently overexposed the ARL13B channel five-fold relative to the images in Figure 3 and acquired measurements at the cilium and the cell body (**Figure 4.2 – Figure supplement 2**). As a control, we used *Arl13b*$^{hnn/hnn}$ MEFs, which are devoid of any ARL13B, and obtained a ratio of 1.0, with or without ciliobrevin-D treatment. We found the same ratio when we analyzed *Arl13b*$^{V358A/V358A}$ MEFs consistent with ARL13B being absent from the cilia. We observed a few instances of ARL13B appearing to co-localize with acetylated α-tubulin, but these are rare (<5%, 2/49) and occurred in both *Arl13b*$^{V358A/V358A}$ and *Arl13b*$^{hnn/hnn}$ (null) cells indicating this is the background staining of the primary antibody. We extended our analysis of overexposed images in *Arl13b*$^{V358A/V358A}$ and *Arl13b*$^{hnn/hnn}$ neural tube sections four-fold relative to the images in Figure 2; we identified no overlap of overexposed ARL13B with cilia marker IFT88 (**Figure 4.2 – Figure supplement 1**). While it is formally possible that an extremely small amount of ARL13B^{V358A} remains in cilia, we are not able to find evidence of it; thus, we designate ARL13B^{V358A} protein as cilia-excluded ARL13B.

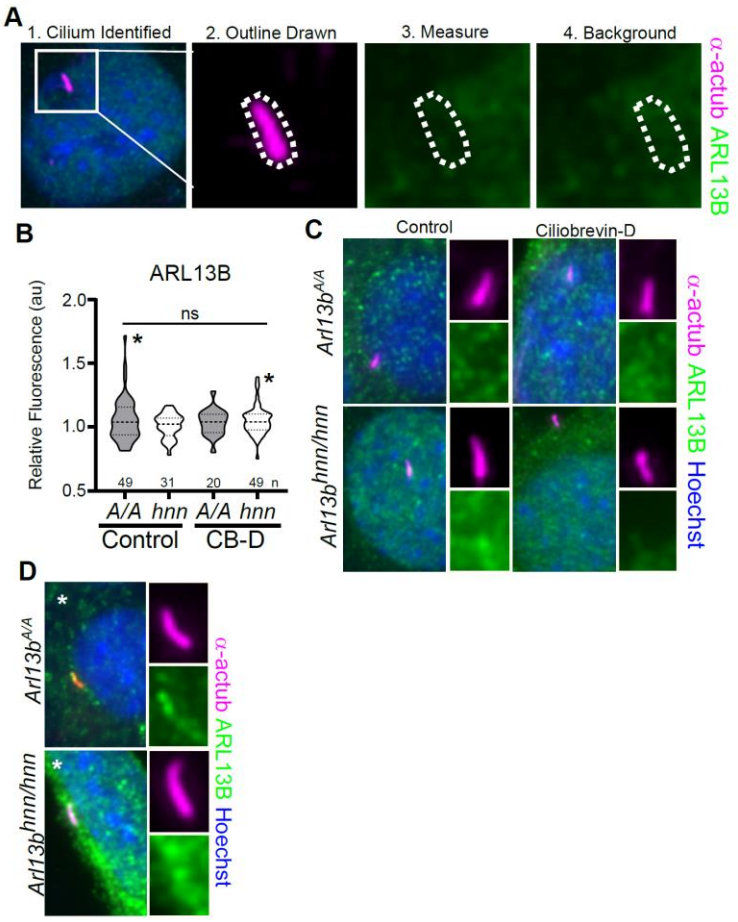

Figure 4.2 – Supplement 2 Overexposure of *Arl13b*$^{V358A/V358A}$ cilia in MEFs reveals no clear Arl13b^{V358A} presence in cilia.

(A) We identified acetylated α-tubulin positive cilia and used the marker to outline the area of the cilium. We quantified ARL13B immunofluorescence detected by Caspary lab polyclonal anti-ARL13B antibody (Caspary et al. 2007) and used the same trace to measure background levels in a different area of the cell body. (B) *Arl13b*$^{V358A/V358A}$ (*A/A*) and *Arl13b*$^{hnn/hnn}$ (*hnn*) MEFs treated with control or ciliobrevin-D 0.5% FBS Media. Samples were overexposed five times longer than normal, saturating the detector in the ARL13B channel. We measured no difference in ciliary ARL13B immunofluorescence between control and ciliobrevin-D treated *Arl13b*$^{V358A/V358A}$ and *Arl13b*$^{hnn/hnn}$ MEFs. Data presented as violin plots and analyzed by one-way ANOVA. Respective number of cilia listed below each plot. Cilia that had ARL13B immunofluorescent readings above background (*) are shown in panel D. (C) Representative images of over exposed *Arl13b*$^{V358A/V358A}$ and *Arl13b*$^{hnn/hnn}$ MEFs in control and ciliobrevin-D treatment conditions. (D) Representative images of cilia with ARL13B levels above background, marked by * in panel B.

We did not observe any obvious cellular ARL13B signal in the cells expressing cilia-excluded ARL13B so we investigated whether we could detect cellular ARL13B in cells lacking cilia, *IFT172*$^{wim/wim}$ MEFs. As controls we used wildtype, *Arl13b*$^{hnn/hnn}$ (lacking ARL13B), and *IFT172*$^{wim/wim}$ *Arl13b*$^{hnn/hnn}$ (lacking ARL13B and cilia) MEFs. We only detected ARL13B staining in *IFT172*$^{wim/wim}$ cells upon overexposure and found it is modestly detectable above the background level we observed in *Arl13b*$^{hnn/hnn}$ or *IFT172*$^{wim/wim}$ *Arl13b*$^{hnn/hnn}$ cells (**Figure 4.3 – Figure supplement 1**). Thus, cellular ARL13B is expressed at an extremely low level.

MICE	Sex	wildtype	*V358A/+*	*V358A/V358A*	
Het x Het	M (46.5%)	3	11	6	
Avg. Litter	F (53.5%)	6	8	9	
7.3	% of Total	20.9	44.2	34.9	$\chi^2 = 0.60$
Het x Hom	M (60%)	-	10	11	
Avg. Litter	F (40%)	-	6	8	
7.5	% of Total	-	45.7	54.3	$\chi^2 = 0.69$
Hom x Hom	M (47.4%)	-	-	9	
Avg. Litter	F (52.6%)	-	-	10	
9.5					

Table 4.1.

Genotype of mice born to heterozygous and/or homozygous carrier parents.

Data analyzed by chi-squared test.

4.3.4 *Arl13b*$^{V358A/V358A}$ mice are viable and fertile.

In order to determine the phenotypic consequence of the *Arl13b*^{V358A} allele, we intercrossed *Arl13b*$^{V358A/+}$ mice. We observed progeny in Mendelian proportions with an average of 7.3 pups per litter, consistent with the reported FVB/NJ litter size of 7-9 (Murray et al. 2010) (**Table 1**). To test whether homozygous mice breed normally, we crossed *Arl13b*$^{V358A/V358A}$ males to heterozygous or homozygous females. We found the *Arl13b*^{V358A} allele segregated in Mendelian

proportions and the litter sizes are normal indicating that *Arl13b*^{V358A} does not impact viability, fertility or fecundity.

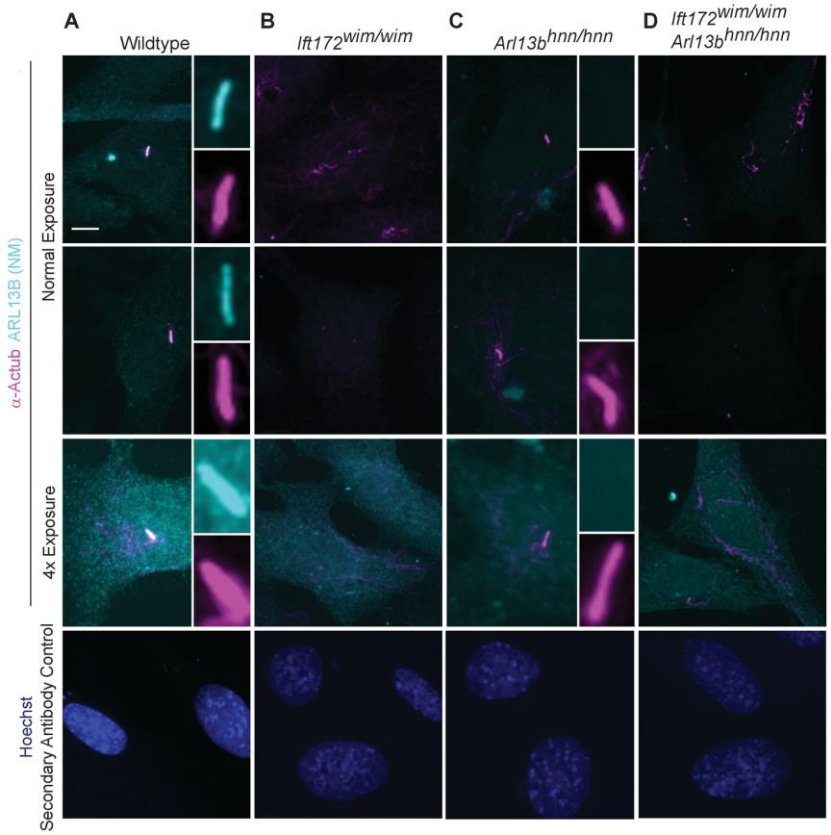

Figure 4.3 – Supplement 1 Endogenous Arl13b is undetectable in the cell body of cilia mutant *IFT172*$^{wim/wim}$ cells.

Immunofluorescent detection of ARL13B (cyan; NeuroMab) and cilia marker acetylated α-tubulin (magenta) in wildtype, *Arl13b*$^{hnn/hnn}$, *IFT172*$^{wim/wim}$, and *IFT172*$^{wim/wim}$ *Arl13b*^{hnn} cell lines. (A) In wildtype cells, ARL13B is detectable in the cilium under non-saturating conditions, these parameters are kept constant across all samples. (B) In *IFT172*$^{wim/wim}$ non-ciliated cells, ARL13B protein is confined to the cell body, but is nearly undetectable by standard immunofluorescence. (C-D) In *Arl13b*$^{hnn/hnn}$ and *IFT172*$^{wim/wim}$ *Arl13b*$^{hnn/hnn}$ cells, null for *Arl13b*, any signal is due primary antibody background. At an exposure rate 4x above normal the ARL13B signal saturates the detector in wildtype cells. In *IFT172*$^{wim/wim}$ cells, overexposure reveals no ARL13B positive stain that is above the background detected in *Arl13b*$^{hnn/hnn}$ and *IFT172*$^{wim/wim}$ *Arl13b*$^{hnn/hnn}$ cells. Images taken at 40x. Scale bar is 5 μm. Experiments repeated in duplicate and examined 4-6 fields of view per condition.

4.3.5 ARL13B^{V358A} permits normal embryonic development and Shh signaling.

Loss of *Arl13b* leads to morphologically abnormal embryos, lethality and neural patterning defects (Caspary et al. 2007). As ARL13B^{V358A} overcame the embryonic lethality, we examined overall embryo morphology at E9.5, E10.5 and E12.5. We found the overall morphology of *Arl13b*$^{V358A/V358A}$ embryos resembled those of *Arl13b*$^{+/+}$ and *Arl13b*$^{V358A/+}$ embryos indicating that ARL13B^{V358A} did not lead to gross morphological defects. (**Figure 4.4A-I**).

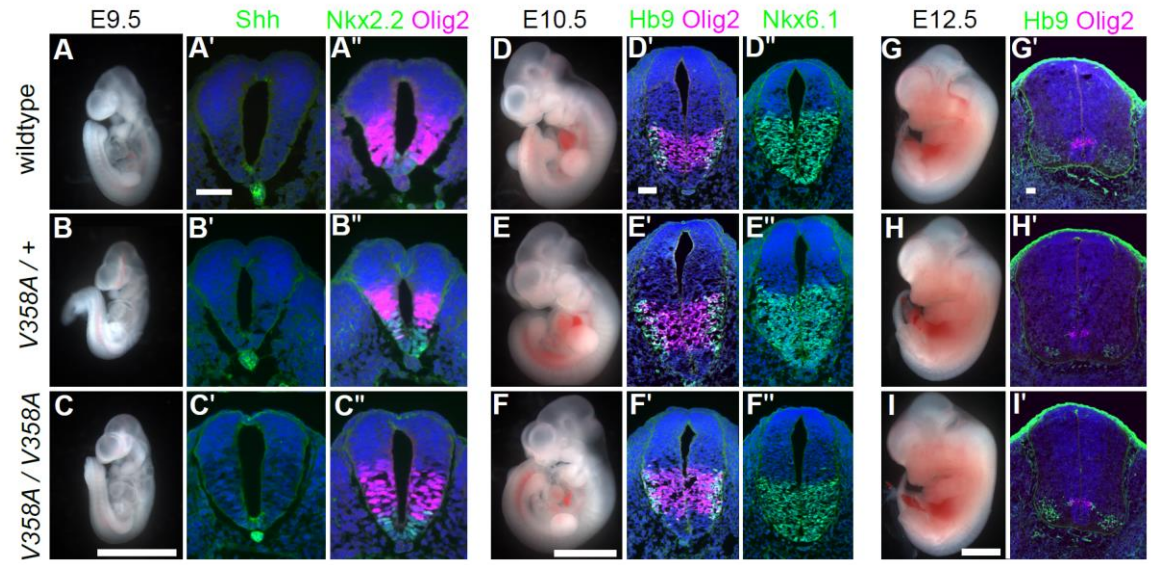

Figure 4.4 Arl13b^{V358A} mediates normal Shh signaling and neural tube patterning.

(A-I) Whole embryo and neural tube sections of somite-matched littermates at E9.5, E10.5, and E12.5 stained with indicated markers of cell fate. Whole embryo scale bars: 2 mm. (A'-I' & A"-F") Shh-dependent neural tube patterning at three separate time points. Cell fate markers are listed above each image. All neural tube scale bars are 50 μm. Neural tube patterning was examined in five embryos for each embryonic stage. E, embryonic day.

At E9.5, Shh is normally expressed in the notochord as well as the floor plate of the ventral neural tube. Moving dorsally, the adjacent domains express Nkx2.2 and subsequently Olig2. In the *Arl13b*$^{hnn/hnn}$ (null) neural tube, the Shh-positive columnar cells of the floor plate are absent resulting in both ventral and dorsal expansion of intermediate Shh-dependent cell fates such as Olig2 (Caspary et al. 2007). To determine whether ARL13B^{V358A} disrupts Shh signaling, we

examined neural tube patterning in *Arl13b*$^{+/+}$, *Arl13b*$^{V358A/+}$, and *Arl13b*$^{V358A/V358A}$ embryos at E9.5, E10.5, and E12.5. At E9.5 we observed no differences in Shh, Nkx2.2 or Olig2 among *Arl13b*$^{+/+}$, *Arl13b*$^{V358A/+}$, and *Arl13b*$^{V358A/V358A}$ embryos (**Figure 4.4A-C**). Cell fates in the neural tube are specified by both the concentration and duration of Shh signaling so we examined neural patterning at subsequent stages (Dessaud et al. 2007). By E10.5, some Olig2 precursors have differentiated to HB9+ motor neurons and all Shh-responsive cells express Nkx6.1. We found that Olig2, HB9 and Nkx6.1 positive cells are normally distributed in all 3 genotypes at E10.5 and E12.5 (**Figure 4.4D-I**). These data indicate that ARL13B^{V358A} mediates normal Shh signaling.

4.3.6 ARL13B regulates ciliary enrichment of Shh components from outside cilia.

In *Arl13b*$^{hnn/hnn}$ cells, SMO is enriched in cilia in a Shh-independent manner, which may be due to defective trafficking of SMO, as many ARL family members regulate protein trafficking (Lim et al. 2011; Larkins et al. 2011). To assess SMO enrichment in *Arl13b*$^{V358A/V358A}$ embryos, we stained for the cilia marker acetylated α-tubulin and SMO in E10.5 embryos. SMO appeared enriched normally in ventral floor plate cilia and the dorsal boundary of SMO ciliary enrichment in ventral neural progenitors is identical in *Arl13b*$^{+/+}$, *Arl13b*$^{V358A/+}$, and *Arl13b*$^{V358A/V358A}$ samples indicating ARL13B^{V358A} mediates normal ciliary SMO enrichment (**Figure 4.5A)**.

To examine SMO traffic in response to Shh stimulation, we treated MEFs with 0.5% FBS or Shh-conditioned media for 24 hours and stained for SMO. As expected in control *Arl13b*$^{hnn/hnn}$ cells, we saw ciliary SMO in unstimulated MEFs which increased upon stimulation with Shh-conditioned media (Larkins et al. 2011) (**Figure 4.5B**). In *Arl13b*$^{+/+}$, *Arl13b*$^{V358A/+}$, and *Arl13b*$^{V358A/V358A}$ MEF cilia, we saw ciliary enrichment of SMO upon Shh stimulation over their respective unstimulated controls (**Figure 4.5B**, left). We found no difference in SMO enrichment

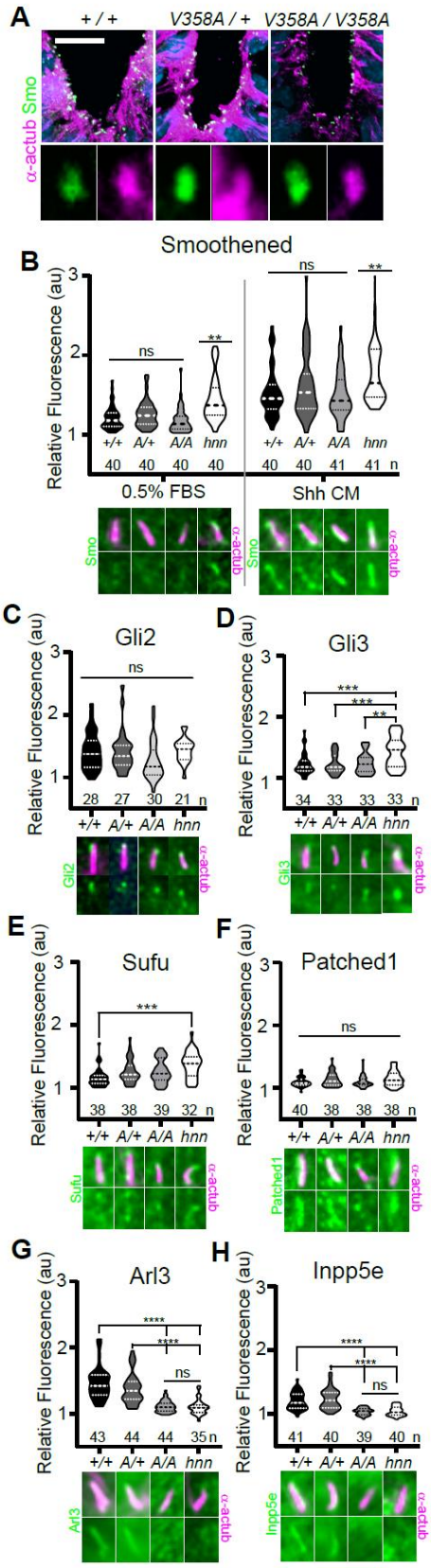

Figure 4.5 Arl13b^{V358A} mediates normal ciliary enrichment of Shh components, but not ARL3 or INPP5E.

(A) SMO (green) enrichment in ventral neural tube cilia (acetylated α-tubulin: magenta) is normal in E10.5 embryos. Images are confocal projections. Scale bar is 25 μm. (B-H, Top) Quantification of average fluorescence intensity in the tip of the cilium (GLI2, GLI3, and Sufu) or the entire cilium (PTCH1, SMO, ARL3, and INPP5E) relative to background level. Violin plots depict relative fluorescent intensity per cilium with number of cilia examined below each plot. (B-H, Bottom) Representative images for each condition and cell type with the cilia marker acetylated α-tubulin (magenta) and indicated protein (green). *Arl13b*$^{+/+}$ (+/+), *Arl13b*$^{V358A/+}$ (*A/+*), *Arl13b*$^{V358A/V358A}$ (*A/A*) and *Arl13b*$^{hnn/hnn}$ (*hnn*). Data analyzed by one-way ANOVA and Tukey's multiple comparisons, except SMO data analyzed by two-way ANOVA and 16 comparisons, corrected $p < 0.003$ deemed significant. (** $p < 0.01$, *** $p < 0.001$, **** $p < 0.0001$).

among these cell lines (**Figure 4.5B**, right). Thus, despite ARL13B being critical for Shh-dependent SMO ciliary enrichment, ARL13B^{V358A} regulates SMO localization normally, arguing this function of ARL13B can occur when the protein is not in cilia.

In addition to aberrations in SMO trafficking, loss of *Arl13b* leads to changes in the cilia localization of other Shh components in MEFs (Larkins et al. 2011). To determine whether these components are disrupted by ARL13B^{V358A}, we examined GLI2, GLI3, Sufu and PTCH1 in MEFs. We observed no differences in distribution of GLI2 or PTCH1 among any of the examined

genotypes (**Figure 4.5C, F**). In contrast, as we previously reported, we observed more GLI3 at the ciliary tip of *Arl13b*$^{hnn/hnn}$ cells and increased Sufu in *Arl13b*$^{hnn/hnn}$ cilia compared to wild type controls (Larkins et al. 2011)(**Figure 4.5D, E**). Thus, Shh components are normally localized in *Arl13b*$^{V358A/V358A}$ MEFs consistent with the normal Shh signal transduction observed in *Arl13b*$^{V358A/V358A}$ embryos (**Figure 4.4**).

4.3.7 ARL13B regulates ciliary enrichment of ARL3 and INPP5E from within cilia.

We next examined the role of ARL13B^{V358A} in the localization of other ciliary proteins. ARL13B is the GEF for ARL3, and we showed that ARL13B^{V358A} GEF activity for ARL3 is retained (**Figure 4.1**). ARL13B is also essential for cilia localization of INPP5E, as the proteins are in a common complex (Humbert et al. 2012). To determine whether the ciliary localization of either ARL3 or INPP5E is affected by ARL13B^{V358A}, we performed immunofluorescence on MEFs. Ciliary ARL3 staining appeared the same in *Arl13b*$^{+/+}$ and *Arl13b*$^{V358A/+}$ MEFs, however ARL3 is not detectable in *Arl13b*$^{V358A/V358A}$ or *Arl13b*$^{hnn/hnn}$ cilia (**Figure 4.5G**). INPP5E is normally detectable in *Arl13b*$^{+/+}$ and *Arl13b*$^{V358A/+}$ MEF cilia, but not in *Arl13b*$^{V358A/V358A}$ and *Arl13b*$^{hnn/hnn}$ MEF cilia (**Figure 4.5H**). These results indicate that ARL13B is required in cilia for the proper localization of ARL3 and INPP5E to the cilium.

4.3.8 Ciliary ARL13B is required for normal cell ciliation and ciliary length

Loss of *Arl13b* leads to defects in the percentage of ciliated MEFs and in cilia length (Caspary et al. 2007; Larkins et al. 2011). To test whether ARL13B^{V358A} impacted cell ciliation, we examined immortalized MEFs and counted the number of ciliated cells 24 hours after induction of ciliation by growth in low serum (0.5% FBS). We found 73% (±11%) of *Arl13b*$^{+/+}$ and 75%, (±9.1%) of *Arl13b*$^{V358A/+}$ MEFs are ciliated, consistent with published results. In contrast, we found

45% (±8.7%) of *Arl13b*$^{V358A/V358A}$ cells and 53% (±6.4%) of *Arl13b*$^{hnn/hnn}$ cells had cilia (**Figure 4.6A**). Thus, *Arl13b*$^{V358A/V358A}$ cells exhibit a similar deficit in percentage of ciliated MEFs as complete loss of ARL13B function.

Arl13b$^{hnn/hnn}$ cilia are about half as long as wild type in both embryos and MEFs (Caspary et al. 2007; Larkins et al. 2011). To determine whether cilia length is affected by ARL13B^{V358A}, we stained MEFs with acetylated α–tubulin and measured the length of the axoneme. We found the average cilia length in *Arl13b*$^{+/+}$ and ARL13B$^{V358A/+}$ MEFs is similar, 2.7 ± 0.8 μm and 2.6 ± 0.9 μm, respectively. However, we found *Arl13b*$^{V358A/V358A}$ MEF cilia are shorter, 1.9 ± 0.7 μm, similar to *Arl13b*$^{hnn/hnn}$ MEF cilia which are 2.15 ± 0.8 μm (**Figure 4.6B**). These results indicate that ARL13B^{V358A} phenocopies complete loss of ARL13B for ciliation and cilia length, indicating these ARL13B functions require ARL13B in cilia. Furthermore, these data show that ARL13B function within cilia is distinct from ARL13B function outside of cilia in a subset of

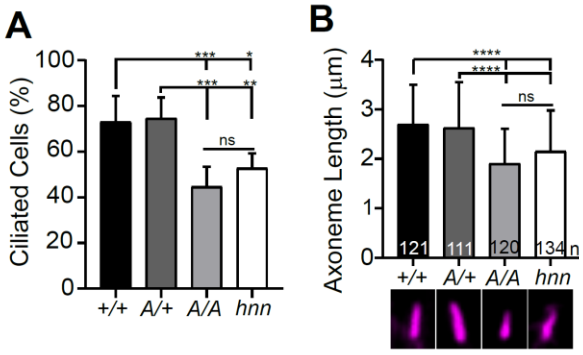

Figure 4.6 ARL13B^{V358A} results in decreased ciliation rates and short cilia.

(A) Quantification of ciliation rates in all cell types; *Arl13b*$^{+/+}$ (+/+), *Arl13b*$^{V358A/+}$ (*A*/+), *Arl13b*$^{V358A/V358A}$ (*A/A*) and *Arl13b*$^{hnn/hnn}$ (*hnn*). Fewer *Arl13b*$^{V358A/V358A}$ and *Arl13b*$^{hnn/hnn}$ MEFs form cilia compared to *Arl13b*$^{+/+}$ or *Arl13b*$^{V358A/+}$ cells. (B) Quantification of axoneme length as labeled by acetylated α-tubulin (magenta) in indicated MEFs. Data are presented as mean (μm) ± standard deviation with the number of cilia measured per genotype depicted at the base of each bar. Data analyzed by one-way ANOVA and Tukey's multiple comparisons. (* $p < 0.05$, ** $p < 0.01$, *** $p < 0.001$, **** $p < 0.0001$)

activities, and that the cilia defects and Shh defects in the complete absence of ARL13B can be uncoupled.

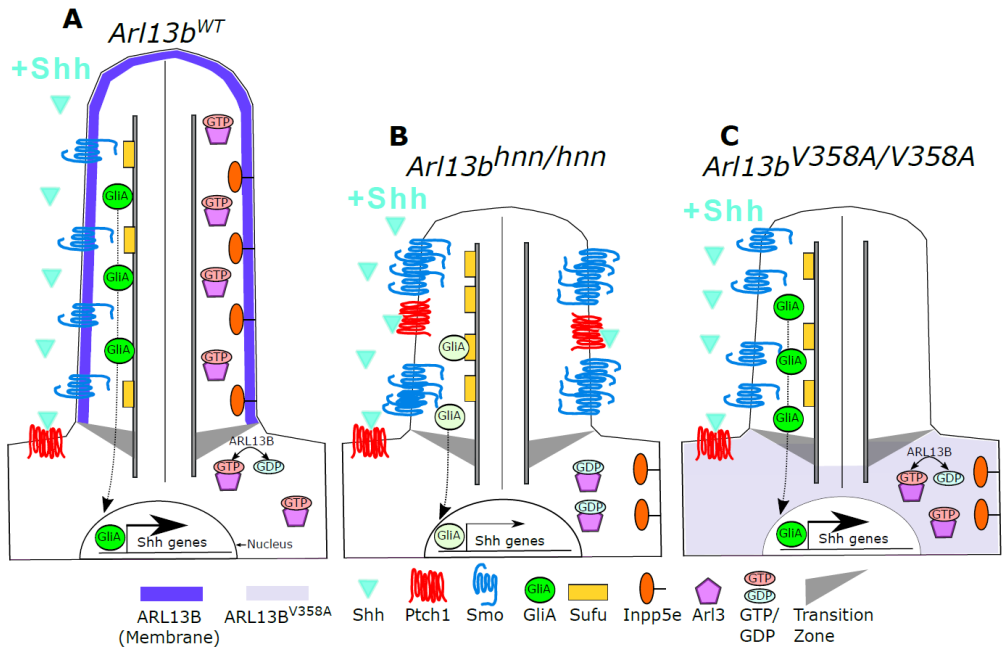

Figure 4.7 Model comparing complete loss of Arl13b function to ciliary loss of Arl13b function

Wildtype (left), *Arl13b*^{hnnhnn} (middle), and *Arl13b*$^{V358A/V358A}$ (right) cilia represented as two halves. On the left half is the organization of Shh components in the presence of Shh ligand and on the right half is the organization of ARL13B interactors ARL3 and INPP5E. (A) ARL13B associates with the ciliary membrane. In the presence of Shh, PTCH1 is removed from cilia and SMO is visibly enriched in cilia. SMO is activated which promotes the processing of full-length GLI transcription factors into their activator forms (GLIA), that are shuttled out of the cilium to promote Shh-dependent gene transcription. In addition, cilia proteins ARL3 and INPP5E are localized to the primary cilium. (B) In *Arl13b*$^{hnn/hnn}$ cells which are null for ARL13B, cilia are shorter than normal. Ciliary PTCH1 and SMO are visible, although SMO appears punctate instead of diffuse. In addition, loss of ARL13B decreases transcription of Shh-dependent genes due to lowered GLIA. *Arl13b*$^{hnn/hnn}$ cilia also display a failure of INPP5E and ARL3 to localize to the cilium. Because ARL13B is the GEF for ARL3, we speculate in this schematic that ARL3 remains GDP bound in *Arl13b*$^{hnn/hnn}$ cells. (C) In *Arl13b*$^{V358A/V358A}$ cells, ARL13B ^{V358A} is not detectable in cilia and appears diffuse within the cell body. *Arl13b*$^{V358A/V358A}$ cilia, like *Arl13b*$^{hnn/hnn}$ cilia, are shorter than wildtype. We observe normal Shh-dependent ciliary SMO enrichment and normal Shh transcriptional output. However, ARL3 and INPP5E are absent from cilia, indicating that ciliary ARL13B is required for ciliary residence of these proteins.

4.4 Discussion

Here we show that ARL13B's role(s) in cell ciliation and cilia length, along with the ciliary enrichment of a subset of proteins, can be uncoupled from ARL13B 's function in regulating Shh signal transduction (**Figure 4.7**). Furthermore, we demonstrate this functional distinction correlates with ARL13B spatial localization to the cilium. By generating a mouse expressing a cilia-excluded variant of ARL13B from the endogenous locus, we showed ARL13B^{V358A} protein is not detectable in cilia of embryonic neural tube or MEFs, even upon retrograde ciliary dynein traffic blockade. Furthermore, we detected 30% less ARL13B protein overall in *Arl13b*$^{V358A/V358A}$ embryos compared to control embryos. While this reduction is statistically significant, it is unclear whether it is biologically significant given that *Arl13b*$^{hnn/hnn}$ null mutations are recessive and no *Arl13b*$^{hnn/+}$ heterozygous phenotype is reported (Caspary et al. 2007; Larkins et al. 2011).

In contrast to the E13.5 lethality of *Arl13b*$^{hnn/hnn}$ embryos, we found *Arl13b*$^{V358A/V358A}$ mice are viable and fertile with correct patterning of the neural tube, indicating normal Shh signal transduction. These results are consistent with our data showing that ARL13B^{V358A} protein retains all known biochemical function including GEF activity (Mariani et al. 2016; Ivanova et al. 2017). However, we observed several *Arl13b*$^{hnn/hnn}$ phenotypes in *Arl13b*$^{V358A/V358A}$ cells, including loss of ARL3 and INPP5E ciliary enrichment, along with low percentage of ciliated cells and shorter average cilia length. Taken together, our data show that despite the normal high ciliary enrichment of wild type ARL13B and the requirement of cilia for Shh signaling, cilia-excluded ARL13B^{V358A} is sufficient for Shh signal transduction.

We regard ARL13B^{V358A} as cilia-excluded based on several lines of evidence. We did not detect ciliary ARL13B^{V358A} *in vivo* or *in vitro* using any of five validated ARL13B antibodies.

These antibodies are against two antigens, the full-length protein or residues 208-427, and are independently generated so are likely to recognize a number of epitopes. Given that 4 of 5 antibodies are polyclonal and ARL13B^{V358A} displays normal GTP binding, intrinsic and GAP-stimulated GTP hydrolysis, and ARL3 GEF activity, it is likely that the ARL13B^{V358A} protein retains the wild type structure enabling antibody recognition. Indeed, we observed little or no loss in sensitivity in detecting protein in the immunoblot assays. Furthermore, we could not forcibly enrich ciliary ARL13B^{V358A} through retrograde transport blockade with ciliobrevin-D nor could we detect any ciliary enrichment of ARL13B^{V358A} upon overexposure of the relevant fluorescent channel. Alternative ways of trafficking proteins out of cilia include BBSome-dependent or diffusion-dependent mechanisms raising the possibility that ARL13B is trafficked via dynein-independent mechanisms. The fact that we observed ciliary phenotypes, namely short cilia and abnormal ciliary ARL3 and INPP5E localization in ARL13B^{V358A} expressing cells, argue that ARL13B normally performs these functions from within cilia (Caspary et al. 2007; Larkins et al. 2011; Zhang et al. 2016; Humbert et al. 2012; Nozaki et al. 2017). While we cannot exclude the possibility that sub-detectable levels of ARL13B^{V358A} are present and functional in cilia, we note such a level would need to be sufficient for Shh signaling yet insufficient for ARL3 or INPP5E ciliary localization along with proper regulation of cilia length.

Our data support ARL13B regulating different biological processes from its distinct subcellular localizations consistent with how other GTPases act from multiple sites in cells through different effectors. ARL13B^{V358A} disrupts cilia localization of INPP5E and ARL3, but not Shh components and thus provides a novel tool with which to identify additional ARL13B effectors. Such effectors may also inform us as to what subcellular compartment ARL13B functions from as the cellular ARL13B antibody staining we observe is inconclusive. It is surprising that

ARL13B^{V358A} is sufficient to regulate Shh signaling because cilia are required for Shh signal transduction and because ARL13B is highly enriched in cilia (Caspary et al. 2007; Huangfu et al. 2003). These observations suggested that the ciliary defects observed in *Arl13b*$^{hnn/hnn}$ mutants caused the Shh defects. However, our data indicate that ARL13B regulates cilia length and Shh signaling through distinct localization. Thus, the cilia defects in *Arl13b*$^{hnn/hnn}$ mutants do not underlie Shh misregulation.

Based on the normal cilia trafficking of Shh components in *Arl13b*$^{V358A/V358A}$ mutants and the abnormal cilia trafficking of Shh components in the complete absence of ARL13B (Larkins et al. 2011), ARL13B likely regulates Shh signaling from the cell body by controlling Shh component traffic to and/or from the primary cilium. Both SMO and ARL13B traffic is linked to endosomes providing one possible non-ciliary organelle (Barral et al. 2012; Wang et al. 2009; Milenkovic et al. 2009). *Arl13b*$^{hnn/hnn}$ cells display constitutive SMO ciliary enrichment along with little enrichment of GLI proteins at the ciliary tip (Larkins et al. 2011). Our data do not distinguish between ARL13B playing direct roles in traffic of multiple Shh components or whether the normal SMO ciliary enrichment with ARL13B^{V358A} subsequently causes normal cilia traffic of downstream components. ARL13B regulates a step downstream of activated SMO that controls transcription factor GLI activation, but not repression (Caspary et al. 2007; Bay et al. 2018). We argue from our results that this step is also intact in the presence of ARL13B^{V358A}.

The fact that ARL13B^{V358A} can mediate normal ciliary SMO enrichment is especially interesting given that ARL3 and INPP5E localization to cilia is compromised by this mutation. This suggests that ARL13B controls cilia enrichment via multiple localizations and effectors. This is consistent with our understanding of ARF family members, as they are known to perform

multiple tasks from different sites within a cell (Sztul et al. 2019). We speculate that ARL3 residence in cilia may require that ARL3 be in (or at least cycle through) its activated, GTP-bound conformation as ARL13B^{V358A} retains its ARL3 GEF activity, but not its cilia localization. ARL13B is in a common protein complex with INPP5E so absence of ARL13B from cilia may disrupt formation or maintenance of the complex there (Humbert et al. 2012; Nozaki et al. 2017). INPP5E regulates Shh signaling through regulation of the phosphoinositol composition of the ciliary membrane. INPP5E loss results in increased ciliary PIP_2 and enrichment of Shh repressors in cilia thus resulting in lowered Shh response (Garcia-Gonzalo et al. 2015; Chavez et al. 2015; Dyson et al. 2017). It is not clear why the absence of ciliary INPP5E in ARL13B^{V358A} cells does not lead to aberrant Shh signal transduction.

In *Arl13b*$^{hnn/hnn}$ embryos and MEFs, cilia are shorter than normal and have a microtubule defect where the B-tubule of the microtubule outer doublet is open (Caspary et al. 2007; Larkins et al. 2011). Consistent with this, we observed shorter cilia in *Arl13b*$^{V358A/V358A}$ MEFs. Similarly, we observed a comparable reduction in the percent of cilia in *Arl13b*$^{hnn/hnn}$ and *Arl13b*$^{V358A/V358A}$ MEFs compared to wild type MEFs. While loss of ARL13B results in short cilia, increased expression of ARL13B promotes cilia elongation so it is not yet clear what ARL13B ’s role is in controlling cilia length (Lu et al. 2015; Hori et al. 2008; Caspary et al. 2007; Larkins et al. 2011). Additionally, it is unclear whether the mechanism from within cilia through which ARL13B controls length or percent of ciliated cells is the same, or distinct from, the mechanism through which ARL13B regulates ARL3 or INPP5E residence in cilia.

Perhaps the most intriguing implication of our data pertains to understanding the evolution of cilia and Hh signaling. ARL13 functions in cilia formation and maintenance in *Chlamydomonas*

and *C. elegans*, neither of which have Hh signaling, consistent with the ancient role of ARL13 controlling ciliation and cilia length (Cevik et al. 2010; Cevik et al. 2013; Stolc et al. 2005; Miertzschke et al. 2014). Our data support ARL13B retaining ARL13's ancient role in ciliogenesis. However, our data show that ARL13B does not work from within the cilium to regulate Shh component ciliary traffic or Shh signal transduction. As an ARL protein involved in membrane traffic, we speculate that ARL13B may have linked Shh component trafficking to the primary cilium, albeit from outside the cilium. That the ARL13 duplication could relate to the mechanism linking primary cilia and Hh signaling within the deuterostome lineage is a possibility worth exploring.

CHAPTER 5

AN ANALYSIS OF OBESITY AND CYSTIC KIDNEYS IN *Arl13b*$^{V358A/V358A}$ AND *Arl13b*$^{V358A/hnn}$ MICE

5.1 Summary

Ciliopathy patients can present with a wide range of syndromes, including cystic kidney disease and obesity. The ciliary mechanism(s) that regulate and prevent either disease is unknown. During my research of Shh signaling defects in *Arl13b*$^{V358A/V358A}$ and *Arl13b*$^{V358A/hnn}$ mice I observed cystic kidney and obesity phenotypes. Adult *Arl13b*$^{V358A/V358A}$ and *Arl13b*$^{V358A/hnn}$ mice developed kidney cysts. Surprisingly, *Arl13b*$^{V358A/hnn}$ mice presented with more severe cystic kidney phenotype, suggesting a potential dosage effect controlled by the amount of ARL13B^{V358A} protein. *Arl13b*$^{V358A/V358A}$ and *Arl13b*$^{V358A/hnn}$ mice maintained on standard or breeder chow gained significantly more weight than their littermate controls. They also presented with insulin and glucose tolerance defects, consistent with hyperglycemia and insulin resistance found in other mouse models of obesity. A preliminary analysis of ARL13B expression levels in control and mutant embryos revealed decreased expression of ARL13B protein in *Arl13b*$^{V358A/hnn}$ embryos compared to levels measured in *Arl13b*$^{V358A/V358A}$. The reduced expression of ARL13B^{V358A} protein is consistent with a possible dosage effect. This correlates with the observed severity of the phenotype in *Arl13b*$^{V358A/hnn}$ mutants compared to *Arl13b*$^{V358A/V358}$ mice. I will use this chapter of my thesis to describe these two ongoing projects.

5.2 Introduction

Throughout ontogeny, nearly every cell type will at some point have a primary cilium (Bangs et al. 2015). In humans, disruptions in cilia proteins, be they involved in trafficking, structure, or signaling, will cause a group of disease states collectively termed ciliopathies (Forsythe et al. 2013; Berbari et al. 2013; Zaghloul et al. 2009; Cantagrel et al. 2008). Ciliopathy patients can have a wide range of phenotypes from retinopathies, polycystic kidney disease (PKD)

and nephronophthisis, and obesity, to name a few (Reiter et al. 2017). Our understanding of cilia function in adult tissues is incomplete, and so there is a surge in focus on researching how cilia gene mutations cause the development of ciliopathies. Characterizing the function of cilia in adult tissues has been hampered by gestational lethality of cilia mutations (Kasarskis et al. 1998). The lethality can be bypassed through conditional alleles under control of cell type specific or inducible promoters. An alternate route is to make non-lethal targeted mutations in cilia genes using CRISPR/Cas9 technology.

5.2.1 Cilia dysfunction is linked to the formation of kidney cysts and kidney disease

Polycystic kidney disease (PKD) is an enlargement of the nephron lumens, caused by fluid buildup, resulting in cyst formation and growth. The consequence is a chronic and progressive loss of kidney function, resulting in end stage renal disease and death (Bergmann et al. 2018; Harris et al. 2009). The lumens that form kidney cysts contain mechanosensitive primary cilia that are responsible for detecting fluid flow through the lumen (Singla et al. 2006). In the kidney, disruptions in cilia and ciliary genes drives cystogenesis through a pathway that is still unclear, but some suppose it is due to a loss of nephron quiescence (Li et al. 2007). The majority of PKD patients have mutations in one of two kidney genes, *PKD1* and *PKD2*, which encode the cilia-localized polycystic proteins PC1 and PC2, respectively(Mochizuki et al. 1996; Cornec-Le Gall et al. 2018; Boettger et al. 2012). Both PC1 and PC2 are required for the suppression of the yet unidentified cilia-dependent cyst activation (CDCA) factor or pathway (Ma et al. 2013; Legué et al. 2019; Ma et al. 2019; Ma et al. 2017). The CDCA is thought to function through cilia because cyst formation from deletion of *PKD1* or *PKD2* can be suppressed when cilia are concomitantly removed (Ma et al. 2013). More recently, evidence linking the CDCA to cilia came from an

analysis of a cilia-excluded form of PC2 that permitted the formation of severe renal cysts (Walker et al. 2019). Thus, PC2 must be in cilia to exert control over the CDCA. Identification of the CDCA has been hampered by the difficulty of uncoupling cilia proteins from their localization to cilia, without removing them entirely.

ARL13B is a ciliary GTPase, and patients with mutations in *ARL13B* develop Joubert Syndrome, a ciliopathy that can be caused by more than 35 different cilia genes (Kniffin 10/30/2018). Kidney dysfunction and nephronophthisis is common among Joubert Syndrome patients, but no *ARL13B* patients with kidney dysfunction have been identified (Doherty 2009). Patients with Joubert Syndrome are often children and so the possibility of them developing kidney dysfunction in the future cannot be ruled out (Cantagrel et al. 2008). In contrast, zebrafish and mouse models have clearly implicated ARL13B in normal kidney development and function (Duldulao et al. 2009; Seixas et al. 2016; Sun et al. 2004; Li et al. 2016b). In mouse, conditional deletion of *Arl13b* in the nervous system and kidneys causes severe cyst formation. Moreover, the nephron cells that typically have cilia are unciliated following *Arl13b* deletion (Seixas et al. 2016). The complete loss of cilia in kidney is unexpected as *Arl13b* deletion in other tissues causes short cilia but does not ablate cilia entirely (Caspary et al. 2007; Larkins et al. 2011). This difference in phenotype suggests ARL13B may play a distinct role in kidney compared to other tissue types, a concept supported by the differential regulation of ARL13B by cilia trafficking protein TULP3 (Badgandi et al. 2017). In kidney, TULP3 targets ARL13B to cilia, but not in other tissues (Legué et al. 2019; Hwang et al. 2019; Han et al. 2019). Loss of *Tulp3* also excludes PC1/2 from cilia, but concomitant loss of *Tulp3* and *Pkd1* suppresses the severe cyst formation caused by loss of *Pkd1* alone (Hwang et al. 2019; Legué et al. 2019). Thus, TULP3 regulation of the CDCA implicates the ciliary localization of ARL13B.

5.2.2 Mutations to cilia genes can cause obesity

Mouse models of ciliopathies often show cystic kidney phenotypes that can be slow growing or severe if organism wide. However, if the deletion occurs after weaning age, it can often lead to excessive weight gain in adults (Li et al. 2007; Guo et al. 2011; Heydet et al. 2013; Jacobs et al. 2016). The most widely known ciliopathy linked to obesity is Bardet-Biedl syndrome (BBS), caused by mutations in genes that encode the BBSome. The BBSome is an octameric protein complex involved in the dynamic shuttling of ciliary proteins and GPCRs out of cilia (Slavotinek et al. 2000; Ansley et al. 2003; Zaghloul et al. 2009; Guo et al. 2011; Forsythe et al. 2013; Loktev et al. 2013). BBS patients are obese due to excessive caloric intake, suggesting that there is a neurological cause for their hyperphagia. In simplest terms, obesity is caused by a caloric intake that far exceeds energy expenditure. Patients that are obese will also often have diabetes because of their excessive weight and/or poor diet. Still, there are several factors that can lead to obesity and diabetes, genetic and environmental.

Signals of satiety largely originate in the periphery, but they act centrally to control feeding behaviors (Chambers et al. 2013). Neurons in the hypothalamic arcuate nucleus, POMC and AgRP, are responsible for receiving and coordinating anorexigenic and orexigenic signals (Cowley et al. 2001). Like most adult neurons, the hypothalamic neurons controlling satiety also have primary cilia. In mice, genetic ablation of cilia in POMC neurons (via *Kif3a* deletion) causes excessive weight gain (Davenport et al. 2007). The cilia of hypothalamic neurons typically contain GPCRs with established function in satiety and metabolism signaling, such as MCHR1, SSTR3, and leptin receptors (Handel et al. 1999; Berbari et al. 2008a; Berbari et al. 2008b; Schulz et al. 2000). Clearly, cilia are part of the homeostatic response these cells exert in response to satiety signals,

but their function in these neural networks and signaling pathways is still being deciphered. GTPases are commonly involved in membrane trafficking pathways and ARL13B is known to regulate the trafficking of Shh pathway components (Larkins et al. 2011; Barral et al. 2012; Gotthardt et al. 2015; Lim et al. 2011). To date, there is only one Joubert Syndrome patient with mutation in *ARL13B* that also presented with obesity (Thomas et al. 2015). Obesity is not commonly linked to Joubert Syndrome but is common in other ciliopathies. One of the causal genes is *BBS3* which encodes the cilia protein ARL6 (Chiang et al. 2004). So, while the link between cilia and obesity is clear and other Arl proteins have been implicated, how ARL13B contributes to the regulation of satiety signals is unknown.

In this chapter, I detail my preliminary investigation of the phenotypes I observed in the *Arl13b*$^{V358A/V358A}$ and *Arl13b*$^{V358A/hnn}$ mutant mice: cystic kidneys and obesity.

5.3 Results

5.3.1 Early characterization of cystic kidney phenotypes in *Arl13b*^{V358A} mutant mice

Conditional deletion of *Arl13b* before P14 causes large kidney cysts and early lethality, as well as a complete loss of kidney cilia (Seixas et al. 2016). To test whether ARL13B is required in cilia for the proper formation of kidney cilia and normal regulation of kidney function I examined kidneys in *Arl13b*$^{V358A/V358A}$ and *Arl13b*$^{V358A/hnn}$ mice. I observed enlarged kidneys in adult, but not in young mice, suggesting the presence of slow growing or late onset kidney cysts. Upon cross section I discovered an expansion of the renal cortex caused by cystic features (**Figure 5.1A**). Cystic index often appeared worse in *Arl13b*$^{V358A/hnn}$ mice, and in some cases, cysts are visible on the surface of the kidney. Through measurement of kidney weights, I found that kidneys in female mutant mice weighed more than their control counterparts, but this difference is not

detected in males (**Figure 5.1B**). Next, I examined kidney cilia to determine whether the kidney cysts are a consequence of lost cilia. In the kidneys of *Arl13b*$^{V358A/+}$control animals, I observed acetylated α-tubulin and ARL13B positive cilia. However, In *Arl13b*$^{V358A/hnn}$ kidneys I observed acetylated α-tubulin positive cilia, but no ARL13B^{V358A} is detectable in those cilia (**Figure 5.2**). These data suggest that ARL13B has a cilia-specific function in kidneys that is lost in *Arl13b*$^{V358A/V358A}$ and *Arl13b*$^{V358A/hnn}$ mutant mice. Moreover, the severity of the cystic phenotype in *Arl13b*$^{V358A/hnn}$ mutants suggests a dosage effect of ARL13B^{V358A}.

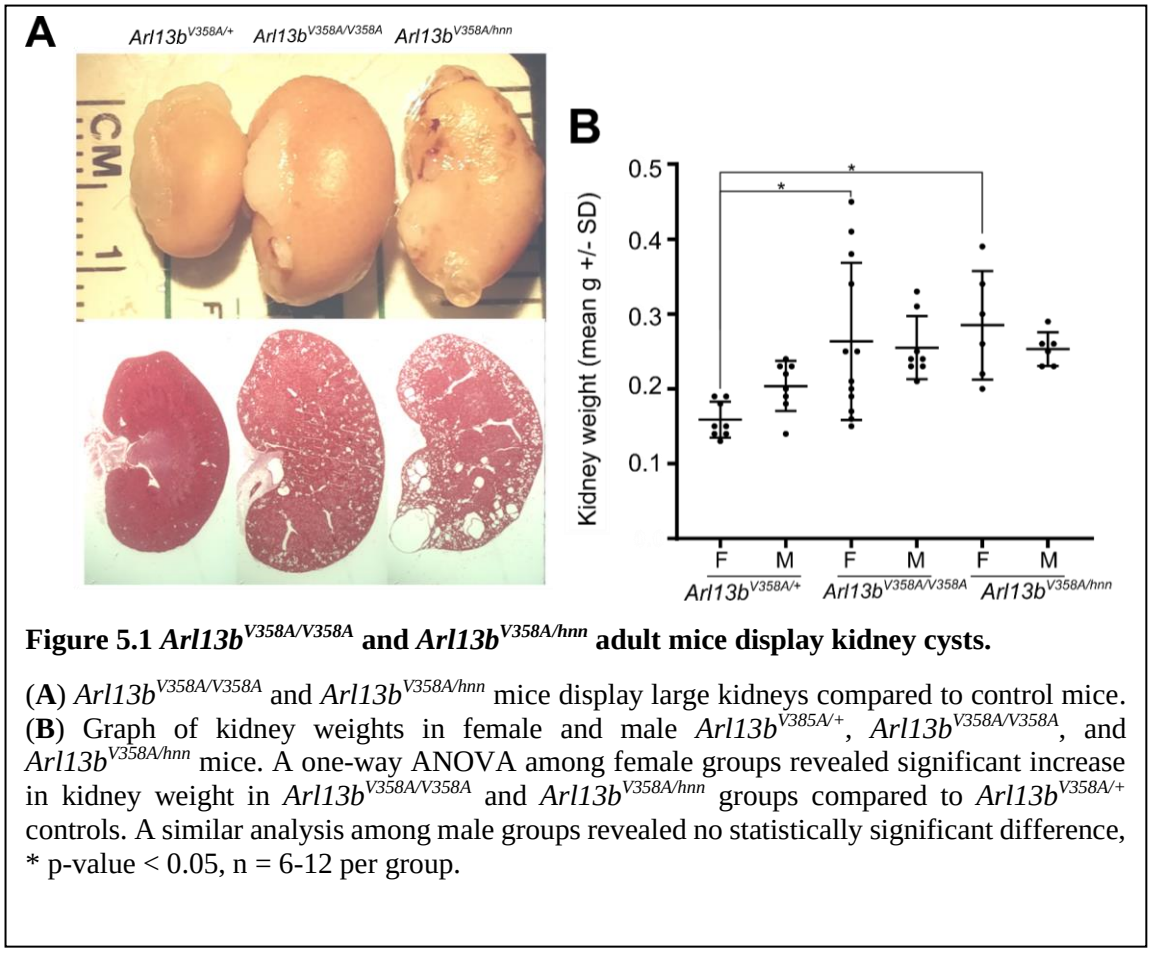

Figure 5.1 *Arl13b*$^{V358A/V358A}$ and *Arl13b*$^{V358A/hnn}$ adult mice display kidney cysts.

(**A**) *Arl13b*$^{V358A/V358A}$ and *Arl13b*$^{V358A/hnn}$ mice display large kidneys compared to control mice. (**B**) Graph of kidney weights in female and male *Arl13b*$^{V385A/+}$, *Arl13b*$^{V358A/V358A}$, and *Arl13b*$^{V358A/hnn}$ mice. A one-way ANOVA among female groups revealed significant increase in kidney weight in *Arl13b*$^{V358A/V358A}$ and *Arl13b*$^{V358A/hnn}$ groups compared to *Arl13b*$^{V358A/+}$ controls. A similar analysis among male groups revealed no statistically significant difference, * p-value < 0.05, n = 6-12 per group.

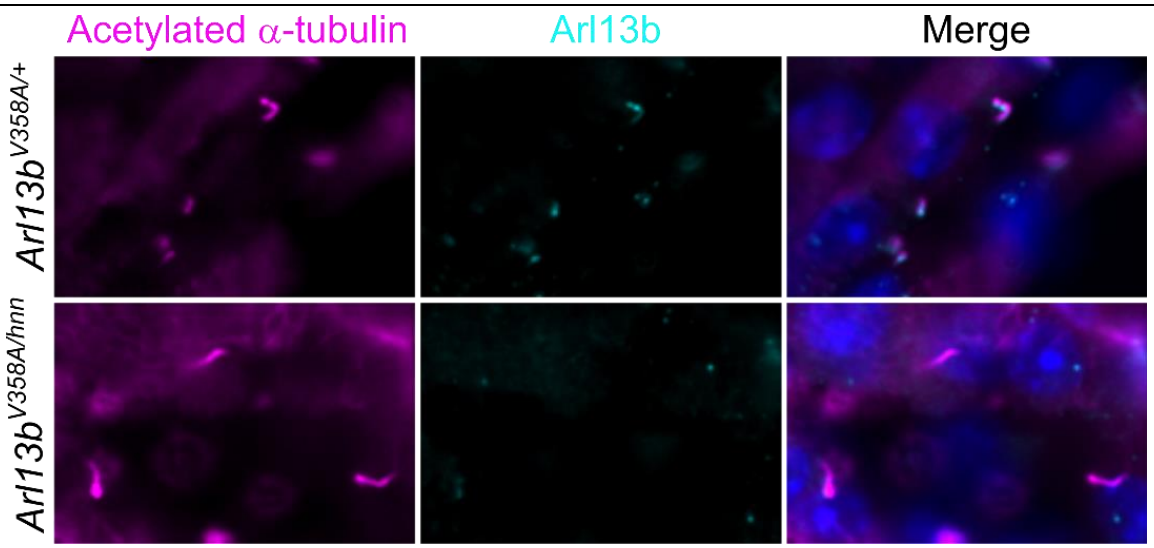

Figure 5.2 *Arl13b*$^{V358A/hnn}$ kidneys have cilia but lack ciliary Arl13b.

Arl13b$^{V358A/hnn}$ mice retain their kidney cilia. Cilia marker is acetylated α-tubulin (anti-mouse) in magenta and ARL13B (anti-rabbit) is in cyan. Images are from a single experiment that was not repeated.

5.3.2 Female and Male *Arl13b*^{V358A} mutants weigh significantly more than control mice

I observed that adult *Arl13b*$^{V358A/V358A}$ mice appeared to weigh more than their wildtype and heterozygous littermates. To test this, I tracked mouse weights weekly from postnatal day (P)21 to P105, or week 3 to week 15 with mice maintained on standard mouse chow with 5% fat content. In both groups, I observed some separation in weights that began around week 10. These preliminary data are not suitable for statistical testing, but the trend suggested that female and male *Arl13b*$^{V358A/V358A}$ mice gain more weight than their littermate controls (**Figure 5.3**).

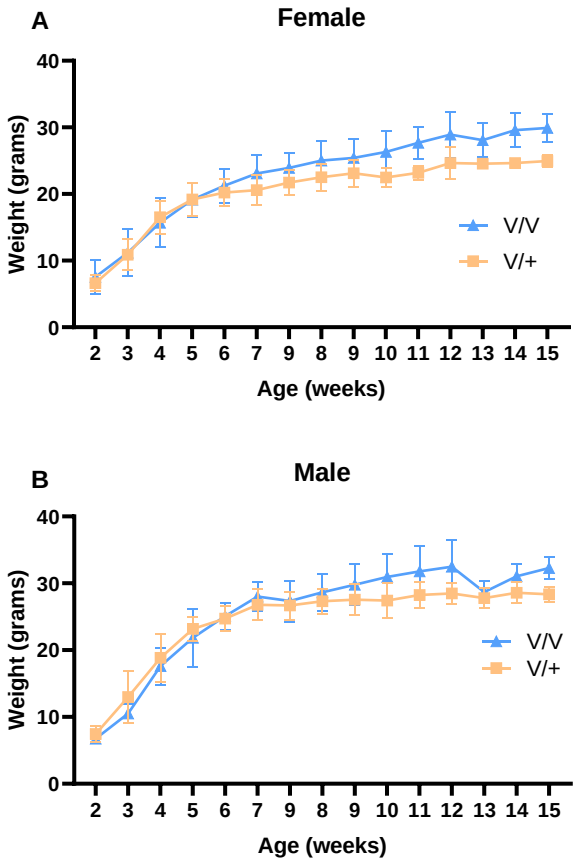

Figure 5.3 *Arl13b*$^{V358A/V358A}$ mice on standard chow gain more weight than heterozygous controls.

Preliminary weight data generated with (A) female and (B) male *Arl13b*$^{V358A/+}$ (*V/+*) and *Arl13b*$^{V358A/V358A}$ (*V/V*) mice maintained on standard chow. The weight phenotype was subtle when mice are maintained on standard chow. This data is preliminary, and its collection was sporadic, therefore it is not suitable for analysis (or publication). It was early evidence that homozygous *Arl13b*$^{V358A/V358A}$ mice were gaining more weight than their control littermates.

To better understand this phenomenon, I placed a second cohort of mice on a higher fat breeder chow diet, raising the fat percentage from 5% to 9%. Due to the higher fat content of the food mice I predicted mice would gain weight faster. In this experiment, I separated all mice by sex and genotype; tracking weights of female and male *Arl13b*$^{+/+}$, *Arl13b*$^{V358A/+}$, and *Arl13b*$^{hnn/+}$ controls, and *Arl13b*$^{V358A/V358A}$ and *Arl13b*$^{V358A/hnn}$ mutant mice (**Figure 5.4 A, B**). There are no

reports of *Arl13b*$^{hnn/+}$ mice presenting with obesity phenotypes, so it is important to track the weights of these mice separate from *Arl13b*$^{+/+}$ and *Arl13b*$^{V358A/+}$ mice (Caspary et al. 2007). As predicted, mice on higher fat mouse chow gained weight faster, and differences between control and mutant groups emerged earlier. Furthermore, at no point during this experiment did *Arl13b*$^{+/+}$, *Arl13b*$^{V358A/+}$, and *Arl13b*$^{hnn/+}$ controls differ in weight for either sex.

In the female cohort, at 5 weeks postnatal, control mice weighed between 19 and 20 grams, and *Arl13b*$^{V358A/V358A}$ mice weighed 22.4 grams (± 4.18), more than *Arl13b*$^{+/+}$, but not *Arl13b*$^{V358A/+}$ and *Arl13b*$^{hnn/+}$ controls. *Arl13b*$^{V358A/hnn}$ mice weighed an average of 21.4 grams (± 3.71), which is not higher than weights in *Arl13b*$^{+/+}$, *Arl13b*$^{V358A/+}$, *Arl13b*$^{hnn/+}$ control groups, or *Arl13b*$^{V358A/V358A}$ mutant mice (**Figure 5.4C**). By the end of the study, female *Arl13b*$^{V358A/V358A}$ mice had an average weight of 31.5 grams (± 5.67) and *Arl13b*$^{V358A/hnn}$ mice had an average weight 31.3 grams (± 4.53). Both groups weighed significantly more than *Arl13b*$^{+/+}$, *Arl13b*$^{V358A/+}$, *Arl13b*$^{hnn/+}$ control groups which only weighed between 22 and 24 grams (**Figure 5.4E**).

I observed a similar trend in male mice. At 5 weeks postnatal, control mice weighed between 22 and 24 grams, compared to 28.6 grams (± 4.18) and 26.9 grams (± 3.26) in *Arl13b*$^{V358A/V358A}$ and *Arl13b*$^{V358A/hnn}$ mice, respectively (**Figure 5.4D**). At this stage, *Arl13b*$^{V358A/V358A}$ and *Arl13b*$^{V358A/hnn}$ mice weighed more than *Arl13b*$^{+/+}$, *Arl13b*$^{V358A/+}$, and *Arl13b*$^{hnn/+}$ controls. The increased weight measured in *Arl13b*$^{V358A/V358A}$ and *Arl13b*$^{V358A/hnn}$ mice persisted throughout the remainder of the time course. By week 10, control mice weighed between 27 and 29 grams, compared to 37.5 grams (± 4.85) and 38.1 grams (± 4.40) in *Arl13b*$^{V358A/V358A}$ and *Arl13b*$^{V358A/hnn}$ mice, respectively. As with previous weeks, both *Arl13b*$^{V358A/V358A}$ and *Arl13b*$^{V358A/hnn}$ groups weighed significantly more than *Arl13b*$^{+/+}$, *Arl13b*$^{V358A/+}$, and *Arl13b*$^{hnn/+}$

controls (**Figure 5.4F**). Furthermore, at no point did I measure differences between *Arl13b*$^{V358A/V358A}$ and *Arl13b*$^{V358A/hnn}$ mice. Together, these data suggest that regardless of sex, *Arl13b*$^{V358A/V358A}$ and *Arl13b*$^{V358A/hnn}$ mice gain significantly more weight than their littermate controls, and that these differences can emerge as early as 5 weeks postnatal. Moreover, *Arl13b*$^{V358A/V358A}$ mice do not weigh more during pre-weaning stages, differences only emerged after weaning. Therefore, *Arl13b*$^{V358A/V358A}$ and *Arl13b*$^{V358A/hnn}$ mice only gain more weight once they can self-feed on mouse chow. This would be consistent with obesity induced by overeating, or hyperphagia. Data in this section are presented as mean (± standard deviation).

Figure 5.4 *Arl13b*$^{V358/V358A}$ and *Arl13b*$^{V358A/hnn}$ mice gain more weight than heterozygous or wildtype controls.

Mice maintained on breeder chow diet were weighed weekly from postnatal day (P)21 to P70. (**A**) Average weight of female *Arl13b*$^{+/+}$(+/+), *Arl13b*$^{V358A/+}$(*V*/+), *Arl13b*$^{hnn/+}$ (*h*/+), *Arl13b*$^{V358A/V358A}$ (*V/V*), and *Arl13b*$^{V358A/hnn}$ (*V/h*) mice over time. The n per group is depicted next to each genotype. (**B**) Average weight of male *Arl13b*$^{+/+}$(+/+), *Arl13b*$^{V358A/+}$(*V*/+), *Arl13b*$^{hnn/+}$ (*h*/+), *Arl13b*$^{V358A/V358A}$ (*V/V*), and *Arl13b*$^{V358A/hnn}$ (*V/h*) mice over time. (**C**) Female and (**D**) male weigh data from postnatal week 5 represented in bar graph form. Control mice did not differ in weight at any time point for either sex. In females, *Arl13b*$^{V358A/V358A}$ mice weighed more than control *Arl13b*$^{+/+}$ mice. In contrast, male *Arl13b*$^{V358A/V358A}$ mice were heavier than all control groups (represented by ***), and *Arl13b*$^{V358A/hnn}$ mice weighed more than *Arl13b*$^{+/+}$ and *Arl13b*$^{V358A/+}$groups, but not *Arl13b*$^{hnn/+}$mice (represented by **). (**E**) Female and (**F**) male weigh data from postnatal week 10 represented in bar graph form. Control mice did not differ in weight at any time point for either sex. In females, *Arl13b*$^{V358A/V358A}$ and *Arl13b*$^{V358A/hnn}$ mice weighed more than control groups (represented by ***). A similar outcome in males, *Arl13b*$^{V358A/V358A}$ and *Arl13b*$^{V358A/hnn}$ mice were heavier than all control groups (represented by ***). The n per group is depicted next to each genotype. Bar graph data analyzed by one-way ANOVA with Tukey's test for multiple comparisons. Significance determined by p-value < 0.05, ns is not significant.

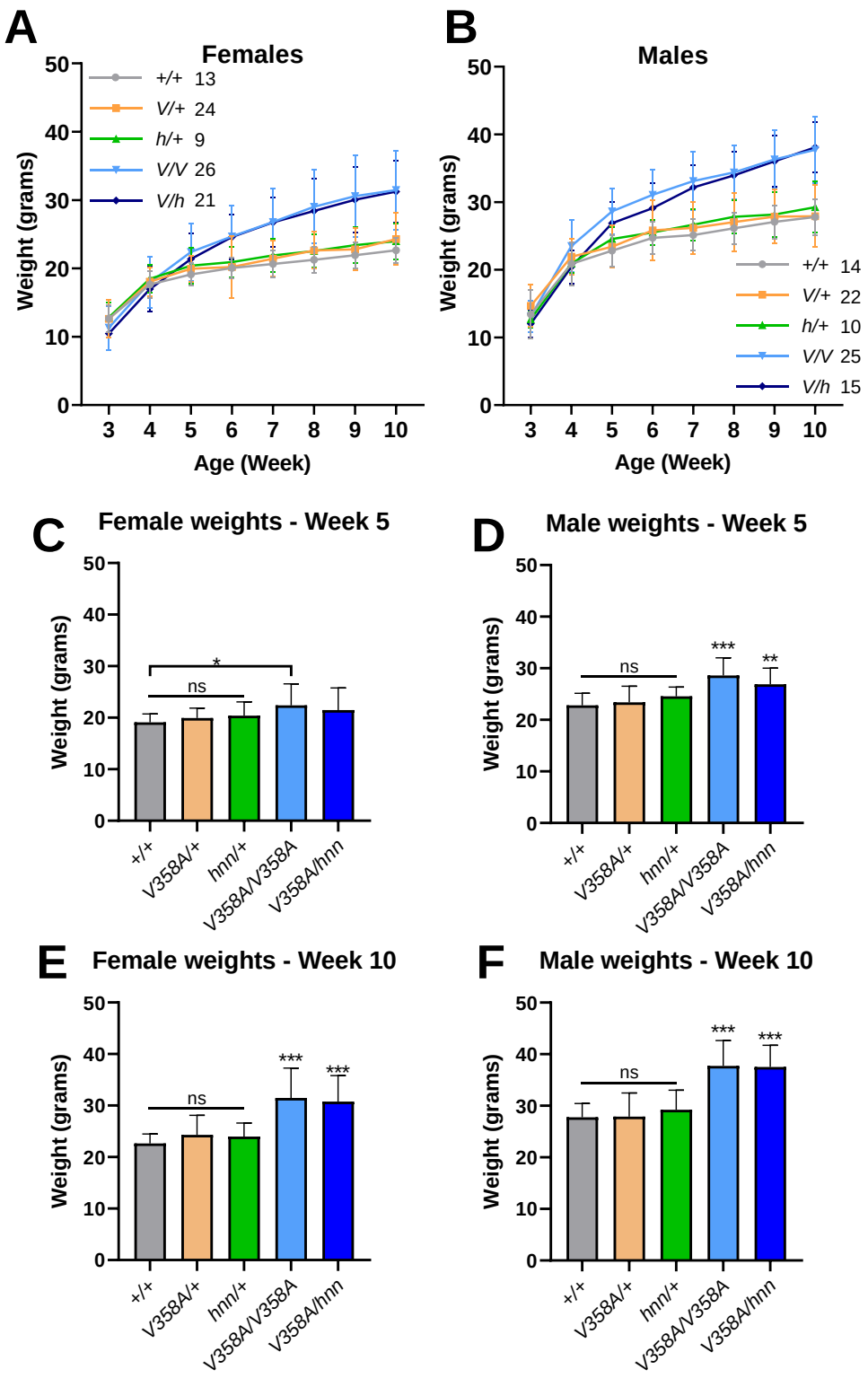
A
Females
+/+ 13
V/+ 24
h/+ 9
V/V 26
V/h 21
Weight (grams)
Age (Week)
B
Males
+/+ 14
V/+ 22
h/+ 10
V/V 25
V/h 15
Weight (grams)
Age (Week)
C
Female weights - Week 5
Weight (grams)
*
ns
+/+
V358A/+
hnn/+
V358A/V358A
V358A/hnn
D
Male weights - Week 5
Weight (grams)
ns
***
**
+/+
V358A/+
hnn/+
V358A/V358A
V358A/hnn
E
Female weights - Week 10
Weight (grams)
ns
***
***
+/+
V358A/+
hnn/+
V358A/V358A
V358A/hnn
F
Male weights - Week 10
Weight (grams)
ns
***
***
+/+
V358A/+
hnn/+
V358A/V358A
V358A/hnn

5.3.3 *Arl13b*^{V358A} carrying mice have impaired glucose tolerance

Because of the observed increases in weight I next wanted to test homeostatic responses in fasted *Arl13b*$^{V358A/V358A}$ and *Arl13b*$^{V358A/hnn}$ mice following a glucose bolus. Mice are fasted overnight for 15-18 hours with access to only water. The following day I acquired a baseline blood glucose level before administering a 1.0 g/kg dose of 0.25g/mL D-Glucose i.p. Comparing baseline, fasted blood glucose levels, female *Arl13b*$^{V358A/V358A}$ mice trended toward higher levels compared to controls, an average of 115.9 mg/dL (± 23.2) compared to 91.9 (± 12.0) mg/dL in controls. In contrast, *Arl13b*$^{V358A/hnn}$ mice had blood glucose levels higher than controls, an average of 128.5 mg/dL (± 38.0) (**Figure 5.5A**). In the male cohort, I measured increased blood glucose levels in *Arl13b*$^{V358A/hnn}$ mice, 151.8 mg/dL (± 32.9) compared to 106.2 mg/dL (± 297.8) in controls (**Figure 5.5B**). In both sexes, *Arl13b*$^{V358A/V358A}$ mice did not have higher baseline blood glucose levels compared to controls. Therefore, the measured increase in *Arl13b*$^{V358A/hnn}$ mice above controls suggests a possible dosage effect of ARL13B^{V358A}.

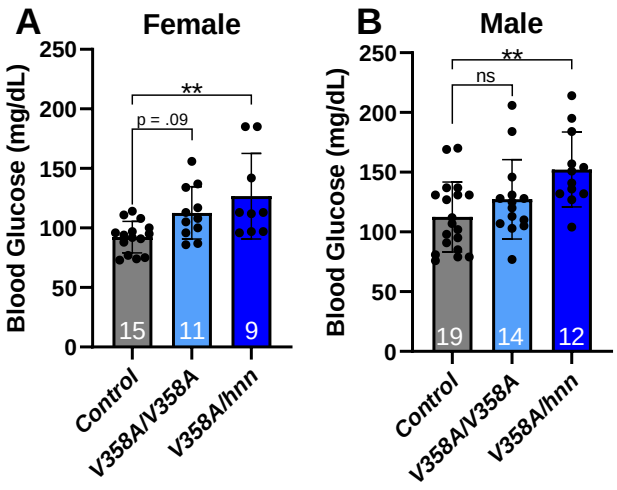

Figure 5.5 Comparisons of fasted, baseline blood glucose levels in female and male mice after overnight fast.

(A) In females, *Arl13b*$^{V358A/hnn}$ mice have higher resting blood glucose levels compared to controls, and *Arl13b*$^{V358A/V358A}$ mice presented with only a trend towards higher levels. (B) In male cohorts, I measured similar outcomes, no differences between *Arl13b*$^{V358A/V358A}$ mice and controls, but an increase in *Arl13b*$^{V358A/hnn}$ mice. These data include fasted levels from mice in 2.0 g/kg experiments (Figure 5.4) and mice from 1.0 g/kg experiments (Figure 5.6). Data are presented as bar graphs with a scatter plot of each data point overlay, separated into female and male cohorts. The n for each group is depicted at the base of each bar. Error bars represent standard deviation. Data analyzed by one-way ANOVA and Tukey's post-hoc. P value < 0.05 *, ns = not significant.

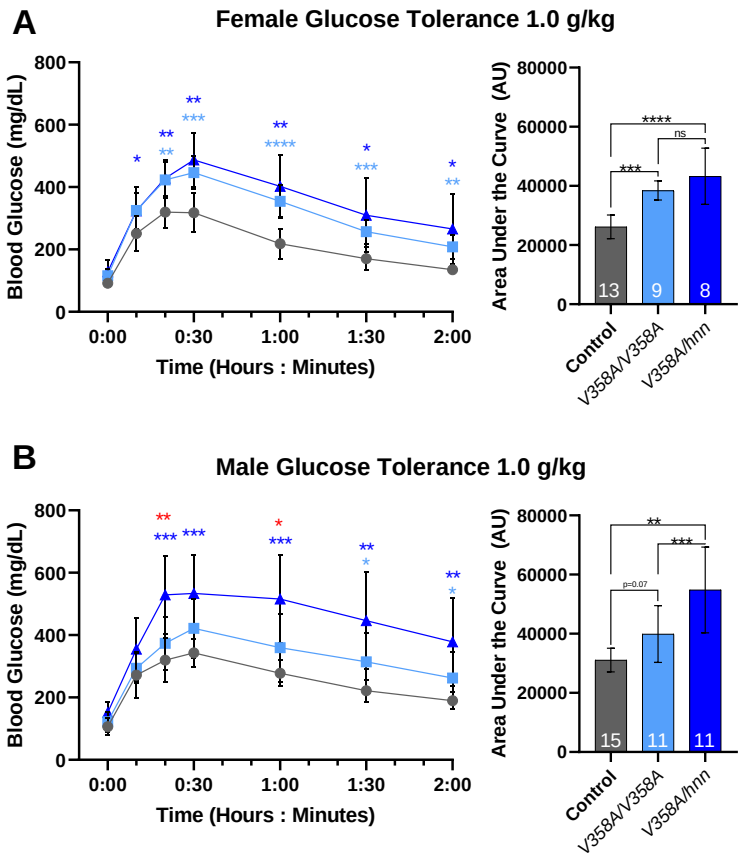

Figure 5.6 *Arl13b*$^{V358A/V358A}$ and *Arl13b*$^{V358A/hnn}$ mice have impaired glucose tolerance.

Glucose tolerance was tested the morning after an overnight fast, 15-18 hours. Baseline blood glucose levels were established at time 0:00 (hours : minutes), before mice received a 1.0 g/kg intraperitoneal (i.p.) bolus of D-glucose. (A) Blood glucose levels of female control, *Arl13b*$^{V358A/V358A}$ (*V358A/V358A*), and *Arl13b*$^{V358A/hnn}$ (*V358A/hnn*) mice over the 2-hour time course and a trapezoidal area under the curve (AUC) analysis of blood glucose data. In *Arl13b*$^{V358A/V358A}$ and *Arl13b*$^{V358A/hnn}$ mice, blood glucose levels were significantly higher than control mice through the time course, but there was no difference between the two mutant groups. (B) Blood glucose levels of male control, *Arl13b*$^{V358A/V358A}$ (*V358A/V358A*), and *Arl13b*$^{V358A/hnn}$ (*V358A/hnn*) mice over the 2-hour time course and a trapezoidal AUC analysis of blood glucose data. As in the female cohort, mutant *Arl13b*$^{V358A/V358A}$ and *Arl13b*$^{V358A/hnn}$ displayed altered sensitivity to glucose. Overall, *Arl13b*$^{V358A/hnn}$ mice had blood glucose levels higher than *Arl13b*$^{V358A/V358A}$ and control groups. In contrast, *Arl13b*$^{V358A/V358A}$ displayed only a trend towards higher levels compared to controls. Control groups are a combination of *Arl13b*$^{+/+}$, *Arl13b*$^{V358A/+}$, and *Arl13b*$^{hnn/+}$ mice, as no obesity phenotype was observed (Figure 5.3), and blood glucose levels did not differ at any time point in this study between the three groups. The n per group is depicted at the bottom of each respective bar. Blood glucose time course analyzed by two-way repeated measures ANOVA and Tukey's post-hoc test for comparisons between genotypes at each time point. For p-values, asterisks in blue corresponding to genotype represent differences between the respective mutant group and the control group. Asterisks in red correspond to significant differences between mutant groups. Blood glucose response AUC data analyzed by one-way ANOVA with Tukey's post-hoc. Error bars represent standard deviation. For p-values ** < 0.01, *** < 0.001, **** < 0.0001, ns is not significant.

To test the homeostatic response to a glucose bolus, I monitored blood glucose levels over a two-hour time course. I observed that control mice typically reach peak blood glucose levels 20-30 minutes post-injection, after which levels gradually decline back near baseline by 2 hours post-injection. In the female cohort, I found *Arl13b*$^{V358A/V358A}$ and *Arl13b*$^{V358A/hnn}$ mice had significantly higher blood glucose levels compared to controls at nearly every time point measured. However, at no point did *Arl13b*$^{V358A/V358A}$ and *Arl13b*$^{V358A/hnn}$ differ from each other. Overall, I measured increased blood glucose levels in *Arl13b*$^{V358A/V358A}$ and *Arl13b*$^{V358A/hnn}$ mice compared to controls, and no differences between *Arl13b*$^{V358A/V358A}$ and *Arl13b*$^{V358A/hnn}$ mice (**Figure 5.6A**). In the male cohort, only *Arl13b*$^{V358A/hnn}$ mice had significantly higher blood glucose levels compared to controls. Furthermore, and in contrast with the female group, I measured increased blood glucose levels in *Arl13b*$^{V358A/hnn}$ mice compared to *Arl13b*$^{V358A/V358A}$ mice at the 20 and 60-minute time points. Overall, I measured a significant increase in blood glucose levels in *Arl13b*$^{V358A/hnn}$ mice compared to controls and a trend towards significance in a comparison of *Arl13b*$^{V358A/V358A}$ to controls. Moreover, blood glucose levels are overall higher in *Arl13b*$^{V358A/hnn}$ compared to *Arl13b*$^{V358A/V358A}$ animals (**Figure 5.6B**). These data represent a significant impairment of homeostatic maintenance of blood glucose levels in *Arl13b*$^{V358A/V358A}$ and *Arl13b*$^{V358A/hnn}$ mice and is consistent with hyperglycemia (Lutz et al. 2012). Moreover, they support the possibility of a dosage effect and more severe phenotype in *Arl13b*$^{V358A/hnn}$ mice.

5.3.4 *Arl13b*^{V358A} carrying mice have impaired insulin response

Due to the increased weight and impaired glucose tolerance, I next wanted to determine whether the mice showed impaired insulin response. Mice are fasted for 2-3 hours before baseline blood glucose levels are taken and a 0.75 U/kg dose of insulin is administered. Control mice

responded as expected, insulin caused blood glucose levels to drop, reaching their lowest levels around 60 minutes post-injection At the 60-minute time point blood glucose levels in controls dropped an average of ~100 mg/dL, from 189 mg/dl to 82.5 mg/dl (**Figure 5.7A**). In contrast, insulin had a reduced affect in *Arl13b*$^{V358A/V358A}$ and *Arl13b*$^{V358A/hnn}$ females. At the 30-minute time point blood glucose reached their lowest levels of ~160 mg/dl before rebounding back to baseline by 60-minutes post injection. In a comparison between genotypes I found that overall blood glucose levels in *Arl13b*$^{V358A/V358A}$ and *Arl13b*$^{V358A/hnn}$ groups are higher than control and measured no differences between *Arl13b*$^{V358A/V358A}$ and *Arl13b*$^{V358A/hnn}$ mice (**Figure 5.7B**). Together, these data suggest that female *Arl13b*$^{V358A/V358A}$ and *Arl13b*$^{V358A/hnn}$ mice have retained some sensitivity to insulin, but this response is impaired. In the male cohort, control mice responded normally to insulin. I measured reduced blood glucose levels at 15-minutes post-insulin, decreased from 218 mg/dl to 182 mg/dl (± 33.2) and by 45-minutes levels decreased ~100 mg/dl from baseline, 218 mg/dl compared to 117 mg/dl (± 25.7). Unexpectedly, I measured *increases* in blood glucose levels post-insulin in *Arl13b*$^{V358A/V358A}$ and *Arl13b*$^{V358A/hnn}$ male mice, relative to their baseline levels and levels in the control group. Furthermore, I measured higher blood glucose levels in *Arl13b*$^{V358A/hnn}$ mice compared to *Arl13b*$^{V358A/V358A}$ mice (**Figure 5.7D**). These data suggest that in males, the biological response to insulin has been dramatically reversed and results in a release of glucose into the blood. Furthermore, differences between *Arl13b*$^{V358A/V358A}$ and *Arl13b*$^{V358A/hnn}$ male mice support a possible dosage effect.

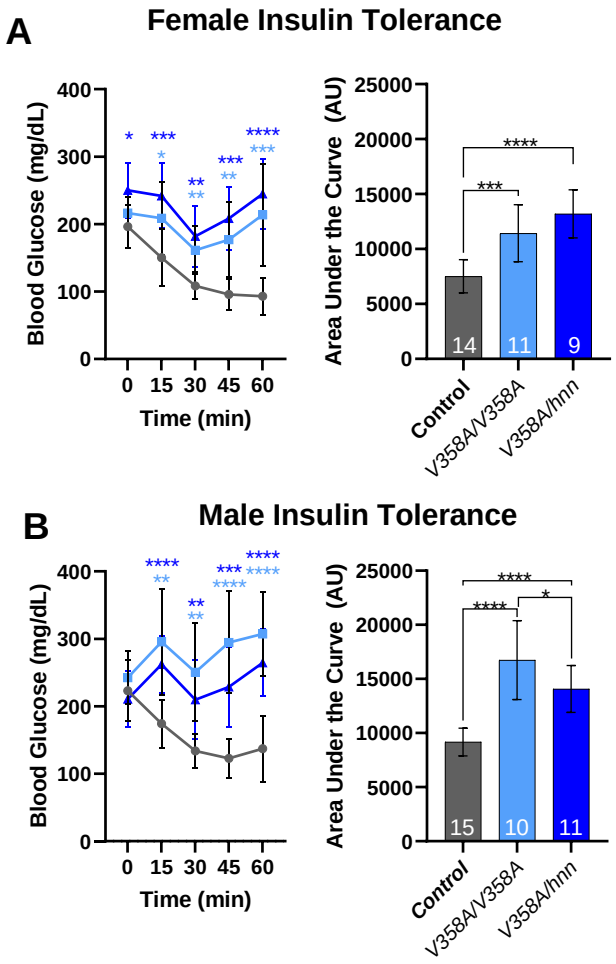

Figure 5.7 *Arl13b*$^{V358A/hnn}$ and *Arl13b*$^{V358A/hnn}$ mice have impaired insulin response.

Insulin tolerance was tested the morning after a 2-3 hour fast. Baseline blood glucose levels were established at time 0 (minutes) before mice received a 0.75 U/kg intraperitoneal (i.p.) bolus of insulin. (A) Blood glucose levels of female control, *Arl13b*$^{V358A/V358A}$ (*V358A/V358A*), and *Arl13b*$^{V358A/hnn}$ (*V358A/hnn*) mice over the 60-minute time course and trapezoidal area under the curve (AUC) analysis. Overall, *Arl13b*$^{V358A/V358A}$ and *Arl13b*$^{V358A/hnn}$ mice had blood glucose levels significantly higher than controls. (B) Blood glucose levels of male control, *Arl13b*$^{V358A/V358A}$ (*V358A/V358A*), and *Arl13b*$^{V358A/hnn}$ (*V358A/hnn*) mice over the 60-minute time course and trapezoidal AUC analysis. Overall, *Arl13b*$^{V358A/V358A}$ and *Arl13b*$^{V358A/hnn}$ mice had blood glucose levels significantly higher than controls, with no difference between the two mutant groups. However, analysis by AUC revealed a small difference between the two groups. Control groups are a combination of *Arl13b*$^{+/+}$, *Arl13b*$^{V358A/+}$, and *Arl13b*$^{hnn/+}$ mice, as no obesity phenotype was observed, and blood glucose levels did not differ between the three groups. The n per group is depicted at the bottom of each respective bar. Time course data analyzed by two-way repeated measures ANOVA and Tukey's post-hoc, AUC data analyzed by one-way ANOVA with Tukey's post-hoc. Error bars represent standard deviation. For p-values, asterisks in blue corresponding to genotype represent differences between the respective mutant group and the control group. P-values * < 0.05, ** < 0.01, *** < 0.001, **** < 0.0001.

5.3.5 Analysis of ARL13B expression in mouse embryos

In my experiments I often observed cystic kidney and obesity severity increased in *Arl13b*$^{V358A/hnn}$ mice compared to *Arl13b*$^{V358A/V358A}$ animals. To understand the possibility of a dose effect by cilia-excluded ARL13B^{V358A}, I examined ARL13B protein expression by western blot. I previously reported data from E10.5 whole embryo lysates showing that ARL13B expression is decreased in *Arl13b*$^{V358A/+}$ and *Arl13b*$^{V358A/V358A}$ embryos compared to *Arl13b*$^{+/+}$ controls (Chapter 4) (Gigante et al. 2020a). Consistent with these data, I measured ARL13B expression in *Arl13b*$^{V358A/+}$ embryos that is 93% of *Arl13b*$^{+/+}$ controls, compared to ~76% of control in *Arl13b*$^{V358A/V358A}$ mutant embryos. Furthermore, in *Arl13b*$^{hnn/+}$ embryo, a heterozygous null, I measured decreased ARL13B expression at ~50% of *Arl13b*$^{+/+}$ controls. *Arl13b*$^{hnn/+}$ mice are

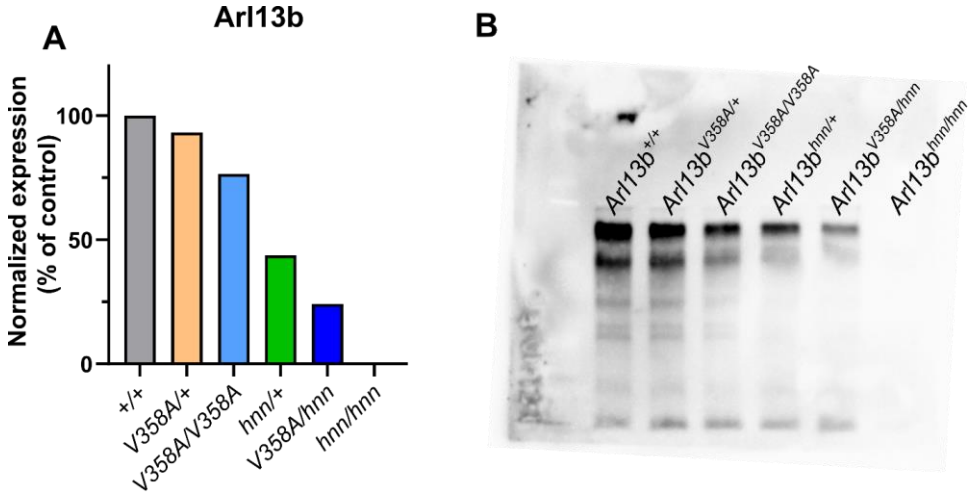

Figure 5.8 ARL13B protein expression in embryonic day E10.5 whole embryo lysates.

(A) ARL13B protein expression levels normalized to wildtype (*Arl13b*$^{+/+}$) control. Protein expression is reduced in *Arl13b*$^{V358A/+}$ and *Arl13b*$^{V358A/V358A}$ embryos by ~7% and 24%, respectively. Expression is halved in *Arl13b*$^{hnn/+}$ embryos, and again in *Arl13b*$^{V358A/hnn}$ embryos expressing only ~25% of normal levels, compared to no expression in *Arl13b*$^{hnn/hnn}$ embryos. (B) Representative blot for all six genotypes of six embryos collected on the same day from three separate litters. The n for all genotypes = 1, this experiment should be repeated.

viable with no previously reported phenotypes, and I have now shown that they do not develop obesity or cystic kidneys. Therefore, these data suggest that 50% of normal ARL13B expression is sufficient. Finally, in *Arl13b*$^{V358A/hnn}$ embryos I measured expression levels at ~24% of *Arl13b*$^{+/+}$ controls (**Figure 5.8**). This decrease may be due to a change in *ARL13B*^{V358A} stability compared to ciliary ARL13B. Alternatively, ARL13B may have a distinct half-life when localized outside of the ciliary compartment. How a decrease in ARL13B^{V358A} expression, which is already excluded from cilia, is driving more severe phenotypes is unclear. It does suggest some underlying dysfunction in ARL13B^{V358A} in addition to its mislocalization or a cellular function that is sensitive to ARL13B protein levels.

5.3.6 Using c-Fos expression to investigate hypothalamic regions' differential response to insulin

Arl13b^{V358A} mutant mice gain significantly more weight than their wildtype and heterozygous control counterparts (**Figure 5.4**). This difference only emerges once the mice are freely feeding post-weaning, suggesting an overall increase in food intake due to hyperphagia. Food metabolism, and hunger and satiety signals originate in the periphery, but they influence feeding behaviors centrally. To determine if *Arl13b*$^{V358A/V358A}$ mice have differential responses to satiety signals, mice are administered a 0.75 U/kg dose of insulin and I examined hypothalamic regions of interest for c-Fos induction. The c-Fos marker is an immediate early response gene, and in neurons it is used as a marker of neuronal activity in response to peripheral stimulation (Bullitt 1990). Nuclei positive for c-Fos are counted in the paraventricular nucleus (PAV) and arcuate nucleus (ARC) of the hypothalamus. In the PAV, I counted an average of 287 c-Fos positive cells in controls compared to 140 in *Arl13b*$^{V358A/V358A}$ mice. In the ARC, I counted an average of ~38 c-

Fos positive cells in controls, compared to 46 cells in *Arl13b*$^{V358A/V358A}$ mice (**Figure 5.9**). The underlying cause for this change is unknown but are consistent with altered insulin-induced neuronal activity in *Arl13b*$^{V358A/V358A}$ mice.

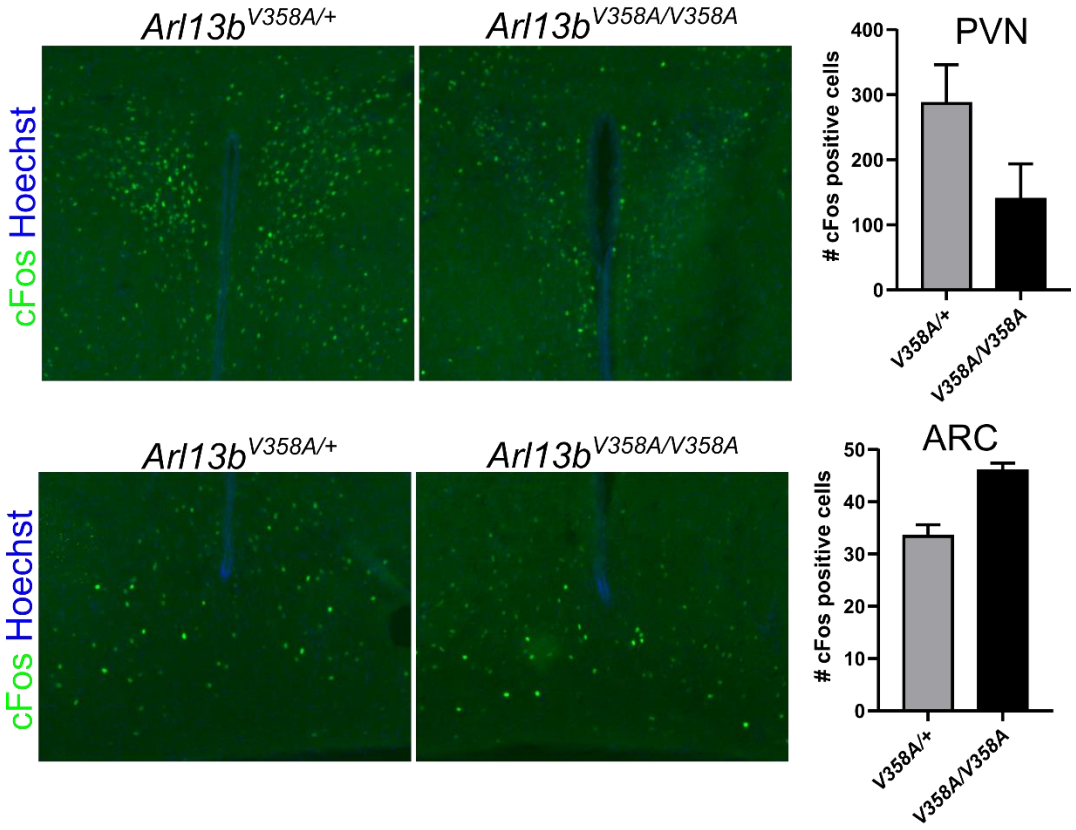

Figure 5.9 Insulin-induced c-Fos expression is altered in *Arl13b*$^{V358A/V358A}$ mice.

In this preliminary experiment, mice were injected with a 0.75 U/kg dose of insulin 90-minutes before perfusion. Brains were sectioned and probed for c-Fos, a marker of neuronal transcriptional activity. Images of hypothalamic regions were isolated and run through a cell counting program in Cell Profiler. Bar graphs are average number of c-Fos positive cells in the paraventricular nucleus (PVN) and arcuate nucleus (ARC). Due to low n (= 2 per genotype) statistical tests were not run on these data.

5.4 Discussion and Future Directions

In this chapter I examined two phenotypes that arise upon excluding ARL13B from cilia. I investigated the formation of slow growing kidney cysts that are not due to a loss of cilia, but the loss of ciliary ARL13B. This clearly points to a ciliary role of ARL13B that is required to prevent

the formation of kidney cysts. I showed that *Arl13b*$^{V358A/V358A}$ and *Arl13b*$^{V358A/hnn}$ mice gain significantly more weight than their control littermates. This weight increase only emerges post-weaning age, suggesting that it is driven by overeating once the mice are free feeding. Furthermore, I show that *Arl13b*$^{V358A/V358A}$ and *Arl13b*$^{V358A/hnn}$ mice have impaired homeostatic maintenance of blood glucose levels in response to a glucose and insulin insult. Together these data suggest that ciliary ARL13B is required for the normal maintenance of blood glucose homeostasis. The underlying mechanism driving either phenotype remains unknown, but it is likely linked to cilia.

5.4.1 ARL13B has a cilia-specific function in kidney to prevent cyst formation

My data support ciliary ARL13B regulation of the yet unknown kidney cyst causing CDCA. There is evidence that ARL13B is differentially regulated in kidney cilia relative to other ciliated tissues. TULP3 is required for ARL13B cilia localization in kidney cilia, but not in other cells (Han et al. 2019). Based on my data here, mislocalization of ARL13B could be partially responsible for the formation of kidney cysts in *Tulp3* mutants (Badgandi et al. 2017; Han et al. 2019; Hwang et al. 2019; Legué et al. 2019). Not only is ARL13B regulated differently in kidney cilia, but it also appears to function differently. In mouse embryos and mouse embryonic fibroblasts (MEFs), loss of *Arl13b* causes short cilia and a microtubule defect in the ciliary axoneme (Caspary et al. 2007; Larkins et al. 2011). In contrast, conditional deletion of *Arl13b* in kidney ablates cilia entirely (Seixas et al. 2016). I previously showed that, like *Arl13b* null cells, *Arl13b*$^{V358A/V358A}$ MEFs also have short cilia, suggesting that ARL13B is required in cilia for normal cilia structure (Chapter 4) (Gigante et al. 2020a). Herein I show that despite this similar phenotype, cilia form normally in the kidneys of *Arl13b*$^{V358A/V358A}$ mutants, but kidney cyst

formation persists. This is consistent with a cilia-specific function of ARL13B regulating the CDCA.

The more severe cystic kidney phenotype observed in *Arl13b*$^{V358A/hnn}$ mice compared to *Arl13b*$^{V358A/V358A}$ mutants is intriguing. Why this is occurring cannot be explained without more data. As discussed above, If ARL13B is required in cilia to regulate the CDCA, then why does expression of one copy of *Arl13b*^{V358A} influence cyst formation? Perhaps there is a ciliary and non-ciliary function of ARL13B in the regulation of the CDCA. The existence of this non-ciliary function would not be detectable in mutants where *Arl13b* is conditionally deleted because it ablates cilia and removes ARL13B cell wide. Moreover, my data suggest that ARL13B function in regulating the CDCA may be influenced by ARL13B protein levels. I observed decreased ARL13B expression in *Arl13b*$^{V358A/hnn}$ mouse embryos, approximately 25% of wildtype and ~50 of levels measured in *Arl13b*$^{V358A/V358A}$ embryos. However, the mouse embryo is far from representative of the adult kidney, and so this experiment could be repeated in the kidney to determine if ARL13B expression is indeed different in *Arl13b*$^{V358A/hnn}$ compared to *Arl13b*$^{V358A/V358A}$ mutants. Regardless, the increased severity of kidney cysts in *Arl13b*$^{V358A/hnn}$ animals with only one copy of *Arl13b*^{V358A} is more evidence that ARL13B is in fact regulating the CDCA.

5.4.2 Could cilia dysfunction in the periphery be contributing to obesity and diabetes in *Arl13b*^{V358A} mutant mice?

The obesity and diabetes phenotypes observed are consistent with previous mouse models of obesity. I observed impaired homeostatic balance of blood glucose levels in *Arl13b*$^{V358A/V358}$ and *Arl13b*$^{V358A/hnn}$ mice in the face of glucose or insulin insult. In fact, *Arl13b*$^{V358A/hnn}$ mice had higher

resting blood glucose levels compared to controls. Both insulin resistance and hyperglycemia are a hallmark of obesity and diabetes caused by hyperphagia in mice (Lutz et al. 2012). Impairment of satiety signaling in *Arl13b*$^{V358A/V358A}$ and *Arl13b*$^{V358A/hnn}$ mutants is unlikely to be specific to dysfunction in the periphery. My data contrast with a *BBS12*$^{-/-}$ mouse model of obesity that displayed classic obesity but had improved glucose and insulin responsiveness compared to their controls. In this model, the obesity phenotype is a result of gene misregulation in adipocytes. This caused overactivation of adipogenic pathways and increased formation of fat tissue and is not due to hyperphagia (Marion et al. 2012). Taken together, my data are consistent with impairment of satiety signaling in *Arl13b*$^{V358A/V358A}$ and *Arl13b*$^{V358A/hnn}$ mice that occurs centrally.

Feeding behavior is controlled centrally, but the metabolism of energy from food occurs in the periphery. Therefore, disruptions in ciliated peripheral tissues may be contributing to obesity phenotypes. The pancreas plays a critical role in metabolism and energy maintenance, and the α and β pancreatic islet cells are ciliated. Loss of cilia on β-cells causes disruptions in glucose homeostasis, giving rise to obesity and diabetes phenotypes (Volta et al. 2019; Yamamoto et al. 1986). In fact, mouse models of PKD have also displayed pancreas cysts, suggesting that the role cilia play in duct formation and/or maintenance is shared among ductal organs (Cano et al. 2004). So, the obesity and diabetes phenotypes I observed could be driven by structural abnormalities in the pancreas created during development or ones that develop over time, like the slow growing kidney cysts. Future experiments could examine *Arl13b*$^{V358A/V358A}$ and *Arl13b*$^{V358A/hnn}$ mice for defects in pancreas formation or disruption of islet cell cilia.

5.4.3 Examining central control of satiety and feeding in *Arl13b*^{V358A} mutant mice

In this study I used c-Fos, an immediate early gene and marker of neuronal activity, to examine the neurons of hypothalamic nuclei. Neurons of the hypothalamus are known to regulate feeding and satiety behaviors, therefore their function may be disrupted by ARL13B^{V358A}, resulting in obesity. A decrease in hypothalamic neuron ciliation in general is sufficient to cause the emergence of obesity phenotypes (Heydet et al. 2013). The ARC, PVN, and VMH are all implicated in hypothalamic control of satiety, cilia play be important in all three regions (Chambers et al. 2013). So, it is unclear if these phenotypes are due to dysfunction in one or many neuronal subtypes in this region. The cilia of the paraventricular nucleus neurons typically contain melanocortin-4 receptors (MCHR4), a GPCR associated with hunger and satiety responses. Loss of ciliary MCHR4 in these neurons drives increased body weight (Siljee et al. 2018). Therefore, the proper localization of these receptors is essential to prevent disruptions of the development of obesity, and so receptor localization to cilia may be disrupted or lost in *Arl13b*^{V358A} mutants. This is supported by published work from the Caspary lab. A complete loss of *Arl13b* disrupts Shh pathway component organization, and ARL13B^{V358A} causes a failure of cilia proteins Arl3 and INPP5E to localize to cilia (Gigante et al. 2020a; Larkins et al. 2011). Future experiments will have to focus on isolating which neuronal subtypes are essential for regulating feeding behaviors and satiety. Furthermore, we need to characterize how cilia receptor organization changes in these cilia when ARL13B is excluded from cilia.

It is possible that hypothalamic regions associated with energy homeostasis are not exclusively responsible for the obesity observed. These are not the only ciliated neurons in the brain, most adult neurons likely have cilia (Bishop et al. 2007). Furthermore, there are regions of interest outside the hypothalamus that could be involved in regulation of feeding behaviors. The role of cilia in reward pathways is largely unknown, so obesity in ciliopathy patients could also be

due to hyperactive reward signaling in areas like the ventral tegmental area (VTA) and the nucleus accumbens. In rats, optogenetic activation of lateral hypothalamic terminals in the VTA are sufficient to drive feeding behavior for as long as the laser is administered (Gigante et al. 2016). This response may be driven primarily by glutamatergic neurons (Stamatakis et al. 2016). Future studies could focus on identifying the role of cilia in established neuronal networks such as the reward pathway.

CHAPTER 6

THE RELATIONSHIP OF ARL13B AND SMOOTHENED

6.1 Summary

This chapter of my thesis is devoted to my overall goal of dissecting and understanding the relationship between ARL13B and SMOOTHENED (SMO). In the course of our analysis of the *Smo* hypomorphic allele *cabbie*, we generated double mutants with the *Arl13b* null allele *hennin.* We found the double mutant embryos displayed a more severe phenotype than either single mutant, suggesting a genetic interaction so I hypothesized that ARL13B is required for SMO activation.

6.2 Introduction

During embryonic development, the neural tube, which will ultimately give rise to the brain and spinal cord, is comprised of neural progenitors that are specified by Sonic Hedgehog (Shh) signaling. The Shh ligand is produced in the notochord and forms a ventral-to-dorsal activity gradient in the neural tube. Progenitors are sensitive to both the concentration and duration of Shh ligand, which together influences their specified cell fate (Echelard et al. 1993; Dessaud et al. 2007; Dessaud et al. 2010). Each progenitor population forms in stereotypic domains within the neural tube. At the most ventral portion of the neural tube floor plate specification requires the highest levels of Shh activity and floor plate cells produce Shh (Ribes et al. 2010). High levels of Shh activity also specify fates such as FoxA2. Adjacent to the floor plate are Nkx2.2 and Olig2, representing moderate and low-level Shh-dependent fates, respectively. Dorsal to the Nkx2.2 domain, Olig2 represents the dorsal spread and edge of Shh influence over neural progenitors. Finally, Hb9, marks differentiated motor neurons which are born from Olig2 expressing cells and require a second exposure to Shh to differentiate (Arber et al. 1999; Ericson et al. 1996; Roelink et al. 1995a). Without *Shh* or *Smo*, no floor plate is specified and the neural tube lacks all markers of ventral cell fates (Chiang et al. 1996; Litingtung et al. 2000; Kasarskis et al. 1998; Zhang et al.

2001). Together, the specific cell fate markers and expression domains provide an *in vivo* readout of Shh signaling (Briscoe et al. 2000).

Shh-dependent neural progenitor specification is mediated by GLI family transcription factors; GLI1, GLI2, and GLI3 (Hui et al. 1994; Matise et al. 1998; Litingtung et al. 2000; Park et al. 2000). The GLIs take two forms, a proteolytically processed repressor form (GLIR) and a modified activator form (GLIA). Within each cell, the Shh activity level corresponds to an intracellular ratio of GLIA-to-GLIR, such that cells closest to the Shh signal have the highest levels of GLIA, and those furthest from the source have the highest levels of GLIR (Stamataki et al. 2005; Lei et al. 2004). This creates opposing gradients of GLIA and GLIR along the dorsal ventral axis. In the neural tube, GLI2 and GLI3 comprise this gradient, GLI2 preferentially takes activator form and GLI3 the prevalent repressor (Matise et al. 1998; Litingtung et al. 2000). The mechanisms that process GLI2/3 into GLIA/R forms requires they translocate through the cilium (Wen et al. 2010; Tukachinsky et al. 2010; Kim et al. 2009). Once exiting cilia, GLIA and GLIR then translocate to the nucleus to influence Hh-dependent gene targets. The mechanisms that process GLI proteins are not the only aspects of vertebrate Hh signaling that involve cilia.

In vertebrates, the Hh pathway's core components traffic dynamically in and out of cilia (Corbit et al. 2005; Haycraft et al. 2005; Rohatgi et al. 2007). The Hh receptor PTCH1 is enriched along the ciliary membrane in the absence of Hh (Rohatgi et al. 2007). When Hh ligand is present, ciliary PTCH1 becomes undetectable and SMO is visibly enriched in cilia (Corbit et al. 2005). The subsequent activation of SMO is dependent on its enrichment in cilia (Rohatgi et al. 2009). Additional Hh components dynamically traffic in and out of cilia to regulate GLI transport and processing, mediating pathway activation (Liem et al. 2009; Barzi et al. 2010; Tuson et al. 2011;

Kim et al. 2009; Wen et al. 2010; Humke et al. 2010). With so many pathway components dynamically linked to cilia, disruptions to cilia proteins can cause serious defects in Hh signaling (Bangs et al. 2017).

ARL13B is a member of the ARF-like family of regulatory GTPases best known for roles in membrane trafficking. ARL13B serves a critical function and in the regulation of Shh pathway and the ciliary organization of the pathway's components. GTPases often act at multiple steps in a given signaling pathway and ARL13B is thought to function in at least two critical steps in the Hh pathway. Evidence for ARL13B function downstream of SMO comes from examination of the *Arl13b* null embryo. Without *Arl13b*, the Shh pathway is constitutively activated in a low-level state, manifesting in neural-patterning defects (Caspary et al. 2007). As the obligate transducer of the Shh pathway, loss of SMO causes a complete loss of Shh-dependent cell fate specification in the neural tube (Caspary et al. 2002; Zhang et al. 2001). If ARL13B simply functions downstream of SMO, then an *Arl13b Smo* mutant would resemble the *Arl13b* single mutant. However, double mutants had some Shh-dependent cell fates established, consistent with loss of *Arl13b* either derepressing or activating GLI transcription factors independent of SMO (Caspary et al. 2007). Analysis of *Gli3 Arl13b*^{hnn} double mutants revealed that the phenotype is not dependent on GLI3, which acts as the predominant repressor in the neural tube (Litingtung et al. 2000; Caspary et al. 2007). Instead, the phenotype is consistent with low-level GLIA, a processed form of GLI2, which primarily functions as an activator (Matise et al. 1998; Litingtung et al. 2000). It is also possible that ARL13B serves a function upstream of SMO that may be masked by loss of ARL13B function downstream of SMO. This is supported by analysis of SMO localization in *Arl13b*^{hnn} cells, revealing abnormal ligand-independent SMO enrichment (Larkins et al. 2011). These data support an additional role of ARL13B in the regulation of the Shh pathway upstream of SMO.

ARL13 is ancient, predicted to be present in the last common eukaryotic ancestor. It appears to have been lost during evolution in organisms that lack cilia and duplicated (to ARL13A and ARL13B) in the urochordates (common ancestor to all vertebrates) (Li et al. 2004; Logsdon et al. 2004; Kahn et al. 2008; East et al. 2012; Schlacht et al. 2013). This duplication coincides with the evolutionary change that linked Hh signaling and cilia, prompting the speculation that ARL13B may hold important clues in deciphering the links between cilia and vertebrate Hh signaling. Given the control ARL13B exerts over the Shh pathway and its unique evolutionary lineage, I hypothesize that ARL13B is required for, and regulates, the processes surrounding the activation of SMO. However, isolating and understanding this upstream function is complicated because it is masked by the downstream influence when *Arl13b* is lost.

Why vertebrate Hh signaling hinges on the cilium is unknown but may be linked to the processes that fully activate SMO. SMO is constantly shuttled throughout the cilium in an inactive state and enriched when activated by endogenous or exogenous means (Ocbina et al. 2008; Corbit et al. 2005). However, the ciliary enrichment of SMO is necessary, but not sufficient, to activate the Shh pathway. The small molecule antagonist cyclopamine prevents SMO activation but permits SMO enrichment in cilia (Chen et al. 2002b; Chen et al. 2002a). This points to SMO activation being a multi-step process that, in part, requires enrichment in cilia (Rohatgi et al. 2009). Moreover, it suggests that SMO activation and enrichment in cilia require distinct changes in SMO receptor conformation. I previously showed that the N223K mutation in the Smo^{cbb} allele disrupts the cystine rich domain (CRD) of SMO, diminishes its enrichment in cilia, and results in a loss of high-level Shh signaling in mice, supporting a model where full receptor activation requires a robust presence in cilia (Gigante et al. 2018). The exact substrate in cilia required for SMO activation remains poorly understood, and the other ciliary mechanisms that regulate the multi-

step process of SMO activation are still being identified. I also sought to define the biologically relevant role of ARL13B in the regulation of Shh signaling in the developing mouse embryo and embryo derived cells.

6.3 Results

6.3.1 *Arl13b*^{hnn} *Smo*^{cbb} embryos are more severely affected than either single mutant

During development, embryos undergo rapid cellular and morphological transformations, governed by the tight regulation of developmental signaling pathways. At this stage, disruptions to cilia genes can have serious effects on embryo health and morphology. To better understand the relationship of ARL13B and SMO in regulating Shh signaling we generated *Arl13b*^{hnn} *Smo*^{cbb} double mutants and examined whole embryo morphology between embryonic day (E)9.5 and E11.5 (**Figure 6.1 A-D**). Through this period of development, *Arl13b*^{hnn} mutants are clearly identified by their open neural tube in the head and caudal

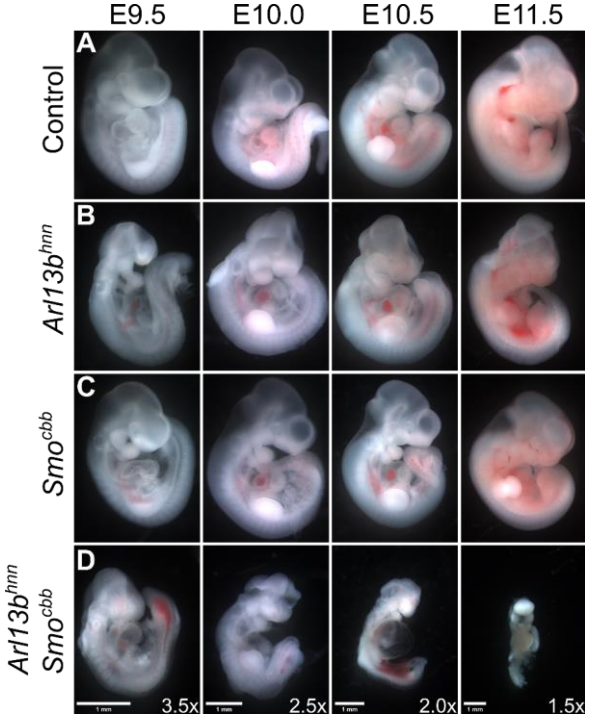

Figure 6.1 Loss of *Arl13b* combined with hypomorph *Smo*^{cbb} causes neural tube closure defects.

Images of whole (A) control, (B) *Arl13b*^{hnn}, (C) *Smo*^{cbb}, and (D) *Arl13b*^{hnn} *Smo*^{cbb} embryos at E9.5, E10.0, E10.5, and E11.5. (A) *Arl13b*^{hnn} and *Smo*^{cbb} are recessive alleles so heterozygotes and wildtype embryos were used as controls. Control embryos rapidly develop and grow between E9.5 and E11.5. (B) *Arl13b*^{hnn} mutants display an early neural tube closure defects in the head that persist throughout development. (C) *Smo*^{cbb} mutants have a mild phenotype and are phenotypically similar to control embryos. (D) *Arl13b*^{hnn} *Smo*^{cbb} mutants resemble *Arl13b*^{hnn} single mutants at E9.5 but fail to grow beyond this stage. The double mutant reaches lethality between E10.0 and E10.5 and resembles a *Smo* null mutant. By E11.5, double mutants are dead and have started to resorb. Scale bars are 1mm and the magnification for each stage is depicted in bottom right corner of images in row D.

spinal cord. These mutants grow at normal rates but reach their point of lethality by E13.5 (**Figure 6.1B**). In contrast, hypomorphic *Smo*^{cbb} mutants display no obvious morphological defects at E9.5. Only at E10.5 is there an identifiable cranial facial defect of the nasal pits (**Figure 6.1C**). These mutants survive until birth, but die shortly afterward with skeletal abnormalities of the head, face, limbs, and spine (Gigante et al. 2018). If ARL13B simply functions downstream of SMO, then we would expect the *Arl13b*^{hnn} *Smo*^{cbb} mutant to phenocopy *Arl13b*^{hnn} embryos. Instead, the *Arl13b*^{hnn} *Smo*^{cbb} double mutant is more severely affected than either *Arl13b*^{hnn} or *Smo*^{cbb} single mutant. At E9.5, *Arl13b*^{hnn} *Smo*^{cbb} mutants display exencephaly, and are morphologically similar to *Arl13b*^{hnn} single mutants (**Figure 6.1D**). However, by E10.0 *Arl13b*^{hnn} *Smo*^{cbb} mutants are noticeably smaller than control or *Arl13b*^{hnn} single mutants, with swelling of the pericardial sac, a defining phenotype in *Smo* null embryos suggestive of defects in cardiac morphogenesis (Zhang et al. 2001). By E10.5, *Arl13b*^{hnn} *Smo*^{cbb} embryos typically exhibit a loss of a beating heart. By E11.5., both *Arl13b*^{hnn} and *Smo*^{cbb} single mutants are present but *Arl13b*^{hnn} *Smo*^{cbb} double mutants are resorbing consistent with lethality around E10.0-10.5. At the point of lethality, these double mutants resemble the *Smo* null phenotype, they have pericardial edema, small and immature somites, hemorrhages in the tail, and a failure to completely turn (Kasarskis et al. 1998). This surprising phenotype suggests ARL13B does not simply function downstream of SMO. ARL13B can have multiple effectors and regulate more than one pathway. Therefore, embryo morphology is a holistic assay for the function of multiple developmental signaling pathways. Taken together, the *Arl13b*^{hnn} *Smo*^{cbb} double mutants suggest ARL13B either has some function upstream of SMO or in a parallel pathway.

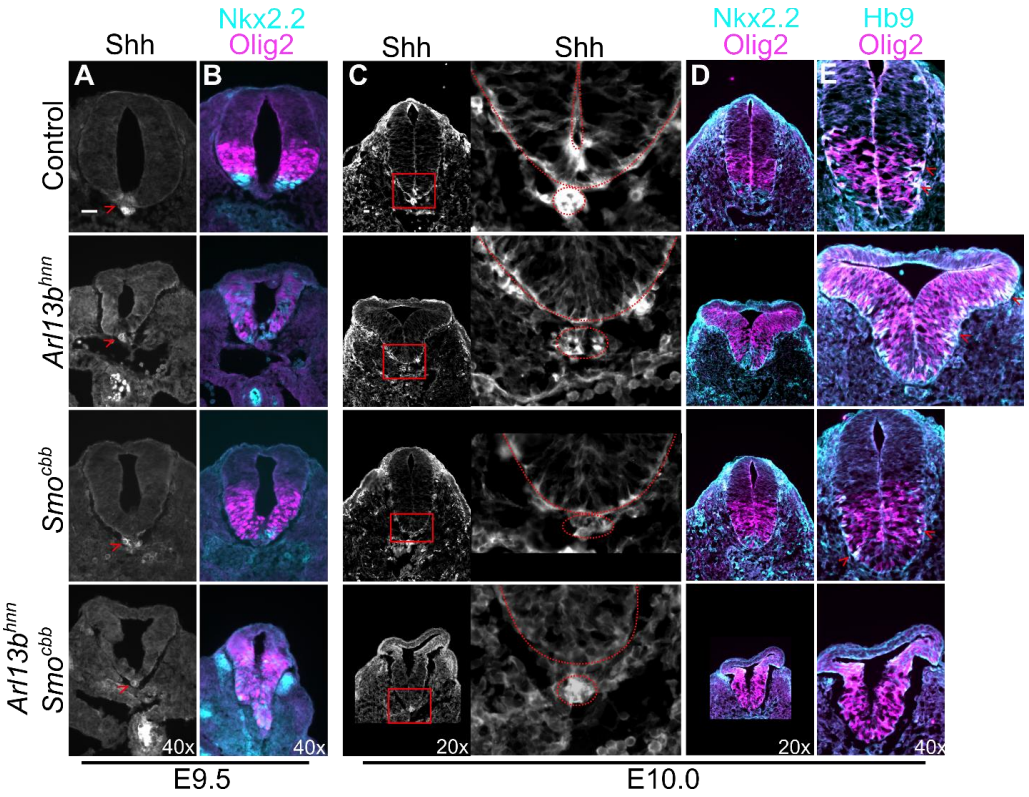

Figure 6.2 *Arl13b*^{hnn} *Smo*^{cbb} mutants lose moderate levels of Shh signaling necessary to maintain Nkx2.2 markers or establish Hb9 expressing differentiated motor neurons.

(A) E9.5 neural tube stained for Shh. In controls Shh is detectable in the notochord at the floor plate. In single and double mutants, only the notochord is positive for Shh and the floor plate is absent. (B) At E9.5, the floor plate is flanked by Nkx2.2 and Olig2 positive cells that form distinct domains. At this stage, the *Arl13b*^{hnn} *Smo*^{cbb} mutant phenocopies *Arl13b*^{hnn} single mutants. (C) At E10.0, Shh signaling begins to increase and the floor plate and notochord retain their Shh expression. The phenotype dose not recover in single or double mutants where only the notochord is Shh positive. Neural tube and notochord outlined in red. (D) Nkx2.2 and Olig2 cell fates retain their distinct domains and dominate the ventral portion of the neural tube. In *Arl13b*^{hnn} mutants, both markers expand ventrally and dorsally, as two largely separate domains. *Smo*^{cbb} mutants resemble controls, except for a ventral shift of Nkx2.2 positive cells towards the ventral midline. Double mutants lose Nkx2.2 positive cells, likely due to loss of high level Shh signaling. (E) Differentiated motor neurons positive for Hb9 emerge along the lateral edge of the neural tube and require a second dose of Shh. In *Arl13b*^{hnn} mutants, due to the expansion of the Olig2 domain, Hb9 cells emerge along the length of the neural tube. In *Smo*^{cbb} mutants, Hb9 cells appear as normal. In double mutants no Hb9 positive cells emerge due to a lack of Shh signaling levels required to specify these cells. Scale bar is 50 μm. Image magnifications depicted at the bottom of each row.

6.3.2 Cell fates requiring high levels of Shh are diminished in *Arl13b*^{hnn} *Smo*^{cbb} mutants.

To focus on the relationship of ARL13B and SMO in regulating Shh signaling, I examined embryonic neural tube patterning in the caudal neural tube at E9.5 and E10.5. At E9.5, the embryo neural tube is closed, and Shh ligand is detectable in the notochord as well as the columnar cells of the ventral floor plate (**Figure 6.2A**). In *Arl13b*^{hnn} mutants, the notochord is producing Shh ligand, but lack a floor plate at the ventral midline and Shh is not detectable in these cells. Similarly, in *Smo*^{cbb} mutants, Shh is detectable in the notochord and not at the ventral midline. The *Arl13b*^{hnn} *Smo*^{cbb} mutant phenotype mirrors both single mutants at this stage with a Shh positive notochord but no floor plate or Shh positive columnar cells. In controls, Nkx2.2 and Olig2 domains are clearly defined, with Nkx2.2 positive cells flanking the floor plate (**Figure 6.2B**). In *Arl13b*^{hnn} mutants, the establishment of ventral cell fates is disrupted due to a persistent low-level activation of the pathway across the region. The ventral midline is populated by Nkx2.2 positive cells and the Olig2 domain has expanded both ventrally and dorsally. In *Smo*^{cbb} mutants, the separation between Nkx2.2 and Olig2 domains remains intact. Though, and much like *Arl13b*^{hnn} mutants, the ventral midline is populated by Nkx2.2 positive cells. The *Arl13b*^{hnn} *Smo*^{cbb} neural patterning is similar to the one observed in *Arl13b*^{hnn} single mutants at this stage. This is consistent with the whole embryo *Arl13b*^{hnn} *Smo*^{cbb} phenotype mirroring *Arl13b*^{hnn} mutants at E9.5. These data support a model where ARL13B functions downstream of SMO.

Neural tube patterning is a dynamic process, sensitive to both the concentration and duration of the Shh signal. If ARL13B functions downstream of SMO, then we would expect to see a phenotype consistent with the *Arl13b*^{hnn} mutant at this stage. To determine how Shh-dependent patterning changes as the duration of the Shh signal lengthens we examined Shh-dependent cell fate markers at E10.0 (**Figure 6.2 C-E**). At this stage, Shh ligand is still detectable

in the notochord and floor plate (**Figure 6.2C**). As observed at E9.5, *Arl13b*^{hnn}, *Smo*^{cbb}, and *Arl13b*^{hnn} *Smo*^{cbb} doubles all lack a Shh positive floor plate but retain a Shh positive notochord. Cells expressing Nkx2.2 and Olig2 are still present (**Figure 6.2D**) and Hb9 positive cells that represent differentiated motor neurons are beginning to emerge along the lateral edge of the neural tube (**Figure 6.2E**). These cells are formerly Olig2 positive cells that require a second, high dose of Shh signal to express Hb9 (Ericson et al. 1996; Arber et al. 1999; Roelink et al. 1995b). In *Arl13b*^{hnn} mutants, Nkx2.2 and Olig2 boundaries are restored. Still, Nkx2.2 positive cells populate the ventral midline and Olig2 cells expand dorsally beyond their normal range. Moreover, Hb9 positive cells are detectable along the lateral edges of the neural tube, but like Olig2 they are expanded dorsally, beyond the normal boundaries and out of range of the Shh signal. Similarly, *Smo*^{cbb} mutants have a ventral midline populated by Nkx2.2 positive cells flanked by Olig2 cells. Though unlike *Arl13b*^{hnn} mutants, this domain that does not expand dorsally beyond its normal range and Hb9 positive cells emerge normally. At this stage in *Arl13b*^{hnn} *Smo*^{cbb} doubles, Nkx2.2 and Hb9 positive cells are absent. This suggests that the high level and duration of the Shh signal required to maintain Nkx2.2 and establish Hb9 differentiated motor neurons is lost. Instead, the neural tube is populated with Olig2-positive cells that have maintained both ventral and dorsal expansion and no longer match *Arl13b*^{hnn} single mutants. Combined with the loss of Nkx2.2 fates that are present in *Smo*^{cbb} single mutants, these data support a role for ARL13B in regulating SMO.

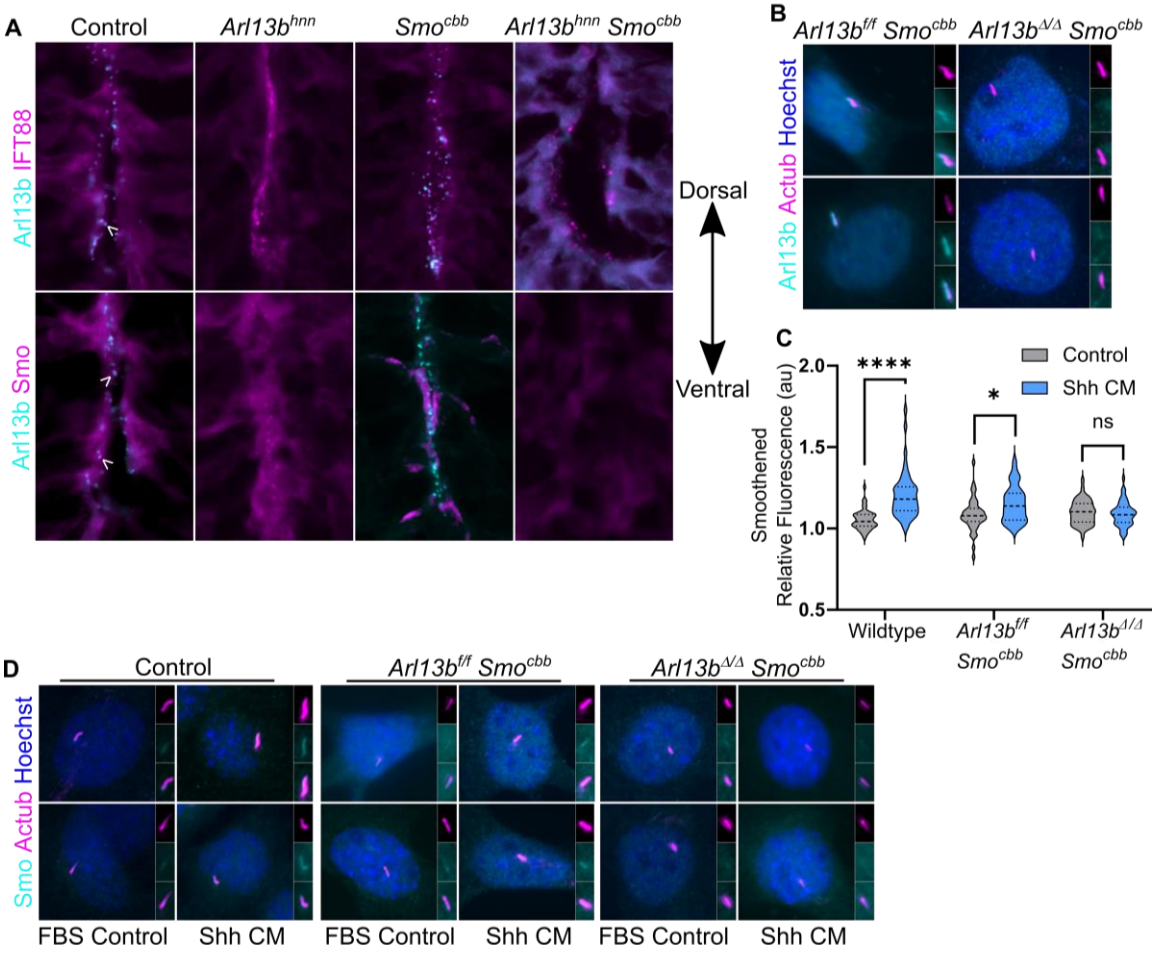

Figure 6.3 Smo is not enriched in the cilia of *Arl13b^{hnn} Smo^{cbb}* mutant embryos and cells.

(A) Images of floor plate and ventral midline of E10.5 mouse neural tube. Stained for Arl13b and IFT88 (Top Row), and Arl13b and Smo (Bottom Row. All embryos have cilia, but mutants with *Arl13b^{hnn}* have cilia that are Arl13b negative. Moreover, Smo is abnormally enriched in the cilia of *Arl13b^{hnn}* mutants and largely undetectable in *Smo^{cbb}* mutants. There are no Smo positive cilia observed in *Arl13b^{hnn} Smo^{cbb}* mutants. (B) MEFs isolated from *Arl13b$^{f/f}$ Smo$^{cbb/cbb}$* mutant embryos before and after treatment with Cre containing adenovirus. Cre recombination deletes Arl13b (cyan), resulting in cilia that are negative for Arl13b, but positive for acetylated a-tubulin (magenta). (C) MEFs treated with Shh conditioned media for 24 hours and Smo immunofluorescence levels measured relative to each cell's background. Smo is highly enriched in wildtype and moderately in *Smo^{cbb}* cells. Smo does not enrich in the cilia of *Arl13b$^{D/D}$ Smo$^{cbb/cbb}$* cells. (D) Representative image pairs of cells and cilia from panel (C). Cilia are stained for acetylated a-tubulin (magenta) and Smo (cyan).

6.3.3 SMO is absent from cilia in *Arl13b^{hnn} Smo^{cbb}* mutants and cells

Cells exposed to Shh have SMO enriched cilia, a hallmark of SMO and Shh pathway activation. In the neural tube, the ventricular lumen is lined with ciliated cells that can be labeled with IFT88 and ARL13B. However, in *Arl13b^{hnn}* mutants, cilia can only be identified by IFT88 and not ARL13B antibody (**Figure 6.3A**). The cilia of cells in and around the ventral floor plate, closest to the source of the Shh signal, are highly positive for SMO. Moving further from the source of the Shh, SMO positive cilia gradually decrease and are absent by the midpoint. Loss of *Arl13b* leads to an aberrant enrichment of SMO in cilia that is independent of the Shh ligand. Therefore, SMO positive cilia are detectable beyond the normal ventral-dorsal range in *Arl13b^{hnn}* mutants. In the *Smo^{cbb}* mutant, SMO is poorly enriched in cilia of the floor plate and surrounding areas, making it extremely difficult to detect. Similarly, the cilia of *Arl13b^{hnn} Smo^{cbb}* double mutants are present and identifiable by IFT88 like in *Arl13b^{hnn}* mutants, and like *Smo^{cbb}* mutants SMO is undetectable in any cilia, even in cells of the floor plate, immediately adjacent to the notochord, the source of the Shh signal.

Neural tube cilia can be difficult to visualize, and so in an effort to quantify the SMO localization phenotype I generated *Arl13b$^{flox/flox}$* S*mo^{cbb}* mutant mouse embryonic fibroblasts (MEFs). I treated a clonal population of MEFs with *Cre* expressing adenovirus to induce deletion of *Arl13b*, generating an *Arl13b$^{\Delta/\Delta}$ Smo^{cbb}* cell line, mimicking the *Arl13b^{hnn} Smo^{cbb}* cells. While *Arl13b$^{flox/flox}$* S*mo^{cbb}* MEFs have ARL13B positive and acetylated α-tubulin positive cilia, *Cre* virus-treated MEFs have acetylated α -tubulin positive cilia with no detectable ARL13B (**Figure 6.3B**). MEFs are treated with Shh conditioned media (Shh CM) or low-serum control media for 24 hours before being probed for SMO positive cilia (**Figure 6.3C**). I measure significantly higher

levels of SMO in cilia of control MEFs treated with Shh media. As expected, *Smo*^{cbb} mutant MEFs have reduced levels of SMO positive cilia compared to wildtype but increased above their own untreated control. In agreement with my data *in vivo*, *Arl13b*$^{\Delta/\Delta}$ *Smo*^{cbb} cells have few SMO positive cilia. In these MEFs I measure no overall increase in relative SMO fluorescence between control and Shh treated conditions. In control MEFs, SMO is visibly enriched above baseline levels following treatment with Shh CM, but less so in *Smo*^{cbb} cells (**Figure 6.3D**). In *Arl13b*$^{\Delta/\Delta}$ *Smo*^{cbb} MEFs, some faint SMO positive cilia are detected, but no cilia are enriched with SMO in either control or Shh CM conditions. Together, these data show that Shh-induced SMO^{N223K} enrichment in cilia, which is already significantly impaired in *Smo*^{cbb} mutants, is nearly lost when *Arl13b* is absent from the cell. For the *in vitro* portion of this experiment, I used Shh CM that had been previously thawed and stored at 4°C for nearly two-years. More recent experiments using this medium revealed poor Shh-dependent transcriptional response by qPCR. Therefore, the marginal change in SMO detected in control cells is likely because of a decay in medium efficacy. This experiment will need to be repeated prior to publication using a more recent batch of Shh medium.

6.3.4 SMO^{N223K} receptor activation by SMO agonist (SAG) is impaired

The *Smo*^{cbb} phenotype and poor SMO^{N223K} receptor enrichment in cilia are consistent with it being a hypomorphic allele. However, these data cannot be used to accurately interpret SMO receptor activation. SMO enrichment is linked to activation and Shh signal transduction is far downstream of SMO. SMO activation is measured by a cAMP-sensitive GloSensor, a firefly luciferase variant, to test SMO^{N223K} receptor activation of G-proteins. HEK-293FT cells are transfected with this GloSensor to measure changes in cAMP when modulated by a SMO^{WT}-G_{ao} or SMO^{N223K}-G_{ao} fusion protein that is activated by SMO agonist (SAG). Treating cells with

forskolin induces the production of cAMP, activating the GloSensor luciferase. High levels of luciferase output represent inactive SMO and low levels of luciferase output represent activated SMO (**Figure 6.4A**). Untreated SMO^{WT}-G_{ao} expressing cells have high levels of luciferase output, compared to SAG treated SMO^{WT}-G_{ao} cells. This decrease in output represents activation of SMO. Untreated SMO^{N223K}-G_{ao} expressing cells have activity levels equal to untreated SMO^{WT}-G_{ao} controls. Like, SMO^{WT}-G_{ao} cells, SAG treated SMO^{N223K}-G_{ao} expressing cells have decreased

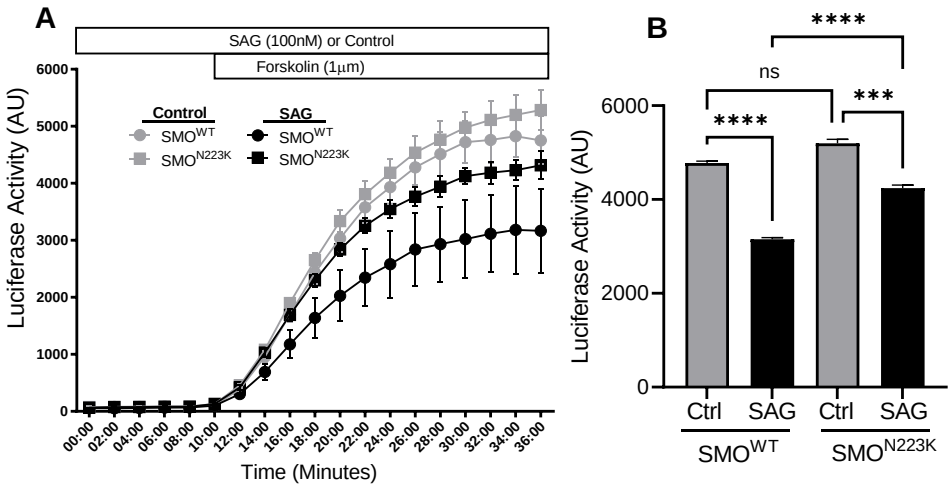

Figure 6.4 SMO^{N223K} activation by SAG is impaired.

Activation of SMO in HEK293-FT cells transfected with cAMP-sensitive GloSensor and SMO^{WT}-G_{ao} or SMO^{N223K}-G_{ao}, treated with control or SAG. SMO activity is represented on the *y* axis; activation of the fused Gao inhibits forskolin activation of AC, high luciferase activity represents inactive SMO and lowered luciferase activity represents higher SMO activity. (A) Untreated cells (grey) represent baseline levels of AC activity when SMO activity is inhibited by PTCH1. Cells expressing SMO^{WT}-G_{ao} and treated with SAG (black circles) have activated SMO-induced decreases in cAMP and GloSensor luciferase activity. Cells expressing SMO^{N223K}-G_{ao} treated with SAG (black squares) are activated but luciferase readout is less than SMO^{WT} cells. Luciferase activity measured in luciferase arbitrary units (AU). Plotted data represent average activity of 5 baseline readings and 14 experimental readings plotted over time (± standard deviation). (B) Average maximal luciferase output of the final three readings. SMO^{WT}-G_{ao} expressing cells treated with SAG activate SMO, inhibiting luciferase activity. SMO^{N223K}-G_{ao} expressing cells treated with SAG are activated, but only ~50% of response measured in SMO^{WT} cells treated with SAG. Untreated cells expressing SMO^{WT} or SMO^{N223K} (grey) have equal activity levels. Data are average of three final readings, representing maximal response (± standard deviation), analyzed by two-way ANOVA and Tukey's post-hoc test for multiple comparisons. Ns is not significant, *** $p < 0.001$, **** $p < 0.0001$.

SMO activation relative to its untreated control. However, luciferase output does not decrease to levels observed in SMO^{WT}-G_{ao} controls, consistent with an impairment of the SMO^{N223K} receptor activation by SAG (**Figure 6.4B**). A loss of SMO activation is consistent with SMO^{N223K} poor enrichment in cilia and the *in vivo* phenotypes of the Smo^{cbb} hypomorph.

6.4 Discussion

In this chapter, I presented *in vivo* data that $Arl13b^{hnn}$ Smo^{cbb} double mutants are more severely affected than either single mutant alone. These mutants have a dramatic delay in embryonic development, resulting in lethality around E10.0. Examination of the neural tube revealed limited specification of Shh-dependent cell fates. I found that whereas SMO is abnormally enriched in the cilia of A$rl13b^{hnn}$ mutants, it is absent from cilia in $Arl13b^{hnn}$ Smo^{cbb} mutants. Using an assay for SMO receptor activation, I showed decreased activity of the SMO^{N223K} receptor by SAG. Together, these data support a model where ARL13B functions at a step upstream of SMO, possibly through the regulation of the ciliary processes that activate SMO.

The reason $Arl13b^{hnn}$ Smo^{cbb} mutants display a more severe phenotype compared to $Arl13b^{hnn}$ or Smo^{cbb} single mutants is unclear. One possibility is that this is a synergistic phenotype, where the loss of *Arl13b* coupled with SMO^{N223K} prevents SMO activation. In *Arl13b* null cells, SMO is trapped in cilia, but GLI proteins are not properly enriched and pathway activation by Shh ligand is weak, suggesting that SMO in cilia is unlikely to be fully activated (Larkins et al. 2011). Perhaps this trapped SMO is unable to adopt an active conformation due to the loss of *Arl13b*. Modelling data show SMO^{N223K} lysine-to-asparagine change occludes the ligand binding pocket at the transmembrane domain, predicting that the receptor cannot easily change to an active confirmation. Together, the $Arl13b^{hnn}$ Smo^{cbb} phenotype can be explained by impaired SMO

activation through loss of *Arl13b*, combined with a hypomorphic and poorly activated SMO^{N223K}. The result is a phenotype consistent with low SMO activation and Shh signaling. Therefore, this genetic interaction reflects a mechanistic interaction and a model where ARL13B functions upstream of SMO, controlling the ciliary processes necessary for SMO activation. Future experiments will focus on measuring SMO receptor activation to test this model.

The presence of some Shh-dependent cell fate specification in the neural tube of $Arl13b^{hnn}$ Smo^{cbb} mutants suggests Shh pathway activation by SMO^{N223K}. However, the specification of cell fates can also be explained by the loss of *Arl13b*. In $Arl13b^{hnn}$ single mutants, Nkx2.2 and Olig2 positive cells are induced in a Shh-ligand independent manner (Caspary et al. 2007). Furthermore, $Arl13b^{hnn}$ *Smo* null mutants also establish some Shh-dependent cell fates despite the loss of SMO and all Shh signaling. In both cases, these cell markers are likely induced by constitutive and low-level GLIA, a consequence of *Arl13b* loss. Therefore, I interpret the presence of Nkx2.2 and Olig2 positive cells in $Arl13b^{hnn}$ Smo^{cbb} mutants to be caused by the loss of *Arl13b*, resulting in low-level GLIA and the establishment of some Nkx2.2 and Olig2 positive cells. Alternatively, it is possible the $Arl13b^{hnn}$ Smo^{cbb} phenotype is simply additive. The establishment of some Shh-dependent cell fates caused by the combination of decreased GLIA levels that are further reduced by a hypomorphic SMO^{N223K}, resulting in a near complete loss of GLIA (Caspary et al. 2007). The expectation would be embryo phenotypes consistent with a near complete loss of Hh signaling and the specification of few Shh-dependent cell fates in the neural tube, similar to what is observed in $Arl13b^{hnn}$ Smo^{cbb} mutants. However, SMO^{N223K} is not enriched in $Arl13b^{hnn}$ Smo^{cbb} ventral midline cilia or cells treated with Shh media. SMO enrichment in cilia is necessary for Shh pathway activation and a loss of SMO^{N223K} presence in cilia would be consistent with no Shh pathway

activation. Therefore, an additive model cannot explain the loss of SMO^{N223K} presence in cilia when *Arl13b* is lost, suggesting a greater role for ARL13B upstream of SMO.

ARL13B is known to regulate more than just the core components of the Shh pathway. So, an alternative model could posit a loss of *Arl13b* function in a pathway that serves to negatively regulate Shh. In cilia, INPP5E removes the 5-phosphate from PIP2 and PIP3 and loss of *Inpp5e* increases PIP2 in cilia (Chavez et al. 2015; Garcia-Gonzalo et al. 2015; Kisseleva et al. 2000). Furthermore, a loss of INPP5E function increases the ciliary presence of GPR161, a negative regulator of the Shh pathway that converges on the pathway downstream of SMO (Constable et al. 2020; Mukhopadhyay et al. 2013). Loss of *Arl13b* prevents the ciliary localization of INPP5E to cilia (Bielas et al. 2009; Humbert et al. 2012). Therefore, GPR161 may be abnormally enriched in the cilia of $Arl13b^{hnn}$ mutants. In this model, poorly activated SMO^{N223K} coupled with increased activity and ciliary presence of GPR161 would further suppress SMO^{N223K} activation of the Shh pathway. Future experiments could examine the neural tube cilia of $Arl13b^{hnn}$ and $Arl13b^{hnn}$ Smo^{cbb} mutants for increased GPR161 presence.

Moving forward, I will attempt to address two outstanding issues. 1) These data suggest that ARL13B performs a necessary function in the activation of SMO, and loss of *Arl13b* would diminish SMO activation. 2) The loss of SMO^{N223K} localization in the $Arl13b^{hnn}$ Smo^{cbb} mutant conflicts with the enrichment of SMO in $Arl13b^{hnn}$ single mutants. This suggests a complicated role of ARL13B in controlling the ciliary presence of SMO. To test my hypothesis, I will use the cell-based luciferase assay for SMO activation, shown in Figure 6.4. Using this assay my goal is to test the functional output of wildtype and mutant SMO receptors in the absence of ARL13B. To

achieve this, I will treat cells with ARL13B targeted shRNA or scrambled control RNA containing lentiviruses to knockdown ARL13B protein and measure SMO receptor activation.

CHAPTER 7

PERSPECTIVES AND DISCUSSION

7.1 Dissecting the ciliary processes that regulate SMO trafficking and SMO activation.

SMO is a 7 transmembrane orphan GPCR and obligate transducer of the Shh signaling pathway. SMO, along with other components of the Shh pathway, is dynamically linked to the primary cilium. However, the ciliary processes that regulate this dynamism remain mysterious. The key to understanding the pathway and its regulation by the cilium is crucial to moving the field forward. The big outstanding questions in the field are 1) what are the endogenous substrates that activate SMO, 2) what is Ptch1 function that regulates the substrates, and 3) what is the role of the cilium in controlling these substrates? These seemingly basic questions have intrigued the field since the discovery that cilia are required for vertebrate Hedgehog and that the pathway components dynamically localize to cilia (Huangfu et al. 2005; Huangfu et al. 2003; Corbit et al. 2005; Rohatgi et al. 2007; Haycraft et al. 2005; Liu et al. 2005). In this section I will discuss the most recent advances in the field. Specifically, I will focus on 1) new information regarding SMO trafficking dynamics in relation to cilia and 2) new models of SMO activation. Functionally, these processes are difficult to separate as SMO trafficking to and from cilia is linked to its activation. Therefore, my discussion of the two topics will blend to some extent.

7.1.1 SMO ciliary exit is regulated by a common GPCR ubiquitination pathway

Trafficking of proteins into and out of cilia is a dynamic process because the ciliary compartment and membrane are exclusive environments, so the trafficking process has several steps and chaperones. The BBSome is an octameric complex that expands the ability of IFT to traffic proteins (Nachury et al. 2007; Berbari et al. 2008b). The BBSome is linked to the ciliary exit of activated GPCRs yet it is unclear how the BBSome distinguishes between active and inactive GPCRs (Ye et al. 2018). Recent work shows that β-arrestin 2 directs the ubiquitination of

activated GPCRs (Shinde et al. 2020). This expands β-arrestin 2's well-known mechanism of retrieving receptors from the plasma membrane via ubiquitination and endocytosis in the cell body (Shenoy et al. 2001; Xiao et al. 2011; Lohse et al. 1992; Lohse et al. 1990). In cilia, β-arrestin 2 facilitates the ciliary exit of activated GPCRs, but how it coupled these GPCRs to active transport proteins was unknown (Green et al. 2016; Pal et al. 2016). This recent study showed that β-arrestin 2 recruits a ubiquitin ligase to build K63 ubiquitin chains on activated GPCRs, marking them for BBSome-mediated ciliary exit. Disabling the BBSome, removing β-arrestin 2, or mutating lysine residues that could be ubiquitinated on GPCRs SSTR3 and GPR161 are all sufficient to block ciliary exit. There are more than two-dozen known ciliary GPCRs that once activated exit cilia (Mykytyn et al. 2017). This suggests that the β-arrestin 2-guided ubiquitination and BBSome mediated exit of activated GPCRs may be a shared mechanism.

Interestingly, SMO is differentially regulated by this mechanism. SMO is only enriched in cilia when activated. Inactive SMO exits cilia, which contrasts with other GPCRs that exit cilia when activated. This recent study, inactive SMO and active GPCRs exit cilia in a β-arrestin 2 targeted ubiquitination mechanism (Shinde et al. 2020). Therefore, activated SMO bypasses ubiquitination to maintain its ciliary location and transduce the Hh signal. Why SMO is differentially regulated by this ciliary process is unclear. Activation of GPCRs involves conformational change that exposes the receptor to endocytic pathways. The mechanism of SMO activation is largely enigmatic, but is thought to occur in multiple steps (Rohatgi et al. 2009). Moreover, low levels of inactive SMO are thought to constantly shuttle into and out of cilia (Ocbina et al. 2008). So, perhaps the conformational change that allows SMO into cilia is the same form that permits its exit. Only when activated does the SMO conformation change to a form that

prevents it from being recognized by exit machinery, allowing it to enrich in cilia. This model fits with our understanding of how Ptch1 suppresses SMO activation and enrichment in cilia. Loss of *Ptch1* is sufficient to fully activate SMO, resulting in Hh pathway hyperactivation that is lethal in embryos (Goodrich et al. 1997). This suggests that without Ptch1 there is no alternate ciliary mechanism capable of suppressing active SMO and removing it from cilia. Therefore, Ptch1 must be influencing SMO conformation, causing it to take an inactive form that promotes SMO removal from cilia. This would explain why an *in vitro* model of SMO activation showed that overexpressed SMO is active and only suppressed by co-expression of Ptch1 (Myers et al. 2017).

In my work, I studied a hypomorphic allele of SMO named *cabbie* (*Smo^{cbb}*). The point mutation, an asparagine-to-lysine change at residue 223, is in the N-terminal portion of the receptor. It sits in a linker domain that bridges between a large N-terminal cysteine rich domain (CRD) and the start of transmembrane domain 1. Homozygous *Smo$^{cbb/cbb}$* embryos had phenotypes consistent with low Hh signaling and the SMO^{N223K} receptor had difficulty enriching in cilia. It could be the SMO^{N223K} receptor is overly susceptible to ubiquitination and BBSome-mediated ciliary exit. This would prevent SMO^{N223K} from enriching in cilia. It is also possible that SMO^{N223K} cannot enter cilia properly, this could explain why it never enriches in response to ligand. However, Shinde et al showed that SMO enrichment in cilia occurs rapidly and reaches peak levels in just minutes (Shinde et al. 2020). If SMO^{N223K} has slow ciliary entry, then it would enrich in cilia after a long period. In my experiments, I treated *Smo^{cbb}* mutant cells for 24 hours with Shh containing media and SAG but observed only a marginal increase in SMO^{N223K} enrichment in cilia. If SMO^{N223K} entry is deficient, then a 24-hour treatment is sufficiently long enough for SMO^{N223K} to overcome this. I interpret this to mean SMO^{N223K} is not simply defective in ciliary entry so propose that it is subject to ubiquitination and exit. Both hypotheses can be tested. A defect in SMO entry

would be revealed if mutations are made to the ubiquitinated residues on the C-terminus and intracellular loop 3 of SMO^{N223K}. If SMO^{N223K} entry is deficient, then blocking ubiquitination will have no effect on SMO^{N223K} enrichment. If SMO^{N223K} is being rapidly trafficked out of cilia by the ubiquitin pathway, then blocking ubiquitination will cause SMO^{N223K} to enrich in cilia. Poor enrichment and activation of the Shh pathway by SMO^{N223K} may not be due to only a trafficking defect. It could also have decreased potential for activation, which this model would not be able to address. In the next section I will discuss new models of SMO activation and apply them to SMO^{N223K}.

7.1.2 SMO activation conformations are modulated by dynamic association with oxysterols

The most important changes in the field are the mounting evidence that (1) cholesterol activates SMO, and (2) Ptch1 may be regulating sterol organization in cilia. There has long been a physiologically relevant implication for cholesterol in the regulation of vertebrate Hedgehog signaling. Patients with Smith-Lemli-Opitz syndrome have dysfunctional dehydrocholesterol reductase *DHCR7*, resulting in diminished cholesterol synthesis. They present with phenotypes that indicate low Hedgehog activity (Blassberg et al. 2016). The evidence that SMO activation is influenced by cholesterol is strong, but the possibility that cholesterol is the "one and only" ligand for SMO is unlikely, but may be a derivative of an endogenous modulator. There are several oxysterols that are shown to bind and modulate SMO activity (Corcoran et al. 2006; Dwyer et al. 2007; Nachtergaele et al. 2012). Still, cell membranes, the ciliary membrane included, are lipid rich environments that cannot exist without cholesterol and its derivatives. All GPCRs that reside in the membrane are dynamically associating with lipidated structures that are part of the membrane composition (Hanson et al. 2008; Hanson et al. 2012; Jafurulla et al. 2019). Finally,

several ligand binding domains have been identified in the SMO structure, including multiple sterol sensing domains (Byrne et al. 2018). Given what we know, the most likely scenario is cholesterol and its derivatives act as a modulator of SMO activity, facilitating the full activation of the SMO and thereby the highest levels of Hh pathway activation that are required during development.

As the data supporting cholesterol-induced activation of SMO continues to grow, the next challenges will be identifying how Ptch1 functions to influence cholesterol and why it occurs in and around the cilium. There is no question that the cilium has a tightly regulated environment, and this includes membrane lipid compositions that are essential for normal cilia structure and function (Maerz et al. 2019). One model proposed that Ptch1 function in cilia is influenced by sodium ion gradients that power its ability to control the SMO-activating substrate (Myers et al. 2017). In another model, Ptch1 acts as a cholesterol transporter, directly modulating lipid dynamics in cilia. This influence in lost in the presence of Hh ligand, thereby facilitating SMO activation (Zhang et al. 2018; Kowatsch et al. 2019). Ptch1 would have to structurally shield or sequester the SMO-activating substrate, as the Ptch1-SMO interaction is sub-stoichiometric (Taipale et al. 2002). A concept supported by increases in ciliary cholesterol by Hh ligand that enhance SMO activation and Hh pathway output (Kinnebrew et al. 2019). Thanks to enhanced microscopy techniques, we are beginning to better understand the dynamics of Ptch1 and SMO in cilia, which will soon allow researchers to identify how sterols bridge the gap between the two receptors (Weiss et al. 2019).

Cholesterol acting as a modulator, and not as the essential ligand fits with my interpretation of the SMO^{N223K} mutation. The SMO^{N223K} mutation is in the linker domain that bridges the CRD

to the transmembrane domains. Initial models characterized the SMO cysteine rich domain (CRD) as a sterol binding site (Byrne et al. 2016; Huang et al. 2016; Luchetti et al. 2016b). Perhaps part of the SMO^{N223K} activation deficiency is linked to a decreased sensitivity to cholesterol induced activation. This could be due to a decreased affinity for cholesterol at the sterol sensing domain of the CRD. Alternatively, cholesterol binding could be normal, but the N223K change prevents the CRD from shifting SMO into an activated conformation. Both hypotheses could be tested using structural biology and protein modelling.

Through protein modelling, structural biologists discovered an additional sterol sensing region in the transmembrane domain of the receptor (Huang et al. 2018; Hedger et al. 2019; Deshpande et al. 2019). This domain is associated with a unique inhibitory π-cation lock that prevents SMO activation. Perhaps not that surprising, this lock appears to be broken in the constitutively active SMO^{A1} cancer causing mutant (Huang et al. 2018). This model fits with our understanding of SMO antagonists that bind the transmembrane domain, blocking activation and enrichment in cilia. The exception is cyclopamine which inhibits SMO activation but causes it to enrich in cilia. This may be because cyclopamine binds to the CRD, helping move SMO into an active confirmation without breaking the π-cation lock (Huang et al. 2018). The significance is the identification of different SMO conformations, helping to separate the distinct processes of SMO trafficking to cilia and SMO activation. These data support a model where SMO^{N223K} defect in activation is linked to a structural inability to assume a more active conformation. The Smo^{cbb} homozygous embryo has improved survivability compared to a *Smo* null embryo (Kasarskis et al. 1998; Zhang et al. 2001). This means SMO^{N223K} can transduce some of the Hh signal, but it cannot reach the high levels required to properly pattern the neural tube or control skeletal development. Breaking the π-cation lock may be the key to fully activating SMO, which SMO^{N223K} cannot

overcome. This could be tested by disabling the π-cation lock on the SMO^{N223K} receptor. If this is the activational defect of SMO^{N223K}, then breaking the π-cation lock will allow SMO^{N223K} to behave like the constitutively active SMO^{A1} mutant. If this has no effect on SMO^{N223K} function, this will point to an inability of SMO^{N223K} to activate G-proteins and its downstream signaling cascade. This could be tested with a [^{35}S]GTPγ binding assay for GPCR activation. If SMO^{N223K} cannot properly bind and activate G-proteins, then it would accumulate less radioactive signal from the [^{35}S]GTPγ compared to a wildtype SMO receptor.

Current dogma in the field is that SMO does not directly bind the Hh ligand. Rather, it is clear that Hh binds to Ptch1 (Marigo et al. 1996; Stone et al. 1996; Fuse et al. 1999). There is evidence that this is true, but there is plenty of justification for the possibility of SMO also interacting with the Hh ligand. SMO belongs to the F-class, or Frizzled family of GPCRs. The only other receptors in this family are Frizzled receptors. SMO shares structural similarities to the Frizzled receptors, including the CRD, but unlike SMO they are not orphan receptors. Frizzled receptors function as part of the Wnt signaling pathway and can bind directly to the Wnt ligand. Wnt processing requires it be cholesterolyated, similar to the Hh ligand. So, the cholesterolyated Wnt ligand binds to the Frizzled receptor's sterol sensing domain in the CRD of the N-terminus. If both SMO and the Hh ligand share this homology and post-translational modification, respectively, then why don't they interact? Did these opposing pathways that share such close homology really diverge at this specific point? To be fair, this discussion excludes the role of Ptch1, as there is no equivalent in the Wnt pathway. So perhaps it is just a matter of competing for Hh ligand and Ptch1 has a much higher affinity for Hh ligand than SMO.

7.1.3 ARL13B functions as an essential regulator of SMO and the Shh pathway

1) Why is SMO enriched in cilia of unstimulated *Arl13b* null mutants and 2) what can this tell us about ARL13B's function in relation to SMO? There is substantial evidence that, in the off-state, SMO cycles through the cilium at low-mostly undetectable levels. Only when the pathway is activated by endogenous or exogenous methods does SMO enrich in cilia. In *Arl13b* null cells, SMO is improperly retained in the off state, resulting in its ciliary enrichment, and this level further increases upon stimulation. The biggest assumption we make is that the SMO trapped in *Arl13b* null cilia is inactive. This assumption is based on *in vivo* and *in vitro* data showing that loss of *Arl13b* causes low-level Shh pathway activation. If the trapped SMO is active, then we would expect to observe higher levels of pathway output, but this is not the case (Mariani et al. 2016; Larkins et al. 2011). Moreover, pathway activation in *Arl13b* null cells increases the amount of SMO present in cilia and activates the pathway, but not to the fullest degree. So, it seems the pathway upstream of SMO is at the very least partially functional. Loss of *Ptch1* removes all suppression of SMO, allowing SMO to fully activate the Hh pathway (Goodrich et al. 1997). Concomitant deletion of *Ptch1* and *Arl13b* suppresses some Hh signaling, but not completely, as *Ptch1 Arl13b* mutants do not resemble *Arl13b* single mutants (Caspary et al. 2007). These genetic data support a role of ARL13B upstream of SMO and show that the endogenous pathway activating SMO is still partially functional when *Arl13b* is lost. If this SMO is inactive, how then is it enriched/retained in cilia, bypassing the normal exit of the inactive receptor? One possibility is that ARL13B aids in coupling SMO to exit machinery that pull active and inactive GPCRs out of the cilium. SMO is not the only GPCR in cilia, but it isn't clear that other GPCRs are also misregulated by loss of *Arl13b*, so this would need to be tested.

Moving forward, I will investigate the role of GPCR ubiquitination in mediating GPCR behaviors in *Arl13b* null cells. Recently, studies have shown that ubiquitination of SMO is

sufficient and necessary for its exit from cilia (Desai et al. 2020; Shinde et al. 2020). Furthermore, activated SMO bypasses ubiquitination to enrich in cilia and avoid the ciliary exit pathway. In *Arl13b*^{hnn} cells, SMO is abnormally enriched in cilia. Coupled with these recent data, this suggests SMO is either 1) not ubiquitinated, or 2) the exit pathway for ubiquitinated GPCR exit is disabled due to the loss of *Arl13b*. I will use ubiquitin tagged GPCR constructs to test the functionality of ubiquitin GPCR exit from cilia in *Arl13b*^{hnn} cells. I will also examine the buildup of endogenously expressed ubiquitinated proteins in *Arl13b*^{hnn} cilia using antibodies specific for K48 and K63 chain ubiquitin. There are no known links between ARL13B and the BBSome other than their localization to cilia. *BBS3* encodes ARL6, so there is a role for GTPases in BBSome function. These experiments will identify a possible mechanism for cilia protein composition disorganization caused by a loss of ARL13B and possibly shed light on its function in the regulation of SMO.

7.1.4 Final thoughts on *Smo*^{cbb}

The importance of *Smo*^{cbb} mutation and its impact on the CRD and SMO conformational states has not been fully realized. Clearly, the CRD plays an essential role in the SMO activation conformation and more specifically, SMO enrichment in cilia. The SMO^{N223K} mutation could disrupt SMO conformational changes required for its enrichment in cilia; this would explain the low levels of ciliary SMO I observe in *Smo*^{cbb} cells and embryos (Gigante et al. 2018). In addition, the activation defect of SMO^{N223K} has not been fully characterized. This is due to an absence of appropriate readouts of SMO activation. The *in vivo* neural tube patterning, SMO enrichment in cilia, and *in vitro* Shh-dependent gene transcription are all downstream or accessory measures of SMO activation. What's missing is a direct method to detect activated SMO. This gap has been

partially filled by the invention of a cell-based luciferase assay for SMO activity. While the assay bypasses the role of the cilium in SMO activation, it is so far the best readout of SMO GPCR activation (Myers et al. 2017). This assay is exciting because it harnesses the yet unknown endogenous mechanisms that regulate and activate SMO. However, the full potential of the assay has not been fully realized. Future experiments will focus on using this assay to expand our knowledge of the SMO and the endogenous pathway that activates it.

7.2 Cilia-excluded ARL13B^{V358A} reveals cilia specific and tissue specific functions of ARL13B.

I observe shorter cilia in MEFs isolated from *Arl13b*^{V358A} mutant embryos, a phenotype reported in the *Arl13b* null embryo and cells (Caspary et al. 2007; Larkins et al. 2011). A further consequence of *Arl13b* loss is a defect in the ciliary axoneme in cilia of the embryonic node (Caspary et al. 2007; Larkins et al. 2011). What's unclear is whether all ciliated tissues share these defects in cilia. Cilia are heterogenous and serve tissue specific functions, so perhaps loss of *Arl13b* or ARL13B^{V358A} cause cilia defects in some, but not all cilia types. This is perhaps best illustrated by the fact that conditional deletion of *Arl13b* in kidneys causes a complete loss of cilia, but not in other ciliated tissues (Seixas et al. 2016; Sun et al. 2004). In analysis of *Arl13b*$^{V358A/V358A}$ cells, I measured short cilia and observe short cilia in the embryonic neural tube. Moreover, I observe cilia in the lumen of the kidney nephron of *Arl13b*^{V358A} mutants. Why ARL13B is necessary for cilia formation in kidney, and not in other tissues is unknown. Furthermore, it's surprising that cilia excluded ARL13B^{V358A} is sufficient for kidney cilia formation, but cannot prevent kidney cyst formation. Based on these data it appears ARL13B is playing a role in a ciliogenesis pathway, a function that may be specific to nephron cells.

Importantly, ARL13B has ciliary and non-ciliary roles in specific tissues. The best evidence for this is the kidney cyst and obesity phenotypes I discovered in *Arl13b*^{V358A} mice. Both cystic kidney disease and obesity are common among patients with ciliopathies. So, it is very likely the *Arl13b*^{V358A} mice have these phenotypes because of a loss of ciliary ARL13B. Hopefully the ARL13B^{V358A} mutant will aid in dissecting ARL13B's functions in the cell body by isolating it from the cilium. The Caspary lab remains focused on what ciliary control is lost in the ARL13B^{V358A} mutant, so there is an opportunity to re-examine cilia-independent functions of this cilia protein.

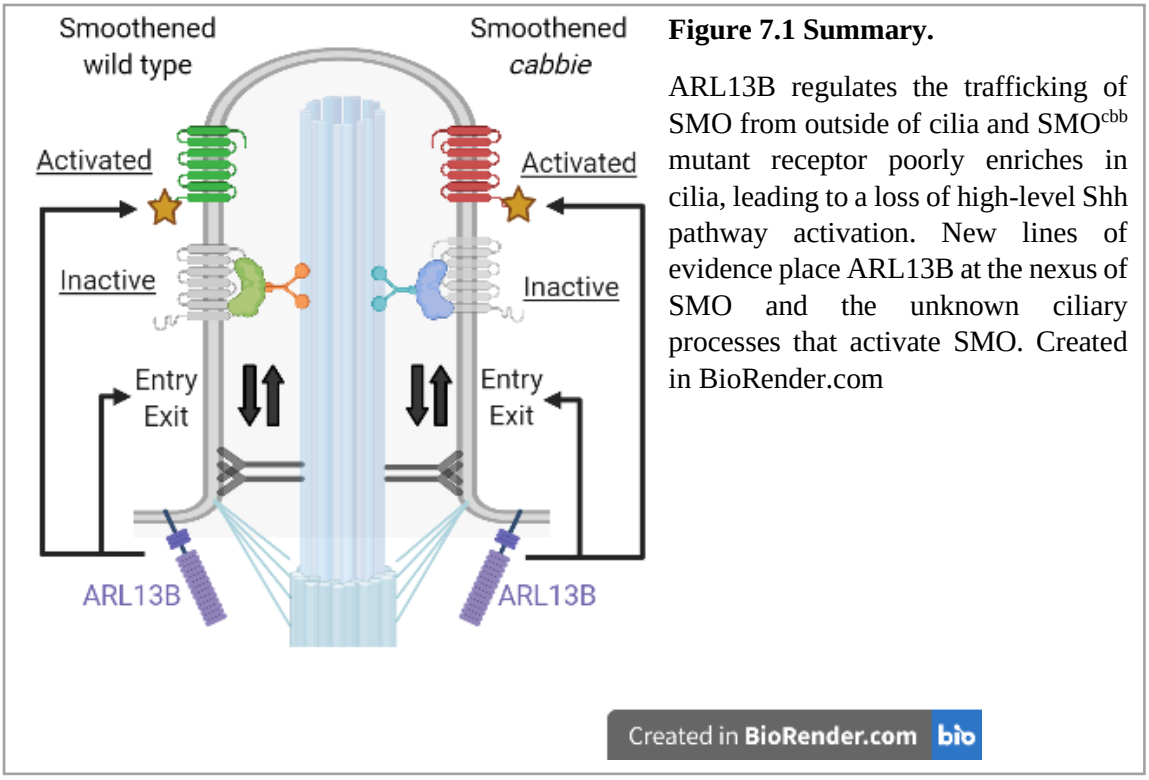

Figure 7.1 Summary.

ARL13B regulates the trafficking of SMO from outside of cilia and SMO^{cbb} mutant receptor poorly enriches in cilia, leading to a loss of high-level Shh pathway activation. New lines of evidence place ARL13B at the nexus of SMO and the unknown ciliary processes that activate SMO. Created in BioRender.com

7.3 Final conclusions

Advancement in genetics fuel scientific discoveries across disciplines. Since the advent of the knockout mouse, we've learned a great deal from generating genetic knockouts. The loss of a gene gave insight into that gene's biological function. However, knocking out a gene is like taking

a sledgehammer to a system, sometimes crippling it. Moreover, because human disease rarely manifests as the complete loss of a gene. Even among ciliopathies, most disease-causing mutations are single residue changes. This thesis uses more delicate genetics to makes small changes to genes. By making single point mutations to two proteins, I have unlocked new knowledge of how they function in relation to the localization in cilia (**Figure 7.1**).

To begin to dissect the mechanisms by which Hh signaling relies on cilia we need more subtle genetic approaches. In this field, the best example is *Smo*. Loss of *Smo* is embryonic lethal at around E9.5, a stage at which Hh signaling only just begins to exert its influence. Because of its important role in development, there are few *Smo* mutations linked to human disease or *in vivo* models. Advancement in scientific discoveries are so often shaped by modeling disease, and so without a disease to model there is a clear lack of knowledge surrounding *Smo*. Moreover, null mutations deplete a protein entirely, making it difficult to study how cilia regulate SMO if SMO is absent. To better understand SMO function and how it is controlled by the unknown ciliary processes that regulate it, we need more delicate genetics that make small changes to SMO while retaining the presence of the protein.

In this body of work, I showed that the Smo^{cbb} mutant provides a unique opportunity to study SMO function and activation. Through this mutant, I have presented evidence that ARL13B functions to regulate SMO activation, either through SMO trafficking to cilia or the unknown ciliary processes that activate SMO. I hope that my work will help fill fundamental gaps in our knowledge of SMO activation and cilia, and provide the field with a deeper, more complete understanding of the relationship between cilia and Hh signaling.

8.0 References

Aanstad, P., Santos, N., Corbit, K. C., Scherz, P. J., Trinh le, A., Salvenmoser, W., Huisken, J., Reiter, J. F., and Stainier, D. Y. 2009. 'The extracellular domain of Smoothened regulates ciliary localization and is required for high-level Hh signaling', *Curr Biol*, 19: 1034-9.

Adams, G. M., Huang, B., and Luck, D. J. 1982. 'Temperature-Sensitive, Assembly-Defective Flagella Mutants of CHLAMYDOMONAS REINHARDTII', *Genetics*, 100: 579-86.

Alcedo, J., Ayzenzon, M., Von Ohlen, T., Noll, M., and Hooper, J. E. 1996. 'The Drosophila smoothened gene encodes a seven-pass membrane protein, a putative receptor for the hedgehog signal', *Cell*, 86: 221-32.

Alexandre, Cyrille, Jacinto, Antonio, and Ingham, Philip W. 1996. 'Transcriptional activation of hedgehog target genes in Drosophila is mediated directly by the cubitus interruptus protein, a member of the GLI family of zinc finger DNA-binding proteins', *Genes Dev*, 10: 2003-13.

Alkanderi, S., Molinari, E., Shaheen, R., Elmaghloob, Y., Stephen, L. A., Sammut, V., Ramsbottom, S. A., Srivastava, S., Cairns, G., Edwards, N., Rice, S. J., Ewida, N., Alhashem, A., White, K., Miles, C. G., Steel, D. H., Alkuraya, F. S., Ismail, S., and Sayer, J. A. 2018. 'ARL3 Mutations Cause Joubert Syndrome by Disrupting Ciliary Protein Composition', *Am J Hum Genet*, 103: 612-20.

Allen, B. L., Song, J. Y., Izzi, L., Althaus, I. W., Kang, J. S., Charron, F., Krauss, R. S., and McMahon, A. P. 2011. 'Overlapping roles and collective requirement for the coreceptors GAS1, CDO, and BOC in SHH pathway function', *Dev Cell*, 20: 775-87.

Ansley, S. J., Badano, J. L., Blacque, O. E., Hill, J., Hoskins, B. E., Leitch, C. C., Kim, J. C., Ross, A. J., Eichers, E. R., Teslovich, T. M., Mah, A. K., Johnsen, R. C., Cavender, J. C., Lewis, R. A., Leroux, M. R., Beales, P. L., and Katsanis, N. 2003. 'Basal body dysfunction is a likely cause of pleiotropic Bardet-Biedl syndrome', *Nature*, 425: 628-33.

Arber, Silvia, Han, Barbara, Mendelsohn, Monica, Smith, Michael, Jessell, Thomas M, and Sockanathan, Shanthini. 1999. 'Requirement for the homeobox gene Hb9 in the consolidation of motor neuron identity', *Neuron*, 23: 659-74.

Arensdorf, A. M., Dillard, M. E., Menke, J. M., Frank, M. W., Rock, C. O., and Ogden, S. K. 2017. 'Sonic Hedgehog Activates Phospholipase A2 to Enhance Smoothened Ciliary Translocation', *Cell Rep*, 19: 2074-87.

Aza-Blanc, P., Lin, H. Y., Ruiz i Altaba, A., and Kornberg, T. B. 2000. 'Expression of the vertebrate Gli proteins in Drosophila reveals a distribution of activator and repressor activities', *Development*, 127: 4293-301.

Aza-Blanc, P., Ramirez-Weber, F. A., Laget, M. P., Schwartz, C., and Kornberg, T. B. 1997. 'Proteolysis that is inhibited by hedgehog targets Cubitus interruptus protein to the nucleus and converts it to a repressor', *Cell*, 89: 1043-53.

Bachmann-Gagescu, R, Dempsey, JC, Phelps, IG, O'Roak, BJ, Knutzen, DM, Rue, TC, Ishak, GE, Isabella, CR, Gorden, N, and Adkins, J. 2015. 'Joubert syndrome: a model for untangling recessive disorders with extreme genetic heterogeneity', *Journal of medical genetics*, 52: 514-22.

Badgandi, H. B., Hwang, S. H., Shimada, I. S., Loriot, E., and Mukhopadhyay, S. 2017. 'Tubby family proteins are adapters for ciliary trafficking of integral membrane proteins', *J Cell Biol*, 216: 743-60.

Baker, K., and Beales, P. L. 2009. 'Making sense of cilia in disease: the human ciliopathies', *Am J Med Genet C Semin Med Genet*, 151C: 281-95.

Bale, A. E., and Yu, K. P. 2001. 'The hedgehog pathway and basal cell carcinomas', *Hum Mol Genet*, 10: 757-62.

Bangs, F., and Anderson, K. V. 2017. 'Primary Cilia and Mammalian Hedgehog Signaling', *Cold Spring Harb Perspect Biol*, 9.

Bangs, F. K., Schrode, N., Hadjantonakis, A. K., and Anderson, K. V. 2015. 'Lineage specificity of primary cilia in the mouse embryo', *Nat Cell Biol*, 17: 113-22.

Bansal, R., Engle, S. E., Antonellis, P. J., Whitehouse, L. S., Baucum, A. J., 2nd, Cummins, T. R., Reiter, J. F., and Berbari, N. F. 2019. 'Hedgehog Pathway Activation Alters Ciliary Signaling in Primary Hypothalamic Cultures', *Front Cell Neurosci*, 13: 266.

Barr, M. M., and Sternberg, P. W. 1999. 'A polycystic kidney-disease gene homologue required for male mating behaviour in C. elegans', *Nature*, 401: 386-9.

Barral, D. C., Garg, S., Casalou, C., Watts, G. F., Sandoval, J. L., Ramalho, J. S., Hsu, V. W., and Brenner, M. B. 2012. 'Arl13b regulates endocytic recycling traffic', *Proc Natl Acad Sci U S A*, 109: 21354-9.

Barzi, M., Berenguer, J., Menendez, A., Alvarez-Rodriguez, R., and Pons, S. 2010. 'Sonic-hedgehog-mediated proliferation requires the localization of PKA to the cilium base', *J Cell Sci*, 123: 62-9.

Barzi, M., Kostrz, D., Menendez, A., and Pons, S. 2011. 'Sonic Hedgehog-induced proliferation requires specific Galpha inhibitory proteins', *J Biol Chem*, 286: 8067-74.

Bay, S. N., Long, A. B., and Caspary, T. 2018. 'Disruption of the ciliary GTPase Arl13b suppresses Sonic hedgehog overactivation and inhibits medulloblastoma formation', *Proc Natl Acad Sci U S A*, 115: 1570-75.

Belloni, E., Muenke, M., Roessler, E., Traverso, G., Siegel-Bartelt, J., Frumkin, A., Mitchell, H. F., Donis-Keller, H., Helms, C., Hing, A. V., Heng, H. H., Koop, B., Martindale, D., Rommens, J. M., Tsui, L. C., and Scherer, S. W. 1996. 'Identification of Sonic hedgehog as a candidate gene responsible for holoprosencephaly', *Nat Genet*, 14: 353-6.

Berbari, N. F., Johnson, A. D., Lewis, J. S., Askwith, C. C., and Mykytyn, K. 2008a. 'Identification of ciliary localization sequences within the third intracellular loop of G protein-coupled receptors', *Mol Biol Cell*, 19: 1540-7.

Berbari, N. F., Lewis, J. S., Bishop, G. A., Askwith, C. C., and Mykytyn, K. 2008b. 'Bardet-Biedl syndrome proteins are required for the localization of G protein-coupled receptors to primary cilia', *Proc Natl Acad Sci U S A*, 105: 4242-6.

Berbari, N. F., Pasek, R. C., Malarkey, E. B., Yazdi, S. M. Z., McNair, A. D., Lewis, W. R., Nagy, T. R., Kesterson, R. A., and Yoder, B. K. 2013. 'Leptin resistance is a secondary consequence of the obesity in ciliopathy mutant mice', *Proceedings of the National Academy of Sciences*, 110: 7796-801.

Bergmann, C., Guay-Woodford, L. M., Harris, P. C., Horie, S., Peters, D. J. M., and Torres, V. E. 2018. 'Polycystic kidney disease', *Nature Reviews Disease Primers*, 4: 1-24.

Bielas, S. L., Silhavy, J. L., Brancati, F., Kisseleva, M. V., Al-Gazali, L., Sztriha, L., Bayoumi, R. A., Zaki, M. S., Abdel-Aleem, A., Rosti, R. O., Kayserili, H., Swistun, D., Scott, L. C., Bertini, E., Boltshauser, E., Fazzi, E., Travaglini, L., Field, S. J., Gayral, S., Jacoby, M., Schurmans, S., Dallapiccola, B., Majerus, P. W., Valente, E. M., and Gleeson, J. G. 2009. 'Mutations in INPP5E, encoding inositol polyphosphate-5-phosphatase E, link phosphatidyl inositol signaling to the ciliopathies', *Nat Genet*, 41: 1032-6.

Bishop, G. A., Berbari, N. F., Lewis, J., and Mykytyn, K. 2007. 'Type III adenylyl cyclase localizes to primary cilia throughout the adult mouse brain', *J Comp Neurol*, 505: 562-71.

Bitgood, M. J., Shen, L., and McMahon, A. P. 1996. 'Sertoli cell signaling by Desert hedgehog regulates the male germline', *Curr Biol*, 6: 298-304.

Blassberg, R., Macrae, J. I., Briscoe, J., and Jacob, J. 2016. 'Reduced cholesterol levels impair Smoothened activation in Smith-Lemli-Opitz syndrome', *Hum Mol Genet*, 25: 693-705.

Boehlke, C., Bashkurov, M., Buescher, A., Krick, T., John, A. K., Nitschke, R., Walz, G., and Kuehn, E. W. 2010. 'Differential role of Rab proteins in ciliary trafficking: Rab23 regulates smoothened levels', *J Cell Sci*, 123: 1460-7.

Boettger, L. M., Handsaker, R. E., Zody, M. C., and McCarroll, S. A. 2012. 'Structural haplotypes and recent evolution of the human 17q21.31 region', *Nat Genet*, 44: 881-5.

Brailov, I., Bancila, M., Brisorgueil, M. J., Miquel, M. C., Hamon, M., and Verge, D. 2000. 'Localization of 5-HT(6) receptors at the plasma membrane of neuronal cilia in the rat brain', *Brain Res*, 872: 271-5.

Breslow, D. K., Koslover, E. F., Seydel, F., Spakowitz, A. J., and Nachury, M. V. 2013. 'An in vitro assay for entry into cilia reveals unique properties of the soluble diffusion barrier', *J Cell Biol*, 203: 129-47.

Briscoe, J., Chen, Y., Jessell, T. M., and Struhl, G. 2001. 'A hedgehog-insensitive form of patched provides evidence for direct long-range morphogen activity of sonic hedgehog in the neural tube', *Mol Cell*, 7: 1279-91.

Briscoe, J., Pierani, A., Jessell, T. M., and Ericson, J. 2000. 'A homeodomain protein code specifies progenitor cell identity and neuronal fate in the ventral neural tube', *Cell*, 101: 435-45.

Briscoe, J., Sussel, L., Serup, P., Hartigan-O'Connor, D., Jessell, T. M., Rubenstein, J. L., and Ericson, J. 1999. 'Homeobox gene Nkx2.2 and specification of neuronal identity by graded Sonic hedgehog signalling', *Nature*, 398: 622-7.

Briscoe, J., and Therond, P. P. 2013. 'The mechanisms of Hedgehog signalling and its roles in development and disease', *Nat Rev Mol Cell Biol*, 14: 416-29.

Buck, Linda, and Axel, Richard. 1991. 'A novel multigene family may encode odorant receptors: a molecular basis for odor recognition', *Cell*, 65: 175-87.

Bullitt, Elizabeth. 1990. 'Expression of c-fos-like protein as a marker for neuronal activity following noxious stimulation in the rat', *Journal of Comparative Neurology*, 296: 517-30.

Byrne, E. F. X., Sircar, R., Miller, P. S., Hedger, G., Luchetti, G., Nachtergaele, S., Tully, M. D., Mydock-McGrane, L., Covey, D. F., Rambo, R. P., Sansom, M. S. P., Newstead, S., Rohatgi, R., and Siebold, C. 2016. 'Structural basis of Smoothened regulation by its extracellular domains', *Nature*, 535: 517-22.

Byrne, Eamon FX, Luchetti, Giovanni, Rohatgi, Rajat, and Siebold, Christian. 2018. 'Multiple ligand binding sites regulate the Hedgehog signal transducer Smoothened in vertebrates', *Current opinion in cell biology*, 51: 81-88.

Cano, D. A., Murcia, N. S., Pazour, G. J., and Hebrok, M. 2004. 'Orpk mouse model of polycystic kidney disease reveals essential role of primary cilia in pancreatic tissue organization', *Development*, 131: 3457-67.

Cantagrel, V., Silhavy, J. L., Bielas, S. L., Swistun, D., Marsh, S. E., Bertrand, J. Y., Audollent, S., Attie-Bitach, T., Holden, K. R., Dobyns, W. B., Traver, D., Al-Gazali, L., Ali, B. R., Lindner, T. H., Caspary, T., Otto, E. A., Hildebrandt, F., Glass, I. A., Logan, C. V., Johnson, C. A., Bennett, C., Brancati, F., International Joubert Syndrome Related Disorders Study, Group, Valente, E. M., Woods, C. G., and Gleeson, J. G. 2008. 'Mutations in the cilia gene ARL13B lead to the classical form of Joubert syndrome', *Am J Hum Genet*, 83: 170-9.

Casalou, C., Seixas, C., Portelinha, A., Pintado, P., Barros, M., Ramalho, J. S., Lopes, S. S., and Barral, D. C. 2014. 'Arl13b and the non-muscle myosin heavy chain IIA are required for circular dorsal ruffle formation and cell migration', *J Cell Sci*, 127: 2709-22.

Caspary, T., Garcia-Garcia, M. J., Huangfu, D., Eggenschwiler, J. T., Wyler, M. R., Rakeman, A. S., Alcorn, H. L., and Anderson, K. V. 2002. 'Mouse Dispatched homolog1 is required for long-range, but not juxtacrine, Hh signaling', *Curr Biol*, 12: 1628-32.

Caspary, T., Larkins, C. E., and Anderson, K. V. 2007. 'The graded response to Sonic Hedgehog depends on cilia architecture', *Dev Cell*, 12: 767-78.

Cavenagh, M. M., Breiner, M., Schurmann, A., Rosenwald, A. G., Terui, T., Zhang, C., Randazzo, P. A., Adams, M., Joost, H. G., and Kahn, R. A. 1994. 'ADP-ribosylation factor (ARF)-like 3, a new member of the ARF family of GTP-binding proteins cloned from human and rat tissues', *J Biol Chem*, 269: 18937-42.

Cevik, S., Hori, Y., Kaplan, O. I., Kida, K., Toivenon, T., Foley-Fisher, C., Cottell, D., Katada, T., Kontani, K., and Blacque, O. E. 2010. 'Joubert syndrome Arl13b functions at ciliary membranes and stabilizes protein transport in Caenorhabditis elegans', *J Cell Biol*, 188: 953-69.

Cevik, S., Sanders, A. A., Van Wijk, E., Boldt, K., Clarke, L., van Reeuwijk, J., Hori, Y., Horn, N., Hetterschijt, L., Wdowicz, A., Mullins, A., Kida, K., Kaplan, O. I., van Beersum, S. E., Man Wu, K., Letteboer, S. J., Mans, D. A., Katada, T., Kontani, K., Ueffing, M., Roepman, R., Kremer, H., and Blacque, O. E. 2013. 'Active transport and diffusion barriers restrict Joubert Syndrome-associated ARL13B/ARL-13 to an Inv-like ciliary membrane subdomain', *PLoS Genet*, 9: e1003977.

Chaki, Moumita, Airik, Rannar, Ghosh, Amiya K, Giles, Rachel H, Chen, Rui, Slaats, Gisela G, Wang, Hui, Hurd, Toby W, Zhou, Weibin, and Cluckey, Andrew. 2012. 'Exome capture reveals ZNF423 and CEP164 mutations, linking renal ciliopathies to DNA damage response signaling', *Cell*, 150: 533-48.

Chambers, Adam P, Sandoval, Darleen A, and Seeley, Randy J. 2013. 'Integration of satiety signals by the central nervous system', *Current Biology*, 23: R379-R88.

Chavez, M., Ena, S., Van Sande, J., de Kerchove d'Exaerde, A., Schurmans, S., and Schiffmann, S. N. 2015. 'Modulation of Ciliary Phosphoinositide Content Regulates Trafficking and Sonic Hedgehog Signaling Output', *Dev Cell*, 34: 338-50.

Chen, J. K., Taipale, J., Cooper, M. K., and Beachy, P. A. 2002a. 'Inhibition of Hedgehog signaling by direct binding of cyclopamine to Smoothened', *Genes Dev*, 16: 2743-8.

Chen, J. K., Taipale, J., Young, K. E., Maiti, T., and Beachy, P. A. 2002b. 'Small molecule modulation of Smoothened activity', *Proc Natl Acad Sci U S A*, 99: 14071-6.

Chen, W., Ren, X. R., Nelson, C. D., Barak, L. S., Chen, J. K., Beachy, P. A., de Sauvage, F., and Lefkowitz, R. J. 2004. 'Activity-dependent internalization of smoothened mediated by beta-arrestin 2 and GRK2', *Science*, 306: 2257-60.

Chen, Y., Sasai, N., Ma, G., Yue, T., Jia, J., Briscoe, J., and Jiang, J. 2011. 'Sonic Hedgehog dependent phosphorylation by CK1alpha and GRK2 is required for ciliary accumulation and activation of smoothened', *PLoS Biol*, 9: e1001083.

Chess, A., Simon, I., Cedar, H., and Axel, R. 1994. 'Allelic inactivation regulates olfactory receptor gene expression', *Cell*, 78: 823-34.

Chiang, Annie P, Nishimura, Darryl, Searby, Charles, Elbedour, Khalil, Carmi, Rivka, Ferguson, Amanda L, Secrist, Jenifer, Braun, Terry, Casavant, Thomas, and Stone, Edwin M. 2004. 'Comparative genomic analysis identifies an ADP-ribosylation factor–like gene as the cause of Bardet-Biedl syndrome (BBS3)', *The American Journal of Human Genetics*, 75: 475-84.

Chiang, C., Litingtung, Y., Lee, E., Young, K. E., Corden, J. L., Westphal, H., and Beachy, P. A. 1996. 'Cyclopia and defective axial patterning in mice lacking Sonic hedgehog gene function', *Nature*, 383: 407-13.

Chih, B., Liu, P., Chinn, Y., Chalouni, C., Komuves, L. G., Hass, P. E., Sandoval, W., and Peterson, A. S. 2011. 'A ciliopathy complex at the transition zone protects the cilia as a privileged membrane domain', *Nat Cell Biol*, 14: 61-72.

Chung, M. I., Kwon, T., Tu, F., Brooks, E. R., Gupta, R., Meyer, M., Baker, J. C., Marcotte, E. M., and Wallingford, J. B. 2014. 'Coordinated genomic control of ciliogenesis and cell movement by RFX2', *Elife*, 3: e01439.

Chung, M. I., Peyrot, S. M., LeBoeuf, S., Park, T. J., McGary, K. L., Marcotte, E. M., and Wallingford, J. B. 2012. 'RFX2 is broadly required for ciliogenesis during vertebrate development', *Dev Biol*, 363: 155-65.

Collingridge, P., Brownlee, C., and Wheeler, G. L. 2013. 'Compartmentalized calcium signaling in cilia regulates intraflagellar transport', *Curr Biol*, 23: 2311-18.

Consortium, C. elegans Sequencing. 1998. 'Genome sequence of the nematode C. elegans: a platform for investigating biology', *Science*, 282: 2012-8.

Constable, S., Long, A. B., Floyd, K. A., Schurmans, S., and Caspary, T. 2020. 'The ciliary phosphatidylinositol phosphatase Inpp5e plays positive and negative regulatory roles in Shh signaling', *Development*, 147.

Cooper, A. F., Yu, K. P., Brueckner, M., Brailey, L. L., Johnson, L., McGrath, J. M., and Bale, A. E. 2005. 'Cardiac and CNS defects in a mouse with targeted disruption of suppressor of fused', *Development*, 132: 4407-17.

Corbit, K. C., Aanstad, P., Singla, V., Norman, A. R., Stainier, D. Y., and Reiter, J. F. 2005. 'Vertebrate Smoothened functions at the primary cilium', *Nature*, 437: 1018-21.

Corcoran, R. B., and Scott, M. P. 2006. 'Oxysterols stimulate Sonic hedgehog signal transduction and proliferation of medulloblastoma cells', *Proc Natl Acad Sci U S A*, 103: 8408-13.

Cornec-Le Gall, E., Torres, V. E., and Harris, P. C. 2018. 'Genetic Complexity of Autosomal Dominant Polycystic Kidney and Liver Diseases', *J Am Soc Nephrol*, 29: 13-23.

Cortellino, S., Wang, C., Wang, B., Bassi, M. R., Caretti, E., Champeval, D., Calmont, A., Jarnik, M., Burch, J., Zaret, K. S., Larue, L., and Bellacosa, A. 2009. 'Defective ciliogenesis, embryonic lethality and severe impairment of the Sonic Hedgehog pathway caused by inactivation of the mouse complex A intraflagellar transport gene Ift122/Wdr10, partially overlapping with the DNA repair gene Med1/Mbd4', *Dev Biol*, 325: 225-37.

Cowley, Michael A, Smart, James L, Rubinstein, Marcelo, Cerdán, Marcelo G, Diano, Sabrina, Horvath, Tamas L, Cone, Roger D, and Low, Malcolm J. 2001. 'Leptin activates anorexigenic POMC neurons through a neural network in the arcuate nucleus', *Nature*, 411: 480-84.

D'Souza-Schorey, C., and Chavrier, P. 2006. 'ARF proteins: roles in membrane traffic and beyond', *Nat Rev Mol Cell Biol*, 7: 347-58.

Dann, Charles E, Hsieh, Jen-Chih, Rattner, Amir, Sharma, Divya, Nathans, Jeremy, and Leahy, Daniel J. 2001. 'Insights into Wnt binding and signalling from the structures of two Frizzled cysteine-rich domains', *Nature*, 412: 86-90.

Davenport, J. R., Watts, A. J., Roper, V. C., Croyle, M. J., van Groen, T., Wyss, J. M., Nagy, T. R., Kesterson, R. A., and Yoder, B. K. 2007. 'Disruption of intraflagellar transport in adult mice leads to obesity and slow-onset cystic kidney disease', *Curr Biol*, 17: 1586-94.

DeCamp, D. L., Thompson, T. M., de Sauvage, F. J., and Lerner, M. R. 2000. 'Smoothened activates Galphai-mediated signaling in frog melanophores', *J Biol Chem*, 275: 26322-7.

Delling, M., Indzhykulian, A. A., Liu, X., Li, Y., Xie, T., Corey, D. P., and Clapham, D. E. 2016. 'Primary cilia are not calcium-responsive mechanosensors', *Nature*, 531: 656-60.

Desai, P. B., Stuck, M. W., Lv, B., and Pazour, G. J. 2020. 'Ubiquitin links smoothened to intraflagellar transport to regulate Hedgehog signaling', *J Cell Biol*, 219.

Deshpande, I., Liang, J., Hedeen, D., Roberts, K. J., Zhang, Y., Ha, B., Latorraca, N. R., Faust, B., Dror, R. O., Beachy, P. A., Myers, B. R., and Manglik, A. 2019. 'Smoothened stimulation by membrane sterols drives Hedgehog pathway activity', *Nature*, 571: 284-88.

Dessaud, E., Ribes, V., Balaskas, N., Yang, L. L., Pierani, A., Kicheva, A., Novitch, B. G., Briscoe, J., and Sasai, N. 2010. 'Dynamic assignment and maintenance of positional identity in the ventral neural tube by the morphogen sonic hedgehog', *PLoS Biol*, 8: e1000382.

Dessaud, E., Yang, L. L., Hill, K., Cox, B., Ulloa, F., Ribeiro, A., Mynett, A., Novitch, B. G., and Briscoe, J. 2007. 'Interpretation of the sonic hedgehog morphogen gradient by a temporal adaptation mechanism', *Nature*, 450: 717-20.

Ding, Q., Motoyama, J., Gasca, S., Mo, R., Sasaki, H., Rossant, J., and Hui, C. C. 1998. 'Diminished Sonic hedgehog signaling and lack of floor plate differentiation in Gli2 mutant mice', *Development*, 125: 2533-43.

Dobell, Clifford. 1932. 'Antony van Leeuwenhoek and his" Little Animals." Being Some Account of the Father of Protozoology and Bacteriology and his Multifarious Discoveries in these Disciplines. Collected, Translated, and Edited, from his Printed Works, Unpublished Manuscripts, and Contemporary Records. Published on the 300th Anniversary of his Birth', *Antony van Leeuwenhoek and his" Little Animals." Being Some Account of the Father of Protozoology and Bacteriology and his Multifarious Discoveries in these Disciplines. Collected, Translated, and Edited, from his Printed Works, Unpublished Manuscripts, and Contemporary Records. Published on the 300th Anniversary of his Birth.*

Doherty, D. 2009. 'Joubert syndrome: insights into brain development, cilium biology, and complex disease', *Semin Pediatr Neurol*, 16: 143-54.

Domire, J. S., Green, J. A., Lee, K. G., Johnson, A. D., Askwith, C. C., and Mykytyn, K. 2011. 'Dopamine receptor 1 localizes to neuronal cilia in a dynamic process that requires the Bardet-Biedl syndrome proteins', *Cell Mol Life Sci*, 68: 2951-60.

Dorn, K. V., Hughes, C. E., and Rohatgi, R. 2012. 'A Smoothened-Evc2 complex transduces the Hedgehog signal at primary cilia', *Dev Cell*, 23: 823-35.

Douglas, A. E., Heim, J. A., Shen, F., Almada, L. L., Riobo, N. A., Fernandez-Zapico, M. E., and Manning, D. R. 2011. 'The alpha subunit of the G protein G13 regulates activity of one or more Gli transcription factors independently of smoothened', *J Biol Chem*, 286: 30714-22.

Duldulao, N. A., Lee, S., and Sun, Z. 2009. 'Cilia localization is essential for in vivo functions of the Joubert syndrome protein Arl13b/Scorpion', *Development*, 136: 4033-42.

Dwyer, J. R., Sever, N., Carlson, M., Nelson, S. F., Beachy, P. A., and Parhami, F. 2007. 'Oxysterols are novel activators of the hedgehog signaling pathway in pluripotent mesenchymal cells', *J Biol Chem*, 282: 8959-68.

Dyson, J. M., Conduit, S. E., Feeney, S. J., Hakim, S., DiTommaso, T., Fulcher, A. J., Sriratana, A., Ramm, G., Horan, K. A., Gurung, R., Wicking, C., Smyth, I., and Mitchell, C. A. 2017. 'INPP5E regulates phosphoinositide-dependent cilia transition zone function', *J Cell Biol*, 216: 247-63.

East, M. P., Bowzard, J. B., Dacks, J. B., and Kahn, R. A. 2012. 'ELMO domains, evolutionary and functional characterization of a novel GTPase-activating protein (GAP) domain for Arf protein family GTPases', *J Biol Chem*, 287: 39538-53.

Echelard, Y., Epstein, D. J., St-Jacques, B., Shen, L., Mohler, J., McMahon, J. A., and McMahon, A. P. 1993. 'Sonic hedgehog, a member of a family of putative signaling molecules, is implicated in the regulation of CNS polarity', *Cell*, 75: 1417-30.

Eggenschwiler, J. T., Bulgakov, O. V., Qin, J., Li, T., and Anderson, K. V. 2006. 'Mouse Rab23 regulates hedgehog signaling from smoothened to Gli proteins', *Dev Biol*, 290: 1-12.

Eggenschwiler, J. T., Espinoza, E., and Anderson, K. V. 2001. 'Rab23 is an essential negative regulator of the mouse Sonic hedgehog signalling pathway', *Nature*, 412: 194-8.

Eguether, T., San Agustin, J. T., Keady, B. T., Jonassen, J. A., Liang, Y., Francis, R., Tobita, K., Johnson, C. A., Abdelhamed, Z. A., Lo, C. W., and Pazour, G. J. 2014. 'IFT27 links the BBSome to IFT for maintenance of the ciliary signaling compartment', *Dev Cell*, 31: 279-90.

Eichel, K., and von Zastrow, M. 2018. 'Subcellular Organization of GPCR Signaling', *Trends Pharmacol Sci*, 39: 200-08.

Eickelbeck, Dennis, Karapinar, Raziye, Jack, Alexander, Suess, Sandra T, Barzan, Ruxandra, Azimi, Zohre, Surdin, Tatjana, Grömmke, Michelle, Mark, Melanie D, and Gerwert, Klaus. 2019. 'CaMello-XR enables visualization and optogenetic control of G q/11 signals and receptor trafficking in GPCR-specific domains', *Communications biology*, 2: 60.

Endoh-Yamagami, S., Evangelista, M., Wilson, D., Wen, X., Theunissen, J. W., Phamluong, K., Davis, M., Scales, S. J., Solloway, M. J., de Sauvage, F. J., and Peterson, A. S. 2009. 'The mammalian Cos2 homolog Kif7 plays an essential role in modulating Hh signal transduction during development', *Curr Biol*, 19: 1320-6.

Ericson, J., Briscoe, J., Rashbass, P., van Heyningen, V., and Jessell, T. M. 1997. 'Graded sonic hedgehog signaling and the specification of cell fate in the ventral neural tube', *Cold Spring Harb Symp Quant Biol*, 62: 451-66.

Ericson, J., Morton, S., Kawakami, A., Roelink, H., and Jessell, T. M. 1996. 'Two critical periods of Sonic Hedgehog signaling required for the specification of motor neuron identity', *Cell*, 87: 661-73.

Fan, C. W., Chen, B., Franco, I., Lu, J., Shi, H., Wei, S., Wang, C., Wu, X., Tang, W., Roth, M. G., Williams, N. S., Hirsch, E., Chen, C., and Lum, L. 2014. 'The Hedgehog pathway effector smoothened exhibits signaling competency in the absence of ciliary accumulation', *Chem Biol*, 21: 1680-9.

Farzan, Shohreh F, Ascano Jr, Manuel, Ogden, Stacey K, Sanial, Matthieu, Brigui, Amira, Plessis, Anne, and Robbins, David J. 2008. 'Costal2 functions as a kinesin-like protein in the hedgehog signal transduction pathway', *Current Biology*, 18: 1215-20.

Fawcett, Don W, and Porter, Keith R. 1954. 'A study of the fine structure of ciliated epithelia', *Journal of Morphology*, 94: 221-81.

Ferent, J., Constable, S., Gigante, E. D., Yam, P. T., Mariani, L. E., Legue, E., Liem, K. F., Jr., Caspary, T., and Charron, F. 2019. 'The Ciliary Protein Arl13b Functions Outside of the Primary Cilium in Shh-Mediated Axon Guidance', *Cell Rep*, 29: 3356-66 e3.

Firestone, A. J., Weinger, J. S., Maldonado, M., Barlan, K., Langston, L. D., O'Donnell, M., Gelfand, V. I., Kapoor, T. M., and Chen, J. K. 2012. 'Small-molecule inhibitors of the AAA+ ATPase motor cytoplasmic dynein', *Nature*, 484: 125-9.

Flock, T., Hauser, A. S., Lund, N., Gloriam, D. E., Balaji, S., and Babu, M. M. 2017. 'Selectivity determinants of GPCR-G-protein binding', *Nature*, 545: 317-22.

Follit, J. A., Li, L., Vucica, Y., and Pazour, G. J. 2010. 'The cytoplasmic tail of fibrocystin contains a ciliary targeting sequence', *J Cell Biol*, 188: 21-8.

Forsythe, E., and Beales, P. L. 2013. 'Bardet-Biedl syndrome', *Eur J Hum Genet*, 21: 8-13.

Frank-Kamenetsky, M., Zhang, X. M., Bottega, S., Guicherit, O., Wichterle, H., Dudek, H., Bumcrot, D., Wang, F. Y., Jones, S., Shulok, J., Rubin, L. L., and Porter, J. A. 2002. 'Small-molecule modulators of Hedgehog signaling: identification and characterization of Smoothened agonists and antagonists', *J Biol*, 1: 10.

Fry, D., Dayton, B., Brodjian, S., Ogiela, C., Sidorowicz, H., Frost, L. J., McNally, T., Reilly, R. M., and Collins, C. A. 2006. 'Characterization of a neuronal cell line expressing native human melanin-concentrating hormone receptor 1 (MCHR1)', *Int J Biochem Cell Biol*, 38: 1290-9.

Fumoto, K., Hoogenraad, C. C., and Kikuchi, A. 2006. 'GSK-3beta-regulated interaction of BICD with dynein is involved in microtubule anchorage at centrosome', *EMBO J*, 25: 5670-82.

Fuse, Naoyuki, Maiti, Tapan, Wang, Baolin, Porter, Jeffery A, Hall, Traci M Tanaka, Leahy, Daniel J, and Beachy, Philip A. 1999. 'Sonic hedgehog protein signals not as a hydrolytic enzyme but as an apparent ligand for patched', *Proceedings of the National Academy of Sciences*, 96: 10992-99.

Garcia-Garcia, M. J., Eggenschwiler, J. T., Caspary, T., Alcorn, H. L., Wyler, M. R., Huangfu, D., Rakeman, A. S., Lee, J. D., Feinberg, E. H., Timmer, J. R., and Anderson, K. V. 2005. 'Analysis of mouse embryonic patterning and morphogenesis by forward genetics', *Proc Natl Acad Sci U S A*, 102: 5913-9.

Garcia-Gonzalo, F. R., Phua, S. C., Roberson, E. C., Garcia, G., 3rd, Abedin, M., Schurmans, S., Inoue, T., and Reiter, J. F. 2015. 'Phosphoinositides Regulate Ciliary Protein Trafficking to Modulate Hedgehog Signaling', *Dev Cell*, 34: 400-09.

Geng, L., Okuhara, D., Yu, Z., Tian, X., Cai, Y., Shibazaki, S., and Somlo, S. 2006. 'Polycystin-2 traffics to cilia independently of polycystin-1 by using an N-terminal RVxP motif', *J Cell Sci*, 119: 1383-95.

Gigante, E. D., Long, A. B., Ben-Ami, J., and Caspary, T. 2018. 'Hypomorphic Smo mutant with inefficient ciliary enrichment disrupts the highest level of vertebrate Hedgehog response', *Dev Biol*, 437: 152-62.

Gigante, E. D., Taylor, M. R., Ivanova, A. A., Kahn, R. A., and Caspary, T. 2020a. 'ARL13B regulates Sonic hedgehog signaling from outside primary cilia', *Elife*, 9: e50434.

Gigante, Eduardo D, Benaliouad, Faiza, Zamora-Olivencia, Veronica, and Wise, Roy A. 2016. 'Optogenetic activation of a lateral hypothalamic-ventral tegmental drive-reward pathway', *PLoS One*, 11: e0158885.

Gigante, Eduardo D, Taylor, Megan R, Ivanova, Anna A, Kahn, Richard A, and Caspary, Tamara. 2020b. 'Arl13b regulates Sonic Hedgehog signaling from outside primary cilia', *bioRxiv*: 711671.

Glazer, A. M., Wilkinson, A. W., Backer, C. B., Lapan, S. W., Gutzman, J. H., Cheeseman, I. M., and Reddien, P. W. 2010a. 'The Zn finger protein Iguana impacts Hedgehog signaling by promoting ciliogenesis', *Dev Biol*, 337: 148-56.

Glazer, Andrew M, Wilkinson, Alex W, Backer, Chelsea B, Lapan, Sylvain W, Gutzman, Jennifer H, Cheeseman, Iain M, and Reddien, Peter W. 2010b. 'The Zn finger protein Iguana impacts Hedgehog signaling by promoting ciliogenesis', *Developmental biology*, 337: 148-56.

Goetz, S. C., and Anderson, K. V. 2010. 'The primary cilium: a signalling centre during vertebrate development', *Nat Rev Genet*, 11: 331-44.

Goetz, S. C., Ocbina, P. J., and Anderson, K. V. 2009. 'The primary cilium as a Hedgehog signal transduction machine', *Methods Cell Biol*, 94: 199-222.

Goodrich, L. V., Johnson, R. L., Milenkovic, L., McMahon, J. A., and Scott, M. P. 1996. 'Conservation of the hedgehog/patched signaling pathway from flies to mice: induction of a mouse patched gene by Hedgehog', *Genes Dev*, 10: 301-12.

Goodrich, L. V., Milenkovic, L., Higgins, K. M., and Scott, M. P. 1997. 'Altered neural cell fates and medulloblastoma in mouse patched mutants', *Science*, 277: 1109-13.

Gotthardt, K., Lokaj, M., Koerner, C., Falk, N., Giessl, A., and Wittinghofer, A. 2015. 'A G-protein activation cascade from Arl13B to Arl3 and implications for ciliary targeting of lipidated proteins', *Elife*, 4.

Green, J. A., Schmid, C. L., Bley, E., Monsma, P. C., Brown, A., Bohn, L. M., and Mykytyn, K. 2016. 'Recruitment of beta-Arrestin into Neuronal Cilia Modulates Somatostatin Receptor Subtype 3 Ciliary Localization', *Mol Cell Biol*, 36: 223-35.

Guo, D. F., and Rahmouni, K. 2011. 'Molecular basis of the obesity associated with Bardet-Biedl syndrome', *Trends Endocrinol Metab*, 22: 286-93.

Hahn, H., Christiansen, J., Wicking, C., Zaphiropoulos, P. G., Chidambaram, A., Gerrard, B., Vorechovsky, I., Bale, A. E., Toftgard, R., Dean, M., and Wainwright, B. 1996. 'A mammalian patched homolog

is expressed in target tissues of sonic hedgehog and maps to a region associated with developmental abnormalities', *J Biol Chem*, 271: 12125-8.

Hammerschmidt, M., Bitgood, M. J., and McMahon, A. P. 1996. 'Protein kinase A is a common negative regulator of Hedgehog signaling in the vertebrate embryo', *Genes Dev*, 10: 647-58.

Hamon, M., Doucet, E., Lefevre, K., Miquel, M. C., Lanfumey, L., Insausti, R., Frechilla, D., Del Rio, J., and Verge, D. 1999. 'Antibodies and antisense oligonucleotide for probing the distribution and putative functions of central 5-HT6 receptors', *Neuropsychopharmacology*, 21: 68S-76S.

Han, Sarina, Miyoshi, Ko, Shikada, Sho, Amano, Genki, Wang, Yinshengzhuoma, Yoshimura, Takeshi, and Katayama, Taiichi. 2019. 'TULP3 is required for localization of membrane-associated proteins ARL13B and INPP5E to primary cilia', *Biochemical and biophysical research communications*, 509: 227-34.

Handel, M., Schulz, S., Stanarius, A., Schreff, M., Erdtmann-Vourliotis, M., Schmidt, H., Wolf, G., and Hollt, V. 1999. 'Selective targeting of somatostatin receptor 3 to neuronal cilia', *Neuroscience*, 89: 909-26.

Hanke-Gogokhia, C., Frederick, J. M., Zhang, H., and Baehr, W. 2018. 'Binary Function of ARL3-GTP Revealed by Gene Knockouts', *Adv Exp Med Biol*, 1074: 317-25.

Hanke-Gogokhia, C., Wu, Z., Gerstner, C. D., Frederick, J. M., Zhang, H., and Baehr, W. 2016. 'Arf-like Protein 3 (ARL3) Regulates Protein Trafficking and Ciliogenesis in Mouse Photoreceptors', *J Biol Chem*, 291: 7142-55.

Hanson, M. A., Cherezov, V., Griffith, M. T., Roth, C. B., Jaakola, V. P., Chien, E. Y., Velasquez, J., Kuhn, P., and Stevens, R. C. 2008. 'A specific cholesterol binding site is established by the 2.8 A structure of the human beta2-adrenergic receptor', *Structure*, 16: 897-905.

Hanson, M. A., Roth, C. B., Jo, E., Griffith, M. T., Scott, F. L., Reinhart, G., Desale, H., Clemons, B., Cahalan, S. M., Schuerer, S. C., Sanna, M. G., Han, G. W., Kuhn, P., Rosen, H., and Stevens, R. C. 2012. 'Crystal structure of a lipid G protein-coupled receptor', *Science*, 335: 851-5.

Harris, Peter C, and Torres, Vicente E. 2009. 'Polycystic kidney disease', *Annual review of medicine*, 60: 321-37.

Hatten, M. E., and Roussel, M. F. 2011. 'Development and cancer of the cerebellum', *Trends Neurosci*, 34: 134-42.

Haycraft, C. J., Banizs, B., Aydin-Son, Y., Zhang, Q., Michaud, E. J., and Yoder, B. K. 2005. 'Gli2 and Gli3 localize to cilia and require the intraflagellar transport protein polaris for processing and function', *PLoS Genet*, 1: e53.

Hedger, George, Koldsø, Heidi, Chavent, Matthieu, Siebold, Christian, Rohatgi, Rajat, and Sansom, Mark SP. 2019. 'Cholesterol interaction sites on the transmembrane domain of the hedgehog signal transducer and class FG protein-coupled receptor smoothened', *Structure*, 27: 549-59. e2.

Heydet, D., Chen, L. X., Larter, C. Z., Inglis, C., Silverman, M. A., Farrell, G. C., and Leroux, M. R. 2013. 'A truncating mutation of Alms1 reduces the number of hypothalamic neuronal cilia in obese mice', *Dev Neurobiol*, 73: 1-13.

Higginbotham, H., Eom, T. Y., Mariani, L. E., Bachleda, A., Hirt, J., Gukassyan, V., Cusack, C. L., Lai, C., Caspary, T., and Anton, E. S. 2012. 'Arl13b in primary cilia regulates the migration and placement of interneurons in the developing cerebral cortex', *Dev Cell*, 23: 925-38.

Higginbotham, Holden, Guo, Jiami, Yokota, Yukako, Umberger, Nicole L, Su, Chen-Ying, Li, Jingjun, Verma, Nisha, Hirt, Joshua, Caspary, Tamara, and Anton, ES. 2013. 'Arl13b-regulated activities of primary cilia are essential for the formation of the polarized radial glial scaffold', *Nature neuroscience*, 16: 1000.

Hori, Y., Kobayashi, T., Kikko, Y., Kontani, K., and Katada, T. 2008. 'Domain architecture of the atypical Arf-family GTPase Arl13b involved in cilia formation', *Biochem Biophys Res Commun*, 373: 119-24.

Houde, C., Dickinson, R. J., Houtzager, V. M., Cullum, R., Montpetit, R., Metzler, M., Simpson, E. M., Roy, S., Hayden, M. R., Hoodless, P. A., and Nicholson, D. W. 2006. 'Hippi is essential for node cilia assembly and Sonic hedgehog signaling', *Dev Biol*, 300: 523-33.

Huang, B., Rifkin, M. R., and Luck, D. J. 1977. 'Temperature-sensitive mutations affecting flagellar assembly and function in Chlamydomonas reinhardtii', *J Cell Biol*, 72: 67-85.

Huang, P., Nedelcu, D., Watanabe, M., Jao, C., Kim, Y., Liu, J., and Salic, A. 2016. 'Cellular Cholesterol Directly Activates Smoothened in Hedgehog Signaling', *Cell*, 166: 1176-87 e14.

Huang, P., and Schier, A. F. 2009. 'Dampened Hedgehog signaling but normal Wnt signaling in zebrafish without cilia', *Development*, 136: 3089-98.

Huang, P., Zheng, S., Wierbowski, B. M., Kim, Y., Nedelcu, D., Aravena, L., Liu, J., Kruse, A. C., and Salic, A. 2018. 'Structural Basis of Smoothened Activation in Hedgehog Signaling', *Cell*, 174: 312-24 e16.

Huangfu, D., and Anderson, K. V. 2005. 'Cilia and Hedgehog responsiveness in the mouse', *Proc Natl Acad Sci U S A*, 102: 11325-30.

———. 2006. 'Signaling from Smo to Ci/Gli: conservation and divergence of Hedgehog pathways from Drosophila to vertebrates', *Development*, 133: 3-14.

Huangfu, D., Liu, A., Rakeman, A. S., Murcia, N. S., Niswander, L., and Anderson, K. V. 2003. 'Hedgehog signalling in the mouse requires intraflagellar transport proteins', *Nature*, 426: 83-7.

Hui, Chi-Chung, Slusarski, Diane, Platt, Kenneth A, Holmgren, Robert, and Joyner, Alexandra L. 1994. 'Expression of three mouse homologs of the Drosophila segment polarity gene cubitus interruptus, Gli, Gli-2, and Gli-3, in ectoderm-and mesoderm-derived tissues suggests multiple roles during postimplantation development', *Dev Biol*, 162: 402-13.

Humbert, M. C., Weihbrecht, K., Searby, C. C., Li, Y., Pope, R. M., Sheffield, V. C., and Seo, S. 2012. 'ARL13B, PDE6D, and CEP164 form a functional network for INPP5E ciliary targeting', *Proc Natl Acad Sci U S A*, 109: 19691-6.

Humke, E. W., Dorn, K. V., Milenkovic, L., Scott, M. P., and Rohatgi, R. 2010. 'The output of Hedgehog signaling is controlled by the dynamic association between Suppressor of Fused and the Gli proteins', *Genes Dev*, 24: 670-82.

Hwang, Sun-Hee, Somatilaka, Bandarigoda N, Badgandi, Hemant, Palicharla, Vivek Reddy, Walker, Rebecca, Shelton, John M, Qian, Feng, and Mukhopadhyay, Saikat. 2019. 'Tulp3 regulates renal cystogenesis by trafficking of cystoproteins to cilia', *Current Biology*, 29: 790-802. e5.

Ingham, P. W., and McMahon, A. P. 2001. 'Hedgehog signaling in animal development: paradigms and principles', *Genes Dev*, 15: 3059-87.

Ingham, P. W., Nakano, Y., and Seger, C. 2011. 'Mechanisms and functions of Hedgehog signalling across the metazoa', *Nat Rev Genet*, 12: 393-406.

Ishikawa, H., Kubo, A., Tsukita, S., and Tsukita, S. 2005. 'Odf2-deficient mother centrioles lack distal/subdistal appendages and the ability to generate primary cilia', *Nat Cell Biol*, 7: 517-24.

Ivanova, A. A., Caspary, T., Seyfried, N. T., Duong, D. M., West, A. B., Liu, Z., and Kahn, R. A. 2017. 'Biochemical characterization of purified mammalian ARL13B protein indicates that it is an atypical GTPase and ARL3 guanine nucleotide exchange factor (GEF)', *J Biol Chem*, 292: 11091-108.

Izzi, L., Levesque, M., Morin, S., Laniel, D., Wilkes, B. C., Mille, F., Krauss, R. S., McMahon, A. P., Allen, B. L., and Charron, F. 2011. 'Boc and Gas1 each form distinct Shh receptor complexes with Ptch1 and are required for Shh-mediated cell proliferation', *Dev Cell*, 20: 788-801.

Jacobs, D. T., Silva, L. M., Allard, B. A., Schonfeld, M. P., Chatterjee, A., Talbott, G. C., Beier, D. R., and Tran, P. V. 2016. 'Dysfunction of intraflagellar transport-A causes hyperphagia-induced obesity and metabolic syndrome', *Dis Model Mech*, 9: 789-98.

Jacoby, M., Cox, J. J., Gayral, S., Hampshire, D. J., Ayub, M., Blockmans, M., Pernot, E., Kisseleva, M. V., Compere, P., Schiffmann, S. N., Gergely, F., Riley, J. H., Perez-Morga, D., Woods, C. G., and Schurmans, S. 2009. 'INPP5E mutations cause primary cilium signaling defects, ciliary instability and ciliopathies in human and mouse', *Nat Genet*, 41: 1027-31.

Jafurulla, Md, Kumar, G Aditya, Rao, Bhagyashree D, and Chattopadhyay, Amitabha. 2019. 'A critical analysis of molecular mechanisms underlying membrane cholesterol sensitivity of GPCRs.' in, *Cholesterol Modulation of Protein Function* (Springer).

Jan, L. Y., and Revel, J. P. 1974. 'Ultrastructural localization of rhodopsin in the vertebrate retina', *J Cell Biol*, 62: 257-73.

Janda, C. Y., Waghray, D., Levin, A. M., Thomas, C., and Garcia, K. C. 2012. 'Structural basis of Wnt recognition by Frizzled', *Science*, 337: 59-64.

Jansen, V., Alvarez, L., Balbach, M., Strunker, T., Hegemann, P., Kaupp, U. B., and Wachten, D. 2015. 'Controlling fertilization and cAMP signaling in sperm by optogenetics', *Elife*, 4.

Jeong, J., and McMahon, A. P. 2005. 'Growth and pattern of the mammalian neural tube are governed by partially overlapping feedback activities of the hedgehog antagonists patched 1 and Hhip1', *Development*, 132: 143-54.

Jiang, J. Y., Falcone, J. L., Curci, S., and Hofer, A. M. 2019. 'Direct visualization of cAMP signaling in primary cilia reveals up-regulation of ciliary GPCR activity following Hedgehog activation', *Proc Natl Acad Sci U S A*, 116: 12066-71.

Jin, H., White, S. R., Shida, T., Schulz, S., Aguiar, M., Gygi, S. P., Bazan, J. F., and Nachury, M. V. 2010. 'The conserved Bardet-Biedl syndrome proteins assemble a coat that traffics membrane proteins to cilia', *Cell*, 141: 1208-19.

Jin, X., Mohieldin, A. M., Muntean, B. S., Green, J. A., Shah, J. V., Mykytyn, K., and Nauli, S. M. 2014. 'Cilioplasm is a cellular compartment for calcium signaling in response to mechanical and chemical stimuli', *Cell Mol Life Sci*, 71: 2165-78.

Johnson, K. A., and Rosenbaum, J. L. 1992. 'Polarity of flagellar assembly in Chlamydomonas', *J Cell Biol*, 119: 1605-11.

Jonassen, J. A., San Agustin, J., Follit, J. A., and Pazour, G. J. 2008. 'Deletion of IFT20 in the mouse kidney causes misorientation of the mitotic spindle and cystic kidney disease', *J Cell Biol*, 183: 377-84.

Jung, B., Padula, D., Burtscher, I., Landerer, C., Lutter, D., Theis, F., Messias, A. C., Geerlof, A., Sattler, M., Kremmer, E., Boldt, K., Ueffing, M., and Lickert, H. 2016. 'Pitchfork and Gprasp2 Target Smoothened to the Primary Cilium for Hedgehog Pathway Activation', *PLoS One*, 11: e0149477.

Kahn, R. A., Bruford, E., Inoue, H., Logsdon, J. M., Jr., Nie, Z., Premont, R. T., Randazzo, P. A., Satake, M., Theibert, A. B., Zapp, M. L., and Cassel, D. 2008. 'Consensus nomenclature for the human ArfGAP domain-containing proteins', *J Cell Biol*, 182: 1039-44.

Kahn, Richard A, East, Michael P, and Francis, Joshua W. 2014. 'ARF-Like (ARL) Proteins.' in, *Ras Superfamily Small G Proteins: Biology and Mechanisms 2* (Springer).

Kalderon, D. 2004. 'Hedgehog signaling: Costal-2 bridges the transduction gap', *Curr Biol*, 14: R67-9.

Kasarskis, A., Manova, K., and Anderson, K. V. 1998. 'A phenotype-based screen for embryonic lethal mutations in the mouse', *Proc Natl Acad Sci U S A*, 95: 7485-90.

Keady, B. T., Samtani, R., Tobita, K., Tsuchya, M., San Agustin, J. T., Follit, J. A., Jonassen, J. A., Subramanian, R., Lo, C. W., and Pazour, G. J. 2012. 'IFT25 links the signal-dependent movement of Hedgehog components to intraflagellar transport', *Dev Cell*, 22: 940-51.

Kee, H. L., Dishinger, J. F., Blasius, T. L., Liu, C. J., Margolis, B., and Verhey, K. J. 2012. 'A size-exclusion permeability barrier and nucleoporins characterize a ciliary pore complex that regulates transport into cilia', *Nat Cell Biol*, 14: 431-7.

Kim, J., Kato, M., and Beachy, P. A. 2009. 'Gli2 trafficking links Hedgehog-dependent activation of Smoothened in the primary cilium to transcriptional activation in the nucleus', *Proc Natl Acad Sci U S A*, 106: 21666-71.

Kinnebrew, Maia, Iverson, Ellen J, Patel, Bhaven B, Pusapati, Ganesh V, Kong, Jennifer H, Johnson, Kristen A, Luchetti, Giovanni, Eckert, Kaitlyn M, McDonald, Jeffrey G, and Covey, Douglas F. 2019. 'Cholesterol accessibility at the ciliary membrane controls hedgehog signaling', *Elife*, 8.

Kisseleva, M. V., Wilson, M. P., and Majerus, P. W. 2000. 'The isolation and characterization of a cDNA encoding phospholipid-specific inositol polyphosphate 5-phosphatase', *J Biol Chem*, 275: 20110-6.

Klink, B. U., Zent, E., Juneja, P., Kuhlee, A., Raunser, S., and Wittinghofer, A. 2017. 'A recombinant BBSome core complex and how it interacts with ciliary cargo', *Elife*, 6.

Kniffin, CL. 10/30/2018. 'Joubert Syndrome Causative Genes', *Online Mendelian Inheritance in Man*, Joubert Syndrome.

Kong, J. H., Siebold, C., and Rohatgi, R. 2019. 'Biochemical mechanisms of vertebrate hedgehog signaling', *Development*, 146.

Kopinke, Daniel, Roberson, Elle C, and Reiter, Jeremy F. 2017. 'Ciliary hedgehog signaling restricts injury-induced adipogenesis', *Cell*, 170: 340-51. e12.

Kotani, M., Detheux, M., Vandenbogaerde, A., Communi, D., Vanderwinden, J. M., Le Poul, E., Brezillon, S., Tyldesley, R., Suarez-Huerta, N., Vandeput, F., Blanpain, C., Schiffmann, S. N., Vassart, G., and Parmentier, M. 2001. 'The metastasis suppressor gene KiSS-1 encodes kisspeptins, the natural ligands of the orphan G protein-coupled receptor GPR54', *J Biol Chem*, 276: 34631-6.

Kovacs, J. J., Whalen, E. J., Liu, R., Xiao, K., Kim, J., Chen, M., Wang, J., Chen, W., and Lefkowitz, R. J. 2008. 'Beta-arrestin-mediated localization of smoothened to the primary cilium', *Science*, 320: 1777-81.

Kowatsch, Christiane, Woolley, Rachel E, Kinnebrew, Maia, Rohatgi, Rajat, and Siebold, Christian. 2019. 'Structures of vertebrate Patched and Smoothened reveal intimate links between cholesterol and Hedgehog signalling', *Current opinion in structural biology*, 57: 204-14.

Kozminski, K. G., Beech, P. L., and Rosenbaum, J. L. 1995. 'The Chlamydomonas kinesin-like protein FLA10 is involved in motility associated with the flagellar membrane', *J Cell Biol*, 131: 1517-27.

Kozminski, K. G., Johnson, K. A., Forscher, P., and Rosenbaum, J. L. 1993. 'A motility in the eukaryotic flagellum unrelated to flagellar beating', *Proc Natl Acad Sci U S A*, 90: 5519-23.

Krauss, S., Concordet, J. P., and Ingham, P. W. 1993. 'A functionally conserved homolog of the Drosophila segment polarity gene hh is expressed in tissues with polarizing activity in zebrafish embryos', *Cell*, 75: 1431-44.

Kuwabara, P. E., Lee, M. H., Schedl, T., and Jefferis, G. S. 2000. 'A C. elegans patched gene, ptc-1, functions in germ-line cytokinesis', *Genes Dev*, 14: 1933-44.

Kwon, Ronald Y, Temiyasathit, Sara, Tummala, Padmaja, Quah, Clarence C, and Jacobs, Christopher R. 2010. 'Primary cilium-dependent mechanosensing is mediated by adenylyl cyclase 6 and cyclic AMP in bone cells', *The FASEB journal*, 24: 2859-68.

Lambright, D. G., Sondek, J., Bohm, A., Skiba, N. P., Hamm, H. E., and Sigler, P. B. 1996. 'The 2.0 A crystal structure of a heterotrimeric G protein', *Nature*, 379: 311-9.

Larkins, C. E., Aviles, G. D., East, M. P., Kahn, R. A., and Caspary, T. 2011. 'Arl13b regulates ciliogenesis and the dynamic localization of Shh signaling proteins', *Mol Biol Cell*, 22: 4694-703.

Latorraca, N. R., Wang, J. K., Bauer, B., Townshend, R. J. L., Hollingsworth, S. A., Olivieri, J. E., Xu, H. E., Sommer, M. E., and Dror, R. O. 2018. 'Molecular mechanism of GPCR-mediated arrestin activation', *Nature*, 557: 452-56.

Law, S. F., Yasuda, K., Bell, G. I., and Reisine, T. 1993. 'Gi alpha 3 and G(o) alpha selectively associate with the cloned somatostatin receptor subtype SSTR2', *J Biol Chem*, 268: 10721-7.

Lechtreck, K. F., Johnson, E. C., Sakai, T., Cochran, D., Ballif, B. A., Rush, J., Pazour, G. J., Ikebe, M., and Witman, G. B. 2009. 'The Chlamydomonas reinhardtii BBSome is an IFT cargo required for export of specific signaling proteins from flagella', *J Cell Biol*, 187: 1117-32.

Lechtreck, Karl-Ferdinand, Teltenkotter, A, and Grunow, Andrea. 1999. 'A 210 kDa protein is located in a membrane-microtubule linker at the distal end of mature and nascent basal bodies', *Journal of cell science*, 112: 1633-44.

Lee, K. L., Guevarra, M. D., Nguyen, A. M., Chua, M. C., Wang, Y., and Jacobs, C. R. 2015. 'The primary cilium functions as a mechanical and calcium signaling nexus', *Cilia*, 4: 7.

Legué, Emilie, and Liem Jr, Karel F. 2019. 'Tulp3 is a ciliary trafficking gene that regulates polycystic kidney disease', *Current Biology*, 29: 803-12. e5.

Lei, Qiubo, Zelman, Alice K, Kuang, Ed, Li, Shike, and Matise, Michael P. 2004. 'Transduction of graded Hedgehog signaling by a combination of Gli2 and Gli3 activator functions in the developing spinal cord', *Development*, 131: 3593-604.

Li, G., Vega, R., Nelms, K., Gekakis, N., Goodnow, C., McNamara, P., Wu, H., Hong, N. A., and Glynne, R. 2007. 'A role for Alstrom syndrome protein, alms1, in kidney ciliogenesis and cellular quiescence', *PLoS Genet*, 3: e8.

Li, S., Li, S., Han, Y., Tong, C., Wang, B., Chen, Y., and Jiang, J. 2016a. 'Regulation of Smoothened Phosphorylation and High-Level Hedgehog Signaling Activity by a Plasma Membrane Associated Kinase', *PLoS Biol*, 14: e1002481.

Li, Y., Kelly, W. G., Logsdon, J. M., Jr., Schurko, A. M., Harfe, B. D., Hill-Harfe, K. L., and Kahn, R. A. 2004. 'Functional genomic analysis of the ADP-ribosylation factor family of GTPases: phylogeny among diverse eukaryotes and function in C. elegans', *FASEB J*, 18: 1834-50.

Li, Y., Tian, X., Ma, M., Jerman, S., Kong, S., Somlo, S., and Sun, Z. 2016b. 'Deletion of ADP Ribosylation Factor-Like GTPase 13B Leads to Kidney Cysts', *J Am Soc Nephrol*, 27: 3628-38.

Li, Y., Wei, Q., Zhang, Y., Ling, K., and Hu, J. 2010. 'The small GTPases ARL-13 and ARL-3 coordinate intraflagellar transport and ciliogenesis', *J Cell Biol*, 189: 1039-51.

Liem, K. F., Jr., Ashe, A., He, M., Satir, P., Moran, J., Beier, D., Wicking, C., and Anderson, K. V. 2012. 'The IFT-A complex regulates Shh signaling through cilia structure and membrane protein trafficking', *J Cell Biol*, 197: 789-800.

Liem, K. F., Jr., He, M., Ocbina, P. J., and Anderson, K. V. 2009. 'Mouse Kif7/Costal2 is a cilia-associated protein that regulates Sonic hedgehog signaling', *Proc Natl Acad Sci U S A*, 106: 13377-82.

Liew, G. M., Ye, F., Nager, A. R., Murphy, J. P., Lee, J. S., Aguiar, M., Breslow, D. K., Gygi, S. P., and Nachury, M. V. 2014. 'The intraflagellar transport protein IFT27 promotes BBSome exit from cilia through the GTPase ARL6/BBS3', *Dev Cell*, 31: 265-78.

Lim, Y. S., Chua, C. E., and Tang, B. L. 2011. 'Rabs and other small GTPases in ciliary transport', *Biol Cell*, 103: 209-21.

Litingtung, Y., and Chiang, C. 2000. 'Specification of ventral neuron types is mediated by an antagonistic interaction between Shh and Gli3', *Nat Neurosci*, 3: 979-85.

Liu, A., Wang, B., and Niswander, L. A. 2005. 'Mouse intraflagellar transport proteins regulate both the activator and repressor functions of Gli transcription factors', *Development*, 132: 3103-11.

Logsdon, J. M., Jr., and Kahn, R. A. (ed.)^(eds.). 2004. *Arf Family GTPases. In: Kahn RA, editor.*

Lohse, M. J., Andexinger, S., Pitcher, J., Trukawinski, S., Codina, J., Faure, J. P., Caron, M. G., and Lefkowitz, R. J. 1992. 'Receptor-specific desensitization with purified proteins. Kinase dependence and receptor specificity of beta-arrestin and arrestin in the beta 2-adrenergic receptor and rhodopsin systems', *J Biol Chem*, 267: 8558-64.

Lohse, M. J., Benovic, J. L., Codina, J., Caron, M. G., and Lefkowitz, R. J. 1990. 'beta-Arrestin: a protein that regulates beta-adrenergic receptor function', *Science*, 248: 1547-50.

Loktev, A. V., and Jackson, P. K. 2013. 'Neuropeptide Y family receptors traffic via the Bardet-Biedl syndrome pathway to signal in neuronal primary cilia', *Cell Rep*, 5: 1316-29.

Lu, H., Toh, M. T., Narasimhan, V., Thamilselvam, S. K., Choksi, S. P., and Roy, S. 2015. 'A function for the Joubert syndrome protein Arl13b in ciliary membrane extension and ciliary length regulation', *Dev Biol*, 397: 225-36.

Lu, Q. R., Yuk, D., Alberta, J. A., Zhu, Z., Pawlitzky, I., Chan, J., McMahon, A. P., Stiles, C. D., and Rowitch, D. H. 2000. 'Sonic hedgehog--regulated oligodendrocyte lineage genes encoding bHLH proteins in the mammalian central nervous system', *Neuron*, 25: 317-29.

Luchetti, G., Sircar, R., Kong, J. H., Nachtergaele, S., Sagner, A., Byrne, E. F., Covey, D. F., Siebold, C., and Rohatgi, R. 2016a. 'Cholesterol activates the G-protein coupled receptor Smoothened to promote Hedgehog signaling', *Elife*, 5: e20304.

———. 2016b. 'Cholesterol activates the G-protein coupled receptor Smoothened to promote Hedgehog signaling', *Elife*, 5.

Lutz, Thomas A, and Woods, Stephen C. 2012. 'Overview of animal models of obesity', *Current protocols in pharmacology*, 58: 5.61. 1-5.61. 18.

Ma, M., Tian, X., Igarashi, P., Pazour, G. J., and Somlo, S. 2013. 'Loss of cilia suppresses cyst growth in genetic models of autosomal dominant polycystic kidney disease', *Nat Genet*, 45: 1004-12.

Ma, Ming, Gallagher, Anna-Rachel, and Somlo, Stefan. 2017. 'Ciliary mechanisms of cyst formation in polycystic kidney disease', *Cold Spring Harbor Perspectives in Biology*, 9: a028209.

Ma, Ming, Legué, Emilie, Tian, Xin, Somlo, Stefan, and Liem, Karel F. 2019. 'Cell-autonomous Hedgehog signaling is not required for cyst formation in autosomal dominant polycystic kidney disease', *Journal of the American Society of Nephrology*, 30: 2103-11.

Maerz, L. D., Burkhalter, M. D., Schilpp, C., Wittekindt, O. H., Frick, M., and Philipp, M. 2019. 'Pharmacological cholesterol depletion disturbs ciliogenesis and ciliary function in developing zebrafish', *Commun Biol*, 2: 31.

Manton, I, and Clarke, B. 1952. 'An electron microscope study of the spermatozoid of Sphagnum', *Journal of experimental botany*: 265-75.

Maria, Bernard L, Hoang, Karin BN, Tusa, Ronald J, Mancuso, Anthony A, Hamed, Latif M, Quisling, Ronald G, Hove, Martin T, Fennell, Eileen B, Booth-Jones, Margaret, and Ringdahl, Deborah M. 1997. '" Joubert syndrome" revisited: key ocular motor signs with magnetic resonance imaging correlation', *Journal of child neurology*, 12: 423-30.

Mariani, L. E., Bijlsma, M. F., Ivanova, A. A., Suciu, S. K., Kahn, R. A., and Caspary, T. 2016. 'Arl13b regulates Shh signaling from both inside and outside the cilium', *Mol Biol Cell*.

Marigo, V., and Tabin, C. J. 1996. 'Regulation of patched by sonic hedgehog in the developing neural tube', *Proc Natl Acad Sci U S A*, 93: 9346-51.

Marion, Vincent, Mockel, Anaïs, De Melo, Charlie, Obringer, Cathy, Claussmann, Aurélie, Simon, Alban, Messaddeq, Nadia, Durand, Myriam, Dupuis, Luc, and Loeffler, Jean-Philippe. 2012. 'BBS-induced ciliary defect enhances adipogenesis, causing paradoxical higher-insulin sensitivity, glucose usage, and decreased inflammatory response', *Cell metabolism*, 16: 363-77.

Marley, A., and von Zastrow, M. 2010. 'DISC1 regulates primary cilia that display specific dopamine receptors', *PLoS One*, 5: e10902.

Marshall, W. F. 2008. 'Basal bodies platforms for building cilia', *Curr Top Dev Biol*, 85: 1-22.
Marshall, W. F., and Rosenbaum, J. L. 2001. 'Intraflagellar transport balances continuous turnover of outer doublet microtubules: implications for flagellar length control', *J Cell Biol*, 155: 405-14.
Matise, M. P., Epstein, D. J., Park, H. L., Platt, K. A., and Joyner, A. L. 1998. 'Gli2 is required for induction of floor plate and adjacent cells, but not most ventral neurons in the mouse central nervous system', *Development*, 125: 2759-70.
May, Scott R, Ashique, Amir M, Karlen, Mattias, Wang, Baolin, Shen, Yiguo, Zarbalis, Kostantinos, Reiter, Jeremy, Ericson, Johan, and Peterson, Andrew S. 2005. 'Loss of the retrograde motor for IFT disrupts localization of Smo to cilia and prevents the expression of both activator and repressor functions of Gli', *Dev Biol*, 287: 378-89.
McGrath, J., Somlo, S., Makova, S., Tian, X., and Brueckner, M. 2003. 'Two populations of node monocilia initiate left-right asymmetry in the mouse', *Cell*, 114: 61-73.
Meloni, A. R., Fralish, G. B., Kelly, P., Salahpour, A., Chen, J. K., Wechsler-Reya, R. J., Lefkowitz, R. J., and Caron, M. G. 2006. 'Smoothened signal transduction is promoted by G protein-coupled receptor kinase 2', *Mol Cell Biol*, 26: 7550-60.
Mick, D. U., Rodrigues, R. B., Leib, R. D., Adams, C. M., Chien, A. S., Gygi, S. P., and Nachury, M. V. 2015. 'Proteomics of Primary Cilia by Proximity Labeling', *Dev Cell*, 35: 497-512.
Miertzschke, Mandy, Koerner, Carolin, Spoerner, Michael, and Wittinghofer, Alfred. 2014. 'Structural insights into the small G-protein Arl13B and implications for Joubert syndrome', *Biochemical Journal*, 457: 301-11.
Milenkovic, L., Scott, M. P., and Rohatgi, R. 2009. 'Lateral transport of Smoothened from the plasma membrane to the membrane of the cilium', *J Cell Biol*, 187: 365-74.
Milenkovic, L., Weiss, L. E., Yoon, J., Roth, T. L., Su, Y. S., Sahl, S. J., Scott, M. P., and Moerner, W. E. 2015. 'Single-molecule imaging of Hedgehog pathway protein Smoothened in primary cilia reveals binding events regulated by Patched1', *Proc Natl Acad Sci U S A*, 112: 8320-5.
Mo, R., Freer, A. M., Zinyk, D. L., Crackower, M. A., Michaud, J., Heng, H. H., Chik, K. W., Shi, X. M., Tsui, L. C., Cheng, S. H., Joyner, A. L., and Hui, C. 1997. 'Specific and redundant functions of Gli2 and Gli3 zinc finger genes in skeletal patterning and development', *Development*, 124: 113-23.
Mochizuki, Toshio, Wu, Guanqing, Hayashi, Tomohito, Xenophontos, Stavroulla L, Veldhuisen, Barbera, Saris, Jasper J, Reynolds, David M, Cai, Yiqiang, Gabow, Patricia A, and Pierides, Alkis. 1996. 'PKD2, a gene for polycystic kidney disease that encodes an integral membrane protein', *Science*, 272: 1339-42.
Muenke, M., and Beachy, P. A. 2000. 'Genetics of ventral forebrain development and holoprosencephaly', *Curr Opin Genet Dev*, 10: 262-9.
Mukherjee, S., Jansen, V., Jikeli, J. F., Hamzeh, H., Alvarez, L., Dombrowski, M., Balbach, M., Strunker, T., Seifert, R., Kaupp, U. B., and Wachten, D. 2016. 'A novel biosensor to study cAMP dynamics in cilia and flagella', *Elife*, 5.
Mukhopadhyay, S., Wen, X., Chih, B., Nelson, C. D., Lane, W. S., Scales, S. J., and Jackson, P. K. 2010. 'TULP3 bridges the IFT-A complex and membrane phosphoinositides to promote trafficking of G protein-coupled receptors into primary cilia', *Genes Dev*, 24: 2180-93.
Mukhopadhyay, S., Wen, X., Ratti, N., Loktev, A., Rangell, L., Scales, S. J., and Jackson, P. K. 2013. 'The ciliary G-protein-coupled receptor Gpr161 negatively regulates the Sonic hedgehog pathway via cAMP signaling', *Cell*, 152: 210-23.
Muller, P., Rogers, K. W., Jordan, B. M., Lee, J. S., Robson, D., Ramanathan, S., and Schier, A. F. 2012. 'Differential diffusivity of Nodal and Lefty underlies a reaction-diffusion patterning system', *Science*, 336: 721-4.

Murdoch, J. N., and Copp, A. J. 2010. 'The relationship between sonic Hedgehog signaling, cilia, and neural tube defects', *Birth Defects Res A Clin Mol Teratol*, 88: 633-52.

Murray, S. A., Morgan, J. L., Kane, C., Sharma, Y., Heffner, C. S., Lake, J., and Donahue, L. R. 2010. 'Mouse gestation length is genetically determined', *PLoS One*, 5: e12418.

Myers, B. R., Neahring, L., Zhang, Y., Roberts, K. J., and Beachy, P. A. 2017. 'Rapid, direct activity assays for Smoothened reveal Hedgehog pathway regulation by membrane cholesterol and extracellular sodium', *Proc Natl Acad Sci U S A*, 114: E11141-E50.

Myers, B. R., Sever, N., Chong, Y. C., Kim, J., Belani, J. D., Rychnovsky, S., Bazan, J. F., and Beachy, P. A. 2013. 'Hedgehog pathway modulation by multiple lipid binding sites on the smoothened effector of signal response', *Dev Cell*, 26: 346-57.

Mykytyn, K., and Askwith, C. 2017. 'G-Protein-Coupled Receptor Signaling in Cilia', *Cold Spring Harb Perspect Biol*, 9: a028183.

Nachtergaele, S., Mydock, L. K., Krishnan, K., Rammohan, J., Schlesinger, P. H., Covey, D. F., and Rohatgi, R. 2012. 'Oxysterols are allosteric activators of the oncoprotein Smoothened', *Nat Chem Biol*, 8: 211-20.

Nachtergaele, S., Whalen, D. M., Mydock, L. K., Zhao, Z., Malinauskas, T., Krishnan, K., Ingham, P. W., Covey, D. F., Siebold, C., and Rohatgi, R. 2013. 'Structure and function of the Smoothened extracellular domain in vertebrate Hedgehog signaling', *Elife*, 2: e01340.

Nachury, M. V. 2014. 'How do cilia organize signalling cascades?', *Philos Trans R Soc Lond B Biol Sci*, 369.

Nachury, M. V., Loktev, A. V., Zhang, Q., Westlake, C. J., Peranen, J., Merdes, A., Slusarski, D. C., Scheller, R. H., Bazan, J. F., Sheffield, V. C., and Jackson, P. K. 2007. 'A core complex of BBS proteins cooperates with the GTPase Rab8 to promote ciliary membrane biogenesis', *Cell*, 129: 1201-13.

Nager, A. R., Goldstein, J. S., Herranz-Perez, V., Portran, D., Ye, F., Garcia-Verdugo, J. M., and Nachury, M. V. 2017. 'An Actin Network Dispatches Ciliary GPCRs into Extracellular Vesicles to Modulate Signaling', *Cell*, 168: 252-63 e14.

Nanni, L., Ming, J. E., Bocian, M., Steinhaus, K., Bianchi, D. W., Die-Smulders, C., Giannotti, A., Imaizumi, K., Jones, K. L., Campo, M. D., Martin, R. A., Meinecke, P., Pierpont, M. E., Robin, N. H., Young, I. D., Roessler, E., and Muenke, M. 1999. 'The mutational spectrum of the sonic hedgehog gene in holoprosencephaly: SHH mutations cause a significant proportion of autosomal dominant holoprosencephaly', *Hum Mol Genet*, 8: 2479-88.

Nauli, S. M., Alenghat, F. J., Luo, Y., Williams, E., Vassilev, P., Li, X., Elia, A. E., Lu, W., Brown, E. M., Quinn, S. J., Ingber, D. E., and Zhou, J. 2003. 'Polycystins 1 and 2 mediate mechanosensation in the primary cilium of kidney cells', *Nat Genet*, 33: 129-37.

Nonaka, S., Shiratori, H., Saijoh, Y., and Hamada, H. 2002. 'Determination of left-right patterning of the mouse embryo by artificial nodal flow', *Nature*, 418: 96-9.

Nonaka, S., Tanaka, Y., Okada, Y., Takeda, S., Harada, A., Kanai, Y., Kido, M., and Hirokawa, N. 1998. 'Randomization of left-right asymmetry due to loss of nodal cilia generating leftward flow of extraembryonic fluid in mice lacking KIF3B motor protein', *Cell*, 95: 829-37.

Norman, R. X., Ko, H. W., Huang, V., Eun, C. M., Abler, L. L., Zhang, Z., Sun, X., and Eggenschwiler, J. T. 2009. 'Tubby-like protein 3 (TULP3) regulates patterning in the mouse embryo through inhibition of Hedgehog signaling', *Hum Mol Genet*, 18: 1740-54.

Nozaki, S., Katoh, Y., Terada, M., Michisaka, S., Funabashi, T., Takahashi, S., Kontani, K., and Nakayama, K. 2017. 'Regulation of ciliary retrograde protein trafficking by the Joubert syndrome proteins ARL13B and INPP5E', *J Cell Sci*, 130: 563-76.

Nusslein-Volhard, C., and Wieschaus, E. 1980. 'Mutations affecting segment number and polarity in Drosophila', *Nature*, 287: 795-801.

Ocbina, P. J., and Anderson, K. V. 2008. 'Intraflagellar transport, cilia, and mammalian Hedgehog signaling: analysis in mouse embryonic fibroblasts', *Dev Dyn*, 237: 2030-8.

Ogden, S. K., Fei, D. L., Schilling, N. S., Ahmed, Y. F., Hwa, J., and Robbins, D. J. 2008. 'G protein Galphai functions immediately downstream of Smoothened in Hedgehog signalling', *Nature*, 456: 967-70.

Pal, K., Hwang, S. H., Somatilaka, B., Badgandi, H., Jackson, P. K., DeFea, K., and Mukhopadhyay, S. 2016. 'Smoothened determines beta-arrestin-mediated removal of the G protein-coupled receptor Gpr161 from the primary cilium', *J Cell Biol*, 212: 861-75.

Parisi, M. A. 2019. 'The molecular genetics of Joubert syndrome and related ciliopathies: The challenges of genetic and phenotypic heterogeneity', *Transl Sci Rare Dis*, 4: 25-49.

Parisi, Melissa, and Glass, Ian. 2017. 'Joubert syndrome', *GeneReviews®[Internet]*.

Park, HL, Bai, C, Platt, KA, Matise, MP, Beeghly, A, Hui, CC, Nakashima, M, and Joyner, AL. 2000. 'Mouse Gli1 mutants are viable but have defects in SHH signaling in combination with a Gli2 mutation', *Development*, 127: 1593-605.

Park, T. J., Haigo, S. L., and Wallingford, J. B. 2006. 'Ciliogenesis defects in embryos lacking inturned or fuzzy function are associated with failure of planar cell polarity and Hedgehog signaling', *Nat Genet*, 38: 303-11.

Pazour, G. J., Baker, S. A., Deane, J. A., Cole, D. G., Dickert, B. L., Rosenbaum, J. L., Witman, G. B., and Besharse, J. C. 2002a. 'The intraflagellar transport protein, IFT88, is essential for vertebrate photoreceptor assembly and maintenance', *J Cell Biol*, 157: 103-13.

Pazour, G. J., Dickert, B. L., Vucica, Y., Seeley, E. S., Rosenbaum, J. L., Witman, G. B., and Cole, D. G. 2000. 'Chlamydomonas IFT88 and its mouse homologue, polycystic kidney disease gene tg737, are required for assembly of cilia and flagella', *J Cell Biol*, 151: 709-18.

Pazour, G. J., Wilkerson, C. G., and Witman, G. B. 1998. 'A dynein light chain is essential for the retrograde particle movement of intraflagellar transport (IFT)', *J Cell Biol*, 141: 979-92.

Pazour, Gregory J, San Agustin, Jovenal T, Follit, John A, Rosenbaum, Joel L, and Witman, George B. 2002b. 'Polycystin-2 localizes to kidney cilia and the ciliary level is elevated in orpk mice with polycystic kidney disease', *Current Biology*, 12: R378-R80.

Pettersen, E. F., Goddard, T. D., Huang, C. C., Couch, G. S., Greenblatt, D. M., Meng, E. C., and Ferrin, T. E. 2004. 'UCSF Chimera--a visualization system for exploratory research and analysis', *J Comput Chem*, 25: 1605-12.

Phua, S. C., Lin, Y. C., and Inoue, T. 2015. 'An intelligent nano-antenna: Primary cilium harnesses TRP channels to decode polymodal stimuli', *Cell calcium*, 58: 415-22.

Placzek, M., and Briscoe, J. 2018. 'Sonic hedgehog in vertebrate neural tube development', *Int J Dev Biol*, 62: 225-34.

Polizio, A. H., Chinchilla, P., Chen, X., Manning, D. R., and Riobo, N. A. 2011. 'Sonic Hedgehog activates the GTPases Rac1 and RhoA in a Gli-independent manner through coupling of smoothened to Gi proteins', *Sci Signal*, 4: pt7.

Porter, J. A., Young, K. E., and Beachy, P. A. 1996. 'Cholesterol modification of hedgehog signaling proteins in animal development', *Science*, 274: 255-9.

Qi, X., Liu, H., Thompson, B., McDonald, J., Zhang, C., and Li, X. 2019. 'Cryo-EM structure of oxysterol-bound human Smoothened coupled to a heterotrimeric Gi', *Nature*, 571: 279-83.

Rafiullah, R., Long, A. B., Ivanova, A. A., Ali, H., Berkel, S., Mustafa, G., Paramasivam, N., Schlesner, M., Wiemann, S., Wade, R. C., Bolthauser, E., Blum, M., Kahn, R. A., Caspary, T., and Rappold, G. A. 2017. 'A novel homozygous ARL13B variant in patients with Joubert syndrome impairs its guanine nucleotide-exchange factor activity', *Eur J Hum Genet*, 25: 1324-34.

Raleigh, D. R., and Reiter, J. F. 2019. 'Misactivation of Hedgehog signaling causes inherited and sporadic cancers', *J Clin Invest*, 129: 465-75.
Rao, R., Salloum, R., Xin, M., and Lu, Q. R. 2016. 'The G protein Galphas acts as a tumor suppressor in sonic hedgehog signaling-driven tumorigenesis', *Cell Cycle*, 15: 1325-30.
Reiter, J. F., Blacque, O. E., and Leroux, M. R. 2012. 'The base of the cilium: roles for transition fibres and the transition zone in ciliary formation, maintenance and compartmentalization', *EMBO Rep*, 13: 608-18.
Reiter, J. F., and Leroux, M. R. 2017. 'Genes and molecular pathways underpinning ciliopathies', *Nat Rev Mol Cell Biol*, 18: 533-47.
Revenkova, E., Liu, Q., Gusella, G. L., and Iomini, C. 2018. 'The Joubert syndrome protein ARL13B binds tubulin to maintain uniform distribution of proteins along the ciliary membrane', *J Cell Sci*, 131.
Ribes, V., Balaskas, N., Sasai, N., Cruz, C., Dessaud, E., Cayuso, J., Tozer, S., Yang, L. L., Novitch, B., Marti, E., and Briscoe, J. 2010. 'Distinct Sonic Hedgehog signaling dynamics specify floor plate and ventral neuronal progenitors in the vertebrate neural tube', *Genes Dev*, 24: 1186-200.
Riddle, R. D., Johnson, R. L., Laufer, E., and Tabin, C. 1993. 'Sonic hedgehog mediates the polarizing activity of the ZPA', *Cell*, 75: 1401-16.
Rink, J. C., Gurley, K. A., Elliott, S. A., and Sanchez Alvarado, A. 2009. 'Planarian Hh signaling regulates regeneration polarity and links Hh pathway evolution to cilia', *Science*, 326: 1406-10.
Riobo, N. A., Saucy, B., Dilizio, C., and Manning, D. R. 2006. 'Activation of heterotrimeric G proteins by Smoothened', *Proc Natl Acad Sci U S A*, 103: 12607-12.
Rivero-Gutiérrez, Belén, Anzola, A, Martínez-Augustin, O, and de Medina, F Sánchez. 2014. 'Stain-free detection as loading control alternative to Ponceau and housekeeping protein immunodetection in Western blotting', *Analytical biochemistry*, 467: 1-3.
Roelink, H, Porter, JA, Chiang, C, Tanabe, Y, Chang, DT, Beachy, PA, and Jessell, TM. 1995a. 'Floor plate and motor neuron induction by different concentrations of the amino-terminal cleavage product of sonic hedgehog autoproteolysis', *Cell*, 81: 445-55.
Roelink, H., Augsburger, A., Heemskerk, J., Korzh, V., Norlin, S., Ruiz i Altaba, A., Tanabe, Y., Placzek, M., Edlund, T., Jessell, T. M., and et al. 1994. 'Floor plate and motor neuron induction by vhh-1, a vertebrate homolog of hedgehog expressed by the notochord', *Cell*, 76: 761-75.
Roelink, H., Porter, J. A., Chiang, C., Tanabe, Y., Chang, D. T., Beachy, P. A., and Jessell, T. M. 1995b. 'Floor plate and motor neuron induction by different concentrations of the amino-terminal cleavage product of sonic hedgehog autoproteolysis', *Cell*, 81: 445-55.
Roessler, E., Belloni, E., Gaudenz, K., Jay, P., Berta, P., Scherer, S. W., Tsui, L. C., and Muenke, M. 1996. 'Mutations in the human Sonic Hedgehog gene cause holoprosencephaly', *Nat Genet*, 14: 357-60.
Roessler, E., Belloni, E., Gaudenz, K., Vargas, F., Scherer, S. W., Tsui, L. C., and Muenke, M. 1997. 'Mutations in the C-terminal domain of Sonic Hedgehog cause holoprosencephaly', *Hum Mol Genet*, 6: 1847-53.
Rohatgi, R., Milenkovic, L., Corcoran, R. B., and Scott, M. P. 2009. 'Hedgehog signal transduction by Smoothened: pharmacologic evidence for a 2-step activation process', *Proc Natl Acad Sci U S A*, 106: 3196-201.
Rohatgi, R., Milenkovic, L., and Scott, M. P. 2007. 'Patched1 regulates hedgehog signaling at the primary cilium', *Science*, 317: 372-6.
Röhlich, Pál. 1975. 'The sensory cilium of retinal rods is analogous to the transitional zone of motile cilia', *Cell and tissue research*, 161: 421-30.
Romani, Marta, Micalizzi, Alessia, and Valente, Enza Maria. 2013. 'Joubert syndrome: congenital cerebellar ataxia with the molar tooth', *The Lancet Neurology*, 12: 894-905.

Rosenbaum, J. L., and Child, F. M. 1967. 'Flagellar regeneration in protozoan flagellates', *J Cell Biol*, 34: 345-64.
Rosenbaum, J. L., and Witman, G. B. 2002. 'Intraflagellar transport', *Nat Rev Mol Cell Biol*, 3: 813-25.
Roy, K., Jerman, S., Jozsef, L., McNamara, T., Onyekaba, G., Sun, Z., and Marin, E. P. 2017. 'Palmitoylation of the ciliary GTPase ARL13b is necessary for its stability and its role in cilia formation', *J Biol Chem*, 292: 17703-17.
Roy, S. 2012. 'Cilia and Hedgehog: when and how was their marriage solemnized?', *Differentiation*, 83: S43-8.
Ruat, M., Traiffort, E., Arrang, J. M., Tardivel-Lacombe, J., Diaz, J., Leurs, R., and Schwartz, J. C. 1993. 'A novel rat serotonin (5-HT6) receptor: molecular cloning, localization and stimulation of cAMP accumulation', *Biochem Biophys Res Commun*, 193: 268-76.
Rudolf, A. F., Kinnebrew, M., Kowatsch, C., Ansell, T. B., El Omari, K., Bishop, B., Pardon, E., Schwab, R. A., Malinauskas, T., Qian, M., Duman, R., Covey, D. F., Steyaert, J., Wagner, A., Sansom, M. S. P., Rohatgi, R., and Siebold, C. 2019. 'The morphogen Sonic hedgehog inhibits its receptor Patched by a pincer grasp mechanism', *Nat Chem Biol*, 15: 975-82.
Ruel, L., Rodriguez, R., Gallet, A., Lavenant-Staccini, L., and Therond, P. P. 2003. 'Stability and association of Smoothened, Costal2 and Fused with Cubitus interruptus are regulated by Hedgehog', *Nat Cell Biol*, 5: 907-13.
Ruiz i Altaba, A. 1998. 'Combinatorial Gli gene function in floor plate and neuronal inductions by Sonic hedgehog', *Development*, 125: 2203-12.
Saarikangas, J., Zhao, H., and Lappalainen, P. 2010. 'Regulation of the actin cytoskeleton-plasma membrane interplay by phosphoinositides', *Physiol Rev*, 90: 259-89.
Sakuma, R., Ohnishi Yi, Y., Meno, C., Fujii, H., Juan, H., Takeuchi, J., Ogura, T., Li, E., Miyazono, K., and Hamada, H. 2002. 'Inhibition of Nodal signalling by Lefty mediated through interaction with common receptors and efficient diffusion', *Genes Cells*, 7: 401-12.
Scherz, P. J., McGlinn, E., Nissim, S., and Tabin, C. J. 2007. 'Extended exposure to Sonic hedgehog is required for patterning the posterior digits of the vertebrate limb', *Dev Biol*, 308: 343-54.
Schlacht, A., Mowbrey, K., Elias, M., Kahn, R. A., and Dacks, J. B. 2013. 'Ancient complexity, opisthokont plasticity, and discovery of the 11th subfamily of Arf GAP proteins', *Traffic*, 14: 636-49.
Schulz, S., Handel, M., Schreff, M., Schmidt, H., and Hollt, V. 2000. 'Localization of five somatostatin receptors in the rat central nervous system using subtype-specific antibodies', *J Physiol Paris*, 94: 259-64.
Seixas, C., Choi, S. Y., Polgar, N., Umberger, N. L., East, M. P., Zuo, X., Moreiras, H., Ghossoub, R., Benmerah, A., Kahn, R. A., Fogelgren, B., Caspary, T., Lipschutz, J. H., and Barral, D. C. 2016. 'Arl13b and the exocyst interact synergistically in ciliogenesis', *Mol Biol Cell*, 27: 308-20.
Shaheen, R., Szymanska, K., Basu, B., Patel, N., Ewida, N., Faqeih, E., Al Hashem, A., Derar, N., Alsharif, H., Aldahmesh, M. A., Alazami, A. M., Hashem, M., Ibrahim, N., Abdulwahab, F. M., Sonbul, R., Alkuraya, H., Alnemer, M., Al Tala, S., Al-Husain, M., Morsy, H., Seidahmed, M. Z., Meriki, N., Al-Owain, M., AlShahwan, S., Tabarki, B., Salih, M. A., Ciliopathy, WorkingGroup, Faquih, T., El-Kalioby, M., Ueffing, M., Boldt, K., Logan, C. V., Parry, D. A., Al Tassan, N., Monies, D., Megarbane, A., Abouelhoda, M., Halees, A., Johnson, C. A., and Alkuraya, F. S. 2016. 'Characterizing the morbid genome of ciliopathies', *Genome Biol*, 17: 242.
Shen, J., Bronson, R. T., Chen, D. F., Xia, W., Selkoe, D. J., and Tonegawa, S. 1997. 'Skeletal and CNS defects in Presenilin-1-deficient mice', *Cell*, 89: 629-39.
Shenoy, S. K., McDonald, P. H., Kohout, T. A, and Lefkowitz, R. J. 2001. 'Regulation of receptor fate by ubiquitination of activated β2-adrenergic receptor and β-arrestin', *Science*, 294: 1307-13.

Shetty, A. C., Athri, P., Mondal, K., Horner, V. L., Steinberg, K. M., Patel, V., Caspary, T., Cutler, D. J., and Zwick, M. E. 2010. 'SeqAnt: a web service to rapidly identify and annotate DNA sequence variations', *BMC Bioinformatics*, 11: 471.

Shi, Xiaoyu, Garcia III, Galo, Van De Weghe, Julie C, McGorty, Ryan, Pazour, Gregory J, Doherty, Dan, Huang, Bo, and Reiter, Jeremy F. 2017. 'Super-resolution microscopy reveals that disruption of ciliary transition-zone architecture causes Joubert syndrome', *Nature cell biology*, 19: 1178.

Shimada, M., Tritos, N. A., Lowell, B. B., Flier, J. S., and Maratos-Flier, E. 1998. 'Mice lacking melanin-concentrating hormone are hypophagic and lean', *Nature*, 396: 670-4.

Shinde, Swapnil Rohidas, Nager, Andrew R, and Nachury, Maxence V. 2020. 'Ubiquitin chains earmark GPCRs for BBSome-mediated removal from cilia', *Journal of Cell Biology*, 219.

Sigg, M. A., Menchen, T., Lee, C., Johnson, J., Jungnickel, M. K., Choksi, S. P., Garcia, G., 3rd, Busengdal, H., Dougherty, G. W., Pennekamp, P., Werner, C., Rentzsch, F., Florman, H. M., Krogan, N., Wallingford, J. B., Omran, H., and Reiter, J. F. 2017. 'Evolutionary Proteomics Uncovers Ancient Associations of Cilia with Signaling Pathways', *Dev Cell*, 43: 744-62 e11.

Siljee, Jacqueline E, Wang, Yi, Bernard, Adelaide A, Ersoy, Baran A, Zhang, Sumei, Marley, Aaron, Von Zastrow, Mark, Reiter, Jeremy F, and Vaisse, Christian. 2018. 'Subcellular localization of MC4R with ADCY3 at neuronal primary cilia underlies a common pathway for genetic predisposition to obesity', *Nature genetics*, 50: 180-85.

Singla, V., and Reiter, J. F. 2006. 'The primary cilium as the cell's antenna: signaling at a sensory organelle', *Science*, 313: 629-33.

Slaats, G. G., Isabella, C. R., Kroes, H. Y., Dempsey, J. C., Gremmels, H., Monroe, G. R., Phelps, I. G., Duran, K. J., Adkins, J., Kumar, S. A., Knutzen, D. M., Knoers, N. V., Mendelsohn, N. J., Neubauer, D., Mastroyianni, S. D., Vogt, J., Worgan, L., Karp, N., Bowdin, S., Glass, I. A., Parisi, M. A., Otto, E. A., Johnson, C. A., Hildebrandt, F., van Haaften, G., Giles, R. H., and Doherty, D. 2016. 'MKS1 regulates ciliary INPP5E levels in Joubert syndrome', *J Med Genet*, 53: 62-72.

Slavotinek, A. M., Stone, E. M., Mykytyn, K., Heckenlively, J. R., Green, J. S., Heon, E., Musarella, M. A., Parfrey, P. S., Sheffield, V. C., and Biesecker, L. G. 2000. 'Mutations in MKKS cause Bardet-Biedl syndrome', *Nat Genet*, 26: 15-6.

Sorokin, S. P. 1968. 'Reconstructions of centriole formation and ciliogenesis in mammalian lungs', *J Cell Sci*, 3: 207-30.

St-Jacques, B., Hammerschmidt, M., and McMahon, A. P. 1999. 'Indian hedgehog signaling regulates proliferation and differentiation of chondrocytes and is essential for bone formation', *Genes Dev*, 13: 2072-86.

Stamataki, D., Ulloa, F., Tsoni, S. V., Mynett, A., and Briscoe, J. 2005. 'A gradient of Gli activity mediates graded Sonic Hedgehog signaling in the neural tube', *Genes Dev*, 19: 626-41.

Stamatakis, Alice M, Van Swieten, Maaike, Basiri, Marcus L, Blair, Grace A, Kantak, Pranish, and Stuber, Garret D. 2016. 'Lateral hypothalamic area glutamatergic neurons and their projections to the lateral habenula regulate feeding and reward', *Journal of Neuroscience*, 36: 302-11.

Stolc, V., Samanta, M. P., Tongprasit, W., and Marshall, W. F. 2005. 'Genome-wide transcriptional analysis of flagellar regeneration in Chlamydomonas reinhardtii identifies orthologs of ciliary disease genes', *Proc Natl Acad Sci U S A*, 102: 3703-7.

Stone, D. M., Hynes, M., Armanini, M., Swanson, T. A., Gu, Q., Johnson, R. L., Scott, M. P., Pennica, D., Goddard, A., Phillips, H., Noll, M., Hooper, J. E., de Sauvage, F., and Rosenthal, A. 1996. 'The tumour-suppressor gene patched encodes a candidate receptor for Sonic hedgehog', *Nature*, 384: 129-34.

Su, S., Phua, S. C., DeRose, R., Chiba, S., Narita, K., Kalugin, P. N., Katada, T., Kontani, K., Takeda, S., and Inoue, T. 2013. 'Genetically encoded calcium indicator illuminates calcium dynamics in primary cilia', *Nat Methods*, 10: 1105-7.

Sun, Zhaoxia, Amsterdam, Adam, Pazour, Gregory J, Cole, Douglas G, Miller, Mark S, and Hopkins, Nancy. 2004. 'A genetic screen in zebrafish identifies cilia genes as a principal cause of cystic kidney', *Development*, 131: 4085-93.

Svard, J., Heby-Henricson, K., Persson-Lek, M., Rozell, B., Lauth, M., Bergstrom, A., Ericson, J., Toftgard, R., and Teglund, S. 2006. 'Genetic elimination of Suppressor of fused reveals an essential repressor function in the mammalian Hedgehog signaling pathway', *Dev Cell*, 10: 187-97.

Sztul, E., Chen, P. W., Casanova, J. E., Cherfils, J., Dacks, J. B., Lambright, D. G., Lee, F. S., Randazzo, P. A., Santy, L. C., Schurmann, A., Wilhelmi, I., Yohe, M. E., and Kahn, R. A. 2019. 'ARF GTPases and their GEFs and GAPs: concepts and challenges', *Mol Biol Cell*, 30: 1249-71.

Taipale, J., Chen, J. K., Cooper, M. K., Wang, B., Mann, R. K., Milenkovic, L., Scott, M. P., and Beachy, P. A. 2000. 'Effects of oncogenic mutations in Smoothened and Patched can be reversed by cyclopamine', *Nature*, 406: 1005-9.

Taipale, J., Cooper, M. K., Maiti, T., and Beachy, P. A. 2002. 'Patched acts catalytically to suppress the activity of Smoothened', *Nature*, 418: 892-7.

Takeda, S., Kadowaki, S., Haga, T., Takaesu, H., and Mitaku, S. 2002. 'Identification of G protein-coupled receptor genes from the human genome sequence', *FEBS Lett*, 520: 97-101.

Tay, S. Y., Ingham, P. W., and Roy, S. 2005. 'A homologue of the Drosophila kinesin-like protein Costal2 regulates Hedgehog signal transduction in the vertebrate embryo', *Development*, 132: 625-34.

Tay, Shang Yew, Yu, Xianwen, Wong, Kangli Noel, Panse, Pallavi, Ng, Chee Peng, and Roy, Sudipto. 2010. 'The iguana/DZIP1 protein is a novel component of the ciliogenic pathway essential for axonemal biogenesis', *Developmental Dynamics*, 239: 527-34.

Taylor, S. P., Dantas, T. J., Duran, I., Wu, S., Lachman, R. S., University of Washington Center for Mendelian Genomics, Consortium, Nelson, S. F., Cohn, D. H., Vallee, R. B., and Krakow, D. 2015. 'Mutations in DYNC2LI1 disrupt cilia function and cause short rib polydactyly syndrome', *Nat Commun*, 6: 7092.

Thacker, Jonathan S, Yeung, Derrick H, Staines, W Richard, and Mielke, John G. 2016. 'Total protein or high-abundance protein: Which offers the best loading control for Western blotting?', *Analytical biochemistry*, 496: 76-78.

Thomas, S., Cantagrel, V., Mariani, L., Serre, V., Lee, J. E., Elkhartoufi, N., de Lonlay, P., Desguerre, I., Munnich, A., Boddaert, N., Lyonnet, S., Vekemans, M., Lisgo, S. N., Caspary, T., Gleeson, J., and Attie-Bitach, T. 2015. 'Identification of a novel ARL13B variant in a Joubert syndrome-affected patient with retinal impairment and obesity', *Eur J Hum Genet*, 23: 621-7.

Tran, P. V., Haycraft, C. J., Besschetnova, T. Y., Turbe-Doan, A., Stottmann, R. W., Herron, B. J., Chesebro, A. L., Qiu, H., Scherz, P. J., Shah, J. V., Yoder, B. K., and Beier, D. R. 2008. 'THM1 negatively modulates mouse sonic hedgehog signal transduction and affects retrograde intraflagellar transport in cilia', *Nat Genet*, 40: 403-10.

Tukachinsky, H., Lopez, L. V., and Salic, A. 2010. 'A mechanism for vertebrate Hedgehog signaling: recruitment to cilia and dissociation of SuFu-Gli protein complexes', *J Cell Biol*, 191: 415-28.

Tuson, M., He, M., and Anderson, K. V. 2011. 'Protein kinase A acts at the basal body of the primary cilium to prevent Gli2 activation and ventralization of the mouse neural tube', *Development*, 138: 4921-30.

Tuz, K., Bachmann-Gagescu, R., O'Day, D. R., Hua, K., Isabella, C. R., Phelps, I. G., Stolarski, A. E., O'Roak, B. J., Dempsey, J. C., Lourenco, C., Alswaid, A., Bonnemann, C. G., Medne, L., Nampoothiri, S., Stark, Z., Leventer, R. J., Topcu, M., Cansu, A., Jagadeesh, S., Done, S., Ishak, G. E., Glass, I. A.,

Shendure, J., Neuhauss, S. C., Haldeman-Englert, C. R., Doherty, D., and Ferland, R. J. 2014. 'Mutations in CSPP1 cause primary cilia abnormalities and Joubert syndrome with or without Jeune asphyxiating thoracic dystrophy', *Am J Hum Genet*, 94: 62-72.

Van Eps, N., Altenbach, C., Caro, L. N., Latorraca, N. R., Hollingsworth, S. A., Dror, R. O., Ernst, O. P., and Hubbell, W. L. 2018. 'Gi- and Gs-coupled GPCRs show different modes of G-protein binding', *Proc Natl Acad Sci U S A*, 115: 2383-88.

Van Valkenburgh, H., Shern, J. F., Sharer, J. D., Zhu, X., and Kahn, R. A. 2001. 'ADP-ribosylation factors (ARFs) and ARF-like 1 (ARL1) have both specific and shared effectors: characterizing ARL1-binding proteins', *J Biol Chem*, 276: 22826-37.

Volta, Francesco, Scerbo, M Julia, Seelig, Anett, Wagner, Robert, O'Brien, Nils, Gerst, Felicia, Fritsche, Andreas, Häring, Hans-Ulrich, Zeigerer, Anja, and Ullrich, Susanne. 2019. 'Glucose homeostasis is regulated by pancreatic β-cell cilia via endosomal EphA-processing', *Nat Commun*, 10: 1-17.

Vorechovsky, I., Tingby, O., Hartman, M., Stromberg, B., Nister, M., Collins, V. P., and Toftgard, R. 1997. 'Somatic mutations in the human homologue of Drosophila patched in primitive neuroectodermal tumours', *Oncogene*, 15: 361-6.

Walker, Rebecca V, Keynton, Jennifer L, Grimes, Daniel T, Sreekumar, Vrinda, Williams, Debbie J, Esapa, Chris, Wu, Dongsheng, Knight, Martin M, and Norris, Dominic P. 2019. 'Ciliary exclusion of Polycystin-2 promotes kidney cystogenesis in an autosomal dominant polycystic kidney disease model', *Nat Commun*, 10: 1-11.

Walton, K. D., Warner, J., Hertzler, P. H., and McClay, D. R. 2009. 'Hedgehog signaling patterns mesoderm in the sea urchin', *Dev Biol*, 331: 26-37.

Wang, C., Wu, H., Evron, T., Vardy, E., Han, G. W., Huang, X. P., Hufeisen, S. J., Mangano, T. J., Urban, D. J., Katritch, V., Cherezov, V., Caron, M. G., Roth, B. L., and Stevens, R. C. 2014. 'Structural basis for Smoothened receptor modulation and chemoresistance to anticancer drugs', *Nat Commun*, 5: 4355.

Wang, C., Wu, H., Katritch, V., Han, G. W., Huang, X. P., Liu, W., Siu, F. Y., Roth, B. L., Cherezov, V., and Stevens, R. C. 2013. 'Structure of the human smoothened receptor bound to an antitumour agent', *Nature*, 497: 338-43.

Wang, Q., Cobo-Stark, P., Patel, V., Somlo, S., Han, P. L., and Igarashi, P. 2018. 'Adenylyl cyclase 5 deficiency reduces renal cyclic AMP and cyst growth in an orthologous mouse model of polycystic kidney disease', *Kidney Int*, 93: 403-15.

Wang, Y., Zhou, Z., Walsh, C. T., and McMahon, A. P. 2009. 'Selective translocation of intracellular Smoothened to the primary cilium in response to Hedgehog pathway modulation', *Proc Natl Acad Sci U S A*, 106: 2623-8.

Warburton-Pitt, S. R., Silva, M., Nguyen, K. C., Hall, D. H., and Barr, M. M. 2014. 'The nphp-2 and arl-13 genetic modules interact to regulate ciliogenesis and ciliary microtubule patterning in C. elegans', *PLoS Genet*, 10: e1004866.

Warner, J. F., McCarthy, A. M., Morris, R. L., and McClay, D. R. 2014. 'Hedgehog signaling requires motile cilia in the sea urchin', *Mol Biol Evol*, 31: 18-22.

Waters, A. M., and Beales, P. L. 2011. 'Ciliopathies: an expanding disease spectrum', *Pediatr Nephrol*, 26: 1039-56.

Weiss, L. E., Milenkovic, L., Yoon, J., Stearns, T., and Moerner, W. E. 2019. 'Motional dynamics of single Patched1 molecules in cilia are controlled by Hedgehog and cholesterol', *Proc Natl Acad Sci U S A*, 116: 5550-57.

Wen, X., Lai, C. K., Evangelista, M., Hongo, J. A., de Sauvage, F. J., and Scales, S. J. 2010. 'Kinetics of hedgehog-dependent full-length Gli3 accumulation in primary cilia and subsequent degradation', *Mol Cell Biol*, 30: 1910-22.

Wilson, C. W., Chen, M. H., and Chuang, P. T. 2009. 'Smoothened adopts multiple active and inactive conformations capable of trafficking to the primary cilium', *PLoS One*, 4: e5182.

Wolter, M., Reifenberger, J., Sommer, C., Ruzicka, T., and Reifenberger, G. 1997. 'Mutations in the human homologue of the Drosophila segment polarity gene patched (PTCH) in sporadic basal cell carcinomas of the skin and primitive neuroectodermal tumors of the central nervous system', *Cancer Res*, 57: 2581-5.

Xiao, K., and Shenoy, S. K. 2011. 'β2-adrenergic receptor lysosomal trafficking is regulated by ubiquitination of lysyl residues in two distinct receptor domains', *Journal of Biological Chemistry*, 286: 12785-95.

Xiao, X., Tang, J. J., Peng, C., Wang, Y., Fu, L., Qiu, Z. P., Xiong, Y., Yang, L. F., Cui, H. W., He, X. L., Yin, L., Qi, W., Wong, C. C., Zhao, Y., Li, B. L., Qiu, W. W., and Song, B. L. 2017. 'Cholesterol Modification of Smoothened Is Required for Hedgehog Signaling', *Mol Cell*, 66: 154-62 e10.

Xie, J., Murone, M., Luoh, S. M., Ryan, A., Gu, Q., Zhang, C., Bonifas, J. M., Lam, C. W., Hynes, M., Goddard, A., Rosenthal, A., Epstein, E. H., Jr., and de Sauvage, F. J. 1998. 'Activating Smoothened mutations in sporadic basal-cell carcinoma', *Nature*, 391: 90-2.

Yamamoto, M., and Kataoka, K. 1986. 'Electron microscopic observation of the primary cilium in the pancreatic islets', *Arch Histol Jpn*, 49: 449-57.

Yang, C., Chen, W., Chen, Y., and Jiang, J. 2012. 'Smoothened transduces Hedgehog signal by forming a complex with Evc/Evc2', *Cell Res*, 22: 1593-604.

Yang, T Tony, Tran, Minh Nguyet Thi, Chong, Weng Man, Huang, Chia-En, and Liao, Jung-Chi. 2019. 'Single-particle tracking localization microscopy reveals nonaxonemal dynamics of intraflagellar transport proteins at the base of mammalian primary cilia', *Mol Biol Cell*, 30: 828-37.

Yang, T. T., Chong, W. M., Wang, W. J., Mazo, G., Tanos, B., Chen, Z., Tran, T. M. N., Chen, Y. D., Weng, R. R., Huang, C. E., Jane, W. N., Tsou, M. B., and Liao, J. C. 2018. 'Super-resolution architecture of mammalian centriole distal appendages reveals distinct blade and matrix functional components', *Nat Commun*, 9: 2023.

Yasuda, K., Rens-Domiano, S., Breder, C. D., Law, S. F., Saper, C. B., Reisine, T., and Bell, G. I. 1992. 'Cloning of a novel somatostatin receptor, SSTR3, coupled to adenylylcyclase', *J Biol Chem*, 267: 20422-8.

Yavari, A., Nagaraj, R., Owusu-Ansah, E., Folick, A., Ngo, K., Hillman, T., Call, G., Rohatgi, R., Scott, M. P., and Banerjee, U. 2010. 'Role of lipid metabolism in smoothened derepression in hedgehog signaling', *Dev Cell*, 19: 54-65.

Ye, F., Nager, A. R., and Nachury, M. V. 2018. 'BBSome trains remove activated GPCRs from cilia by enabling passage through the transition zone', *J Cell Biol*, 217: 1847-68.

Yoon, Joshua, Comerci, Colin J, Weiss, Lucien E, Milenkovic, Ljiljana, Stearns, Tim, and Moerner, WE. 2019. 'Revealing nanoscale morphology of the primary cilium using super-resolution fluorescence microscopy', *Biophysical journal*, 116: 319-29.

Yoshiba, S., Shiratori, H., Kuo, I. Y., Kawasumi, A., Shinohara, K., Nonaka, S., Asai, Y., Sasaki, G., Belo, J. A., Sasaki, H., Nakai, J., Dworniczak, B., Ehrlich, B. E., Pennekamp, P., and Hamada, H. 2012. 'Cilia at the node of mouse embryos sense fluid flow for left-right determination via Pkd2', *Science*, 338: 226-31.

Yuan, S., Zhao, L., Brueckner, M., and Sun, Z. 2015. 'Intraciliary calcium oscillations initiate vertebrate left-right asymmetry', *Curr Biol*, 25: 556-67.

Zaghloul, N. A., and Brugmann, S. A. 2011. 'The emerging face of primary cilia', *Genesis*, 49: 231-46.

Zaghloul, N. A., and Katsanis, N. 2009. 'Mechanistic insights into Bardet-Biedl syndrome, a model ciliopathy', *J Clin Invest*, 119: 428-37.

Zhang, B., Zhuang, T., Lin, Q., Yang, B., Xu, X., Xin, G., Zhu, S., Wang, G., Yu, B., Zhang, T., Jiang, Q., and Zhang, C. 2019. 'Patched1-ArhGAP36-PKA-Inversin axis determines the ciliary translocation of Smoothened for Sonic Hedgehog pathway activation', *Proc Natl Acad Sci U S A*, 116: 874-79.

Zhang, C., Williams, E. H., Guo, Y., Lum, L., and Beachy, P. A. 2004. 'Extensive phosphorylation of Smoothened in Hedgehog pathway activation', *Proc Natl Acad Sci U S A*, 101: 17900-7.

Zhang, Q., Li, Y., Zhang, Y., Torres, V. E., Harris, P. C., Ling, K., and Hu, J. 2016. 'GTP-binding of ARL-3 is activated by ARL-13 as a GEF and stabilized by UNC-119', *Sci Rep*, 6: 24534.

Zhang, Q., Nishimura, D., Seo, S., Vogel, T., Morgan, D. A., Searby, C., Bugge, K., Stone, E. M., Rahmouni, K., and Sheffield, V. C. 2011. 'Bardet-Biedl syndrome 3 (Bbs3) knockout mouse model reveals common BBS-associated phenotypes and Bbs3 unique phenotypes', *Proc Natl Acad Sci U S A*, 108: 20678-83.

Zhang, W., Zhao, Y., Tong, C., Wang, G., Wang, B., Jia, J., and Jiang, J. 2005. 'Hedgehog-regulated Costal2-kinase complexes control phosphorylation and proteolytic processing of Cubitus interruptus', *Dev Cell*, 8: 267-78.

Zhang, X. M., Ramalho-Santos, M., and McMahon, A. P. 2001. 'Smoothened mutants reveal redundant roles for Shh and Ihh signaling including regulation of L/R symmetry by the mouse node', *Cell*, 106: 781-92.

Zhang, Y., Bulkley, D. P., Xin, Y., Roberts, K. J., Asarnow, D. E., Sharma, A., Myers, B. R., Cho, W., Cheng, Y., and Beachy, P. A. 2018. 'Structural Basis for Cholesterol Transport-like Activity of the Hedgehog Receptor Patched', *Cell*, 175: 1352-64 e14.

Zhao, Y., Tong, C., and Jiang, J. 2007. 'Hedgehog regulates smoothened activity by inducing a conformational switch', *Nature*, 450: 252-8.

Zimmermann, Karl Wilhelm. 1898. 'Beiträge zur Kenntniss einiger Drüsen und Epithelien', *Archiv für mikroskopische Anatomie*, 52: 552-706.

Zugasti, O., Rajan, J., and Kuwabara, P. E. 2005. 'The function and expansion of the Patched- and Hedgehog-related homologs in C. elegans', *Genome Res*, 15: 1402-10.